Sub-Cycle Light Field Synthesizer for Attosecond Science

Dissertation
zur Erlangung des Doktorgrades Doctor rerum naturalium
der Fakultät für Mathematik, Informatik und Naturwissenschaften
Fachbereich Physik
der Universität Hamburg

vorgelegt von:

Dipl.-Phys. Roland E. Mainz

Hamburg

2018

Gutachter der Dissertation:	Prof. Dr. Franz X. Kärtner *Universität Hamburg*
	Prof. Dr. Wilfried Wurth *Universität Hamburg*
Zusammensetzung der Prüfungskommission:	Prof. Dr. Franz X. Kärtner *Universität Hamburg*
	Prof. Dr. Markus Drescher *Universität Hamburg*
	Prof. Dr. Francesca Calegari *Universität Hamburg*
	PD. Dr. Guido Meier *Universität Hamburg*
	Prof. Dr. Daniela Pfannkuche *Universität Hamburg*
Vorsitzende der Prüfungskommission:	Prof. Dr. Daniela Pfannkuche
Datum der Disputation:	09.07.2019
Vorsitzender Fach-Promotionsausschusses PHYSIK:	Prof. Dr. Michael Potthoff
Leiter des Fachbereiches PHYSIK:	Prof Dr. Wolfgang Hansen
Dekan der Fakultät MIN:	Prof. Dr. Heinrich Graener

Abstract

The generation of energetic laser pulses with durations below one optical cycle is one of the current frontiers of ultrafast optics. Such sources attract enormous attention due to the implications they hold for studying extreme light-matter interactions and to harness attosecond pulse production via high harmonic generation (HHG). This thesis presents the implementation of a parallel parametric waveform synthesizer which generates sub-cycle pulses of light spanning more than two octaves of spectral bandwidth (500 nm to 2.2 µm) by coherent combination of individual ultra-broadband OPA sources covering different spectral ranges in the visible, near-infrared and infrared. The parallel approach to parametric waveform synthesis offers unique scaling potential with respect to bandwidth and pulse energy and it provides several control knobs to custom-sculpture the synthesized light-field transient.

Challenges of the parallel scheme are the required active timing stabilization and control system to stabilize such a complex multi-path interferometer to sub-cycle precision and to custom-sculpture the synthesized waveform. In the frame work of this thesis, several techniques to implement such a complex experiment with enhanced mechanical stability were demonstrated and furthermore this thesis introduces and demonstrates the first full timing control system for such a synthesizer. This includes newly developed optical timing tools, for which an active timing synchronization down to few tens of attoseconds is demonstrated. Furthermore, unique FPGA-based timing sensors were developed and allow to gain a deeper understanding of the timing and phase dynamics in such parametric sources. A novel scheme for carrier-envelope phase stable multi-octave-wide seed generation is also proposed and experimentally investigated. These efforts allowed for the very first controlled HHG driven with sub-cycle pulses from such a parallel parametric waveform synthesizer.

A full characterization of these novel pulses via attosecond streaking to fully recover the electric field transient of the synthesized waveform is ongoing. The synthesized pulse has a center wavelength of 1.8 µm and aims for efficient isolated attosecond pulse (IAP) production up to the water-window (284 eV - 543 eV). This source can be scaled potentially beyond the mJ-level of pulse energy by using novel pump laser technologies, which holds great potential for attosecond science.

Zusammenfassung

Die Erzeugung von hochenergetischen Laserpulsen mit Pulslängen unter einer optischen Periode ist einer der gegenwärtigen Forschungsschwerpunkte in der Nichtlinearen Optik und der Ultrakurzzeit-Spektroskopie. Die Entwicklung derartiger Laserquellen stößt auf großes Interesse, da sie neue Wege zur Untersuchung extremer Licht-Materie-Wechselwirkungen bieten und zur Erzeugung von Attosekunden-Lichtblitze genutzt werden können, welche durch hohe Harmonische generiert werden (HHG).

In dieser Arbeit wird der Aufbau eines parallel parametrischen Wellenformensynthesizers präsentiert, welcher in der Lage ist Pulse mit Subzyklen-Pulslängen zu generieren, die mehr als zwei Oktaven spektraler Bandbreite überspannen (500 nm bis 2.2 µm). Diese Bandbreite wird durch die kohärente Kombination von separaten ultrabreitbandigen optisch parametrischen Verstärkern (OPA) im sichtbaren, nahinfraroten und infraroten Spektralbereich erreicht. Eine Implementierung mittels paralleler Synthese bietet die einzigartige Perspektive derartige Quellen sowohl hinsichtlich ihrer Pulsenergie als auch ihrer spektralen Bandbreite weiter zu skalieren. Darüber hinaus bieten sich vielfältige Einstellmöglichkeiten um die synthetisierte Wellenform nach Bedarf zu formen.

Mit dem parallelen Ansatz gehen allerdings auch Herausforderungen einher, wie z.B. die Notwendigkeit ein Zeitsynchronisierungs- und Stabilisierungssystem zu implementieren. Dieses System ist erforderlich um den komplexen interferometrischen Aufbau mit meterlangen Lichtwegen so zu synchronisieren, dass die Lichtwege zueinander auf einem Bruchteil einer optischen Wellenlänge stabilisiert sind. Es wird weiterhin benötigt um den Lichtpuls gezielt formen zu können. Im Rahmen dieser Arbeit wurden verschiedene Techniken implementiert um den komplexen optischen Aufbau mit ausreichender mechanischer Stabilität zu versehen. Weiterhin führt diese Arbeit neue Techniken ein um erstmals eine volle Kontrolle über die synthetisierten Wellenformen zu gewinnen. Diese innovativen Techniken beinhalten ebenfalls neuartige optische Methoden zur Zeitmessung, welche die Synchronisierung zwischen den verschiedenen Laserblitzen mit Attosekundenauflösung ermöglichen. Weiterhin wurden einzigartige Synchronisationsdetektoren auf Basis von FPGAs entwickelt, welche u.a. einen tieferen Einblick in die Zeit- und Phasendynamik in einem parallelen Synthesizer erlauben. Auch eine neue Anordnung zur Erzeugung oktavenspannender

Quellpulse (Seeds) mit stabiler Träger-Einhüllenden-Phase (CEP) wurde nicht nur vorgeschlagen, sondern auch experimentell untersucht. Die zuvor genannten Maßnahmen ermöglichten erstmals die Erzeugung hoher Harmonischer getrieben durch Subzyklen-Laserblitze, welche von einem parallelen parametrischen Wellenformsynthesizer generiert wurden.
An einer vollständigen Charakterisierung dieser neuartigen Lichtblitze mittels Attosekunden-Ablenkung wird gegenwärtig gearbeitet. Diese Technik erlaubt es den zeitlichen Verlauf des optischen Lichtfeldes direkt und eindeutig zu bestimmen. Die synthetisierten Pulse haben eine Mittenwellenlänge von 1,8 µm und zielen damit auf die Erzeugung von isolierten Attosekunden-Lichtblitzen ab, dessen Photonenenergien das gesamte Wasserfenster abdecken (284 eV - 543 eV). Der Synthesizer bietet das Potential zur Skalierung jenseits von Pulsenergien im mJ-Breich mittels Verwendung neuartiger Pumplasertechnologien. Damit bietet diese Quelle neue experimentelle Zugänge zur Attosekundenphysik.

Acknowledgements

I am very thankful for having the opportunity to contribute to the development of sub-cycle ultrafast laser sources. This endeavor is impossible without talented colleagues and great friends along the way, whom I would like to thank.

First and foremost my deep gratitude goes to my supervisor Prof. Franz Kärtner. The Ultrafast Optics and X-Rays Division at the Center for Free-Electron Laser Science is a unique and highly inspiring environment full of opportunities. Franz leadership is gifted with encouragement, valuable advice and a wider view on things. He grants his students great freedom for their scientific development.

I also thank Prof. Wurth for mentoring my PhD-studies throughout the years.

The presented synthesizer was developed in close collaboration with my colleague and friend Giulio Maria Rossi. I experienced this collaboration as a prime example of scientific teamwork, shaped by constant inspiring exchange and a common vision to work on. This is similarly true for Dr. Yudong Yang, with whom we were able to apply the synthesized pulses to HHG in an attosecond beamline. I also thank Fabian Scheiba for joining and contributing to the project as well as performing the 2DSI pulse characterizations. It was amazing to spend time in the lab, on conferences and on holiday with you guys!

We are grateful for the work of Dr. Giovanni Cirmi, Dr. Oliver Mücke, and Dr. Shaobo Fang for starting to develop the first synthesizer prototype at CFEL, which provided the basis for the further advancement towards synthesized sub-cycle pulses. The synthesizer also benefited from the double-chirped mirrors designed by Dr. Shih-Hsuan Chia and from his advice on pulse compression in general. Furthermore, the simulations performed by Lu Wang were an important step towards modeling the dynamics of such an OPA-based system. I want to thank Dr. Giovanni Cirmi and Dr. Oliver Mücke also explicitly for leading the synthesizer and the attosecond-science subgroups respectively, for manifold contributions to our work, for sharing their scientific knowledge and for organizing our fruitful meetings. I also acknowledge the helpful discussions and enjoyable chats with Ravi Koustuban, Dr. Hüseyin Çankaya and Nico Klemke among many other amazing colleagues. Administrational tasks were easy thanks to the good soul of our group, Christine Berber.

I want to express my gratitude to my friends and parents and family who always supported me and with whom I had many joyful and memorable moments along my PhD journey. I also enjoyed the regular Friday evening dinners including Alice Cantaluppi and Francois Lemery.
My parents supported my curiosity for science and technology since my earliest childhood and laid an important foundation for my future development. Andres Bergmann was my first mentor and gifted me my first HeNe-laser at age 7 and sparked my passion for the unique light that lasers magically create. And last but not least, I want to thank my girlfriend Susanne for enchanting my life with your smile and gentle soul.

Contents

List of Abbreviations

2DSI	two dimensional spectral shearing interferometry
AC	alternating current
ADC	analog to digital converter
ATD	arrival time difference
ATI	above-threshold ionization
BBO	Beta barium borate
BOC	balanced optical cross-correlator
CAD	computer-aided design
CCD	charge-coupled device
CEP	carrier envelope phase
CMRR	common mode rejection ratio
CPA	chirped pulse amplifier
DAC	digital to analog converter
DC	direct current
DCM	double chirped mirror
DFG	difference-frequency generation
DM	dichroic mirror
DOPA	degenerate OPA
ENOB	effective number of bits
ETH	Ethernet network interface
f-2f	frequency-double-frequency interferometry
FEL	Free-electron laser
FFT	fast Fourier-transform
FP	Fourier-Plane
FPGA	field programmable gate array
FROG	frequency resolved optical gating
FT	Fourier-transform
GD	group delay
GDD	group delay dispersion
GVD	group velocity dispersion
HH	high harmonic(s)

HHG	high harmonic generation
HWP	half-wave plate
IP	internet protocol
IR	infrared radiation
KLM	Kerr-lens more-locking
LSB	least-significant bit(s)
NIR	near-IR radiation
NOPA	noncollinear OPA
OPA	optical parametric amplifier
OPCPA	optical parametric chirped-pulse amplifier
PCB	printed circuit board
PID	proportional integral differential (controller)
PHY	physical layer (at the signal-level)
PUT	pulse under test
PZT	piezo-(driven), based on piezo-effect
RAM	relative arrival-time difference random access memory
RF	radio frequency ($\sim$ MHz)
RP	relative phase
RMII	reduced media independent interface
SASE	self-amplified spontaneous emission
SFG	sum-frequency generation
SHG	second harmonic generation
SNR	signal-to-noise ratio
SPM	self-phase modulation
TCP	transmission control protocol
TEC	thermoelectric cooler
TFP	thin-film polarizer
THG	third-harmonic generation
Ti:Sa	Titanium doped sapphire
TL	transform limited (Fourier-limited)
TOD	third order dispersion
TOF	time-of-flight
VGA	video graphics array
VHDL	very high speed hardware description language
VIS	visible radiation
XUV	extreme ultra violet radiation
YAG	Yttrium aluminum garnet
WLG	white-light generation

Publication List

Peer-Reviewed Papers

[1] Giulio Maria Rossi, Lu Wang, **Roland E. Mainz**, Hüseyin Çankaya, Franz X. Kärtner and Giovanni Cirmi. CEP dependence of signal and idler upon pump-seed synchronization in optical parametric amplifiers. *Optics Letters*, 43(2):178-181, 2018.

[2] **Roland E. Mainz**, Giulio Maria Rossi, Giovanni Cirmi, Yudong Yang, Oliver D. Mücke, and Franz X. Kärtner. High-dynamic-range arrival time control for flexible, accurate and precise parametric sub-cycle waveform synthesis. *Optics Express*, 25(4):3052-3068, 2017.

[3] Oliver D. Mücke, Shaobo Fang, Giovanni Cirmi, Giulio Maria Rossi, Shih-Hsuan Chia, Hong Ye, Yudong Yang, **Roland E. Mainz**, Cristian Manzoni, Paolo Farinello, Giulio Cerullo and Franz X. Kärtner. Toward waveform nonlinear optics using multimillijoule sub-cycle waveform synthesizers. *IEEE Journal on Selected Topics in Quantum Electronics*, 21(5):1-12, 2015.

International Patents

[4] **Roland E. Mainz**, Giulio Maria Rossi, Franz X. Kärtner, Oliver D. Mücke and Giovanni Cirmi. Optical parametric waveform synthesizer and method for synthesizing optical waveforms. *Issued United States Patent* US10216064(B2), 2019.

[5] Giulio Maria Rossi, **Roland E. Mainz**, Franz X. Kärtner, Oliver D. Mücke, Giovanni Cirmi. Device and method for determining a temporal relationship of laser pulses, and applications thereof. *Published European Patent* EP3264540(A1), 2018.

[6] **Roland E. Mainz**, Giulio Maria Rossi, Franz X. Kärtner, Oliver D. Mücke and Giovanni Cirmi. Optical parametric waveform synthesizer and method for synthesizing optical waveforms. *Issued European Patent* EP3273550(B1), 2019.

Internaltional Conferences

[7] **Roland E. Mainz**, Giulio Maria Rossi, Fabian Scheiba, Yudong Yang, Giovanni Cirmi and Franz X. Kärtner. Relative-Phase Synchronization in a Sub-Cycle Parametric Waveform Synthesizer. *In CLEO: 2019*, (Optical Society of America, 2019), talk: SW4E.4, 2019.

[8] Yudong Yang, Giulio Maria Rossi, **Roland E. Mainz**, Fabian Scheiba, Giovanni Cirmi and Franz X. Kärtner. Controlling HHG with a Sub-Cycle mJ-Level Parametric Waveform Synthesizer. *In CLEO: 2019*, (Optical Society of America, 2019), talk: FF2C.3, 2019.

[9] Giulio Maria Rossi, **Roland E. Mainz**, Fabian Scheiba, Yudong Yang, Giovanni Cirmi and Franz X. Kärtner. Half-cycle mJ-level CEP-stable Pulses from ParametricWaveform Synthesis. *CLEO Pacific Rim Conference 2018*, (Optical Society of America, 2018), talk: F2A.1, 2018.

[10] **Roland E. Mainz**, Yudong Yang, Giulio Maria Rossi, Fabian Scheiba, Giovanni Cirmi and Franz X. Kärtner. Controlled HHG with a Sub-Cycle mJ-Level Parametric Waveform Synthesizer. *CLEO Pacific Rim Conference 2018*, (Optical Society of America, 2018), talk: Th3B.5, 2018.

[11] **Roland E. Mainz**, Giulio Maria Rossi, Yudong Yang, Oliver D. Mücke, Giovanni Cirmi and Franz X. Kärtner. Three-octave-wide phase-stable seeding scheme for parallel parametric waveform synthesizers. *In CLEO: 2018*, (Optical Society of America, 2018), talk: SF3N.5, 2018.

[12] Fabian Scheiba, Giulio Maria Rossi, **Roland E. Mainz**, Yudong Yang, Giovanni Cirmi, and Franz X. Kärtner. Millijoule-Level Sub-Cycle Pulses from Two Channels of a Parallel Parametric Waveform Synthesizer. *In XXIth Conference on Ultrafast Phenomena 2018*, (European Physical Society 2018), poster: WED.PO.50, 2018.

[13] Nicolai Klemke, Nicolas Tancogne-Dejean, Giulio Maria Rossi, Yudong Yang, **Roland E. Mainz**, Giuseppe Di Sciacca, Angel Rubio, Franz X. Kärtner and Oliver D. Mücke, Millijoule-Level Polarization states of high-harmonics generated in silicon from elliptical drivers. *In XXIth Conference on Ultrafast Phenomena 2018*, (European Physical Society 2018), talk: THU.2B.2, 2018.

[14] **Roland E. Mainz**, Giulio Maria Rossi, Fabian Scheiba, Shih-Hsuan Chia Yudong Yang, Oliver D. Mücke, Giovanni Cirmi and Franz X. Kärtner. Sub-Cycle Optical Parametric Synthesizer. *Frühjahrstagung der Deutschen Physikalischen Gesellschaft 2018*, (Deutsche Physikalische Gesellschaft 2018), talk: K 3.5, 2018.

[15] **Roland E. Mainz**, Giulio Maria Rossi, Giovanni Cirmi, Yudong Yang, Oliver D. Mücke, and Franz X. Kärtner. High-Dynamic-Range Relative Arrival Time Measurement for Accurate and Precise Parametric Waveform Synthesis. *In CLEO: 2017*, (Optical Society of America, 2017), talk: SM2I.3, 2017.

[16] Nicolai Klemke, Giuseppe Di Sciacca, Yudong Yang, Giulio Maria Rossi, **Roland E. Mainz**, Nicolas Tancogne-Dejean, Angel Rubio, Franz X. Kärtner, and Oliver D. Mücke. Generation of circularly polarized high-order harmonics in solids driven by single-color infrared pulses. *Laser Science 2017*, (Optical Society of America, 2017), talk: JTu3A.18, 2017.

[17] **Roland E. Mainz**, Giulio Maria Rossi, Giovanni Cirmi, Yudong Yang, Oliver D. Mücke, and Franz X. Kärtner. Shot-to-shot and long-term CEP-stable front-end for a parallel optical waveform synthesizer. *CLEO Pacific Rim Conference 2017*, (Optical Society of America, 2017), talk: 3-2H-6, 2017.

[18] Nicolai Klemke, Giuseppe Di Sciacca, Yudong Yang, Giulio M. Rossi, **Roland E. Mainz**, Nicolas Tancogne-Dejean, Angel Rubio, Franz X. Kärtner, and Oliver Mücke. Circularly polarized high-order harmonics from solids driven by single-color infrared pulses. *In 6th International Conference on Attosecond Physics (ATTO 2017)*, talk: 031, 2017.

[19] Giulio Maria Rossi, **Roland E. Mainz**, Giovanni Cirmi, Yudong Yang, Oliver Mücke, and Franz X. Kärtner. Orthogonal control for stable parallel waveform synthesis. *In Nonlinear Optics Conference 2017*, (Optical Society of America, 2017), talk: NF2A.6., 2017.

[20] Nicolai Klemke, Giuseppe Di Sciacca, Yudong Yang, Giulio Maria Rossi, **Roland E. Mainz**, Nicolas Tancogne-Dejean, Angel Rubio, Franz X. Kärtner, and Oliver D. Mücke. Ellipticity dependence of higher-order harmonics in solids: unraveling the coupled intraband and interband dynamics. *In CLEO: 2017*, (Optical Society of America, 2017), talk: JTh5B-10., 2017.

[21] Giulio Maria Rossi, **Roland E. Mainz**, Giovanni Cirmi, Yudong Yang, Oliver D. Mücke, and Franz X. Kärtner. High-dynamic-range relative arrival time measurement for accurate and precise parametric waveform synthesis. *In CLEO: 2017*, (Optical Society of America, 2017), talk: SM2I-3., 2017.

[22] **Roland E. Mainz**, Giulio Maria Rossi, Giovanni Cirmi, Yudong Yang, Shih-Hsuan Chia, Eiji J Takahashi, Oliver D. Mücke, and Franz X. Kärtner. Can sub-optical-cycle parametric waveform synthesizers be seeded by separate bulk white-light supercontinua? *In CLEO: 2016*, (Optical Society of America, 2016), talk: STu1I-6., 2016.

[23] Shih-Hsuan Chia, Giulio Maria Rossi, Giovanni Cirmi, **Roland E. Mainz**, Yudong Yang, Oliver D. Mücke, and Franz X. Kärtner. Two-octave-wide dispersive mirrors based on dualadiabatic-matching structures. *Optical Interference Coatings 2016*, (Optical Society of America, 2016), talk: TD-3., 2016.

[24] Shaobo Fang, **Roland E. Mainz**, Giulio Maria Rossi, Yudong Yang, Giovanni Cirmi, Shih-Hsuan Chia, Cristian Manzoni, Giulio Cerullo, Oliver D. Mücke, and Franz X. Kärtner. Sub-cycle timing lock in a multi-mj parametric waveform synthesizer. *In European Conference on Lasers and Electro-Optics - European Quantum Electronics Conference (CLEO/Europe-EQEC)*, (Optical Society of America, 2017), poster: CG-P-4., 2015.

[25] **Roland E. Mainz**, Giulio Maria Rossi, Cristian Manzoni, Giovanni Cirmi, Yudong Yang, Shih-Hsuan Chia, Shaobo Fang, Oliver D. Mücke, Giulio Cerullo, and Franz X. Kärtner. Timing jitter characterization of a high-energy sub-cycle optical waveform synthesizer. In Advanced Solid State Lasers 2014 (ASSL), (Optical Society of America, 2014) talk: ATu5A-3. 2014.

Chapter 1

Motivation

From today's perspective the laser is one of the most important inventions of the 20th century, although significant advances in laser science were repeatedly not realized as such at first sight. The theoretical concept of light amplification by stimulated emission was first perceived by Albert Einstein in 1916 [1], but the implication of his discovery were not realized. The world needed to wait till Theodore Maiman demonstrated the first functioning laser in 1960 [2]. Also Maiman underestimated its potential; he suffered from bad support and said himself, that he 'invented a solution which seeks the corresponding problem'. Today, laser radiation is the central and most important part of optics experiments. The properties of radiation emitted from a laser are very well defined. Coherence of the radiation allows laser interferometers to measure distances with ultra-high precision, enabling us for example to listen to the sound of black-hole mergers by detecting gravitational waves for the first time in 2017 [3]. Lasers can concentrate tremendous power on a very small area or volume allowing e.g. the industry to precisely process materials with high throughput. Pulsed laser sources concentrate the energy further into smallest timescales reaching relativistic regimes of the electromagnetic field ($10^{21}\,\mathrm{W/cm^2}$) and generating the shortest man-made events [4, 5]. Such attosecond flashes of light are as far away from our everyday 'human' timescales (seconds) as the time elapsed since the big bang, (each scale separated by roughly 18 decades). Femto- and attosecond science enables us to observe dynamics on the molecular and atomic level, which allows to gain a more profound insight into chemical and biological processes [6, 7]. Structural and dynamical understanding of complex processes and molecules, such as photosynthesis [8] or proteins [9] respectively, are a first step towards harnessing new forms of energy production and novel biomedical tools and procedures.

To generate attosecond pulses, intense femtosecond-laser pulses are focused into matter, e. g. a noble gas to drive a process dubbed high-harmonic generation (HHG). The focused laser pulse easily reaches an intensity of the electric field which applies a force to the bound electron(s) in the gas comparable to the atomic potential itself. By highly nonlinear interaction, the electron can be first tunnel-ionized, then accelerated in the continuum by the laser pulse and finally recombine at return to the parent ion. This highly energetic recollision process generates a burst of broadband (extreme) ultra-violet radiation with attosecond pulse-duration. This laser-driven rescattering process repeats twice for every period of the optical field and the electron excursion lasts also less than one full optical cycle. This repetition creates an attosecond-pulse train (APT) and correspondingly, a comb of high harmonic lines in the spectral domain is observed. For time-resolved experiments, such an APT is very unfavorable compared to a single isolated attosecond pulse (IAP). To limit the repeating emission of these attosecond bursts from an HHG source driven by pulses with few or more optical cycles, extensive *gating* techniques have been developed [10, 11].

Currently, the generation of IAPs is one of the most demanding applications for contemporary ultrafast sources and technologies. With a whole toolbox of well-developed femtosecond laser amplifiers, by exploiting additional nonlinear spectral broadening techniques and additional gating, IAPs with pulse durations down to tens of attoseconds can be produced [4]. Nevertheless, limitations of current laser technology either allows for a short laser pulse or for high pulse energy to drive the HHG process. Further considerations play a role when setting the requirements on a hypothetical laser source for optimal generation of high harmonics and ultimately for IAPs:

- Center wavelength in the IR to drive HHG reaching photon energies in the water window
- Pulse duration at or below the single-cycles regime to directly create IAPs (without additional gating techniques)
- Pulse energy reaching and exceeding the millijoule-level for intense IAPs
- Shot-to-shot stable electric field transient (e. g. CEP stability)
- Pulse repetition rates in the kHz range:
  - for fast experimental data acquisition
  - to compensate for drifts by active stabilization
- Low fluctuations in pulse energy and beam pointing
- Ability to generate and custom-sculpture non-sinusoidal electric-field transients
- Good beam mode structure

Reaching into the realms of single- and eventually sub-cycle pulses requires the exploitation of secondary laser sources such as optical parametric amplifiers (OPAs) among others. Such OPA-based sources can emit ultra-broadband few-cycle pulses and offer excellent aspects towards gain bandwidth and energy scalability. Still bandwidth limitations in OPAs do not allow to create intense sub-cycle pulses of light. A possible mitigation of this bandwidth limitation is the coherent combination of different ultra-broadband OPA sources. In this thesis one particular approach of this *parametric synthesis* is discussed and experimentally demonstrated. The latter includes the generation of sub-cycle millijoule-level pulses which drive the HHG in a quasi-continuum regime indicating the production of IAPs. Manifold control knobs furthermore allow to custom-sculpture the non-sinusoidal light-field transient.

Thesis Outline

The thesis will introduce briefly fundamentals on the development of laser technology with the focus on the creation of intense laser pulses with few-cycle pulse duration or below. Those can be generated by nonlinear techniques and can also be used to study nonlinear effects in return. (Chapter 2). Then upcoming light-field synthesizers will be introduced as coherent combination of multiple broadband OPA-based sources to scale the bandwidth beyond one octave. The thesis presents the implemented parallel parametric waveform synthesizer developed at CFEL altogether with initial timing synchronization measurements on the system and gained insights (Chapter 3). For waveform synthesis it is of fundamental importance to generate CEP-stable ultra-broadband seeds. A passive CEP-stabilized and actively CEP controlled seeding front-end based on DFG within an OPA-system is built and characterized. Altogether novel seeding schemes for parallel waveform synthesis are proposed and experimentally explored (Chapter 4). The complex timing dynamics of the parallel parametric waveform synthesizer is a challenge towards the synchronization and synthesis system. The author presents novel timing tools and their experimental implementation. Furthermore a novel low-latency timing synchronization scheme is introduced and a home-made FPGA-based system is experimentally implemented (Chapter 5). Finally a complete rebuilt of the experimental setup combined with multiple novel techniques implemented, achieved the first HHG from parallel parametric waveform synthesizers (Chapter 6).

Chapter 2

The Quest for Ultrashort Laser Pulses

This section focuses on the introduction of fundamentals on ultrashort laser pulse generation and characterization. Furthermore current state-of-the-art nonlinear sources, which can be harnessed for few-cycle pulse production, will be briefly reviewed with a special focus on achievable pulse duration and the pulse energy. Furthermore, aspects for future scaling of certain technologies will be discussed. A special emphasis will be put on optical parametric amplifiers due to their unique and promising prospects.

2.1 Laser Fundamentals

Before the advent of the laser, only a limited light focusability of conventional light sources could be achieved. Then already the first ruby-laser [2] allowed to generate significantly more intensive pulses of light. Further laser materials where discovered or engineered and each lasing medium can store a certain amount of energy in the form of an electronic/vibronic/phononic excitation. This energy is deposited by pumping the material, stays for the duration of the upper-state lifetime τ and can be released within a short time by lasing. A requirement for the controlled release of the stored energy is to have influence on the quality-factor Q of the resonator cavity. Electro-optic or acousto-optic devices can be utilized for switching the Q-factor of a laser cavity within nanoseconds [12]. Such Q-switched lasers emit radiation in a pulsed mode. A finite energy can be emitted within a short time-scale ($\sim$nanoseconds), which increases the instantaneous intensity compared to the CW-operation of a laser.

2.2 Femtosecond Lasers

In theory a laser resonator will emit several narrow spectral lines spaced according to the free spectral range (FSR) of the cavity and the gain-bandwidth of the lasing medium (see Fig. 2.1a). These modes, if assumed a fixed phase relation between them correspond to a pulse in time which is usually significantly shorter than the cavity round-trip time itself. Intracavity non-linearities in the form of saturable absorbers where exploited to achieve an interaction between the modes, which led to passive mode-locking [13]. Later Kerr-lens mode locking in Ti:Sa allowed for sub-100 fs [14]. Correctly phased modes which correspond to a short pulse in time lead to an increased focusing by non-linearities within a *Kerr-Lens* (see Fig. 2.1c/b). Such pulses can pass an aperture with less energy-loss and diffraction. Further passive mode locking techniques e.g. the semiconductor saturable absorbers (SESAM, [15]) were developed. To date, Titanium-ions embedded in a sapphire-host (Ti:Sa) is known to have the broadest bandwidth of all available lasing media [16]. The very broad fluorescence band spans from 670 nm to 1070 nm with a peak around 800 nm. The accumulated normal dispersion ($\partial n/\partial\omega > 0$), e.g. in the gain medium, the passive mode locker or air of a broadband pulse per cavity roundtrip needs to be compensated with anomalous dispersion ($\partial n/\partial\omega < 0$). One compression technique is based on prisms and the

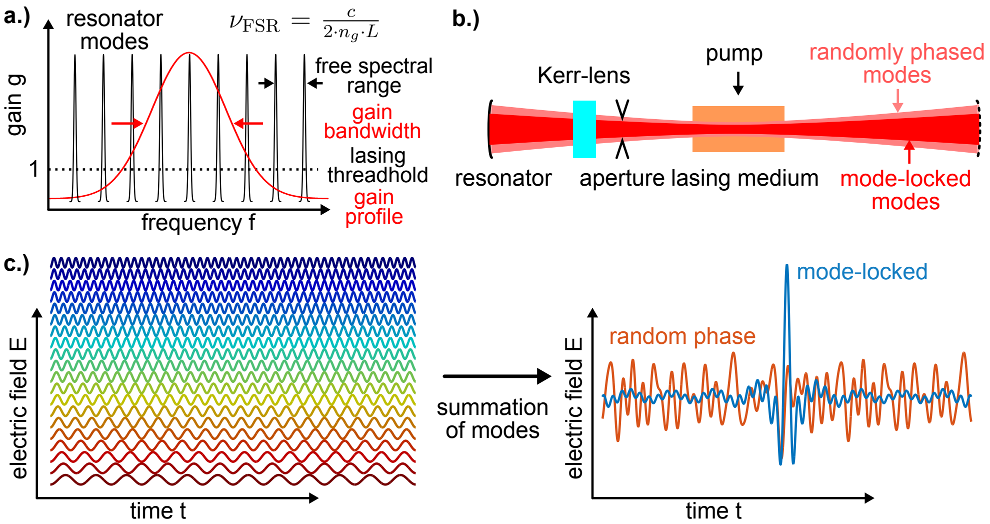

Figure 2.1: a.) Narrow spectral lines of a laser resonator spaced by the free spectral range FSR of the cavity. All modes in the cavity which are within the gain-bandwidth of the lasing media (red, gain $g > 1$) can be emitted. **b.)** All amplified modes can have a random or a fixed phase relation with each other. A mode locking technique can favor correctly phased modes. **c.)** Possible resonator modes (left) and their summation (right): with random phases (orange) and locked-phases (blue). The mode-locked operation creates significantly higher peak intensities.

anomalous dispersion can be adjusted by further insertion of a prism (see Fig. 2.2a, [17]). In this configuration the light need to pass several interfaces with subsequent energy loss and also experience the bulk glass dispersion of the prisms. To circumvent this problem and to improve the throughput grating-based compressors can be used instead (see Fig. 2.2b, [18]). Due to the low amount of dispersion compensation required in a Ti:Sa oscillator and the ability to custom design the dispersion characteristics, dielectric chirped multi-layer mirrors (CM, [19, 20]) are commonly used for intra-cavity pulse compression. By careful design of the layering-structure of the mirrors, even a partial reshaping of the gain bandwidth of the lasing medium is possible without compromising the ability to mode-lock [21]. The passive mode locking and general dynamics in a Ti:Sa oscillator are theoretically well understood [22], and also extensively verified by experiments [23]. Broadband Ti:Sa oscillators can deliver up to an octave of spectral bandwidth [24–26], this corresponds to a sub-5 fs pulses in time and just a few oscillations of the electromagnetic field $E(t)$ (few-cycle pulse). For such short electric field transients E(z,t), there is a significant relation between the peak of the pulse envelope $A(z,t)$ and the carrier $e^{i\omega_0 t}$ beneath expressed as phase ϕ_{CE} (see Fig. 2.3):

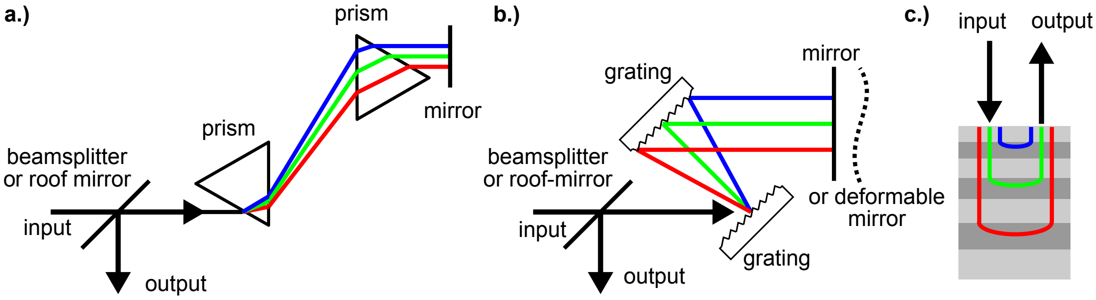

Figure 2.2: **a.)** A prism based compressor can create negative dispersion by geometrically creating a shorter propagation path for higher frequency-components. **b.)** A grating-compressor operates similar but avoids optical interfaces and bulk-material transmissions, which results in a higher throughput and damage threshold. A deformable mirror or a liquid crystal array can shape the spectral intensity/phase with high customization. **c.)** A deposition of thin dielectric layers with a varying layer-thickness creates a Bragg-stack called chirped mirror. The structure can be adapted within certain limitations to compensate almost any dispersed pulse and compress it close to the Fourier-transform limit.

$$E(z,t) = A(z,t) \cdot e^{i(kz-\omega_0 t+\phi_{CE})} + \text{c.c.}$$

In frequency domain such a pulse train emitted from a mode-locked oscillator can be expressed as:

$$f_m = m f_r + f_{CEO}$$

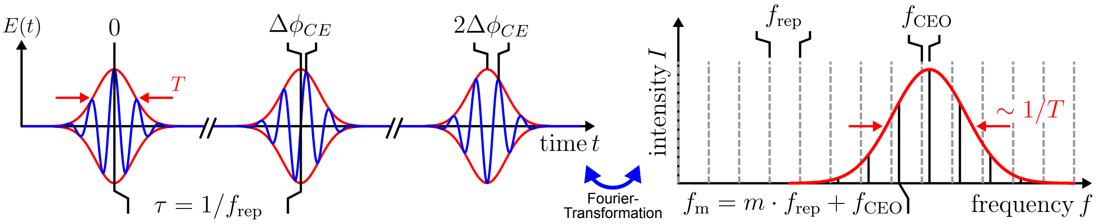

Figure 2.3: a.) Emitted pulse train from a laser oscillator in time with the FWHM pulse duration T and the repetition period $\tau = 1/f_{rep}$. The CE-phase ϕ_{CE} is defined by the phase between the peak of the carrier (blue) and the peak of the envelope (red). **b.)** In frequency domain, the cycling of the ϕ_{CE} is given by the carrier-envelope offset frequency f_{CEO}.

Where a comb of frequencies f_m is equally spaced by the repetition rate fof the laser f_r and shifted by the carrier-envelope offset frequency f_{CEO}. The Carrier-Envelope-Phase (CEP, ϕ_{CE}) and its measurement and control is of special interest when studying light-matter interactions on short time scales [27–29] and for using the laser frequency comb in frequency metrology for ultra-precise frequency measurements [30]. A more detailed look on the CEP measurement and stabilization will be given in Chapter 2.7. The output pulse energy of a laser oscillator is limited by parasitic effects like thermal lensing and instabilities in the mode-locking. Common pulse energies are on the scale of nJ with output powers in the range up to a few Watts [31].

2.3 Ultrafast Amplifiers

For higher output powers and higher pulse energies, a separate Ti:Sa amplifier needs to be used to further amplify the output of a laser oscillator. Optical switches can be employed to pulse-pick a small fraction of the emitted pulses from the oscillator to reduce the repetition rate to the lower kHz-range and in return increase the pulse energy in a consecutive laser amplifier at a given average power. Such femtosecond pulses can easily reach intensities related to damage thresholds of the lasing material during amplification. An important technique to overcome this limitation was invented by Strickland and Mourou in 1985. The chirped-pulse amplification (CPA, [32]) marked a mile-stone in high-energy laser development and was awarded the Nobel Prize in 2018. CPA-based amplifiers can be operated either in a multi-pass configuration or in a regenerative amplifier configuration (REGEN). The average output power of e.g. a Ti:Sa amplifier is limited by the thermal effects. Especially the quantum defect $\eta_{\mathrm{Ti:Sa}} = 66\%$ between pump photon energy and lasing photon energy leads to a significant dissipation within the Ti:Sa material. The thermal conductivity of Ti:Sa can be increased by operating the lasing medium unter cryogenic temperatures [33].

Currently the average output power from Ti:Sa is limited to 20-40 W with cryo-cooling employed, corresponding to 20-40 mJ pulses at a repetition rate of 1 kHz. Unfortunately the sub-5 fs pulses created by Ti:Sa laser oscillators cannot be amplified while maintaining their broad bandwidth. Especially the effect of gain-narrowing limits either the pulse energy or the pulse duration during amplification. Commonly milijoule-level Ti:Sa amplifiers are above 25 fs pulse durations.

2.4 Nonlinear Optics

The ultrashort nature of femtosecond pulses and the sizeable electric field strengths which can be contained in such a pulse, allows to reach and exploit effects beyond linear refraction of light propagating in matter. In classical electrodynamics, the propagation of light is described by the coupling of electric and magnetic fields $\vec{E}$ and $\vec{H}$. James Clerk Maxwell developed a set of differential equations explaining the phenomena of light interacting with matter. The electric displacement field $\vec{D}$ and magnetic field-strength $\vec{H}$ inside the material can be obtained by taking the response from the matter by the electric polarization density $\vec{P}$ and the magnetization $\vec{M}$ into account:

$$\vec{D} = \varepsilon_0 \cdot \vec{E} + \vec{P}$$

$$\vec{H} = \frac{1}{\mu_0} \cdot \vec{B} - \vec{M}$$

Where ε_0 is the electric permittivity and μ_0 the magnetic permeability with $\varepsilon_0 \cdot \mu_0 = c_0^{-2}$ and c_0 beeing the vacuum speed of light.
Ultrashort pulses of light are wave packets and represent a solution to a wave equation obtained from coupled Maxwell equations. The simplest case is a linearly polarized plane wave of light traveling through a non-magnetic isotropic media without external charges of currents thereof. A one dimensional scalar wave equation in the direction of propagation z would be obtained by:

$$\left(\frac{\partial}{\partial z^2} - \frac{1}{c^2}\frac{\partial}{\partial t^2}\right) \cdot E(z,t) = \mu_0 \frac{\partial^2}{\partial t^2} P(z,t)$$

Where P(z,t) acts as a source term for radiation and describes the response of the medium under presence of an electric field. The polarization is given by the incident field strength and the electric susceptibility χ according to:

$$\vec{P} = \varepsilon_0 \chi \vec{E}$$

On the microscopic level, charges in e.g. metals or (induced) dipoles in transparent media react linearly to the electric field, which leads to refraction. For increasing field strengths the intrinsic boundaries of the e.g. dipole polarization start to deviate from a harmonic oscillator potential and contribute additionally non-linear response terms $\vec{P}_{NL}$. This non-linear response can be expressed by a taylor expansion in $\vec{P}$ with:

$$\vec{P} = \vec{P}_L + \vec{P}_{NL} = \varepsilon_0 \left[\chi^{(1)}\vec{E} + \chi^{(2)}\vec{E}^2 + \chi^{(3)}\vec{E}^3 + \dots\right]$$

The symmetry of the nonlinear response governs the new appearing mixing terms (see Fig. 2.4). For a vanishing $\chi^{(2)}$, for example in the form of e.g. inversion symmetric crystals, no even order mixing terms will appear. Regardless from that a $\chi^{(3)}$ will be present in all materials and contribute cubic wave terms $P \sim E^3(\omega)$ such that a new light-field of third order mixing products, e.g. with 3ω (third order harmonic, THG) will be present. For crystal materials, such as beta-barium-oxide (BBO), KTP, BiBo, LN, also the inversion symmetry is broken and even terms e.g. in the form of 2ω appear (second order harmonic, SHG).

Instead of one input field to such a non-linear process, two or more fields can be superimposed and the resulting non-linear material response can be treated as instantaneous. This opens up to a broad set of possible configurations to exploit these nonlinear interactions and to obtain mixing products.

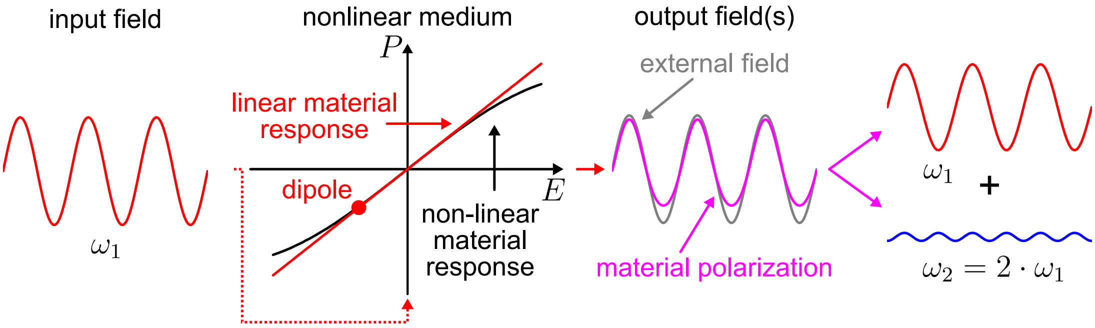

Figure 2.4: A monochromatic external field (left) drives a dipole within a transparent media and leads to polarization (middle). For extended elongations the dipole potential will deviate from a linear material response. The reemitted waves from those driven dipoles contain a non-sinusoidal material polarization, which can be decomposed into its Fourier-components (right). In this example, a $\chi^{(2)}$-nonlinearity, e.g. in non-inversion symmetric crystals generate the second harmonic (SHG)

Beside the generation of mixing products, also an incident pulse can experience spectral or spatial reconfiguration as a result of nonlinear interaction with the medium. One effect is the electro-optical Kerr-Effect, which was discovered 1875 by John Kerr. The optical properties where altered if external electric fields are applied to a material. For ultrashort laser pulses, these fields can be created in-situ by the pulse itself. The time-dependent refractive index $n(t)$ is a function of the instantaneous intensity $I(t)$ according to:

$$n(t) = n_0 + n_2 \cdot I(t)$$

This dynamic self-induced modulation of the refractive index can have two manifestations. Spatially the pulse induces by itself a lensing effect, the *Kerr-Lens*. A similar effect appears temporally where the peak of the pulse is retarded more than its temporal wings. This temporal reordering of the energy structure of the pulse corresponds to a spectral broadening in the frequency domain and is hence called self-phase modulation (SPM) or self-steepening. Beyond small perturbations of e.g. electric dipoles in the crystal also highly nonlinear interactions such as saturable absorption, multi-photon processes, above-threshold ionization and tunnel ionization can contribute. Such strong-field phenomena creates free electrons/ions as nonlinear media and can generate up to hundreds-order mixing products [34, 35]. In such configurations the perturbative approach via Taylor-expansion of the (n-1)-rank tensor $\vec{\chi}$ breaks down.

Several nonlinear techniques are exploited to generate laser-like radiation. The most significant impact of nonlinear optics is the ability to generate new spectral components and to generate ultra-wide spectral bandwidths. The spectral width of radiation generated by nonlinear processes can overcome the gain bandwidth of laser materials multiple times, supporting ultrashort laser pulses at or below the few-cycle regime. If a configuration is used, where the nonlinear material is not absorbing any of the involved beams to a significant degree, the instantaneous interaction is not limited in average power by thermal effects.

2.5 Nonlinearities for Supercontinuum Generation

After the introduction of a host of nonlinear interactions the focus should be on how to exploit this processes in a simple experimental implementation to broaden the spectrum of a pico- or femtosecond laser pulse to a *Supercontinuum* in order to lower its pulse duration. For this purpose three methods based mainly on SPM and self-steepening in gases and glasses or crystals are discussed. The main difference is how the laser beam is guided through the medium to accumulate sufficient nonlinearieties.

The effects of self-focusing and self-defocusing of a laser pulse in a medium can create a fragile yet self-stabilizing integration for extending the integration length [36, 37]. In such laser-filaments, a core is surrounded by a reservoir region, which fuels the core with energy and compensated for energy-loss in the core [36]. The prolonged interaction in a nonlinear medium can be achieved also by guiding the laser mode with a quasi-waveguide in a setup called hollow-core fiber compressor (HCFC, [38]). Usually straight aligned glass tubes with a core hole of few hundreds of µm diameter are used. Both techniques, the self-guiding filament as well as the hollow-core fiber are common to create few-cycle pulses from a many-cycle Ti:Sa amplifier output [39–41]. Good efficiencies around 50% are achieved and a compressible spectral phase allow to compress those pulses close to their Fourier-transform limit. The scalability of gas-phase broadening schemes with respect to pulse energy and average power is limited by detrimental nonlinearities, ionization losses, thermal problems and material damage.

On the contrary for some applications only a low pulse energy or an ultra-broadband spectrum is required. Ultra-broadband spectra can be produced by increasing the material density, e.g. using a glass material instead of a gas. This spectral broadening process is called supercontinuum generation in bulk or more commonly *white-light generation* (WLG, [42]) due to the whitish appearance of the output beam. If the pulses are of too low energy to self-focus in bulk, a guiding and confining effect can be achieved by photonic-crystal fibers (PCF, [43]). These glass-fibers are structured by holes and allow to confine a beam to a core diameter on the order of the light's wavelength (few µm). Such PCFs are highly relevant for e.g. CEP measurements on low pulse energy sources like ultrafast laser oscillators. Such supercontinua can exhibit bandwidths of up to several octaves [43, 44]. WLGs and PCFs can be operated in a certain experimental window with high spectral and phase stability (see Chapter 4.3). The output pulses are chirped mainly due to the material dispersion and can be recompressed close to their fourier-transform limited pulse duration. Such ultra-broadband sources have a high importance for seeding applications [45], such as optical parametric amplifiers (OPA).

2.6 Optical Parametric Amplifiers

The OPA is one of the most common non-linear techniques exploited in ultrafast science. The term parametric derives from the set of mathematical equations which are used to describe the amplification process [46]. An OPA has two inputs, an energetic pump beam and a seed beam which should be amplified. The main technical difference to a laser is the lack of energy storage in the gain medium due to an absence of a real transition, therefore the absence of a fixed gain-spectrum. The interaction between the input pulses appears instantaneous, which requires that all three waves needs to be overlapped in space and time to get mixed (see Fig. 2.5a). The non-linear interaction can be also understood by virtual energy levels within the nonlinear media (see Fig. 2.5b).

A highly energetic *pump*-pulse is used to pump an excitation to a virtual level, where a weak *seed*-pulse is amplified by coherent emission to form the *signal*-beam. Due to the quantized nature of the integration, energy conservation requires (on average) the emergence of a third *idler*-beam to fulfill conservation of energy:

$$hv_p = hv_s + hv_i$$

Due to the virtual energy-levels, any photon-energy within the materials band-gap can be used for the pump and seed-pulses, as long as $v_p > v_s$. The idler is generated according to this relation and contains as much photons as the signal output (subtracted by the seed input). By this energy conservation it is clear that

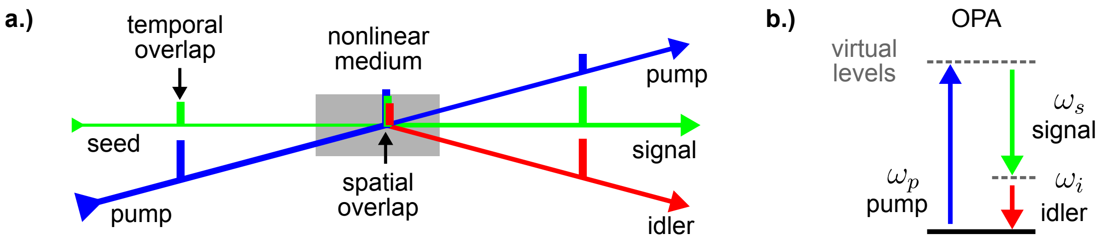

Figure 2.5: a.) Scheme of an OPA. A pump and a seed pulse needs to be spatially and temporally overlapped within a nonlinear medium. The seed is amplified by energy transfer from the pump pulse. Due to energy conservation also a third beam, the idler is generated. **b.)** Representation of the OPA-process in a virtual energy-level diagram. The pump excites to a virtual state and the signal transition amplifies the seed input while the idler, is emitted with the remaining quantum of energy.

each beam has another center wavelength and due to material dispersion in the nonlinear medium another group-velocity v_g and phase-velocity v_p. For efficient energy transfer, all involved pulses need to maintain a fixed phase relation during the nonlinear interaction which leads to the second conservation rule, momentum conservation:

$$\vec{k_p} = \vec{k_s} + \vec{k_i}$$

This requirement either limits the maximum gain length L without negative amplification to occur (back conversion) or in return the spectral amplification bandwidth. For a given bandwidth the missmatch in v_p will limit the length of amplification (coherence length L_c) where a phase-slip of $\Delta\phi = \pi/2$ accumulated. The gain G of an OPA is given by the pulse parameters, e.g. instantaneous pulse intensity of the signal I_S, by the non-linear coefficient Γ and the interaction length L [45].

$$G = \frac{I_s(L)}{I_{s0}} = \left[1 + \frac{\Gamma^2}{g^2}\sinh^2(gL)\right]$$

With $g = \sqrt{\Gamma^2 - \left(\frac{\Delta k}{2}\right)^2}$, Δk and $\Gamma^2 = \frac{8\pi^2 d_{eff}^2 I_p}{n_i n_s n_p \lambda_i \lambda_s \varepsilon_0 c_0}$. Under the assumption of perfect phase-matching and with large gain approximation ($\Gamma L \gg 1$) it can be simplified to:

$$G = \frac{I_s(L)}{I_{s0}} = \frac{1}{4}e^{2\Gamma L}$$

The exponential gain of the signal (and idler) beams is different from other $\chi^{(2)}$-processes like SHG which only exhibit a quadratic growth.
There are multiple techniques to fulfill the phase-matching condition (see Fig. 2.6). Commonly phase-matching either exploits the birefringence of the nonlinear crystals (with bi- or triaxial refractive index ellipsoids) together with different polarization states of the input beams to match their phase-velocities. Matching can also be achieved by tuning the refractive indexes via temperature changes.

Since poling techniques are available for growing crystals, another technique became available, which periodically poles the crystal orientation [47] for quasi-phasematching (see Fig. 2.6c). Achieved phase-matching does not mean that the group velocities $v_g$of the involved pulses are matched as well (see Fig. 2.7a). Below the pump envelope, the signal and idler envelopes can separate and generate new signal from the idler and vice versa. To overcome such a separation in time, the pulses can have an angle of incidence between them in a non-collinear OPA geometry (NOPA, see Fig. 2.7b [48, 49]). The downside on the contrary is a loss of spatial overlap after a certain propagation distance and corresponding loss of amplification. Another disadvantage is spatial chirp of the amplified signal [49, 50]. Another broadband OPA-configuration would be to have the signal and idler with same spectral content (hence same v_g), which means around half the pump wavelength (see Fig. 2.7c). Such an OPA-configuration is called degenerate (DOPA, [51]) and allows for broadband amplification. For each OPA phase-matching configuration, it need to be checked if other non-linear effects such as parasitic second harmonic or similar are also phase-matched.

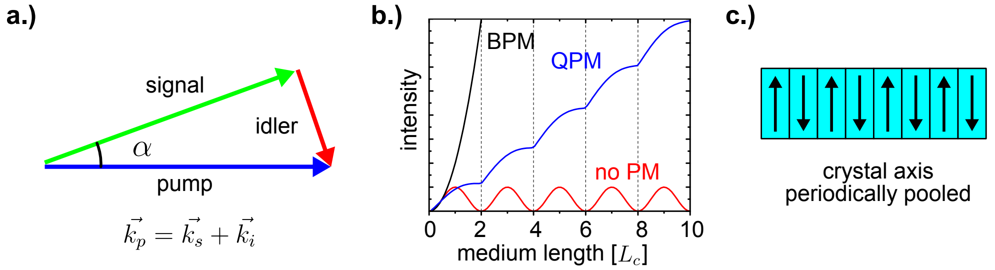

Figure 2.6: a.) The phase-matching condition need to be fulfilled for continuous amplification during propagation in the nonlinear medium. **b.)** Intensity growth for different phase-matching schemes in units of coherence lengths L_c. No phase-matching (no PM) experiences deamplification (back conversion) after one coherence length L_c while broadband-PM (BPM) experiences exponential growth. **c.)** A Quasi-PM (QPM) is e.g. achieved by periodically pooling of the crystal orientation to exploit its birefringence.

In analogy to chirped-pulse amplification in ultrafast laser amplifiers, also here the achievable output energy can be increased, by lowering the peak intensity with amplification of chirped pulses (OPCPA, [52, 53]). In general the signal-gain per lenth-unit of an OP(CP)A can easily be orders of magnitude higher compared to lasing media. A gain of $g = 10^6$ is achievable within a single pass of a few mm long nonlinear crystal [54, 55]. At too high signal-gain amplified spontaneous emission (super-fluorescence) can become a significant channel of energy loss. One mitigation is to use multiple OPAs with lower gain in series, instead of one single high-gain OPA [56].

OPA-crystals experience no significant heat load from the laser beams. Prerequisite is that the crystal is highly transparent for all involved pulses. Due to that,

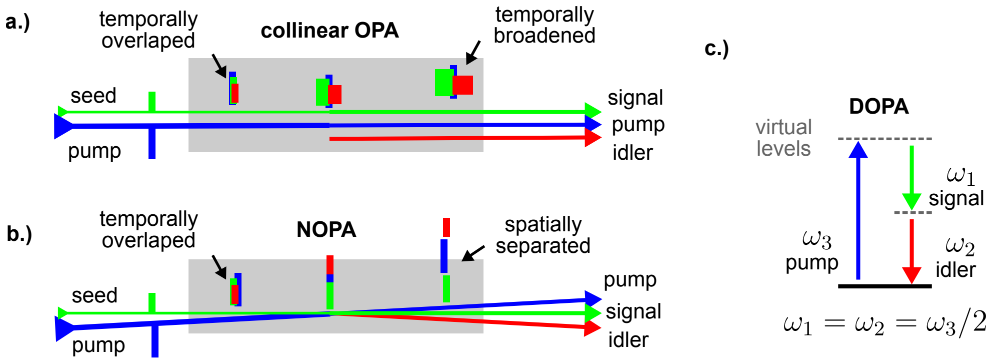

Figure 2.7: a.) A unmatched group velocity v_g within the nonlinear media temporally separates the amplified signal and the generated idler. In return, the idler front creates new signal while the signal trailling end creates new idler radiation. **b.)** Possible mitigation of group velocity mismatch with a non-collinear OPA-geometry (NOPA), a temporal broadening is traded in for spatial separation. **c.)** A type-I phase-matched degenerate-OPA (DOPA) solves this problem by creating the same spectral content in signal and idler at the point of degeneracy ($\omega_{pump}/2 = \omega_{signal} = \omega_{idler}$).

OPAs can be operated at high repetition-rates with high average-power output [57, 58], and compared to lasing media also without bifurcation instabilities [59]. Especially with Ti:Sa lasers at 800 nm and their second harmonic at 400 nm, very broadband OPAs can be built with BBO, LBO and BiBo, covering up to one octave of spectral bandwidth [51].

2.7 Control of the Carrier-Envelope Phase

Previously, a brief overview was given how broadband laser media and nonlinear techniques used to create short pulses, reaching into the realm of few-cycle pulses. Those sources can exhibit a stable spectrum $I(\omega)$ and spectral phase $\phi(\omega)$, which can be also manipulated. Now, an emphasis will be put on how to achieve full control over the electric field transient $E(t)$ of such sources by measuring and controlling the Carrier-Envelope phase ϕ_{CE} (CEP).

$$E(z,t) = A(z,t) \cdot e^{i(kz - \omega_0 t + \phi_{CE})} + \text{c.c.}$$

Where the physical value of the CEP is the modulo 2π wrapped phase-shift between the repetition-rate f_r and the f_{CEO} (see Fig. 2.8a). The CEP measurement was first achieved experimentally on laser oscillators via inter-pulse interference [60] and then later via intra-pulse interferometry [61]. The implication of this technique in the frequency-metrology and for the frequency comb-technique awarded John L. Hall and T. W. Hänsch the Nobel Prize in 2005.

Initially the difficulty was not to perceive the implications of a controlled CEP for strong-field interactions [27, 28], but to measure the CEP in the first place. The measurement was made possible by combining two nonlinear techniques in an nonlinear self-referencing interferometer. First an octave spanning spectrum need to be present (e.g. octave spanning Ti:Sa oscillators) or the spectrum needs to be broadened beyond an octave by spectral broadening techniques (e.g. by PCF). Secondly a harmonic needs to be generated (e.g. SHG) and is required to spectrally overlap with the fundamental spectrum (see Fig. 2.3b). In case SHG is used, the CEP dependence is also doubled.

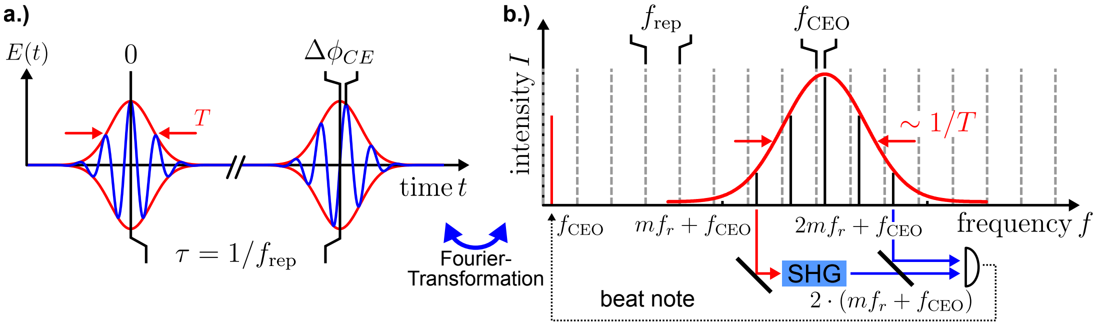

Figure 2.8: a.) Emitted pulse train from a laser oscillator in time-domain with the FWHM pulse duration T and the repetition period $\tau = 1/f_{rep}$. The CE-phase ϕ_{CE} is defined by the phase between the peak of the carrier (blue) and the peak of the envelope (red). **b.)** In frequency-domain, the cycling of the ϕ_{CE} is given by the carrier-envelope frequency offset f_{CEO}. Via SHG an f-2f beat projects an RF-energy with f_{CEO}.

$$f_{\text{CEO}} = f_{\text{SHG}} - f_{\text{FUN}} = 2 \cdot (mf_r + f_{\text{CEO}}) - (2mf_r + f_{\text{CEO}})$$

The interference between SHG and the fundamental part of the spectrum directly project an actual RF-beat in $f_{\text{CEO}} \in [0, f_r]$ representing the CEO-frequency f_{CEO}. The CEO can be manipulated by changing the intra-cavity dispersion. A fast method to affect the intra-cavity dispersion is achieved by pump-power modulation (e.g. by an acousto-optic modulator) inducing a weak Kerr phase shift [62]. An actuated CEO shifts the whole frequency comb and if f_{rep} and f_{CEO} are controlled and synchronized to a time normal (e.g. atomic clock), the frequency of all comb-lines emitted from that oscillator are precisely known. The high-repetition-rate of laser oscillators allow to perform this CEO/CEP measurement, commonly just called f-2f-method, entirely with a photo-diode and RF-equipment.

On the contrary for amplified pulses with kHz repetition rates RF-based techniques are no longer applicable. The spectral broadening in return is simpler to perform, e.g. via WLG in bulk due to significantly higher pulse energy available for CEP measurement. The spectra are now perceived as continuous, be-

cause their line-spacing is now only at a few kHz. Via SHG a broadband long-wavelength leg of a generated supercontinuum can be frequency doubled and will beat with the short wavelength part of the supercontinuum. A spectrum of this beating region will exhibit spectral fringes. Such spectral fringes can be measured with a spectrometer and the CEP can be extracted from it (see Chapter 3.4.2).
Another established method for CEP measurement exploits the strong CEP dependence from photo-electron emission in matter. The CEP modulates the spatial direction of electron emission when a few-cycle pulse is interacting with gas atoms in a regime for above-threshold ionization (ATI). A balanced directional electron detector analyzes a selected kinetic energy range of the photo-electron spectrum [63]. The spatial direction of electron emission leads to the characteristic 'phase-potato' and has a clear correlation with the incident pulse CEP and the pulse duration [64]. This method requires usually a more complex setup including a vacuum apparatus and multi-channel plate (MCP) detectors. Similarly CEP-dependent effects can be exploited by photoemission from tips or structured surfaces [29, 65]. Both electron-emission-based techniques allow to determine an absolute CEP rather than a relative CEP, but require a few-cycle pulse in the first place.

2.8 Strong-field Processes and High Harmonics

Previously it was shown that the non-linear dipole response of matter dressed in intense laser radiation can be expressed by a Taylor expansion. This perturbative approach is well suited for the description of the various $\chi^{(2)}/\chi^{(3)}$-processes but breaks down for higher order processes. Already in the 1980's with picosecond lasers [66, 67], the first high-order harmonic generation (HHG) was observed when an intense laser-field interacts with a gas. Following, spectra of such high harmonics (HH) exhibits new spectral characteristics such as a plateau of equal intense HH orders (see Fig. 2.9a). Such a phenomenon cannot be explained with a perturbative theory, because it would predict a rapid decay in intensity of succeeding high harmonic orders, not a plateau. A perception of the underlying process was already published in 1987 by Kuchiev [68]. Later Corkhum published his popular simple-man's model in 1993 [69]. At the core lays the idea of a three-step process (see Fig. 2.10), where electrons are not bound and perturbed within their potential, but are actually (tunnel-) ionized and recombined. After ionization, the electron can move freely within the laser field. For favorable emission phases with respect to a theoretical cosinusoidal-shaped laser field the electron will be first accelerated away from the parent-ion but returns after the laser field changes its sign of the electric field. With a small probability, the highly accelerated electron will recombine with the ion and emit ultra-broadband vacuum ultraviolet (VUV) to extreme UV (EUV) radiation.

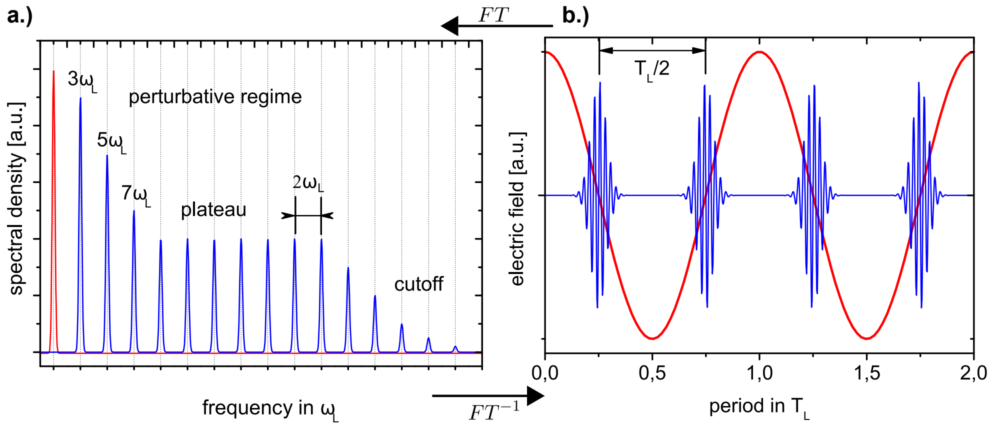

Figure 2.9: a.) Characteristic spectrum of an HHG-source with low order harmonics exhibiting an exponential decay in intensity, a plateau region with equal intense orders and a cut-off region with ceasing HH-intensity. **b.)** Corresponding time-domain behavior of such a spectrum, superimposed with the driving laser (red). An Attosecond burst is emitted every optical half-cycle with alternating sign (blue).

The inversion symmetry of an atomic gaseous medium and the sinusoidal electric field transients of driving laser let this process occur twice each laser cycle. Under the assumption of negligible parasitic ionization, such a train of EUV/XUV-pulses correspond to a frequency comb with a comb line spacing of $2\omega_p$. Due to the inversion symmetry of the gas, only odd harmonics 2N+1 (with $N = 1, 2, 3, ...$) are observed. Even orders can be produced by breaking the symmetry of the medium (e.g. at an interface) [70, 71], or by using asymmetric laser-fields (e.g. via the $\omega - 2\omega$-technique [72]).

The HHG-process is driven by a fully coherent laser source in a repetitive manner and exhibits similar coherence as the driving laser [73–75]. In analogy to second- and third-order nonlinear interactions, here the phase-velocities need to be matched as well [76, 77]:

$$\Delta k = \underbrace{\Delta k_{\text{atom}}}_{>0}(q, p, \eta) + \underbrace{\Delta k_{\text{plasma}}}_{<0}(q, p, (1-\eta)) + \underbrace{\Delta k_{\text{gouy}}}_{>0} + \underbrace{\Delta k_{\text{geo}}}_{>0} \tag{2.1}$$

Where q is the harmonic order, p the gas pressure and η the ionization level, further dispersive contribution can come from the Gouy phase and geometrical factors e.g. in waveguides. Phase-matching can be achieved by manipulating one of the involved parameters e.g. via the gas-density or the level of ionization. One common technique is to influence the pressure of the gas cell. The pressure can be varied to gain control of the level of ionization. Plasma will yield negative dispersion for the HH while neutral gas will contribute positively to the dispersion. Also other phase-matching techniques have been developed such as segmented gas nozzles [78], or modulated waveguides [79].

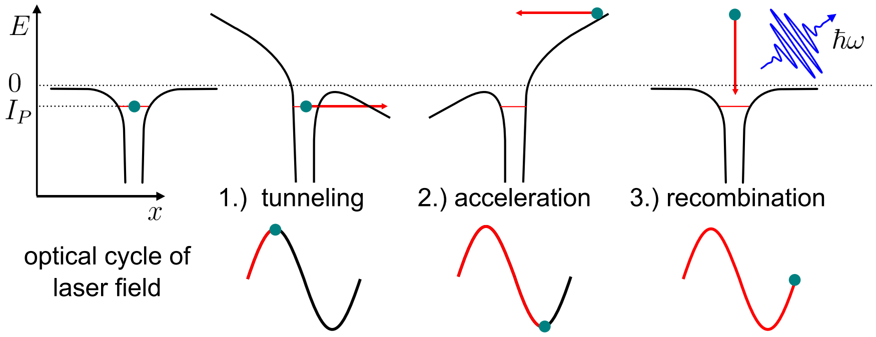

Figure 2.10: Steps of the HH-generation according to the Corkhum-model. 1.) Tunnel ionization of a (valence)-electron due to bending of the atomic potential by the imposed laser field. 2.) Classical acceleration of the free electron in the laser-field. 3.) Possible recombination of the back-accelerated electron with the parent-ion acompanied by the emission of a highly energetic VUV/XUV-photon.

Because even low order harmonics are already above the ionization potential of gases (e.g. air), a HHG source needs to be operated in vacuum to prevent reabsorption of the generated radiation. The highest harmonics which can be generated are approximated by [69]:

$$E_{\max} = 3.17 \cdot U_P + I_P$$

With I_P the ionization potential of the ionized system (e.g. 24.6 eV for helium) and the ponderomotive potential U_P. The scaling factor of 3.17 originates from the maximum possible energy gain of a charge carrier in a sinusoidal driving field and a tunnel-ionization at $\phi = 17°$ after the peak of the electric field. The ponderomotive potential U_P is defined as:

$$U_P = \frac{e^2 E_L^2}{4 m_e \omega_L^2} = 9.38 \cdot 10^{-8} \cdot \lambda_L^2 \left[nm^2\right] \cdot I \left[{}^{W}\!/_{cm^2}\right] \propto \lambda_L^2 I$$

With the driving laser angular frequency ω_L and the laser intensity I_L. Depending on the emission phase, the electron follows a short or long trajectory leading to spectral chirp and different spatial divergence. The ionization potential I_P plays a negligible role for the cutoff energy, which is mainly proportional to λ_L^2 and I_L. The laser intensity must be kept in a rather narrow region of $I = 10^{14}$ to 10^{15} W/cm^2 to allow for sufficient tunnel ionization, yet not over ionize the media. By increasing the wavelength of the laser driver, an electron has more time to be accelerated by the laser field, thus a higher kinetic energy can be achieved. The emitted harmonics can exhibit up to the 1000$^{\text{th}}$ order with keV of photon energy [34, 35]. On the contrary, while being ionized, the electron and the corresponding vacancy form two wave packets with initial coherence [80–82]. The vacancy is locally defined, but the electron wave packet will expand as soon as it is released in the continuum. The recombination amplitude scales inversely to the time spend in the continuum so that there is an expression for the efficiency η of the HHG process given as [83–88]:

$$\eta \sim \lambda^{-5.5} \text{ to } \lambda^{-6.5}$$

This scaling laws give severe limitations to HHG as a source of XUV-radiation. An overall efficiency from the laser pulse energy to the total high harmonics energy generated usually ranges from $\eta \sim 10^{-8}$ to $\eta \sim 10^{-3}$. Depending on the experimental parameters and how the HHG-energy is defined (e.g. single order, whole spectrum, cutoff-radiation). The intrinsically low yield of the electron rescattering cannot be influenced. Because of this aspect, sources like free-electron lasers (FEL) are significantly superior in terms of brightness, brilliance, coherence or maximum photon energy. On the contrary a unique property of HHG is the ability to generate repetitively well defined pulses with attosecond pulse duration. An unseeded FEL in contrast generates pulses with 100 to 30 fs in duration, but extremely structured in time, where every shot exhibits a different temporal structure. HHG-sources are the only sources so far, which are able to generate compressed attosecond pulses [89].

2.9 Isolated Attosecond Pulse Generation

With the discovery of the HHG-process for coherent XUV-generation and the advances in few-cycle lasers pulses, a new range on the timescale became experimentally accessible [90]. The three-step model demonstrates that for a many cycle laser pulse, an attosecond-long burst is generated twice every optical cycle leading to an attosecond pulse train (APT, see Fig. 2.11, [91, 92]). For few-cycle pulses the line-width of the HH-orders become broader, indicating a lower number of attosecond bursts per laser pulse. Laser pulses as short as ~ 4-5 fs can be routinely generated in the lab by a HCFC [40, 41, 93], but such a sources still generates APTs. There are simple yet powerful techniques to achieve a gating

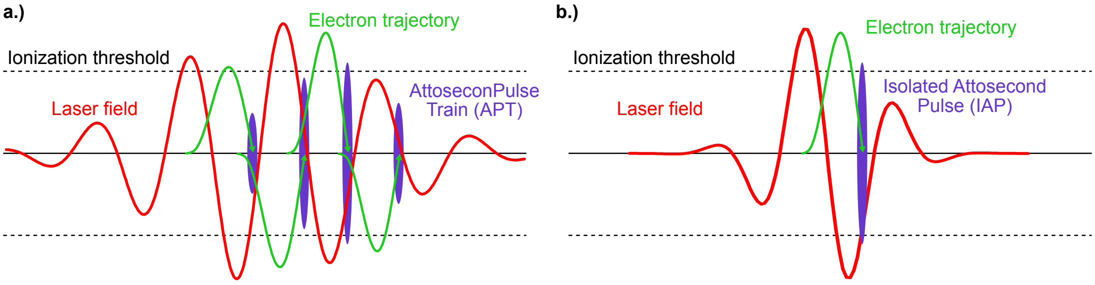

Figure 2.11: a.) Scheme of HHG driven with a few-cycle pulse (red) generating an APT. **b.)** Instead a sub-cycle pulse can limit the HH-emission to a single burst, forming an IAP.

on the HHG emission process if driven with few-cycle sources. One technique exploits the fact, that the cut-off radiation is usually spectrally unstructured for certain CEP-values because these highest photon-energies are only generated by the most intense optical cycle. Careful high-pass filtering of the cutoff radiation allows to generate an IAP [94]. A more elaborate technique uses the extreme dependence for linear polarization of the HHG driver [95], which is required so that the electron can return to the parent-ion for recombination. Additionaly the symmetry of the laser field can be broken by the addition of second harmonic (SHG) radiation. The two latter techniques combined create the generalized double optical gating (GDOG, [10]). This is currently the main method for isolated attosecond pulse production (IAP) from few-cycle laser sources like HCFCs. Attosecond pulses as short as 43 as in pulse duration have been generated by Gaumitz *et al.* and others [4, 96–99], making these attosecond-pulses the shortest controlled man-made events. The availability of attosecond pulses allows to shade light on dynamics occurring on the attosecond time scale by time-resolved experiments [90]. Currently, due to the limited flux of APs, a time-resolved experiment involves a femtosecond and an attosecond pulse. The femtosecond pulse is required because two weak attosecond pulses at or below nJ-level energy cannot generate enough pump-probe signal from a sample. The temporal resolution in pump-probe experiments is partly limited by the duration of the longest pulse. Experiments with fs-as pulses can also reveal dynamics on the attosecond timescale, but the data evaluation needs to rely on retrievals and approximations. Nonlinear interactions between attosecond pulses themselves are demonstrated [100], yet a rarity. An increment in HHG-yield and harnessing sub-cycle sources for IAP-production without gating would open up novel applications for attosecond pulses. Theoretical studies indicate that non-sinusoidal electric field transients are necessary to optimize the HHG-process [101–103].

2.10 Pulse Characterization Techniques

Femtosecond Pulse Characterization

A crucial part in ultrafast laser technology is the compression and characterization of femtosecond laser pulses in time. This requires the measurement of the spectrum and the associated spectral phase of the pulse-under-test (PUT). While the spectrum of a pulse is easily accessible with a spectrometer, the spectral phase is difficult to determine. To characterize femtosecond pulses some other event on a similar time-scale is required. The PUT with $E(t)$, or a tightly synchronized pulse can be replicated and used as a temporal gate $G(t-\tau)$ with the time delay τ. A signal $S(\tau)$ can be generated by convolution, which is temporally integrated due to the slow detection and can be used for pulse retrieval.

$$S(\tau) \propto \int_{-\infty}^{\infty} E(t) \cdot G(t-\tau) \cdot dt$$

Almost all characterization methods for femtosecond pulses are based on cross- or auto-correlation methods with laser pulses derived from the same laser source. To achieve this correlation, nonlinear signals via e.g. the sum- or difference frequency generation (SFG, DFG) need to be derived.

One of the most common pulse characterization techniques is called frequency-resolved-optical-gating (FROG, [104, 105]). The optical setup is identical to an auto-correlator, where a PUT is split, both copies are delayed with respect to each other and recombined (see Fig. 2.12a). The difference to an auto-correlator is the detector, which is a spectrometer instead of a spectrally integrating photodetector. Commonly two pulse copies can be scanned through each other in time by an optical delay line. In the case for the FROG-technique, a complex retrieval algorithm can take the fundamental spectrum of the PUT, guess a spectral phase and compute the theoretically generated non-linear signal. A gauging mechanism judges the similarity between the measured and the theoretical nonlinear signal as a 'FROG-error' parameter. This is fed back to adjust the initially guessed spectrum/ spectral phase. After several loops of the retrieval algorithm, the error parameter might be minimized and the spectral phase can converge to the actual phase of the PUT.

A measurement of a pulse requires up to twice its bandwidth for the SHG-FROG-signal and this bandwidth can create detection difficulties for ultra-broadband pulses (e.g. 1 µm detection-gap in spectrometers). Furthermore for ultra-broadband pulses and more complex pulse structures the retrieved pulse can differ from the measured pulses because the algorithm might got stuck in a local minima of the FROG-error parameter.

Contrary to that, another pulse characterization technique dubbed Two-Dimensional-Spectral-Shearing-Interferometry (2DSI) can be employed (see Fig. 2.12b), and is especially suited for ultra-broadband pulses [106]. The fundamental principle in 2DSI is the up or down conversion (SFG, DFG) of the PUT with narrowband pulses (ancillary pulses). This process, contrary to e.g. FROG does not (significantly) increase the bandwidth of the generated signal. In the case for Ti:Sa pumped OPA systems or HCFCs, these narrowband pulses can be derived directly from the 800 nm output of the laser [107]. For 800 nm ancillary pulses, the PUT spectrum is up-converted to span a range below 800 nm. In such a configuration a huge bandwidth from the far-IR to the UV can be detected all at once with a silicon-based spectrometer (<1 µm). The phase retrieval uses the interference of the nonlinear signal from the PUT with each of the two ancillary pulses. The resulting interference fringes that build up during a shear-scan of the ancillary pulses (spectra from $A(\omega)$ and $A(\omega-\Omega)$ interference) are characteristic to 2DSI measurements and provide information on the spectral phase expressed

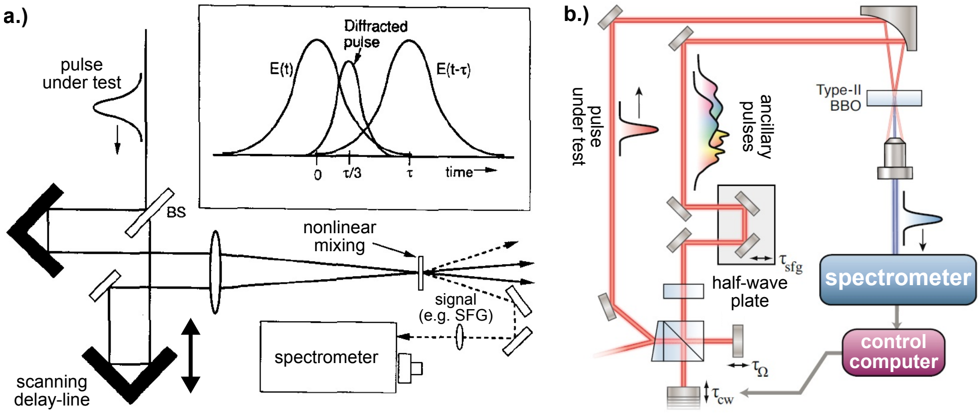

Figure 2.12: a.) Scheme of a FROG setup, where a signal recorded from nonlinear autocorrelation is measured with a spectrometer upon a delay-scan. Figure adapted from [104]. **b.)** Scheme of the two-dimensional spectral-shearing interferometry (2DSI) for pulse characterization. Two narrowband ancillaries individually upconvert/downconvert the PUT in a nonlinear crystal. Figure adapted from [106].

as:

$$\begin{aligned} I(\omega,\phi) &= \left|A(\omega) + A(\omega-\Omega)e^{i\phi}\right|^2 \\ &= 2\left|A(\omega)\cdot A(\omega-\Omega)\right|\cdot\cos\left[\phi + (\varphi(\omega)+\varphi_{CE}) - (\varphi(\omega-\Omega)+\varphi_{CE})\right] + DC \end{aligned}$$

The expression contains components modulated by the shear Ω and not modulated terms (DC). The spectral phase information $\varphi(\omega)$ is encoded within the cosine term in dependence of the shear $\phi = \omega t$. The group delay T_g is given by:

$$T_g = \frac{d\varphi}{d\omega} \approx \frac{\Delta\varphi}{\Omega}$$

Contrary to FROG-traces, the spectral phase of the PUT can be seen easily by eye within the measured 2DSI-trace and can be retrieved by a fast fourier transform (FFT, [108]). The pulse characterisation is usually faster compared to FROG as 2DSI doesn't require an iterative retrieval process. The only dispersion the PUT experiences is happening during the propagation in the non-linear crystal for signal generation, but this can be as thin as a few tens of µm allowing for a ultra-broad phase-matching bandwidth of up to three octaves.

Attosecond Pulse Characterization

The well-established characterization techniques for laser pulses can not be applied to measure attosecond bursts or IAPs emitted from an HHG-source. The main reason is the low intensity of such pulses, which cannot induce sufficient non-linear signal in current experimental implementations. Established characterization methods for attosecond pulses are all based on a similar experimental setup and mainly differ on the exact regime they are performed at. The implementation for attosecond pulse characterization features a laser beam which is split; one part generates the high harmonics and is recombined with the other part and focused inside a low-density gas target. The high photon energy of the high harmonics ionizes the gas species almost instantly and the electrons in the continuum are exposed to the electric field of the laser beam, which modulates the kinetic energy of the electrons (see Fig. 2.13). An electron spectrometer, e.g. a time-of-flight spectrometer (TOF) can measure the raw electron spectrum which is given by the HHG-spectrum convoluted with the ionization cross-section of the gas species and reduced by its ionization energy. Upon linear interaction of the electrons in the continuum with the driving laser field, a change in the electron spectrum can be observed. Because attosecond resolution is crucial in such experiments, the interferometer is usually actively stabilized [4, 109] or an inline geometry with intrinsically low jitter is used [110].

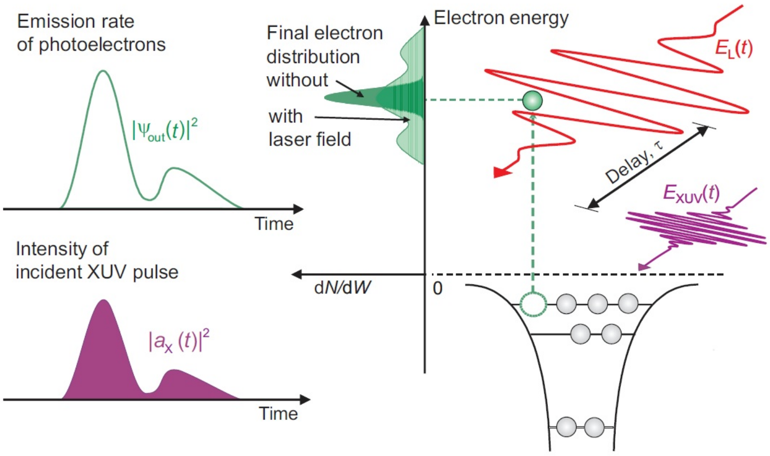

Figure 2.13: Scheme of the principle of attosecond streaking. An atom (gas) is exposed to an XUV pulse, where the release of photoelectron resembles the emission rate of the photons, and the photo electron spectrum correlates with the XUV spectrum. At emission, the electrons are modulated in momentum by a superimposed laser-field. Each photoelectron samples the electric field of the optical pulse at its emission time. A pump-probe fashion delay scan results in an attosecond streaking trace. Picture adapted from [90].

Depending on the presence of IAPs or APTs various methods such as FROG-CRAB [111] can be employed for retrieval of the two involved pulses. Attosecond streaking allows to retrieve the laser pulse in time domain and to retrieve the isolated attosecond pulse. Attosecond streaking is one of very few methods to directly map the electric field transient $E(t)$ of an optical pulse, while usual characterization methods leave the CEP as a an unspecified parameter.

Chapter 3

Towards Lightwave Synthesis

Exploiting nonlinear optics in the form of optical parametric amplifiers marks a big milestone in the development of ultrafast laser source technology. It allows, for the first time, to have an unrestricted choice of wavelengths to be amplified. By using a chain of OPA amplifying stages, the output energy is a scalable quantity up to Joules of pulse energy [112]. Within the limitations imposed mainly by phase-matching, either ultra-broadband or high-gain amplification can be performed. Certain OPA-configurations can reach bandwidths exceeding an octave [51] with moderate gain. Applications in ultrafast laser science, especially strong-field and sub-cycle processes, like attosecond pulse generation or attosecond streaking, demand an even broader bandwidth than an individual OPA-source can be operated at.

As pioneered with the coherent combination of different laser oscillator outputs [113] also the coherent combination of different OPAs can be realized to overcome bandwidth limitations and to reach into the realm of sub-cycle pulses [114, 115]. The combination of two or more entities that form something new together is described by the Latin word *synthesis*. This chapter focuses on the fundamentals of ***lightwave synthesis*** and how it can be experimentally implemented with OP(CP)A-based laser sources. Results and experimental insights of the first synthesizer prototype, implemented at the Kärnter labs in CFEL, are presented. Furthermore initial measurements on that system are shown which have been analyzed to study its system behavior. Following these insights from the initial measurements performed at the beginning of the PhD studies of G. M. Rossi and the author, new conceptual ideas and experimental implementations were suggested to enable stable waveform synthesis and to improve the performance and long-term stability of the system. This enhanced stability is a key requirement to use this source as a novel driver for strong-field and attosecond science experiments.

3.1 Development of Lightwave Synthesis

3.1.1 Early CW Lightwave Synthesizers

The technology of mode-locked lasers has proven itself to create pulses of light with a very high degree of coherence (spatial, temporal (intra- and inter-pulse)). Yet the lasing gain material dictates the wavelength and spectral bandwidth of the generated pulses. To overcome these limitations, the idea to combine the coherent output of separate lasers with different spectral outputs and bandwidths is appealing (see Fig. 3.1). A first theoretical perception of light wave synthesis was given in 1990 from T. W. Hänsch [113]. The simple, yet powerful idea of light wave synthesis sparked a wide interest as presented in the following.

A spatial superposition of two or more laser sources with different spectral properties can be achieved by dielectric mirrors with very low combination loss. The scheme of Hänsch involved CW-lasers so that only the relative phases among the laser sources need to be stabilized, e.g. via heterodyne detection [116], to create a (repetitive) non-sinusoidal electric-field transient. By SFG, SHG, DFG and combination thereof, frequency components of f, $2f$, $3f$, $4f$ and $5f$ could be synthesized with custom amplitude rations and relative phases. Such a light field synthesizer was demonstrated in 2011 by Chan *et al.* [117], although based on molecular modulation [118–120].

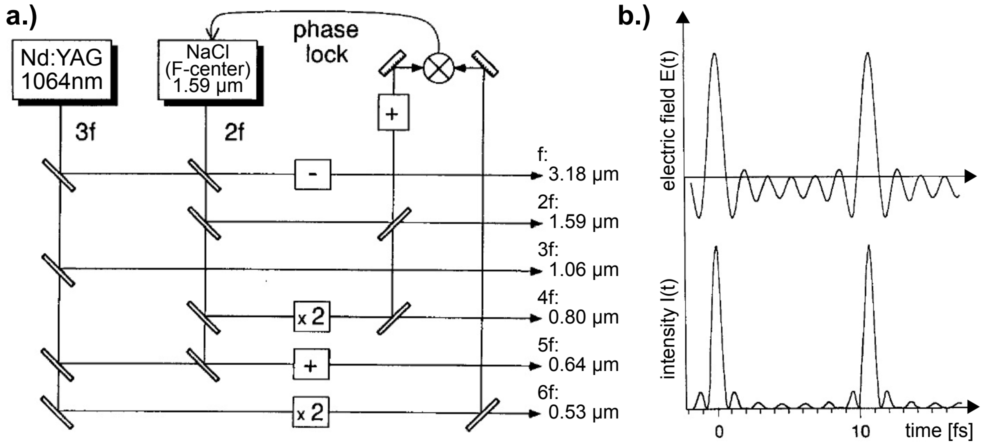

Figure 3.1: **a.)** First proposal of a laser-based electric field synthesizer realized by creating six harmonics from a fundamental and combination of them. **b.)** Corresponding temporal evolution of the electric field $E(t)$ and intensity $I(t)$. Figure adapted from [113].

3.1.2 First Synthesized Pulses

Shelton *et al.* demonstrated the synchronization of two mode locked Ti:Sapphire laser oscillators tuned to different spectral output characteristics [121]. Such a scheme requires low intrinsic phase-noise laser oscillators [122, 123] and tight actively synchronized repetition rates [124]. Such a scheme was also demonstrated using laser oscillators with different gain material, e.g. Ti:sapphire and Cr:forserite [125]. Beside active synchronization two laser oscillators can also be passively locked with each other by using a common Kerr medium to couple the intra-cavity dynamics of both lasers [126].
For the synthesis from two or more pulsed sources, additional degrees of freedom arise (see Fig. 3.2). The CEP ϕ_{CEP} of the involved pulses shape the exact transient of the synthesizer light-field as well as the relative envelope delay τ_{envel}. The exact spectral intensity profile and spectral phase of the individual pulses is controlled by the corresponding dispersion management system of each pulsed source and should be fixed over time. The timing parameters on the contrary requires a constant measurement and active stabilization but also offers an easy method for manipulation of the resulting spectral phase of the synthesized pulse.

Although these early approaches to synthesize pulses originating from mode-locked oscillators were one of the first methods to achieve synthesized few-cycle pulses, the synchronization of separate mode-locked lasers remains challenging and non-practical.

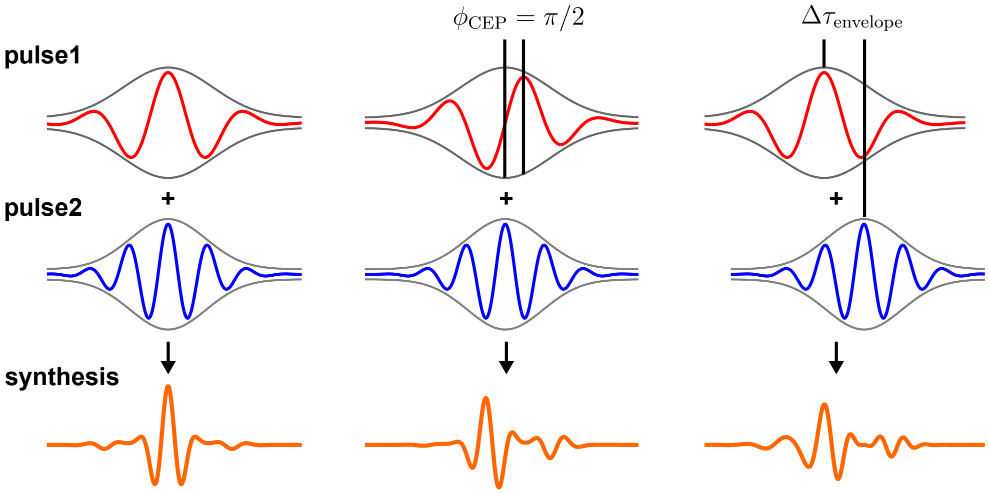

Figure 3.2: Example for the coherent synthesis between two pulses (red/blue) with different wavelentghs and the resulting synthesized transient (orange) in dependence of pulse synthesis parameters relative phase ϕ_{CEP} and relative envelope timing $\Delta\tau_{\mathrm{envelope}}$. Two few-cycle pulses synthesized can result in a sub-cycle light field transient.

3.1.3 High-Energy Single-Cycle Pulse Synthesis

CEP-stabilized Ti:Sapphire laser amplifier systems in return can create a broad bandwidth with high pulse energy by methods like spectral broadening in a hollow-core fiber compression (HCFC). Goulielmakis *et al.* uses such broadband high-pulse energy sources to synthesize single (and sub-cycle) waveforms [127–129]. The broadband HCFC output is split into three to four spectral channels and careful dispersion management of each spectral region is performed (see Fig. 3.3). Also the relative envelope timing(s)/relative phase(s) between the spectral channels can be manipulated to custom sculpture the electric-field transient of the synthesized waveform. The more sophisticated split-compression scheme allows driving the HCFC beyond regular SPM-dominated operation. Such a source can deliver hundreds of µJ of pulse energy and is interesting for attosecond pulse production, attosecond streaking and attosecond pump-probe experiments [130]. Such technically simple implementations of spectral broadening schemes like HCFC, filaments or the newly upcoming multi-plate continuum technique (MPC, [131, 132]) are the main workhorse for few-cycle pulse production, which can be used for isolated attosecond pulse generation by using additional gating methods. For such sources average power limitations and arising instabilities at wide bandwidths limits their further scalability. When the bandwidth of a source becomes wide-enough to support single-cycle or shorter pulses, gating techniques

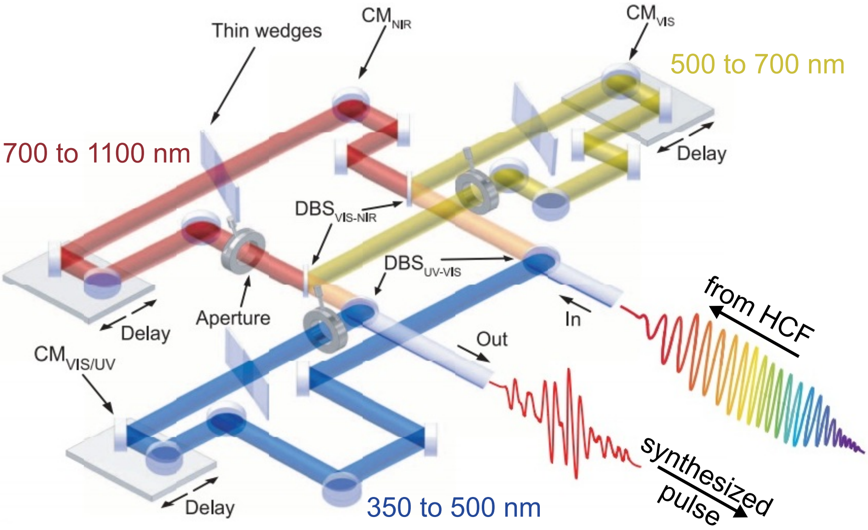

Figure 3.3: Super-octave sub-cycle waveform synthesizer based on an ultra-broadband HCFC. The HCFC-output is split in three spectral channels and individual compression, delay and phase manipulation is performed. Upon recombination the pulse reaches 2.07 fs pulse duration at 750 nm center-wavelength. Active stabilization allows manipulating the synthesized temporal shape of the pulse. Energies of 30-300 μJ are achieved. Figure adapted from [127].

for IAP-generation would not be required anymore. This is advantageous because associated significant pulse energy loss due to gating would be avoided. On the contrary OPAs are more complex to implement but are currently favored by the light wave synthesis community due to their flexibility and unique scaling capabilities, both towards high-energies and ultra-wide bandwidths.

3.1.4 OPA-based Lightwave Synthesis

OPAs offer to transfer energy from pump pulses in the 30 fs to picosecond regime to ultra-broadband pulses corresponding to few and even sub-cycle pulses [58, 133, 134]. Beside Ti:Sapphire lasers, also Yb-based lasers (e.g. as thin-disk, cryo, fiber, REGEN-amplifier) are great choices for pumping OPAs. The gain per unit length of an OPA drastically overcomes that of stimulated emission based laser amplifiers. The output pulse energy of an OPA can be scaled via using a series of OPAs-stages, by chirped-pulse amplification and increasing beam modes into the Joule-level [53, 112]. The output power and repetition rate of OPAs can be scaled as well, because the instantaneous nonlinear effect does not deposit energy in the nonlinear medium nor does the nonlinear material absorb any involved beams significantly. The amplification bandwidth can range up to an octave for special NOPA and DOPA-configurations ([135], see Chapter 2.6). Processes like DFG furthermore allow to generate passively CEP-stabilized pulses which can be used for deriving CEP-stable ultra-broadband seeds, e.g. via WLG in bulk (see Chapter 4).

Three main configurations for light wave synthesis based on OPA sources have been investigated by the community. They differ by the method on how individual OPAs contribute to the spectral intensity of the synthesized pulse. Those schemes are discussed in the following.

3.1.5 Parallel Lightwave Synthesizers

The parallel parametric light-wave synthesizer is based on OPA-sources with different spectral output that are coherently combined (see Fig. 3.4). The scheme consists of at least two spectral channels with at least one OP(CP)A amplification stage. Because the OPA itself can scale with regards to average power and pulse energy, such a scheme can scale easily in pulse energy by adding further cascaded amplification stages. The synthesized bandwidth can be scaled by adding further spectral channels. With single OPAs it is possible to reach almost octave-wide bandwidths, a two or three channel synthesizer can already reach in the realm of sub-cycle pulses. Furthermore the bandwidth scales linearly with the number of channels, the same applies to the pulse energy, while the resulting peak power scales quadratically.

First experimental implementations of the parallel parametric waveform synthesizers were demonstrated by Huang *et al.* [136, 137] and Manzoni *et al.* [138].

The synthesizer presented in this work is based upon commercial Ti:Sa-based pump technology. Efforts in (sub-)picosecond high average power Yb-based thin-disk [134, 139, 140] or coherently combined fiber pump lasers [141–143] could scale this scheme towards higher output power and pulse energy to overcome the current 20-30 W average power limitation of the commercially available Ti:Sa amplifiers. Parametric synthesizers pumped by Yb-based lasers are also currently developed at CFEL [144] and by Krausz *et al.* [134, 145]. For this synthesizer scheme it was proven favorable to not rely on CEP-stabilized laser amplifiers but rather exploit passive CEP stabilization by DFG for broadband CEP-stable seed generation (see Chapter 4). Especially high-power laser amplifiers cannot deliver a sufficiently stable CEP to directly derive an ultra-broadband seed from it. Beside the generation of CEP-stable pulses from a non-CEP-stabilized laser amplifier, the ultra-broadband seed derivation is an experimental challenge too (see Chapter 4.3).

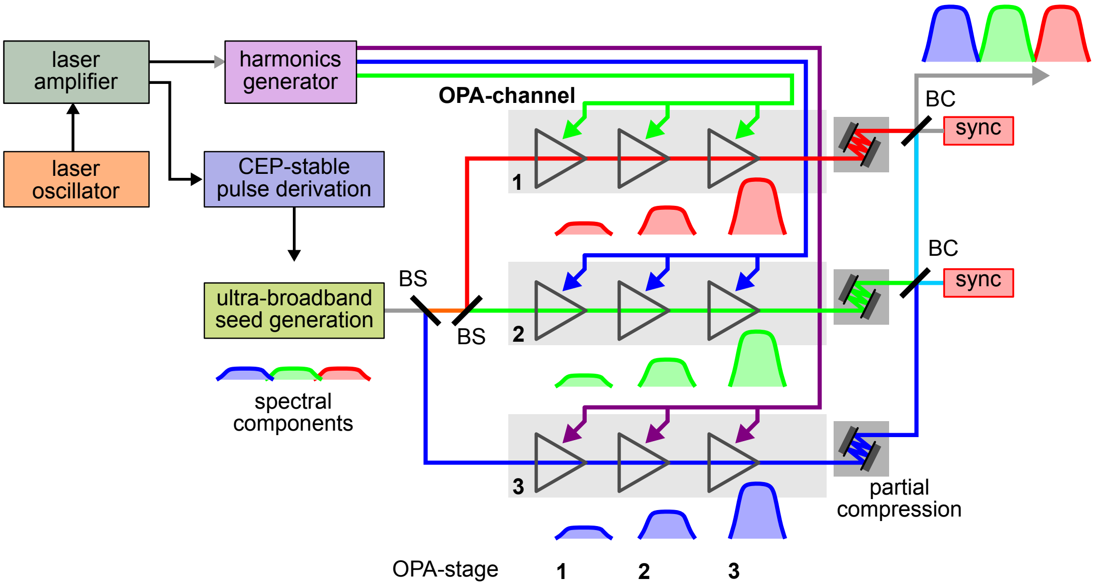

Figure 3.4: Scheme for parallel parametric light field synthesis. An exemplary system shows 3 spectral channels with 3 OPA-based amplification stages each. The broadband seed is spectrally split in 3 adjacent spectral channels seeding the three corresponding amplification systems. At the beam combination (BC) of the amplified outputs, the timing parameters needs to be measured and actively stabilized.

The advantage of this scheme lays in its scalability and that the main dispersion management only needs to handle a limited amount of spectral bandwidth in every spectral channel. Special attention need to be paid to the design of the beam combiner and possible further compression systems, which require to manage the full synthesized bandwidth ([146], see Chapter 3.3). Between the splitting of the seed to the adjacent spectral channels and the recombination of the amplified pulses, a complex nonlinear interferometer with several meters of arm length is formed. Within these interferometric arms, the beams are individually focused/refocused/relay-imaged/stretched, nonlinearly amplified and partially recompressed. Good care need to be taken to measure and actively synchronize these arm lengths to a fraction of a wavelength to achieve stable waveform synthesis at the output (see Chapter 3.4). The requirement to get the pump-seed delay in every OPA matched as well as the relative envelope timing and the relative phase between the output of the spectral channels is a major challenge in this synthesizer scheme. Special attention need to be paid to high mechanical stability, the absence of excess mechanical vibrations as well as low temperature and air fluctuations.

The involved timing parameters such as relative envelope timing, CEP, relative phase and pump-seed delay in the OPA stages form a coupled system which requires a complex synchronization scheme. These challenges were tackled by this thesis to enable the parallel synthesis scheme to create long-term stable and reproducible waveforms with every laser shot (see Chapter 5). The parallel design and its active stabilization system on the contrary also offer a rich set of experimental control knobs to custom-tailor the (down to sub-cycle) electric field transient emitted from such a synthesizer.

3.1.6 Serial Lightwave Synthesizers

The main challenge in parallel light wave synthesis is its active timing synchronization system and the present jitter of the timing observables. The main reason for this jitter arises from interferometric instabilities of the setup. A common technique to prevent timing jitter from occurring is to route beams on a common beam path. An in-line amplification scheme is possible for parametric synthesizers and it avoids the majority of interferometric noise. In serial parametric light-wave synthesizers, a broadband seed is propagating through different OPA stages while each OPA stage amplifies a different spectral region of the initial seed pulse (see Fig. 3.5). Such schemes are pursued by Veisz *et al.* [147–149] by creating the SHG and THG from an Nd:YAG pump laser and pump two adjacent OPAs with 2ω and 3ω and different amplification characteristics. Compression and custom-tailoring of the output pulse can be achieved by acousto-optic modulators (AOM, e.g. DAZZLER). This particular serial implementation uses 78 ps long pump pulses with up to 1 J from a Nd:YAG amplifier with a repetition rate of 10 Hz. Due to the low repetition rate, an active stabilization and control of the timing parameters is not feasible and the synthesized waveform parameters need to be recorded alongside the experimental measurements to employ tagging and corresponding post sorting of the acquired data. A similar two-color-pumped OPCPA system with a high repetition rate of 200 kHz and an output energy of 1 µJ is pursued by Harth *et al.* for coincidence measurements [150]. A similar spectral bandwidth ranging from 430 nm to 1000 nm is amplified in this scheme.

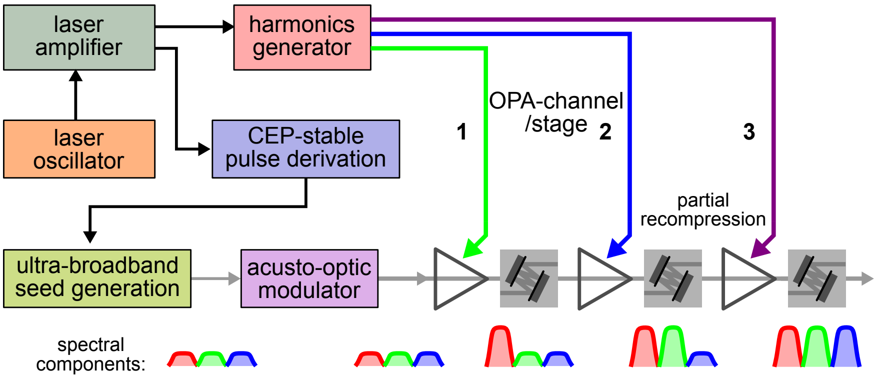

Figure 3.5: Scheme of serial parametric light wave synthesis based on 3 amplification stages. A broadband CEP-stable seed is propagating through OPA-stages while each stage amplifies another spectral range within the seed bandwidth. Partial recompression might be required and the synthesis can be controlled via an acousto-optic modulation on the seed pulses.

Both systems, very different in repetition rate and output power, can compress the output pulses down to roughly 5 fs.

The serial scheme reliefs the constraints on active timing synchronization but adds complexity to the manipulation of the pulse for custom tailoring of the electric field transient. An AOM needs to be used in order to manipulate the spectral phase of the seed. Such complex pulse manipulation usually have a limited throughput (e.g. Fastlite DAZZLER $\eta \sim$ 10-20%) which requires a higher gain in the amplification section to compensate for. Another challenge are the constraints on the dispersion management system, where every transmitting optical component needs to be transparent at the whole bandwidth and the dispersion occurring in each transmission needs to be considered as well as compensated for. This makes the serial schemes difficult to scale in output power and in spectral bandwidth at the same time. The published schemes rely on high-power seed pulses derived from HCFC or similar. To achieve a CEP-stable HCFC output, CEP-stabilized laser amplifiers need to be used that increases complexity and elevated phase-instabilities of the seed.

3.1.7 Frequency-Domain Lightwave Synthesizers

The frequency-domain OPA (FOPA) was invented by Schmidt *et al.* [151] and extends the idea of pulse shaping in 4f-setups [152] by the possibility to also parametrically amplify the spatially dispersed beam in the Fourier-domain (see Fig. 3.6). Previously, spectrally dispersed REGEN [153, 154] and multi-pass amplifiers [155] were already demonstrated in order to mitigate gain narrowing in lasing media.

In ultra-broadband OPAs, effects like gain-narrowing, phase-mismatch and temporal pump envelope walk off limits the maximum bandwidth and pulse energy. With the FOPA an ultra-broadband seed is spatially dispersed in a 4f-configuration. Each spectral region can be amplified with a low phase mismatch when a set of appropriate nonlinear crystals are placed along the Fourier-plane (FP). In the FP, each spatial section consists of temporally extended pulses, so that the advantages of chirped-pulse amplification are also exploited. An amplification of 15x from a HCFC-seeded FOPA was demonstrated in a well-controlled regime and a wide amplification bandwidth spanning from 1.35 µm to 2.25 µm was achieved [151, 156]. The scheme is well suited to generate high-power and high-energy sub-octave output. A special strength of this scheme is the good matching with Yb-based picosecond pump lasers and the ability to generate spectra towards a flattop shape. The intrinsic 4f-system also allows easy manipulation of each spectral component in amplitude and phase with LCDs [157–159] or deformable mirrors [160], giving a very high degree of waveform customization.

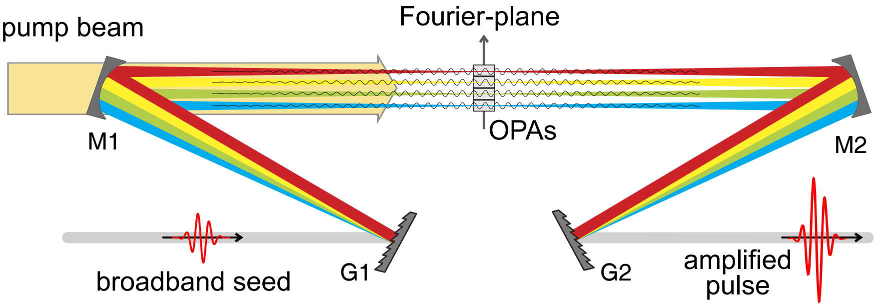

Figure 3.6: Scheme of a Fourier-domain OPA light wave synthesizer. A CEP-stable ultra broadband seed is spectrally dispersed in a 4f geometry where each spectral section is equipped with an OPA to amplify the corresponding spectral range. Figure adapted from [151].

The 4f-setup intrinsically limits the bandwidth of this scheme to an octave. With an amplification of 15x the input seed needs to be derived from an HCFC or an MPC-source. CEP stability in such a case relies on CEP-stable amplifiers and low phase-noise spectral broadening in HCFC or MPC. Such a seed derivation can lead to elevated CEP noise (460 mrad rms in [161]) compared to e.g. passively CEP-stable DFG-based WLG seed preparation.

3.1.8 Comparison of Synthesizer Implementations

Between the different schemes for light wave synthesis, a tradeoff between the complexities in the dispersion management/seed generation versus the complexity in the timing synchronization system needs to be made. An overview of the different aspects between the schemes are made in Tab. 3.1. A parallel scheme offers a promising route with respect to future scalability of pulse energy, average power and spectral bandwidth. The FOPA offers most flexible customization of the synthesized waveform and the ability to create flattop ultra-broadband spectra. For the serial synthesis a high passive stability due to the absence of an interferometer could avoid the requirement for active timing synchronization at all. For both schemes the CEP stability relies on high-energy spectral broadening techniques (e.g. via HCFC) which can result in elevated CEP noise-levels. For the parallel synthesizer an integral requirement is a good passive stability of the optical setup and an additional complex active timing synchronization system.

Table 3.1: Overview and Comparison of different methods for parametric light-wave synthesis.

Synth. Scheme	**parallel**	**serial**	**frequency-domain**
Bandwidth	scalable beyond 2 octaves by adding spectral channels	limited to 1-2 octaves	limited to $<$ 1 octave
Output Energy	scalable by adding channels or stages	limited to 1-3 stages	scalable
Synchronization	strictly required, complicated due to interferometric setup	optional all-inline paths, almost no drifts	optional but requires stable 4f-setup
Seed Generation	single or separate WLGs	single energetic source HCFC or MPC	single energetic source HCFC or MPC
Output Power	scalable	less scalable than parallel/FOPA	scalable
Main Losses at	recombination, compression	AOM, compression	by 4f-gratings
Synthesis	by delay lines and feedback	AOM/DAZZLER of the seed	highly customizable in 4f via LCD/deformable mirror
CEP stability	high seed via DFG and WLG	medium high power seed (HCFC)	medium to high high power seed (HCFC)

3.2 Yb-based Picosecond Pump Laser

This section is a brief consideration of the prospect to scale the pulse energy as well as the average power of parametric waveform synthesizers further by using novel driving laser technology. Currently the synthesizer at CFEL is fueled by a 20 mJ cryogenically cooled Ti:Sa laser delivering 20 W of average power. The Ti:Sa material is an established material system and laser are well engineered around that system. This material is already close to its theoretical throughput limit, which is imposed by limited thermal conductivity, corresponding thermal effects and damage thresholds.

An OPA-based approach itself is quite flexible with regards to the input pulse parameters, for that reason, Yb-based lasers, especially (cryo-cooled) thin-disk lasers [134, 139, 140] or fibers [141–143] offer a significant higher pulse energy and average power capability. Yb-based lasers usually deliver upper hundreds of femtoseconds to few picoseconds of pulse duration, also due to gain-narrowing depending on the pulse energy. In an OPA, the pump-pulse duration is a rather uncritical parameter, chirped-pulse amplification can be operated in the picosecond range and the amplified signals can be compressed back to few femtoseconds. The main technical challenge to switch from Ti:Sa to Yb-based pump-laser technology seems to be the seed generation. If the seed should be derived via WLG, preferably a sub-picosecond laser pulse should be used. Seed generation with longer pulses than that seems to result in WLG which is very difficult to be operated in a stable regime. One possible mitigation is to use cross-polarized wave generation (XPW, [162, 163]) which can shorten a picosecond pulse from the main pump laser [164, 165]. A separate femtosecond seeding front-end, which drives the ultra-broadband seed generation and also seeds the Yb-based high-power laser amplifier could also be a possible solution. Challenges with this approach arise from temporal jitter accumulated in the Yb-based amplifier and compressor with reference to the seed generation.

3.3 Implemented Synthesizer Scheme and Design Considerations

The implemented parallel parametric waveform synthesizer at CFEL is based on three spectral channels with three amplification stages each. Three channels allow for a bandwidth beyond two octaves (500 nm - 2200 nm, see Fig. 3.7a) and a big parameter space for shaping the electric field transient by manipulating the involved relative envelope timing, relative phase and CEP parameters between the three channels. The channels are designed according to well-established broadband OPA implementations like NOPA and DOPA based on beta-barium-borate crystals (BBO) [114]. The output energy distribution among the infrared

(IR), the near-infrared (NIR) and the visible (VIS) channel is tuned towards the application for intense isolated attosecond pulse generation. The majority of the energy is delivered by the IR-channel with up to 1 mJ of pulse energy. Adding the contributions from the NIR channel with 200 µJ and from the VIS channel with 200 µJ results in a synthesized pulse below one optical-cycle pulse duration (see Fig. 3.7b/c) for IAP generation without additional (gating)-techniques. The center wavelength is around 1.7 µm to drive an HHG-source in a regime with high cutoff photon energy reaching the water window (284-543 eV).

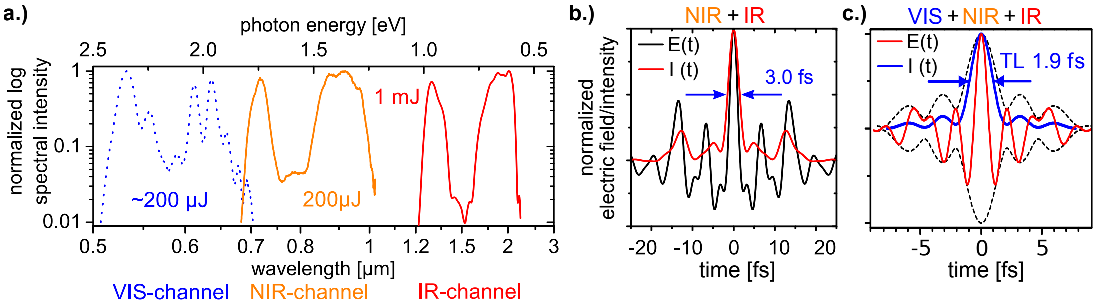

Figure 3.7: a.) Spectral bandwidth and energies of the 3-channel output of the implemented synthesizer. **b.)** Synthesized sub-cycle pulse in time-domain if the NIR and IR-channel where combined and a flat phase is assumed. A FWHM pulse duration of 3.0 fs is achieved, which is further reduced to 1.9 fs if the VIS-channel is added as well (**c.)**).

The pump pulses for the OPA-stages are provided by a commercial cryogenically-cooled Ti:Sa laser system from Coherent (Vitesse 800 + Legend Elite Duo HE+ + Legend Elite cryo-PA). The 800 nm output is used to pump the IR DOPAs, while the SHG at 400 nm is generated to pump the NIR-DOPAs and the VIS-NOPAs (see Fig. 3.8). All the required beams are derived from the pump-laser system which provides a total of 20 mJ 150 fs long pulses at 1 kHz repetition rate. This pump source is to date ideal, because Ti:Sa is a mature technology providing a very good mode-profile and very low intensity fluctuations of 0.3 % as well as long-term stability of the beam parameters. Because the pump laser itself is not CEP stabilized, a CEP-stable pulse needs to be derived to generate a CEP-stable ultra-broadband seed. Initially the CFEL synthesizer used a commercial implementation (Coherent, OPerA Solo) of passive CEP-stabilization via DFG in an OPA (see Chapter 4.1). This commercial source generates a CEP-stable Idler at 2 µm with 45 µJ. This output was frequency doubled and the 1 µm pulses with 15 µJ drove WLG in 2-3 mm of YAG/sapphire. The octaves-wide spectra generated by the WLG was split into three adjacent spectral regions by dichroic ultra-broadband beam splitters.

Each seed is gradually amplified in a three-stage amplifier chain. While the first stage provides an amplification of 10^3 from the 1-10 nJ of seed energy provided, the second stage amplifies 20-40x and the final amplification stage reaches 5-20x.

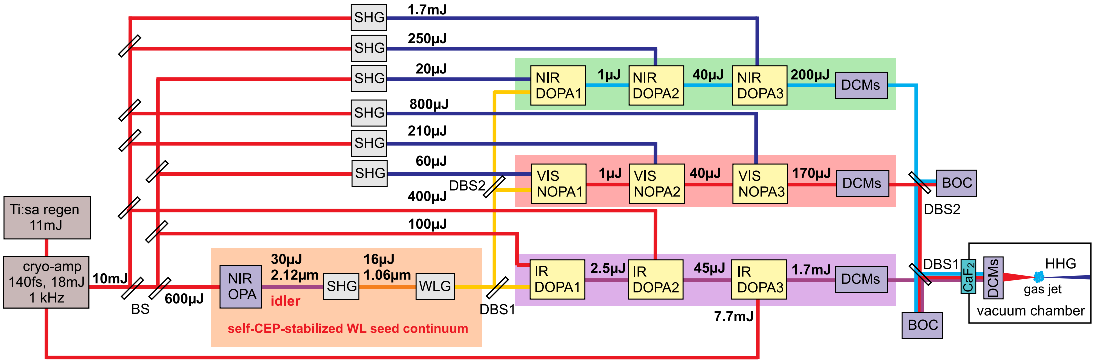

Figure 3.8: Scheme of the first parallel parametric waveform synthesizer at CFEL, which is pumped by a cryogenic Ti:Sa pump laser system. An ultra-broadband CEP-stable seed is derived via a passively CEP-stabilized seeding front-end which drives a WLG broadening stage. The WL-output is spectrally split and used to seed three spectral channels with three amplification stages each. After amplification, partial compression is achieved via DCMS before the beams are coherently combined. Final compression is achieved with ultra-broadband DCMs. Figure adapted from [115].

The last stage is called the *booster stage*, because this stage adds the majority of the absolute energy into the output pulse. The booster stage is operated in saturation, so that the energy fluctuation at the output is mainly defined by the pump laser energy fluctuation [135], which is around 0.3 % rms and 1 % for its SHG. The amplification is performed gradually by three separate stages to avoid super fluorescence [166, 167]. Special attention need to be paid to the first stage due to their higher gain and low seeding energy provided by the WLG source.
A quite complex dispersion management scheme is required for such an experiment (see Fig. 3.9) and demands custom-designed chirped multilayer optics and special dispersive materials. The WL seed needs to be split spectrally with special attention paid to the dispersion introduced by the beam splitter. A custom designed dichroic beam splitter with dual adiabatic impedance matching (DAM) was designed by S.-H. Chia *et al.* to allow for high-reflectivity and smooth GD over the reflecting range and high transmission with side-lobe suppression in the transmission range [115, 146]. These beam splitters furthermore have an intentionally designed leakage of a few % to be used to measure the relative envelope timing between the combined pulses. The GDD and TOD accumulated during amplification within the BBOs is taken into account and partial recompression is performed with double chirped mirrors (DCM) and wedges of glass (fused silica or zinc selenide) in each spectral channel. For the recombination of the channel outputs the same custom designed dichroic beam splitters are used. Because this synthesizer source is primarily developed to drive IAP-production via HHG, the synthesized pulse needs to be transmitted through a window (CaF_2) in a vacuum chamber to drive the HHG. To avoid excess B-integral during the transmission

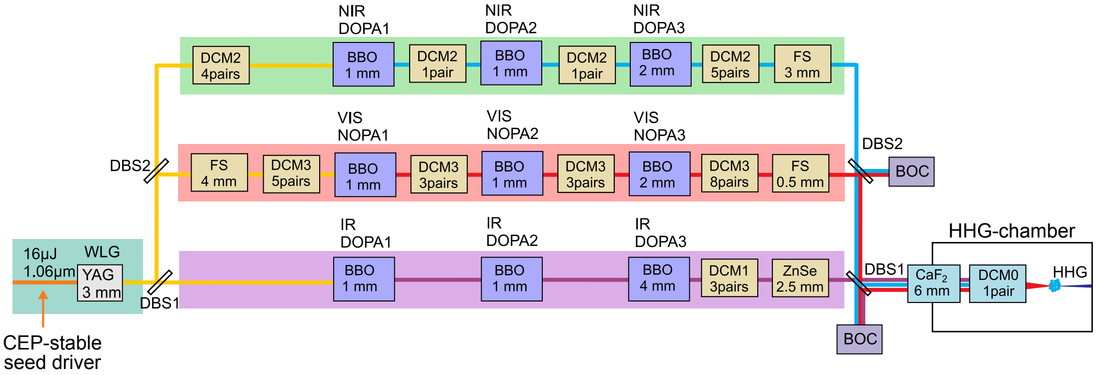

Figure 3.9: Dispersion management scheme for the first CFEL synthesizer. The seed is spectrally split with the same beam splitters as the amplified output is combined with (DBS1/2). The dispersion management is based on glass-wedges in combination with DCMs and allows an effective correction of GDD and TOD and fine tuning of the compression. After recombination, the beam passes a vacuum window before final compression is achieved with ultra-broadband DCMs. Figure adapted from [115].

through the window the synthesizer output is not fully compressed. The final compression is performed with ultra-broadband custom designed DCMs [146], which covers the whole spectral bandwidth of more than two octaves the synthesizer is providing (see Fig. 3.10). The compression of each spectral channel was

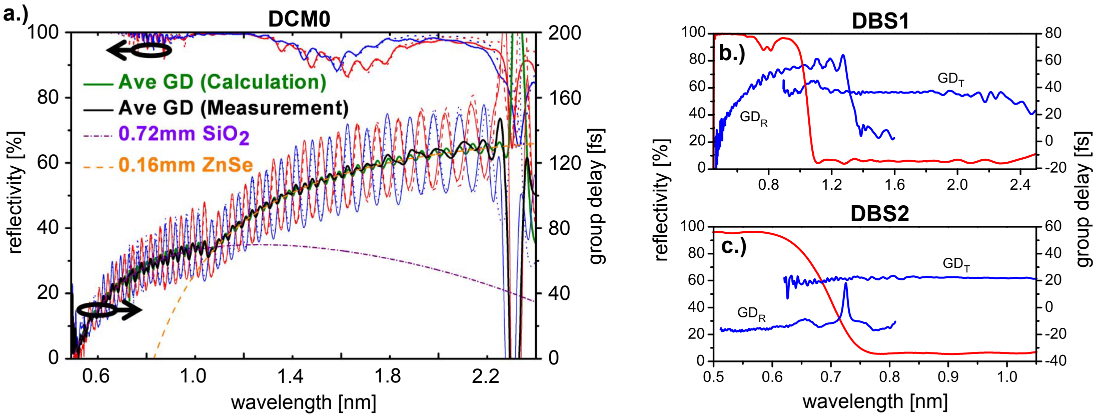

Figure 3.10: Spectral and dispersive characteristics of the final compression-stage with custom-designed DCMs (type: DCM0) supporting the whole spectral bandwidth of the synthesizer output from 550 nm to 2.2 µm. Figure adapted from [146].

characterized by FROG, demonstrating that each channel alone is compressed close to its Fourier-transform limit and provides few-cycle pulses at the output (see Fig. 3.11). For the NIR and VIS-channel a SHG-FROG was used, for the IR-channels was characterized using surface-THG-FROG to avoid the spectrometer detection gap around 1 μm. While the optical layout, the OPA-configurations and the dispersion management were mainly matured, other aspects like the active timing synchronization and the waveform manipulation were still in a developing state. It was expected that a rather high degree of passive stability with respect to timing parameters is present and the amplified pulses at the output will also maintain a drift-free coupling to the CEP of the seed. The timing infrastructure was planned to be implemented by using two balanced optical cross-correlators (BOC, see Chapter 3.4.1) following the original BOC design introduced by Schibli *et al.* [124]. Each BOC was expected to measure the relative envelope timing between two spectral channels and compensate for interferometric drifts and instabilities by moving one output in time by a delay line.

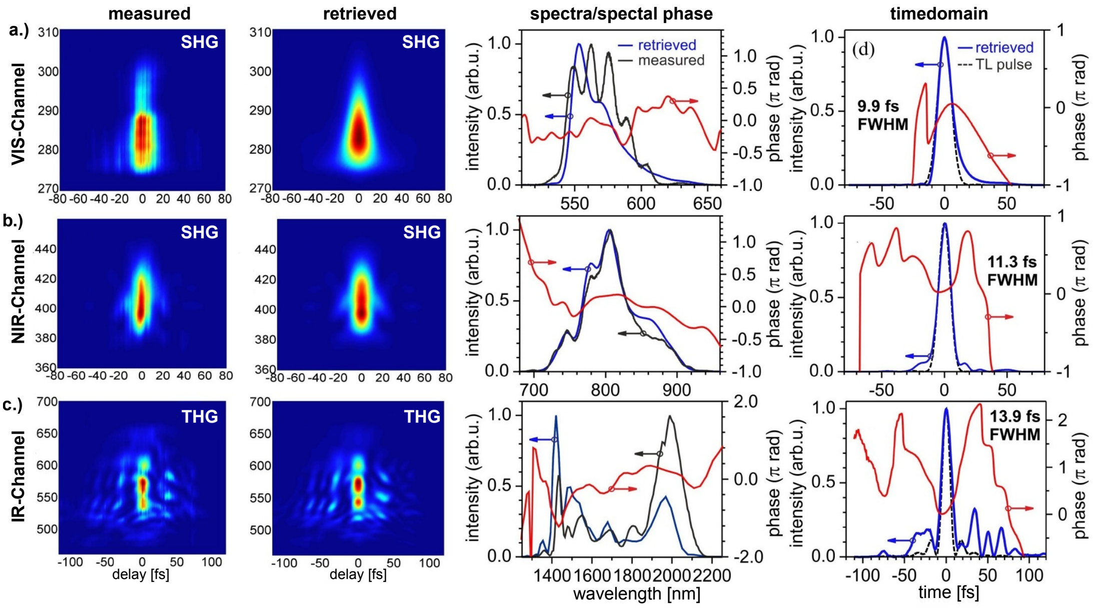

Figure 3.11: Full Panel of the measured and reconstructed FROG-traces of the individual synthesizer channels. SHG-FROG for the VIS and NIR-channel and surface-THG for the IR-channel. Compression of all channels is achieved close to their Fourier-transform limit. Figure adapted from [115].

3.4 Early Experiments and Encountered Problems

This section presents synchronization experiments on the first implementation of the parallel parametric synthesizer at the CFEL labs. During these experiments we gathered valuable insights that revealed challenges concerning the conceptual scheme, the experimental implementation as well as requirements on special instrumentation. At the same time, we were able to demonstrate for the first time, that such a complex nonlinear interferometer with tens of meters of arm length can be stabilized to a fraction of an optical cycle. This proves that mJ-level parallel parametric waveform synthesis achieving two octaves of bandwidth is indeed possible.

3.4.1 Relative Envelope Synchronization

An ultrafast timing tool for the measurement of the relative envelope delay between two pulses was first demonstrated by Schibli *et al.* in the form of a balanced optical cross-correlator. The BOC was initially employed to synchronize (and synthesize) pulses from two mode-locked laser oscillators [124, 168]. The core idea is to utilize cross-correlations between the two pulses using nonlinear crystals (see Fig. 3.12). To resolve the intrinsic coupling to intensity fluctuations of the input pulses, a second cross-correlator with a modification in the time order between the two pulses is used. A signal derived by subtraction of both nonlinear signals yields a characteristic transfer function with a monotonic relation between signal output and relative envelope delay. This characteristic curve is usually called *S-curve* and contains a predominantly linear region which can be used as an error signal in an active stabilization loop. The author implemented a BOC for relative envelope measurement and stabilization between the outputs of the synthesizer. Initial BOC experiments were performed by creating a double pulse of the plain laser output of the 130 fs long laser pulses in an interferometer. These double pulses were fed into a classic BOC setup proposed by

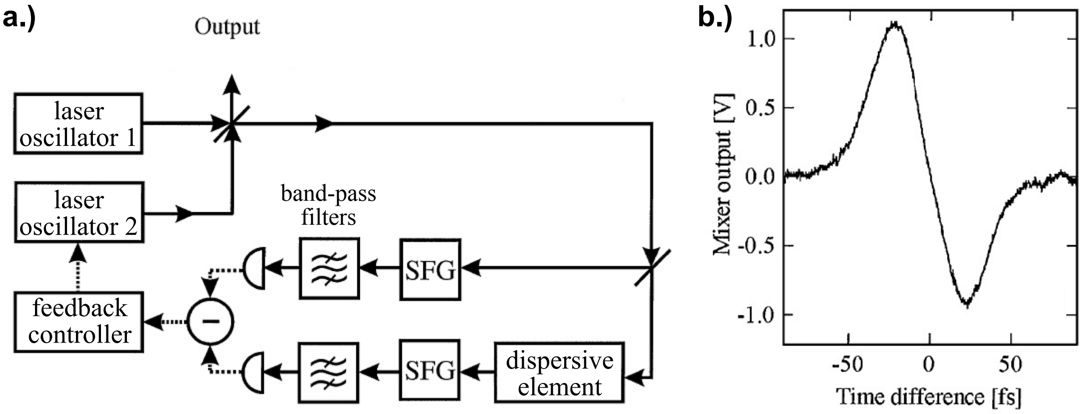

Figure 3.12: a.) Basic setup of a BOC as invented by Schibli *et al.* to measure and actively synchronize the relative envelope timing between two laser sources. Two similar cross correlators are setup where the temporal order of the two pulses for cross-correlation is modified by a dispersive element in one of the BOC arms **b.)** Characteristic S-shaped curve from the two subtracted SFG-signals as a function of relative envelope timing. Both Figures adapted from [124].

Schibli *et al.* [124]. During these experiments, it was found that the SFG-signal from the two BOC arms are difficult to measure with high resolution, due to their pulsed nature. To improve on the resolution of the measurement, the author developed a photodetector with a digitizing and triggered gated-integrator circuit to measure and directly digitize the electron-charge deposited on the photodiode. (This detector as well as the optical schemes of the BOC setup were further developed and will be discussed in detail in Chapter 5.1).
After these initial experiments, a BOC measurement was performed between the IR- and the VIS-channel of the synthesizer (see Fig. 3.13a). The two outputs were roughly synchronized using a manual delay line and could be manipulated by a piezo driven delay line with 100 µm range (Physik-Instrumente, Piezomove P-601.1SL, Controller: E505.00). The BOC setup consists of two 1 mm thick type-I BBO-crystals creating a SFG between 1550 nm from the IR-channel and 580 nm from the VIS-channel. The SFG at 420 nm was filtered using a 10 nm optical bandwidth interference filter (Thorlabs FB420-10) and the two BOC cross-correlations were displaced in time by adding a 3 mm thick glass plate in one arm of the BOC.

The phase-matching of the two BBOs were fine-tuned to pick up a representative frequency component from each synthesizer channel. The interference filters were tuned as well to transmit the spectral SFG maximum. The piezo-driven delay line is controlled by an analog voltage which corresponds to a fixed displacement of the piezo (PZT, 1 µm/V). The BOC S-curve was first optimized and the BOC was then operated within its linear region (see Fig. 3.13b). The PZT was moved sinusoidally with a characteristic amplitude and frequency (1 µm$_{pp}$, 33.3 Hz) in the linear region of the S-curve, which allows to calibrate the BOC data in time. Then a passive BOC measurement was recorded and the data was rescaled to time using the above mentioned calibration procedure. In several

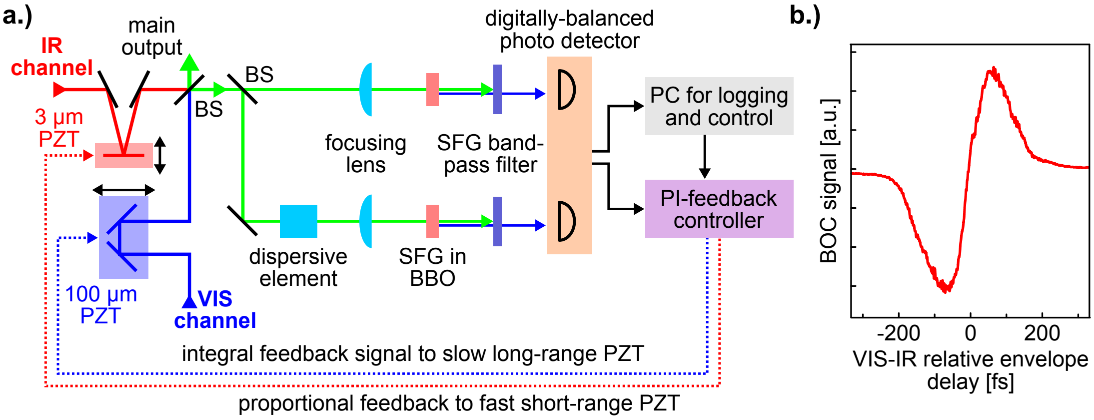

Figure 3.13: a.) Relative envelope measurement between the VIS and IR-channel via BOC. A split feedback allows for fast and long-range feedback. **b.)** Resulting characteristic BOC signal during a relative envelope timing scan.

measurements, the behavior of the synthesizer output was studied by analyzing the BOC data in time and frequency domain. First, we always observed a very strong and monochromatic noise at 85 Hz (see Fig. 3.14c) and a 17 s lasting slow drift of the signal in the BOC. Both noise components had their origin in the commercial laser system itself, we were able to fix it and to completely remove those components from our BOC signals (see Chapter 3.5). Furthermore another strong component at 287 Hz was present which was associated to the piezo-driven delay line which had a mode of mechanical vibration in the retro-reflector assembly (see Chapter 3.6). The home-made BOC detector sends the single-shot data to the PC for data logging, but was also modified to send the acquired signals from both photo-detectors digitally to another circuit. This circuit performed a subtraction (balancing) of the two signals and fed this into a proportional-integral controller (PI-controller), both implemented in software on a microcontroller. The output of this PI-controller is converted to an analog voltage by an digital-to-analog converter (DAC) and fed to the piezo-controller that drives the PZT-driven delay line to achieve active synchronization. During these experiments it became clear that the used PZT-driven retro-reflector assembly was too unstable for proper synchronization experiments. By driving the PZT, significant vibrations in the optical path were introduced. A workaround for this behavior was to use a second piezo actuator assembly with significantly shorter stroke (3 µm), but stiffer mechanical assembly (Noliac, NAC2125-A01, see Chapter 3.6). This second PZT moves only one 1-inch mirror instead of a heavier retro-reflector. The software-based feedback generation allowed to drive the long-range PZT very slowly with the I-component of the feedback, avoiding to induce the mechanical vibrations. While the short-range PZT was used to drive the P-component. With this approach the BOC allowed to synchronize the

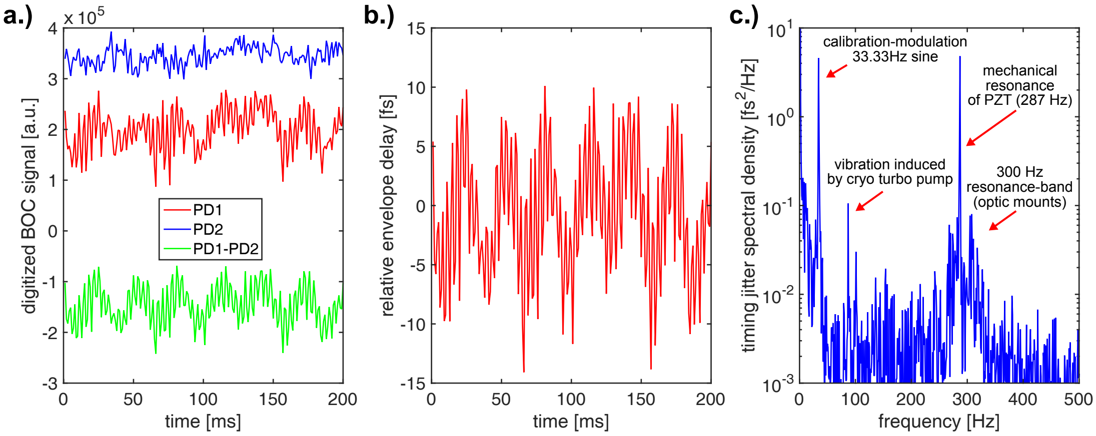

Figure 3.14: a.) Individual photo-detector signals (red/blue) and substation (green) for the BOC measurement. **b.)** BOC signal with induced modulation signal of 33.3 Hz for calibration purposes. **c.)** Noise spectral density of the signal from b.) with indicated noise-sources.

two synthesizer channels with a residual timing jitter below 360 as rms (see Fig. 3.15a, [169]). Achieving such a low relative envelope timing noise is a crucial requirement for waveform synthesis and a significant achievement for the parallel synthesizer scheme which had 30 m of beam propagation in that experimental implementation.

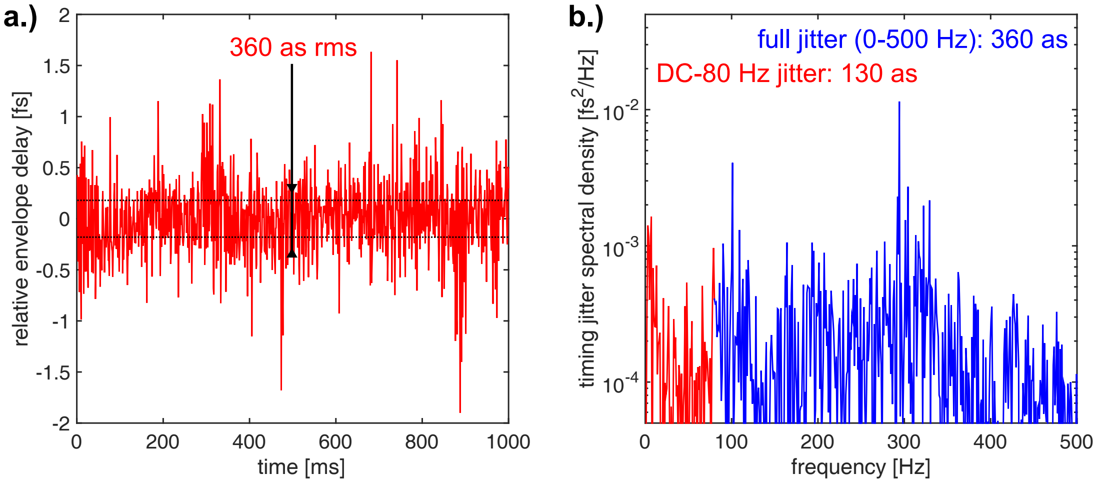

Figure 3.15: a.) Achieved residual relative envelope timing noise of 360 as rms between the VIS and IR-channel of the synthesizer with distributed feedback. **b.)** Corresponding noise spectral density indicating the absence of strong single noise sources.

The spectrum of the noise does not show a significant component (see Fig. 3.15b). A broadband noise band around 300 Hz is usually observed and comes from the intrinsic resonance frequencies of all the optics mounts on the beam path. A reduction of this contribution can be achieved by reducing all sources of mechanical noise influencing the setup which excite these intrinsic modes. The absence of a 50 Hz line-noise proves the good design of the pump laser (Coherent, Evolution) for our Ti:Sa laser system and also the superior approach to directly digitize the photo-detector signal at the detector itself preventing ground-loops and electronic coupling by electro-magnetic-interference (EMI). Depending on the amount of SFG-signal fed to the photodiodes, the noise floor of the detector was characterized to be on the order of 5-20 as rms. The main noise contributions originate from the optical setup of the synthesizer and the optical part of the BOC setup.

During those experiments, it was observed that the synthesizer output intercorporate some pointing fluctuations mainly from air fluctuations as well as elevated intensity fluctuations (if compared to laser amplifiers). The balanced two-arm BOC scheme has cross-sensitivities to these parameters and was also quite complex with many optics involved that required precise alignment. Together with G. M. Rossi, the author invented a new variation of the BOC to overcome these cross-sensitivities and to significantly reduce the complexity and footprint of a BOC setup (see Chapter 5.1).

3.4.2 Relative Phase Synchronization

A synchronization of the relative phase (RP) between the synthesizer outputs is significantly more complicated to perform than the relative envelope synchronization. The problem arises mainly from the detection and processing of the optical signal. To measure the relative phase between two pulses $E_1(t)$ and $E_2(t)$, they must overlap spatially and spectrally with similar divergences. For simplification, it is assumed that both pulses are the same but separated in time by τ with $(E_2(t) = E_1(t-\tau))$. A phase-coherent spectral extension can be achieved either via spectral broadening (e.g. WLG in bulk) or via SHG/THG. When a region with coherent spectral overlap is present spectral fringes can be observed in the frequency domain with:

$$I(\omega) = |E_1(\omega) + E_2(\omega)|^2 = |E_1(\omega)|^2 + |E_2(\omega)|^2 + 2\,|E_1(\omega)| \cdot |E_2(\omega)| \cdot \cos(\omega\tau + \Delta\phi)$$

The intensity spectrum $I(\omega)$ is modulated by the fringe frequency $\omega\tau$, which represents the temporal delay τ between the pulses. The spectral phase of this fringe frequency determines the relative phase, while the *cos*-term only allows to see a modulo-2π phase (wrapped phase). This phase is further influenced by additional phase terms such as the CEP of both pulses $\Delta\phi = (\phi_2 - \phi_1) \mod 2\pi$. By a Fourier-transform on the intensity spectrum $I(\omega)$ the spectral phase of the fringe beating can be extracted (see Fig. 3.16) and can be continuously tracked. One important prerequisite is that the maximum phase difference between two measured spectra is smaller than π, otherwise the phase tracking is lost (phase-jumps). This method is not able to determine an absolute quantity, but can be used to stabilize the phase relation of two pulses and determine the phase noise

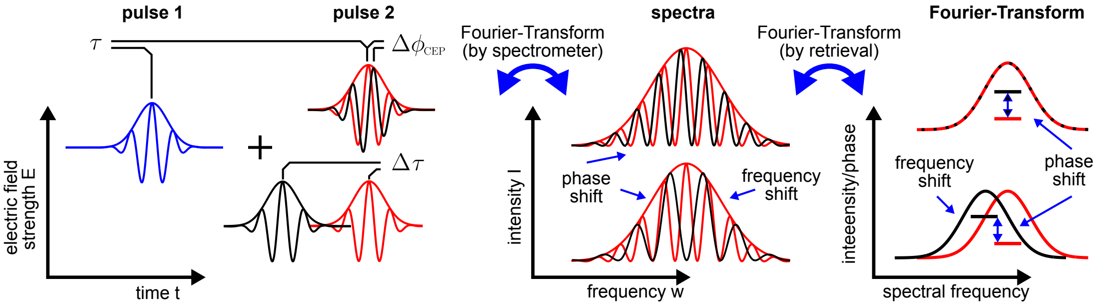

Figure 3.16: Scheme of the coherent combination of two laser pulses. The fringe beat in the spectral domain allows to retrieve a phase information which contains the relative phase difference between the pulses. Top-row: Modification of the CEP of one pulse Bottom Row: change in temporal displacement between the pulses.

within an optical system. Depending on the two input pulses and how the two overlapping spectra are created, a CEP dependence can or cannot be observed, generally the relative phase difference of every frequency component $I(\omega)$ of the input pulses is determined and dependent on the spectral phases $\phi_{1/2}(\omega)$ of both pulses.

To observe the relative phase between two synthesizer outputs via spectral fringes, the output from the IR-channel was frequency doubled in a type-I BBO to beat with the VIS-channel around 650 nm (see Fig. 3.17). The spectral fringes were

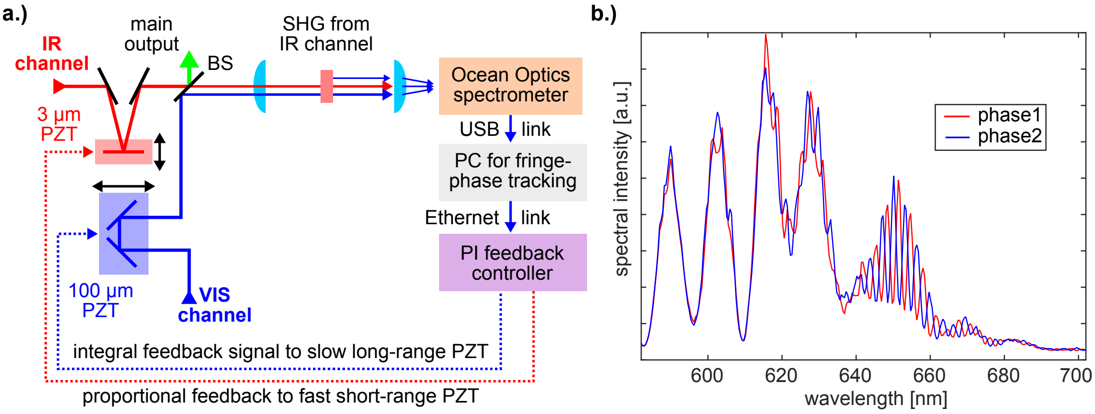

Figure 3.17: a.) Setup for the relative phase measurement and active stabilization between the IR and VIS-channel of the synthesizer. The IR-channel is frequency doubled and overlaps with the VIS-channel. **b.)** Observed spectral fringes with two different relative phases (red/blue).

observed with a USB2000 spectrometer (Ocean Optics) connected to a PC for recording via USB. On the PC a script acquired spectra as fast as possible using MATLAB. The lowest possible integration time of the spectrometer was set (1 ms). The spectrometer acquired for 1 ms and then it took another 1 ms to transfer the data to the PC. Because the spectrometer could not be triggered in that setting, a beat between acquisition rate and 1 kHz laser repetition-rate was present, so that rarely single spectra contained two laser shots but most of them were from a single shot. This is very crucial; otherwise if too many laser shots are integrated over, a fluctuating relative phase would lead just to a decrement of the spectral fringe contrast but not to a detection of relative phase fluctuations. Due to the time it took to transfer the data to the PC, every second laser shot was not measured and hence lost.

Each spectrum was multiplied with a window-function (Hanning) to only observe the region with spectral beating. These windowed spectra were Fourier-transformed (FFT), and then a clear magnitude signal with the fringe frequency could be observed. The phase for this frequency component was extracted and compared to the previous phase to perform an unwrapping from $[-\pi; \pi]$ to yield a continuous phase. For every acquired spectrum, this retrieved phase information was send via an Ethernet UDP data packet to a circuit with a microcontroller. This circuit calculated from the unwrapped phase information a feedback signal via a PI controller. The resulting feedback signal was converted from digital to analog and fed to a piezo-driven delay line (PI, P-753.1CD and home-made PZT assembly), which manipulated the relative phase between the two synthesizer channels by delaying one output. With that system it was possible to achieve a lock of the relative phase with a residual phase noise of less than 220 mrad rms referenced at 1.3 µm (see Fig. 3.18). Similar to the locking of the BOC, this residual phase noise proves that also the relative phase can be locked to a fraction of the optical wavelength to allow for stable and reproducible waveform synthesis. Beside the phase noise introduced by the fluctuations in the arm length of the nonlinear interferometer within the synthesizer, also the CEP stability of the seed generation is observed, due to the involved SHG of the IR-channel, which effectively forms an f-2f-setup (see Chapter 2.7).

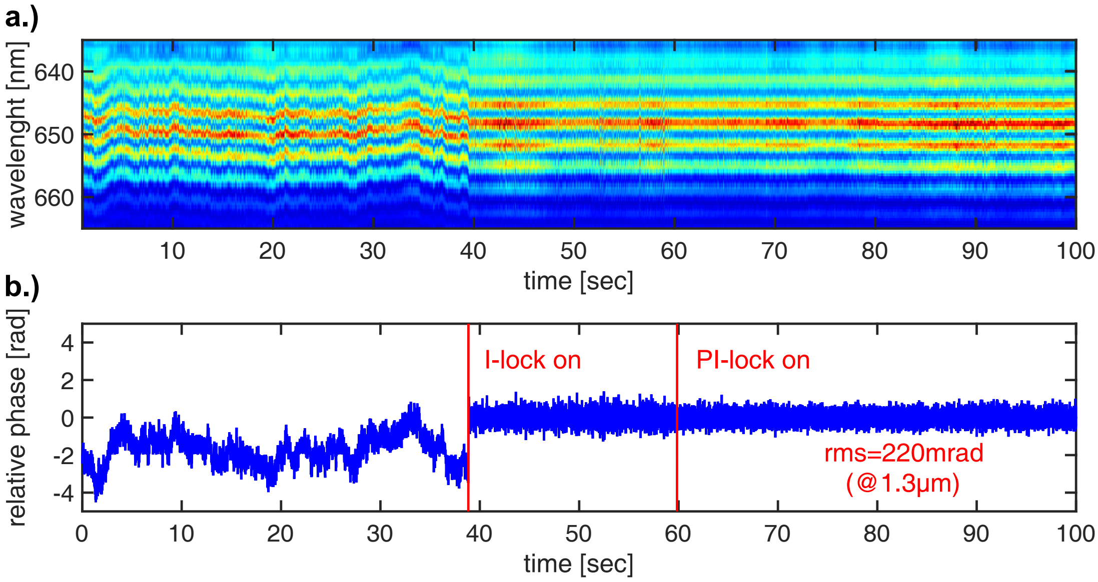

Figure 3.18: First relative phase measurement and active stabilization performed on the synthesizer experiment. **a.)** Recorded spectral fringes around 650 nm via beating the VIS-channel with the SHG of the IR-channel. After 40 s an active phase-lock is activated, stabilizing the spectral fringes. **b.)** Retrieved relative phase which settles to a relative phase noise of 220 mrad rms if referenced to the corresponding 1.3 µm component.

A significant challenge is imposed by the fact that the spectrometer is neither triggered nor able to acquire every laser shot. Both circumstances significantly increase latency and reduce the feedback bandwidth. Also the chance that the phase-tracking is completely lost if two consecutive shots observe a phase which is moved by π or more pose a significant problem for waveform synthesis. Furthermore such a commercial spectrometer, as used here, is designed to measure a very broad spectral range (USB2000: 200 to 850 nm) while spectral fringes usually need to be observed within less than 100 nm of bandwidth in most experimental implementations. In this measurement, a fringe oscillation spans over only 7 pixels of the photo-detector array inside the spectrometer. The overall signal chain in this first relative phase lock consisted of:

- not triggered acquisition of the spectrometer with 1 ms integration time
- transfer of the spectra to the PC via USB
- windowing and FFT-calculation in MATLAB
- unwrapping and outputting of the phase via a UDP-packet
- reception of the UDP-data and performing of the PI-calculation
- digital-to-analog conversion and actuation of the delay line

This complicated data path via a PC with a MATLAB instance led to a input-to-output latency of 7 ms, which effectively limits the feedback bandwidth to less than 35 Hz. Because of all the aforementioned difficulties, the author built a home-made narrowband triggered single-shot every-shot spectrometer. It features an FPGA-based FFT phase-retrieval to reduce the overall feedback latency to $< 300\,\mu s$, which is less than the repetition period of 1 ms from the laser system (see Chapter 5.2.1).

3.4.3 Coupling between Observables

After separate active stabilization experiments for the relative envelope timing and the relative phase, both observables were measured and one was actively stabilized. Here it became obvious that both quantities were actuated together since the PZT delay line rigidly moved the whole pulse in time. If observed changes in relative envelope timing are actively stabilized by moving the delay line, the noise is only transferred and was imprinted on the relative phase instead. Due to this circumstance and to the fact that the optical setup experience drifts in all timing parameters, a complete new active stabilization system was invented decisively by the author and G. M. Rossi with contributions from colleagues (see Chapter 5).

3.5 Modifications to the Ti:Sa Laser System

The cryogenically cooled Coherent laser system offers a stable and reliable high-energy laser source for driving the synthesizer experiment. Nevertheless the experimental setup is very sensitive to instabilities like pointing fluctuations from the pump laser source.

In the relative envelope synchronization experiments with the BOC (see Chapter 3.4.1), two main noise components are tracked down to the laser system. One was a strong sinusoidal noise signal at 85 Hz. This was caused by the turbo molecular pump (Agilent, turbo-V 81M) directly attached to the cryostat of the last-stage laser amplifier (Coherent, Legend Elite cryo-PA). This pump induced a vibration on the Ti:Sa crystal and the optical table at 1085 Hz which was down sampled to 85 Hz by the laser repetition rate at 1 kHz. The vibration caused pointing fluctuations which were seen by the BOC experiment 30 m downstream the laser beam and also induced vibration to all other optical components on the optical table. This mechanical vibration was tracked using an acceleration sensor (MMF, KD41) by measuring the frequency spectrum across the setup (see Fig. 3.19a). The problem was solved by attaching a long vacuum bellow (KF-100) to the Ti:Sa amplifier cryostat and rest a magnet-bearing turbo pump (Pfeiffer, TM 700) on a separate stand isolated from the optical table for vibration isolation (see Fig. 3.19b). Furthermore the new pump controller allowed to tune the rotation frequency of the turbo molecular pump to the repetition rate of the laser at 1 kHz. If still low mechanical couplings are present they are now at zero frequency (DC) and can be easily removed by locking with an active synchronization system. Another very slow fluctuation of the beam pointing was observed in the BOC measurements as well as in separate beam pointing measurements with a beam cam. The fluctuation was monochromatic with a period of 17 s, which is surprisingly low for a periodic noise. After analyzing this pointing and tracking it upstream through the laser system it was found that one of the TEC-cooled Ti:Sa amplifier crystals in the Coherent Legend Elite Duo HE+ should be cooled to -20 °C but the temperature controller was set wrong and the crystal was exposed to 0-to-100% load changes in the TEC-current due to an oscillation of the temperature control system. This problem was fixed by

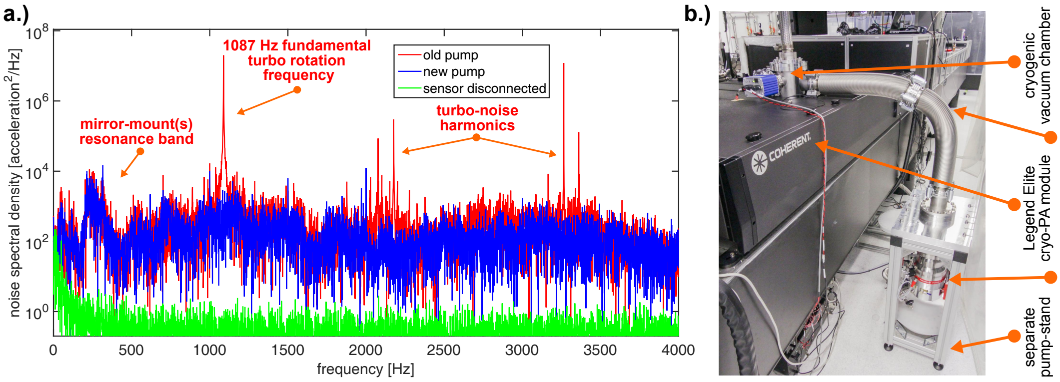

Figure 3.19: a.) Acoustic/Mechanical-noise spectrum recorded via an accelerometer mounted on the optical table. A dominant signal amplitude is attributable to a turbo molecular pump attached onto the cryogenically-cooled Ti:Sa amplifier. Furthermore a broadband noise arises from the vibrational modes of the optics mounts. **b.)** Picture of the modifications to the cryostat vacuum system. Vibration isolation is achieved via a flexible bellow and a low-vibration hybrid-bearing turbo molecular pump is used.

reconfiguration of the temperature controller.
The laser system does not feature a general temperature or pointing stabilization system, only a few subsystems have local temperature regulation. The laser has in total around 70 m of internal beam propagation starting from the oscillator through the REGEN, single-pass and cryo-amplifier. To compensate for drifts, especially during warm-up time, beam pointing stabilizers were introduced in the laser as well as stabilizers which reference the beam with respect to the pumped optical systems (see Chapter 6.1).

3.6 Improvement of the Piezo-driven Delay Lines

In all performed experiments, piezo-driven delay lines were a crucial part of the active timing synchronization and control system. Over time the passive stability of the synthesizer experiment was constantly improved by various measures. A major step towards a high degree of passive stability was achieved by the reengineering of the synthesizer setup as described in Chapter 6. This high stability allows to use piezo-driven actuators with just a few (tens) of µm of actuation range to compensate for all present timing drifts within the optical system. A general tradeoff for piezo-driven actuators is the actuation range versus the driving speed and pointing stability. The first actuator was implemented as a complex retro-reflector assembly actuated by a lever-type piezo with an increased range of 100 μm (Physik-Instrumente, P-601.1SL). This actuation system had several mechanical resonance frequencies and induced significant pointing fluctuations during actuation.
A new compact actuator (Physik-Instrumente, P-753.1CD) was implemented instead and allow to drive an attached 1-inch mirror within a 20 μm travel range in under 1200 μs for small displacements (see Fig. 3.20). The controller (Physik-Instrumente, E753) features a DSP-controlled position feedback system and can be tuned directly to the specific load attached. The actuated and directly attached front mirror can be driven with up to 25 mm/s while maintaining a pointing stability of better than 5 µrad [170]. The controller can be interfaced with a PC or directly driven via an analog-voltage input, the latter is used with our feedback system for lowest latency actuation.

Furthermore, in some applications within our synthesizer experiment, it is only required to shift a phase within 1-2 optical periods, corresponding to few µm of travel. For that, home-made mirror assemblies were combined with a commercial ring piezo (Noliac, NAC2125-A01) which has a nominal travel under load of 3 µm (see Fig. 3.21). The piezos are driven by a high-voltage piezo driver (piezosysteme Jena, 30V300) and a position feedback is not required for such low actuation range because nonlinearities in the characteristic curve of the piezoceramic ($\sim$ 10%) are negligible for short-stroke piezo actuators. The ring-based PZT-actuator is held in a massive metal block (m =200 g) and preloaded with a

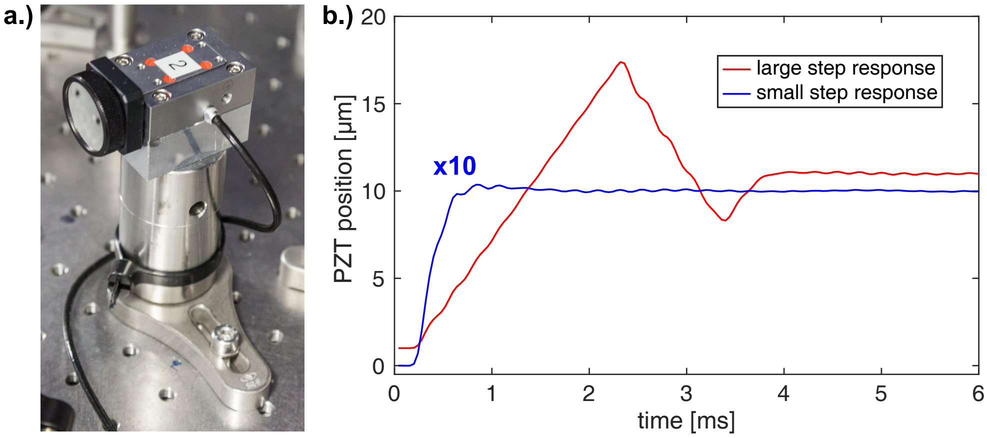

Figure 3.20: a.) New PZT-driven delay line with 1-inch mirror and position feedback for high-bandwidth actuation within a 20 μm-range. **b.)** Step response of a 1 μm-step (blue) and a large 10 μm displacement (red). The system controller was tuned for fastest setting times of up to 2-3 μm-steps to achieve actuation before the next laser shot impinges on the actuator for highest bandwidth.

low resonance disk spring to 2000 N to achieve a stable and fast actuation. The moving component of the assembly is a steel piston with a total weight of 15 g. The introduced pointing is measured to be insignificant with under 200 μrad for a full stroke-actuation.

The behavior of each piezo actuator was studied using a vibrational sensor, pointing and interferometric measurements to determine the displacement per control-voltage and possible resonance frequencies as well as their displacement speed and range.

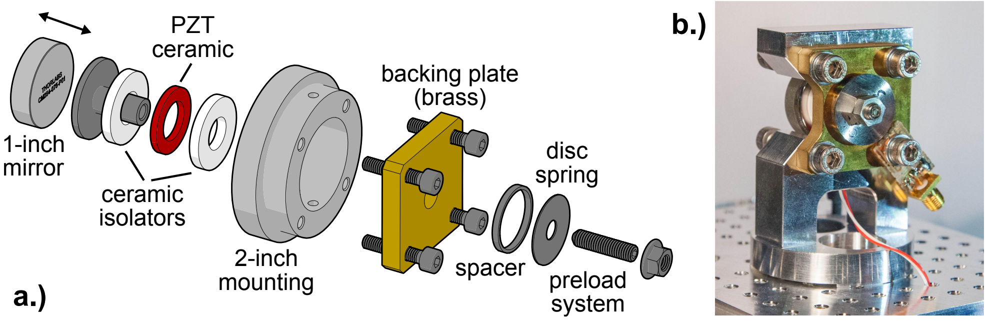

Figure 3.21: a.) CAD-explosion of the PZT-driven mirror mount built for a short-range relative phase manipulation. A ring PZT (Noliac, NAC2125-A01) is preloaded by a plate-spring and moves a piston with a 1-inch mirror attached with kHz-bandwidth within a 3 µm-range. The assembly has a heavy brass backing-mass and can be mounted into a 2-inch mirror mount. CAD-explosion adapted from [171]. **b.)** Picture of the actuator assembly.

3.7 Environmental Stability in the Lab

Optical systems, including commercial laser systems and complex OPA systems like the synthesizer experiment require very stable environmental conditions. Thermal drifts of optical mounts initially seem small but are accumulated over several tens of meters of beam propagation with tens to hundreds of optical mounts the beam need to pass. During initial operation of the synthesizer, some instabilities could be observed which are connected to the temperature stability of the laboratory environment. An early fix was to put a box around the optical setups, which basically acts as a thermal low-pass filter.

To find correlations between malfunctions of the various lab air-conditioning systems and malfunction of the pump laser or synthesizer experiment, the author designed and set up a system that measures and logs important environmental parameters on critical locations. For an easy installation and scaling of the system, a robust and bus-based communication protocol like I^{2}C was chosen. For this type of digital interface, several environmental sensors are available. An easily deployable ribbon cable with crimp connectors was chosen (see Fig. 3.22a/b). The readout system is home-made and based on a microprocessor (Atmel, AT XMEGA128A1). A software-implemented I^2C-protocol for increased noise immunity was used together with noise filtering capacitors at every sensor in the network. With those precautions a bus line can span several tens of meters in the lab with a simple unshielded ribbon-cable. The bus network has 8 lines and each line can currently serve up to ten sensors.

The whole network reads around 40 environmental sensors in the lab and on the optical system every 10 s and prints all values in an ASCII-format via a serial COM-port to a PC terminal. Alongside there is a timer in MATLAB which executes every ten minutes a script that reads the logging file and plots all tem-

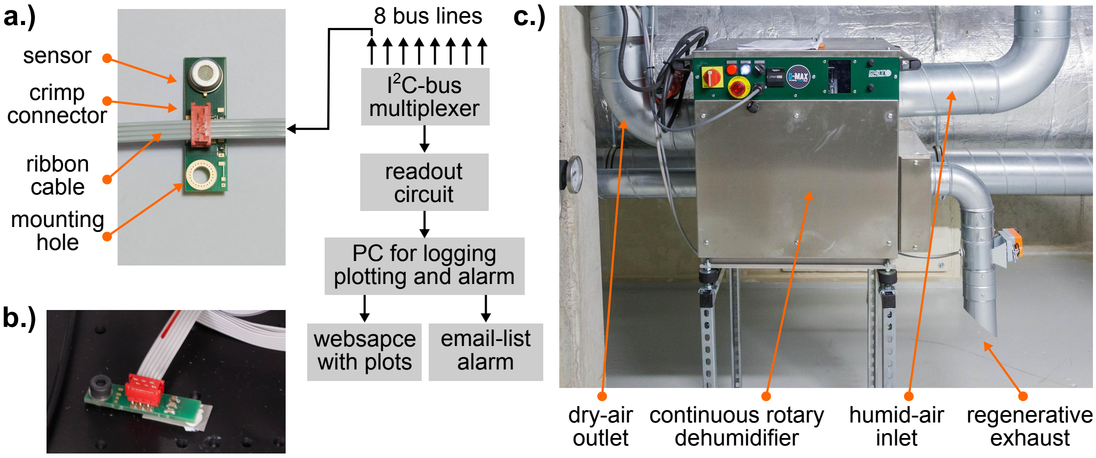

Figure 3.22: a.) Picture/Scheme of the implemented sensor network system for tracking the environmental stability in the lab (temperature/humidity). Several sensors can be attached to a ribbon-cable acting as digital bus line. A system reads the values of the sensor network and sends it to a computer, which e.g. generates temperature plots or send alarm emails. **b.)** Sensors measuring the temperature on the surface of an optical table. **c.)** Picture of implemented rotary dehumidifier in the basement to fix the initially high lab humidity.

perature curves. MATLAB saves the plots as image files and uploads them to a publicly available web space, which allows to access the temperature plots from everywhere, e.g. via a smartphone. Furthermore alert emails with a precise error message can be sent if parameters go out of range.
Initially also the air humidity was quite high (45-55 % r.H. at 21.5 °C) for an optics lab and not well stabilized too. The high humidity above 40% lead to increased degradation of hydroscopic materials like some common nonlinear crystals. To reduce the lab humidity, the fresh air influx was reduced to a minimum and an additional dehumidifier system (Seibu Giken, Consorb, DC-50R) was planned and installed via an external company (see Fig. 3.22c). The system was embedded within the existing air-conditioning system in the lab to achieve a lower overall humidity of around 35% r.H. at 21.5°C. A regulation within the system furthermore stabilizes the humidity at that level (±3%).

3.8 Conclusions

The synthesizer experiment was almost matured with respect to the general layout of the OPA system, the used source-technology for driving of the OPAs and the applied dispersion management scheme when the author joined the project. While the experimental implementation, based on standard optics mounts and no temperature control resulted in significant instability of the optical outputs. The seed generation was based on a passively CEP-stabilized OPA-system lacking of a CEP measurement and control. Furthermore experience showed that the seeding scheme, based on a single WLG, was not performing sufficiently well for ultra-broadband operation (see Chapter 4.3). A timing-synchronization system was missing at that time and pioneering experiments were performed by the author jointly with G. M. Rossi with help by Dr. G. Cirmi. Those experiments prove for the first time, that the waveform synthesis as implemented at CFEL can principally work by showing sub-cycle residual noise for the relative envelope timing and relative phase synchronization. Those insights were addressed by multiple means to achieve an upgraded source which is capable of performing stable enough for attosecond science experiments.

Chapter 4

CEP-stable Ultra-broadband Seeding

This chapter describes the techniques and implementations for passive CEP-stable sources and for multi-octave wide CEP-stable seed derivation, as well as introducing newly developed seeding schemes for parallel parametric waveform synthesizers. A CEP-stable and ultra-broadband seed plays a key role for shot-to-shop stable waveform synthesis. A commercially available passively CEP-stable source (Coherent OPerA Solo) was used as driver for seed generation in the first synthesizer implementation at CFEL, but did not deliver the required long-term stability and was lacking a CEP measurement and active control. The inherent well-known OPA-based scheme was implemented in an improved optical scheme and mechanical setup built by G. M. Rossi with help by the author. Furthermore, important dependence of the CEP in this passively-stabilized scheme upon pump-seed synchronization was not fully understood by the scientific community. In cooperation with L. Wang numerical simulations of these dependences were performed and verified with our experimental observations. The results have been published in Optics Letters [172].

The previously used seeding scheme relied on a single WLG driven by a CEP-stable pulse to generate stable and octave-spanning seeds. Experimentally it was found that it is very difficult to optimize a WLG for a wide bandwidth and a high spectral stability which is required for seeding the synthesizer setup. A novel seeding scheme based on multiple WLGs was envisioned by G. M. Rossi, which relieves the tight constraints and delivers greater flexibility. This novel seeding scheme nevertheless raises questions on the fundamental phase stability between the separate WLG seeds. To test whether this scheme can be applied to the synthesizer experiment, the level of phase stability in different configurations was studied experimentally jointly by G. M. Rossi and by the author.

4.1 CEP-stable Seeding Front-end

Active CEP-stabilization of ultrafast oscillators is a well-known technique and leads by means of frequency combs to a widespread applied technology as ultra-precise (10^{19}, [30]) frequency ruler. CEP stability can be maintained in laser amplifiers [173–175] leading to millijoule pulses with CEP noise in the order of 200-800 mrad rms. For driving the synthesizer experiment, a single pump laser with a high pulse energy at kHz repetition rate is required to avoid temporal jitter as in multi-amplifier pump schemes. To extend the maximum average power of the Ti:Sa technology, we also use a cryogenically cooled Ti:Sa amplifier stage. For such a system, a CEP-stabilization would not be feasible, because the CEP-noise performance of this chain of laser amplifiers (oscillator, REGEN, single-pass, cryo single-pass) would exceed the maximum acceptable CEP noise-level.

The seed generation is the most crucial point for the final shape of the sub-cycle electric-field transient and the stability of the waveform at the output. Firstly, a CEP-stable many-cycle pulse must be derived from the Ti:Sa-based pump laser system. Secondly, this pulse can drive spectral broadening stage(s) to create multi-octave wide seed(s) which ideally should be compressible with standard compression techniques (e.g. DCMs).

DFG in an OPA allows to generate an idler pulse with passive CEP stability independent on the phases of the signal and pump (see Fig. 4.1, [176]). A requirement is that the signal and pump pulse have a fixed phase relation, which can be achieved if the signal is derived from a replica of the pump beam (e.g. via WLG). We used a commercial system (Coherent, OPerA Solo) which implements the passive CEP-stabilization scheme. After initial tests, this system was found to have the following short-comings to deliver a CEP-stable pulse for

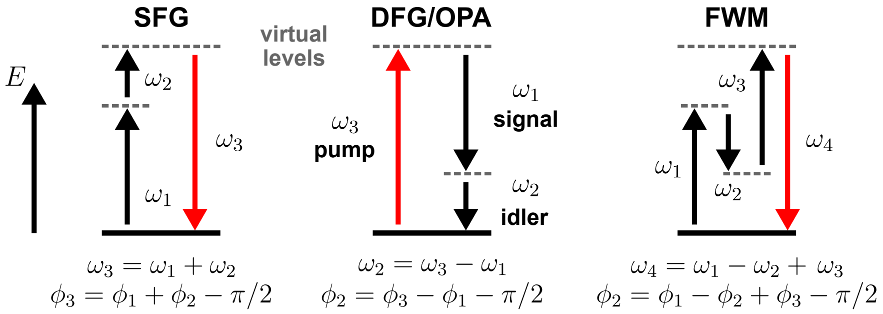

Figure 4.1: Overview of the angular frequency ω and phase relation (ϕ) of three nonlinear mixing processes. Due to the subtraction of the phases from the two input pulses in DFG a CEP-stable pulse can be created without a required CEP stability of the input pulses. If a seed is derived from the same beam as the pump-beam, a fixed phase relation can be kept, e.g. with WLG in bulk.

ultra-broadband seed generation of a parallel parametric waveform synthesizer:

- system initially not designed for CEP-stable operation
  long beam paths within the OPA-stages → higher intrinsic CEP noise
- hard to manipulate and fine tune the optical system for alignment
- optical system exposed to significant thermal drifts and setup is prone to acoustic vibrations
- no internal CEP measurement or CEP manipulation implemented
- no easy way to stabilize the input pointing as well as the output pointing

The inherent well-known OPA-based technique was implemented in an improved optical scheme and mechanical setup designed and built by G. M. Rossi with help by the author (see Fig. 4.2). The optical setup is placed on a temperature-controlled custom-designed monolithic aluminum breadboard and fully sealed with an acrylic glass box. For the input and output beams AR-coated windows are used and the active temperature stabilization achieved better than ±10 mK of temperature stability. All optics are either mounted on low degree-of-freedom custom-made opto-mechanics or ultra-stable commercial mounts (see Chapter 6.1.2). The system is driven with 500 µJ from our cryo Ti:Sa laser system with a pulse duration of $\sim$ 150 fs. By means of a commercial beam-pointing stabilizer from TEM (Aligna 4D BeamLock), the input beam is stabilized with reference to the system breadboard. The optical system is designed to reduce the number of required optics to a minimum and the optical path is implemented with a strict Mach-Zehnder geometry. The beam path of the output beam follows an inline geometry to avoid introduction of beam pointing instabilities. Half-wave-plates (HWP) and thin-film polarizers (TFP) are used to adjust the pump-energy in each arm. A WLG stage (YAG, 2 mm) is used to spectrally broaden the 800 nm pulse to be used as seed. This seed is recombined with a pump beam by means of a custom-fabricated dichroic mirror (LASEROPTIK, 45°, HR800, AR1300, AR2100) in order to amplify the seed spectrum around 1.3 µm in a BBO (type-II, 2.5 mm, 25.9°). The pump-seed delay in the OPA-stages are roughly matched due to the Mach-Zehnder-geometry and are fine-tuned by adjustable AR-coated glass-wedges in the pump arms. The remaining pump from the first OPA is split-off by a dichroic mirror and directed to the detector of the pointing stabilizer. This pump beam is a good representation of the pointing behavior of the input beam and also imprints the pointing of the output beam by the gain-guiding in the OPA. A band-pass-filter (Semrock, 1300 nm, 3 nm BW) rejects the idler and transmits the amplified signal around 1.3 µm. Another dichroic mirror adds a second pump beam to generate the passive-CEP stable idler in a DFG-stage (type-II BBO, 4 mm, 25.9°). In this OPA-stage the amplification is driven in saturation by choosing the phase matching to have the group velocity of the pump between the signal and idler group velocities. This approach imprints predominantly the intensity fluctuations of the pump to the idler rather than the

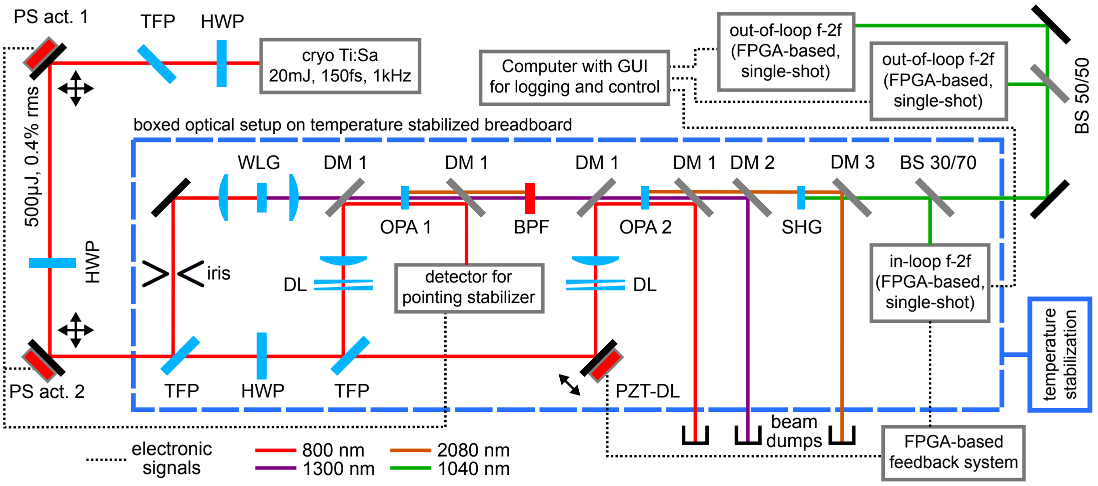

Figure 4.2: Scheme of the passive CEP-stabilization setup based on DFG in an OPA with additional CEP measurement and control. The input pointing is stabilized and referenced to the custom breadboard (PS act). Temperature stabilization, a strict Mach-Zehnder geometry and passive custom-optics and optics mounts are implemented to achieve a stable performance without the need for realignment. An initial WL is used to seed an OPA amplifying around 1.3 µm. A second DFG-stage then creates the passively CEP-stable idler at 2080 nm, which is frequency doubled to be used as CEP-stable seed driver at 1040 nm. Separate f-2f measurements allow to measure and lock the CEP via a PZT-actuator (PZT-DL).

amplified WLG seed [135, 177]. By means of further dichroic mirrors, the pump and signal is stripped off and dumped externally. The generated idler beam at 2080 nm is frequency doubled in a BBO (type-I BBO, 0.5 mm) to 1040 nm and the fundamental is rejected and dumped. A dichroic beam splitter (Ekspla, 1064 nm, 30/70-ratio) splits off a fraction of the beam energy to perform an f-2f by driving a WLG (YAG, 3mm) and frequency double the IR spectral leg (type-I BBO, 0.1 mm) to beat with the VIS-part around 550-650 nm. The resulting broadband-spectral-fringe pattern is observed by our single-shot spectrometer (see Chapter 5.2.1). To manipulate the CEP we introduced a home-made piezo-driven delay line on the pump arm of the DFG-stage (Noliac, NAC2125-A01, see Chapter 3.6) which can move the relative beam path by 5 µm. This actuator can introduce an artificial phase between the pump and seed pulse used in the DFG-stage affecting the CEP of the idler (see Fig. 4.1). The f-2f paired with our feedback system allows to observe the CEP-noise performance, to actively stabilize CEP drifts originating from drifts in the Mach-Zehnder interferometer and to manipulate the output CEP to any desired set point or arbitrary waveform. All these capabilities are crucial to stable and customizable waveform synthesis. The performance of the system was thoroughly analyzed. The active temperature control achieved a temperature stability of the boxed setup (see Fig. 4.3) below 1 mK rms and drifts below 10 mK over 6 months are verified with an out-of-loop measurement. The pulses at 2080 nm have a pulse energy of 35 µJ and the pulses at 1040 nm of 10 µJ correspondingly. The pulse duration of the 1040 nm-pulses was characterized by means of SHG-FROG to be 100 fs and nearly transform limited. The energy fluctuations are characterized by a single-shot pulse-energy measurement (Coherent LabMax Top, J-25MT-10KHZ) to be 0.5% rms at 2080 nm and 1% rms at 1040 nm over a time-span of 15 minutes (see Fig. 4.4).

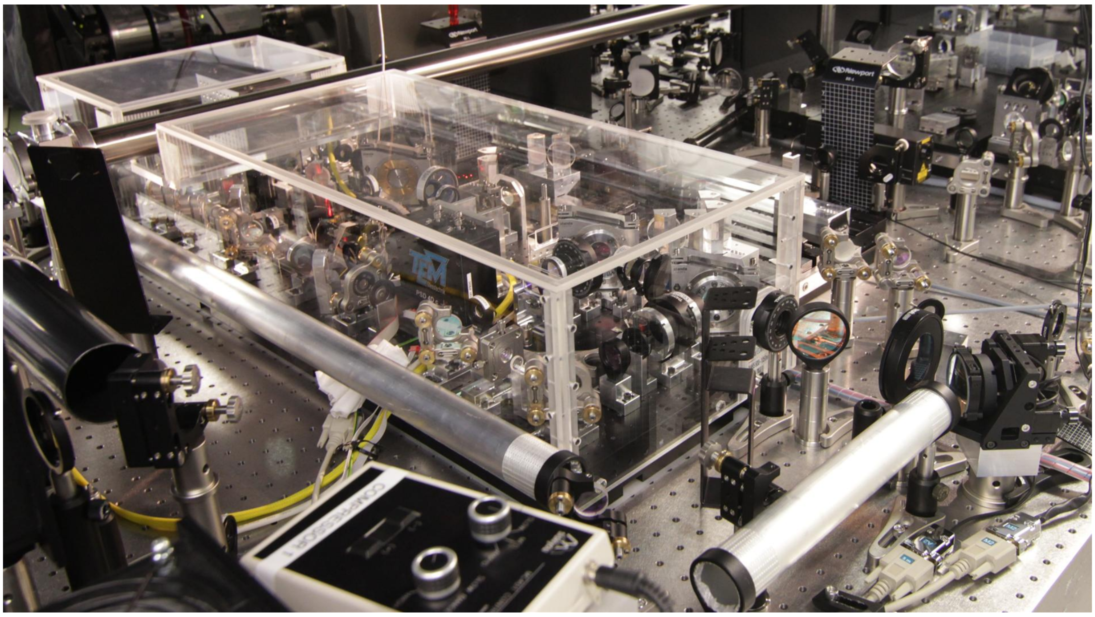

Figure 4.3: Picture of the home-made CEP-stable seeding front-end on a custom breadboard. The system is temperature stabilized and completely boxed with acrylic glass. A pointing stabilizer system (actuator on the right) is used and the pointing is referenced to the system breadboard. The setup performs reliable for weeks without the need for realignment.

The CEP noise was characterized to be 217 mrad rms for the in-loop f-2f and very consistent. This noise reduces to 114 mrad when averaging over 4 shots, or 17 mrad averaging over 100 shots. As it was known that the implemented f-2f scheme has an intrinsic noise which cannot be neglected, two out-of-loops f-2f setups were implemented as well (see Fig. 4.2). By measuring the CEP with three optically and electrically independent systems, we were able to characterize the CEP noise of the front-end system and of the f-2f measurement separately (see Fig. 4.5). While the in-loop rms CEP noise is at 217 mrad the two out-of-loop f-2f yield 270 *mrad* and 290 mrad respectively. A subtraction of the retrieved phase from the two out-of-loop f-2f yield a residual non-common mode phase-noise of $\sim 200\,mrad$ which corresponds to the noise of the f-2f measurement itself. Due to the mostly non-correlated nature of the CEP noise from the source and from

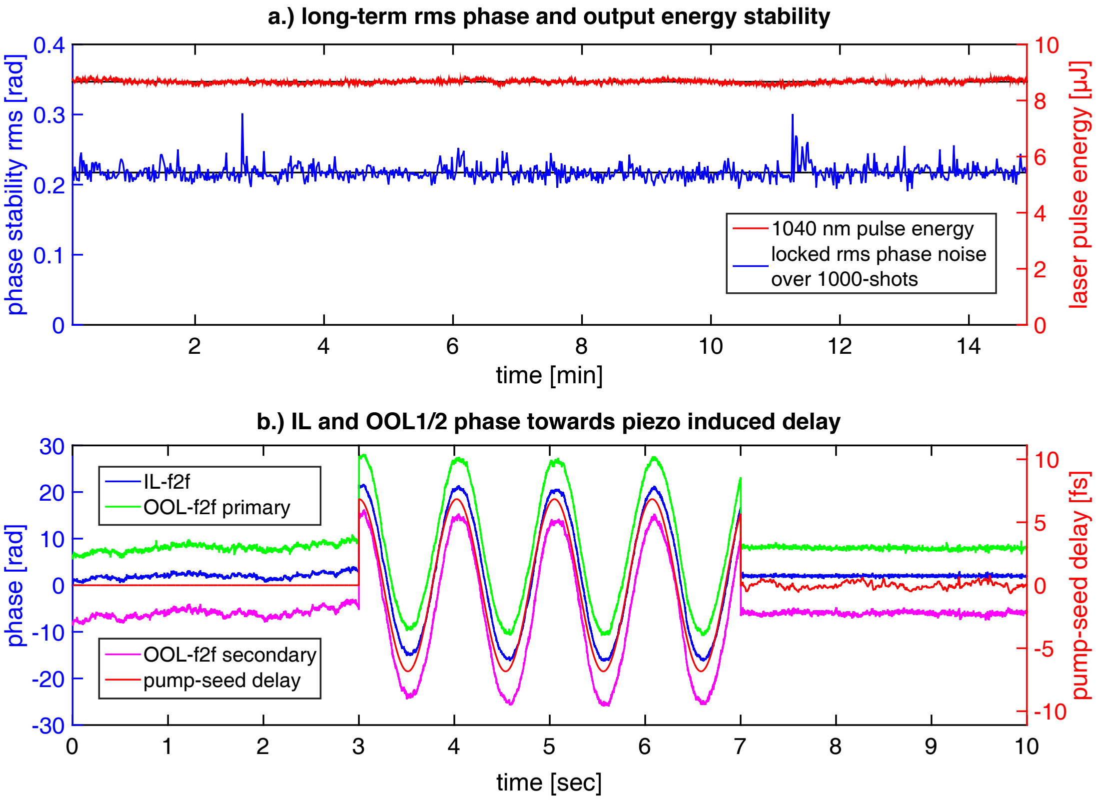

Figure 4.4: a.) Long-term stability of the output pulse energy of the CEP-stable seeding front-end at 1040 nm (red), with 1 % rms over 15 min. In-Loop (IL) CEP-stability with active CEP-lock over 1000 shots each, exhibiting a consistent noise performance of 217 mrad rms. **b.)** Retrieved phase from three independent f-2f measurements while freely drifting (left), modulating the PZT-actuator for CEP manipulation (middle) and during an active CEP-lock (right).

the measurement, one can conclude that the absolute CEP noise of the front-end itself is around 200 $mrad$ or better because both contributions add quadratically (non-correlated) to yield ~300 mrad measured with the two out-of-loop f-2f measurements (with $200^2 + 200^2 \simeq 300^2$).

The new front-end delivers consistent performance for weeks without requiring realignment. The two-color output offers flexibility for seed generation to generate seed(s) without the pump being in the desired seed bandwidth, as discussed in Chapter 4.3.

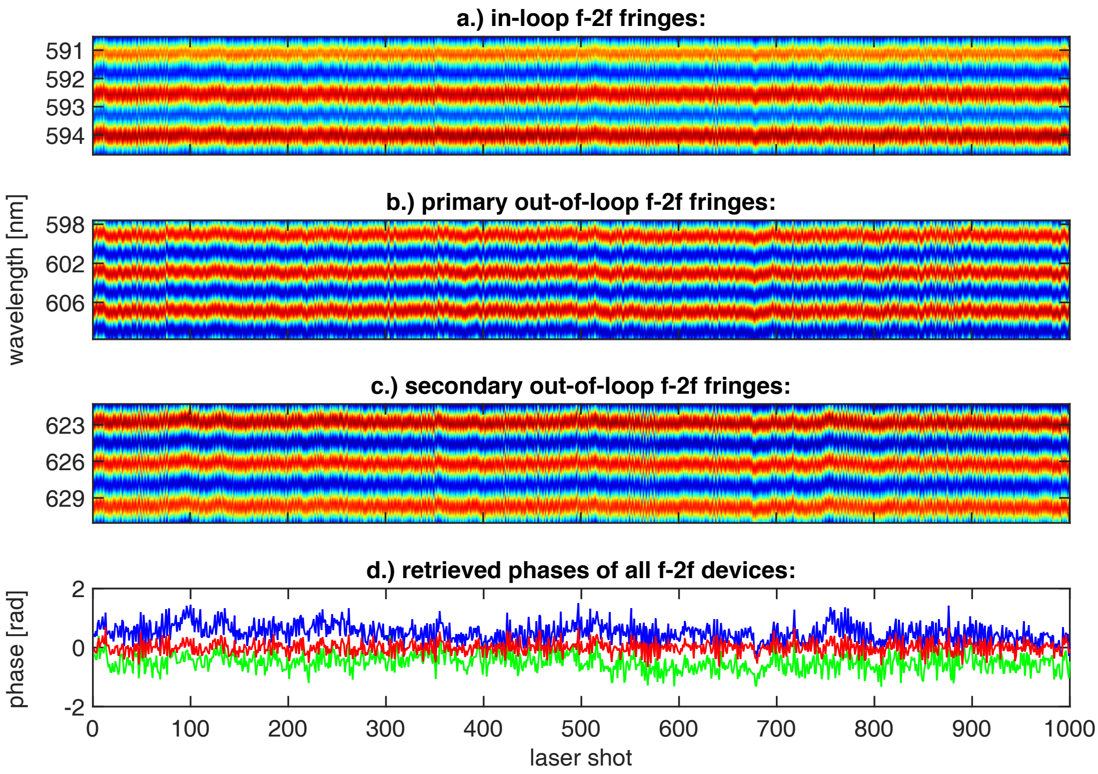

Figure 4.5: a,b,c.) Full set of three independent single-shot f-2f measurements on the output of the CEP-stable seeding front-end. The CEP measurement a.) is further used to perform an active CEP-lock on the system. **d.)** Three retrieved phases: in-loop (red) with 217 mrad rms and two out-of-loops (green, blue) with 270 and 290 mrad rms).

4.2 CEP Dependence upon Pump-Seed Synchronization in OPAs

During the setup of the passively CEP-stable seeding front-end, we found that there was no clear statement in the literature, on the influence of pump-seed timing fluctuations on the CEP of both signal and idler pulses emerging from an OP(CP)A. This is crucial knowledge required to understand the timing behavior in the parallel parametric waveform synthesizer further. In cooperation with L. Wang, numerical simulations were performed and compared to the experimental findings on our passively CEP-stable seeding front-end (see Chapter 4.1). We studied analytically the two limit cases with opposite relationship between the pump τ_p and the seed τ_{seed} pulse duration. Numerical simulations allowed to verify the model and extend it to the intermediate region $\tau_{seed} \sim \tau_p$. Moreover the effect on pump-seed jitter on the CEP of a broadband and stretched signal pulse is considered. An article was published in Optics Letters [172] and is summarized in this section (Section 4.2).

» Begin of citation from G. M. Rossi *et al.* in Optics Letters [172] «

4.2.1 Analytic Model

The parametric amplification process is maximized when the *generalized phase* $\Phi = \phi_p - \phi_s - \phi_i$ is equal to $\pi/2$ [135], in other words $\phi_i = \phi_p - \phi_s - \pi/2$ (see Fig. 4.1). The phases are here absolute phases (AP) with reference to the lab frame. This allows to analytically describe the phase effects in the two limits of $\tau_{seed} \gg \tau_p$ and $\tau_{seed} \ll \tau_p$ via considering the system of three coupled equations to describe the parametric amplification under monochromatic plane wave approximation and perfect phase-matching [46]. The CEP of signal and idler (Ψ_s, Ψ_i) can be, extracted from the AP information.

The case of an amplification with a WL-seeded OPA where the seed has been produced starting from a portion of the pump pulse, can be considered. During the amplification, if $\tau_{seed} \gg \tau_p$, the amplitude envelopes of signal and idler pulses will experience the highest gain at the peak of the pump envelope (see Fig. 4.6), regardless of the precise arrival time difference (ATD, $\Delta T = t_s - t_p$) of the longer seed pulse. This effect locks the envelopes of the three pulses together in the nonlinear crystal until the pump is significantly depleted and back-conversion starts to occur [135]. Analytic considerations result in a signal CEP change of $\Delta\Psi_s = \omega_{seed}\Delta T + \Delta\Psi_p$ (with $\Delta\Psi_p$ being the CEP change of the pump pulse) and an idler CEP change scaling with the temporal displacement times the seed wavelength ($\Delta\Psi_i = -\omega_{seed}\Delta T$).

Similarly for the CEP in the hypothesis that $\tau_{seed} \ll \tau_p$, the envelope of the pump is considered as a constant since it varies in time much slower that the seed's one. The CEPs then become $\Delta\Psi_s \approx \Delta\Psi_p$ for the signal pulse and $\Delta\Psi_i = -\omega_p\Delta T$ for the idler pulse. Differently from the former case, the CEP of the Signal pulse does not depend on ΔT anymore, but only on the CEP of the pulse that drives the seed generation, the pump pulse in our case (Ψ_p). This consideration does not describe the common experimental implementation of an OPA operated usually in an intermediate pulse-duration regime, but provides upper und lower limits for the CEP fluctuation.

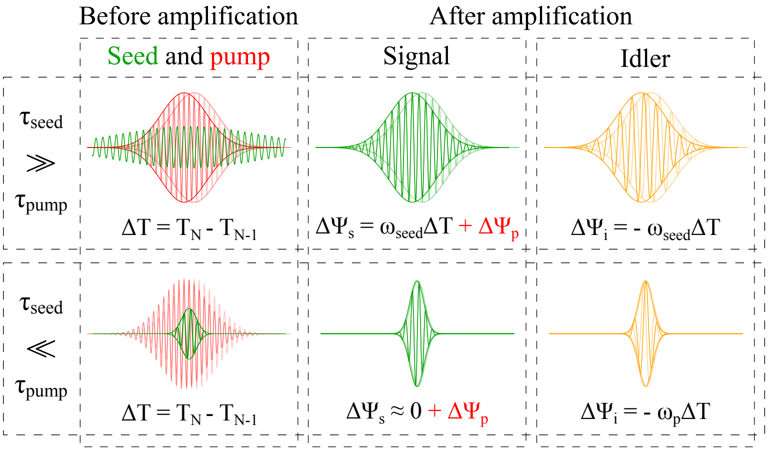

Figure 4.6: Left column: representation of the electric field of the pump and seed pulses before the OPA process begins. Central and left columns: representation of $E(t)$ of the signal and idler pulses after the OPA process. In the upper case, the envelope of the pump (solid red line) is shorter than the seed's one, and it is imprinted on signal and idler envelopes. In the lower case, the envelope of the seed (solid green line) is shorter than the pump's one and it is imprinted on envelopes of signal and idler pulses. The corresponding CEP variations, induced by the pump-seed ATD fluctuation ΔT, are reported. The contributions due pump's CEP variations are shown in red.

4.2.2 Simulation Results

To investigate the intermediate regime and, at the same time, validate the previous model, L. Wang *et al.* performed 1-D split step numerical calculations of the coupled wave equations solved via the 4th order Runge-Kutta method, which takes into account the OPA process (in absence of material absorption), the dispersion of the nonlinear crystal and the self-phase modulation for pump, signal and idler pulses. In all the simulations we varied the Seed pulse duration while keeping the Pump duration fixed to 150 fs FWHM. We started simulating a narrowband OPA (BBO, Type II, $\theta = 25.9$ °, 2.35 mm thickness) configured to generate a CEP-stable Idler as the difference between a Pump pulse, centered at 800 nm, and a phase-locked (as for WL) Gaussian Seed centered at 1300 nm (see Fig. 4.7a). As expected, the simulation shows that the introduced CEP change is directly proportional to the Pump-Seed ATD variation and lies in between $\omega_{seed}\Delta T$ and $\omega_p\Delta T$. We conclude that, in case of designing a narrow-band passively CEP-stable OPA, in order to minimize the influence of timing jitter on the CEP stability of the Idler, it is advantageous to seed with $\tau_{seed} > \tau_p$. Furthermore it is evident that the Pump-Seed jitter has a major role in defining the CEP stability of the Idler emerging from an OP(CP)A.
To further verify the accuracy of the analytic model, we now consider a broadband degenerate OPA configuration (BBO, Type I, $\theta = 19.8$ °, 0.92 mm thick-

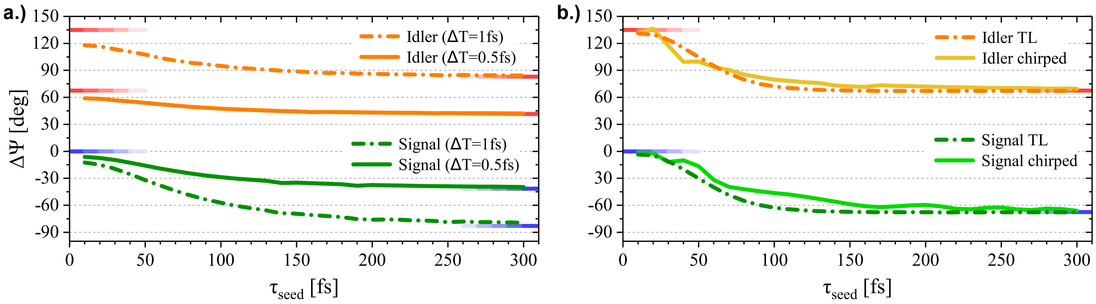

Figure 4.7: a.) CEP variations of Signal (green lines) and Idler (orange lines) induced by a Pump-Seed timing fluctuation of 0.5 fs (solid lines) and 1 fs (dashed lines), as a function of the Seed pulse duration, while τ_p is fixed to 150 fs. The corresponding $\tau_{seed} \ll \tau_p$ and $\tau_{seed} \gg \tau_p$ analytic limits are shown by the blue colored gradients for the Signal, and by the red colored gradients for the Idler. **b.)** Comparison between the CEP fluctuations of Signal and Idler introduced by a ΔT of 1 fs in a broadband OPA in the case of a TL Seed (dashed lines) and broadband chirped Seed (solid lines) as a function of their pulse durations, while τ_p is fixed to 150 fs.

ness), still pumped with 800 nm pulses, generating both Signal and Idler around 1.6 μm [51]. Since the conventional scheme to generate ultrashort pulses via OP(CP)As consists in amplifying a broadband and chirped Seed and compress it afterwards, in the following we focus on how the Pump-Seed jitter is affecting the CEP stability of the Signal once a broadband and chirped pulse is employed to seed the DOPA. As shown in Fig. 4.7b (dashed lines), the agreement between numeric and analytic values improves in the broadband case, where the seed bandwidth is maintained through the amplification even for short seed durations.

This $\Delta\Psi$ behavior upon timing fluctuations changes completely after the Signal pulses are compressed. Once half of the initial GDD is compensated the CEP fluctuations are already suppressed significantly. After full compression, the Signal pulses experience extremely small CEP shifts, in the order of 0.5-2°/fs in our simulation, in agreement with the 0.8/90 rad/fs $\approx$ 0.5 °/fs reported in a former study [178]. In case of a chirped Seed, the Pump envelope AT determines the amplification that different spectral components undergo, but does not significantly influence the spectral phase of the amplified Seed pulse, since $\tau_p \gg 2\pi/\omega_{p,s,i}$. Moreover, the AT of the amplified pulse at the compression point depends exclusively on its chirp and the dispersion of the compressor. Therefore the CEP of the amplified pulses is only marginally affected by Pump timing fluctuations at the compression point. This result is particularly interesting for multi-stage high-energy OP(CP)As, where the Pump for the high-energy stages is frequently obtained by a different laser amplifier with respect to the one that drives the Seed generation. Provided that the jitter between the different laser amplifiers is small compared to the Pump duration (e.g. $\Delta T \approx 10$ fs for a $\tau_p \approx 1$ ps), and the Signal pulses are subsequently compressed close to their TL, their CEP stability should not be significantly affected by this jitter.

4.2.3 Experimental Results

To experimentally verify the numerical simulation in an intermediate regime, we studied the CEP dependence from the Idler emerging from our CEP-stable seeding front-end while manipulating the pump-seed ATD with a calibrated PZT-driven delay line. The Seed pulses, centered around 1300 nm, are obtained by WL generation. Since the WL broadening process maintains the AP of the driving laser pulse, the Idler pulse train theoretically exhibits a stable CEP, even if the driver laser does not. After the first amplification, the Signal pulses that seed the second amplifier are filtered by a 3 nm bandpass filter, to ensure that $\tau_{seed} \gg \tau_p$ (see Fig. 4.2 on page 60). To verify the predictions of our model, we introduced a controlled delay in the path of the Pump beam of the second stage amplifier and recorded the CEP of the emerging Idler pulses via two independent f-2f interferometers, as shown in Fig. 4.8. In both f-2f setups the fringes are obtained by frequency doubling the 1.2 μm region of a WL filament driven by the second harmonic (1040 nm) of the Idler (2080 nm) of the OPA, beating with the 600 nm component of the WL filament itself. To obtain the corresponding CEP for the Idler pulse we then multiplied the measured phase by a factor of $(600/520) \cdot 2$, where the first term comes from the fact that the f-2f fringes are measured around 600 nm and not around 520 nm, that would be the second-harmonic of the WL driver, and the factor of 2 accounts for the fact that we are driving the WL with the second-harmonic (SH) of the Idler beam, thus doubling Idler's original CEP. The experiment agrees with the theory within the measurement error, proving that the formulas in Fig. 4.6, at least in this case, establish a valid model. To stabilize ΔT, and minimize the CEP fluctuations, it is indeed possible to install an actively controlled delaying element, such as a PZT-driven mirror, either in the optical path of the Pump or of the Seed. It is worth noticing that if the controlled delay is introduced in the Seed path, then the CEP variation of Signal and Idler is caused by a variation of the AP of the Seed (and of the Signal), meanwhile the *absolute arrival time* (AAT) of the Signal and Idler pulses is not changing. On the contrary, when the controlled delay is introduced in the beam path of the Pump, the CEP variation is associated with a variation in the AAT of Signal and Idler pulses, meanwhile the AP of the Seed (and Signal) does not change. This distinction, which is irrelevant in many cases, has to be taken into consideration once the CEP-controlled pulses generated by an OPA need to be further synchronized to other pulses originating from the same laser system, as in a multistage OPA amplifier, in an OPA synthesizer, or even a pump-probe setup.

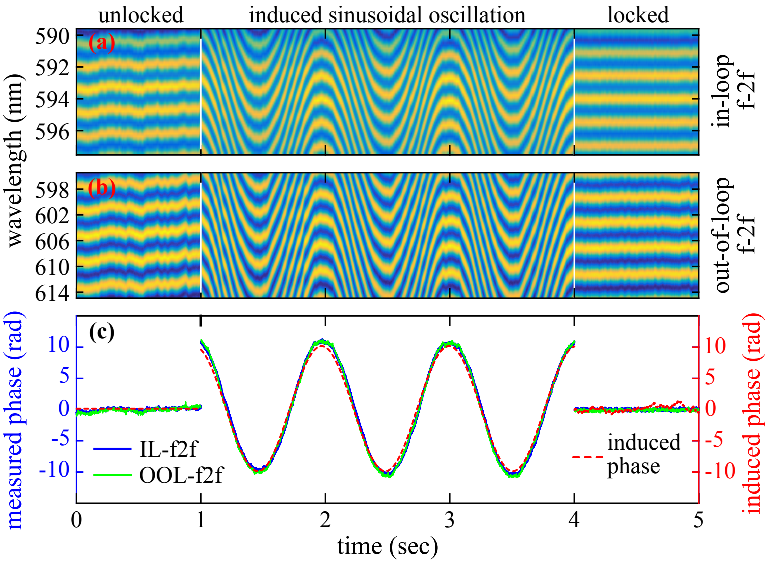

Figure 4.8: Single-shot and every-shot CEP measurement of the SH of the Idler obtained via two independent f-2f setups: in-loop (a) and out-of-loop (b). (c) Extracted phase: during the first second the CEP is freely drifting, afterwards a sinusoidal ATD, with a peak-to-valley amplitude of (14.2±1.4) fs is introduced by a delay line in the Pump path, and in the last second the CEP is locked to a fixed value. The measured peak-to-valley CEP variation, after calibration of the two f-2f setups, is (22.0±2.4) rad, leading to (1.55±0.17) rad/fs or (88.8±9.8) °/fs, whereas the analytic model predicts 83.0 °/fs.

» End of citation from G. M. Rossi *et al.* in Optics Letters [172] «

4.3 Generation of Stable Octave-wide Seeds for Waveform Synthesis

In this section the initial seed generation, one of the core components for waveform synthesis and also OP(CP)A source development in general, is discussed. While OPA-based amplifiers offer freedom to amplify any desired spectral region in general, at first a coherent seed needs to be generated to get amplified via an OPA. In some cases one can derive a seed from laser oscillators with up to one octave of bandwidth [150] or via interband DFG [137]. But usually only a fairly narrowband pump source is available which needs to be spectrally broadened. Also here HCFC were explored due to their high output pulse intensity [134, 151]. But the by far most commonly used method of seed generation for OPA-based amplifiers is WLG in bulk [48, 179]. Usually a pulse with a pulse duration within the femtosecond domain is focused in a few millimeters of glass material (commonly YAG or sapphire). It gets harder to generate stable WLG seeds with (sub)-picosecond pulses due to avalanche ionization, although this was also demonstrated [180]. Fluoride glasses offer some advantages when pump wavelengths below 500 *nm* are used and/or a seed below 300 *nm* is required due to their higher bandgap and hence lower multi-photon ionization cross-sections. It is known that the spectrum generated by WLG can extend several octaves of bandwidth if the full-bandwidth is defined within e.g. a -30 dB spectral intensity. In Fig. 4.9 a WLG is driven in YAG and Sapphire with few µJ of energy and 130 fs long pulses at 2 µm and its second harmonic at 1 µm from our passively CEP-stable seeding front-end is shown. The WLG was measured using a spectrometer based on a Si-detector (Ocean Optics, HR4000) for the visible range. An InGaAs-based spectrometer (OceanOptics, NIRQuest256-2.5) covers the spectral range up to 2.5 µm. Finally the far-IR part of the generated WL spectrum was characterized using a home-made FTIR, borrowed from Prof. A. Cavalleri's lab and built by Dr. Alice Cantaluppi and Dr. Matteo Mitrano. A long-pass filter blocks components in the visible and near-IR region and an indium-antimonide detector (InSb) cooled with liquid nitrogen (LN_2) is used as sensitive bolometer. The long pass filter also has an absorption band around 3 µm, which makes the FTIR blind for WLG generated in that range. Assuming a continuous spectral emission from the WLG also within the detection gap, a WLG driven at 2 µm creates a spectral bandwidth ranging from 500 nm up to 4 µm. As this corresponds to three octaves of bandwidth, such spectra have sufficient bandwidth to seed all the spectral channels of our waveform synthesizer.

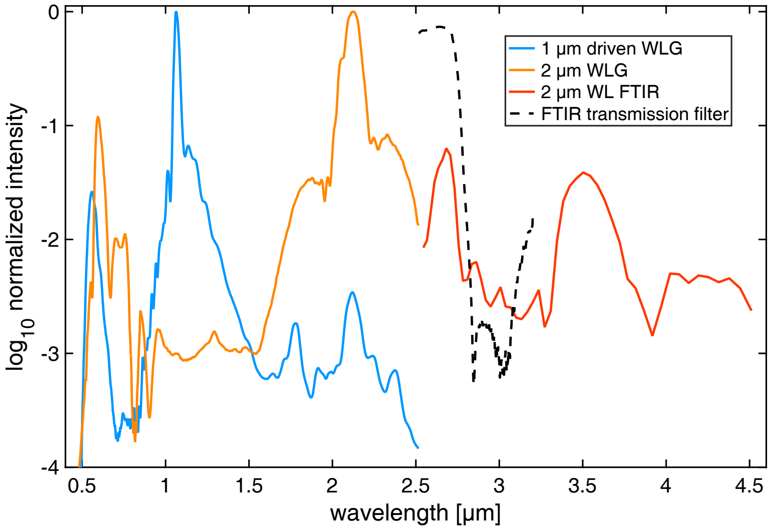

Figure 4.9: Spectra of a WL driven with 2 µm on a logarithmic intensity scale showcasing a octave spanning bandwidth. The WLG spans 3 octaves from 500 nm up to 4 µm with sufficient spectral intensity for OPA-seeding. The IR-part of the spectrum was measured with an FTIR-setup and a required filter cuts a band around 3µm into the signal.

Initially it was thereby planned to drive a WLG by a CEP-stable pulse and split the broadened spectra with dichroic mirrors into three adjacent spectral regions required for each spectral channel of the synthesizer (see Fig. 4.10). This single-WLG approach has a number of practical challenges, such as:

- Custom dispersion-managed dichroic beam splitters required to split the seed for each synthesizer channel
- High chirp introduced by the beam splitter, especially in the short wavelength end of the spectrum
  → needs to be compressed by additional DCMs (loss of output energy)
- Long beam transport of the seed beam until first amplification takes place
  → degradation of the spatial mode and increased beam pointing instability
- Energy splitting and losses on the beam splitters reduce already low nJ-level pulse energies of the WL-seed further
- Optimizing for spectral stability in one region can already cause multiple filaments in another spectral region
  → unstable spectral phase, especially around the pump wavelength and at the spectral wings

Furthermore the practical difficulty to align a single WLG to perform broadband emission paired with high spectral stability leads to the idea to use a WLG for each individual spectral channel of the waveform synthesizer as proposed by G. M. Rossi. (see Fig. 4.10). This approach using multiple WL brings the advantage that each WL can be in close proximity to the first OPA-stage of each spectral channel and no beam splitter and associated energy loss is involved before first amplification place. Furthermore each WL can be optimized with

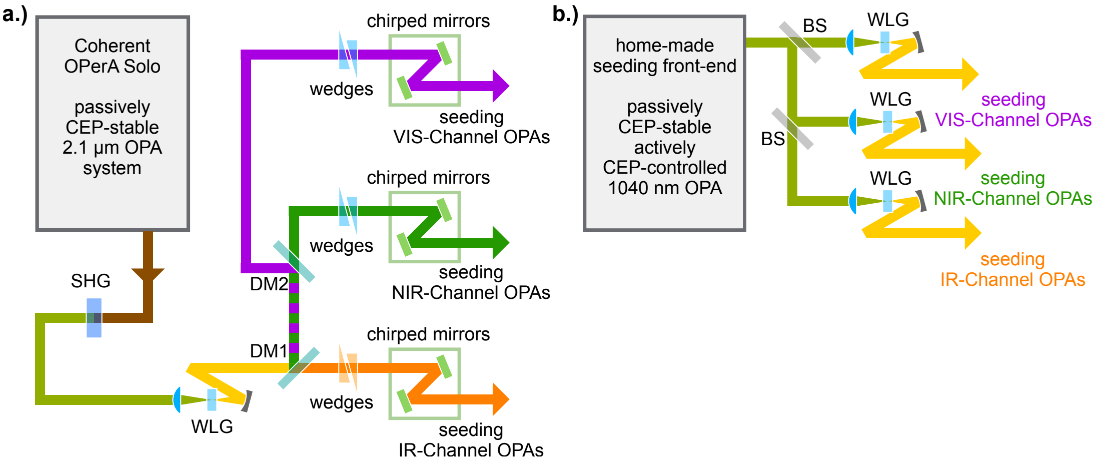

Figure 4.10: a.) Seeding scheme employing one single WLG and splitting of the continuum in three adjacent spectral regions via dichroic mirrors (DM1/2). **b.)** Proposed novel seeding scheme based on separate WLGs optimized to individually seed each spectral channel. Scheme adapted from [171].

respect to driving-energy, WLG material/thickness, focus geometry and beam aperture solely for the requirements of the individual spectral channels. The seeding bandwidth required for each spectral channel is below one octave and the WLG process operates more stable with respect to the stability in spectral intensity and phase if only a moderate spectral broadening needs to be achieved. Additionally such a scheme would allow to drive the WL with different harmonics of the driver, as our CEP-stable seeding front-end for instance provides a dual output with 2 µm and its second harmonic at 1 µm.

With such an approach it is possible to avoid the spectral components around the pump-region as well as around the spectral edges which are known to have intrinsically higher instabilities with regards to phase and intensity. By separate WLG a continuous range of coherent seeds over three octaves can be generated. Such a seeding scheme, regardless of all the advantages, raises the question if separate WLGs can maintain a high degree of coherence, hence phase-stability between each other. For waveform synthesis, the phase-noise at the point of synthesis contains contributions from several noise sources: The CEP noise of the CEP-stable front-end, phase-noise arising from the (separate) WLG seed generation, interferometric noise between the separate amplification chains, pump-seed synchronization in each OPA-stage and detection noise of the relative phase measurement. Some of the noise can be passively reduced or actively stabilized, but these active noise-reduction methods only have limited efficiencies. Hence, the passive relative phase noise between separate WLG is of crucial importance to achieve a stable and reproducible waveform synthesis. For that reason the relative phase noise among separate WLG was analyzed in detail with same and different driving wavelengths by the author jointly with G. M. Rossi.

4.4 Phase Stability between two separate WL seeds

The spectral broadening via WLG is a common technique for seeding OPAs [48, 179]. In most experimental implementations, usually only one WL-seeded broadband OPA is used to create a probe for another narrowband pump pulse for pump-probe experiments. For the parallel parametric synthesizer on the contrary, separate spectral channels need to be seeded with phase-stable broadband pulses. A seeding approach with separate WL would offer significant advantages as laid out in the previous Chapter. In this section, the relative phase between separate WL was characterized experimentally with different driving configurations.

4.4.1 WLG Phase Stability with same Driving Beam

In 2000 Bellini *et al.* demonstrated that two separate WLG driven by the same driver are coherent with each other [181]. Bellini *et al.* observed stable Young's interference fringes and concluded that separate WLG exhibit a negligible random phase jitter (see Fig. 4.11). The reproducibility of the spectral broadening process also includes a high inter-pulse coherence, which allows for the later demonstrated broad frequency combs for ultra-precise measurement of optical frequencies. Baltuska *et al.* demonstrated that a WLG has a stable region within its operating regime where the broadening process is almost insensitive to driving pulse energy variations and in this region low phase fluctuations were observed [173]. In that study the phase of the pump beam driving the spectral broadening was observed via interfering it with a copy of the pump beam. In a certain intensity range of the driving pulse, after the onset of a stable single filament, only a low coupling between pump intensity/energy and a nonlinear phase shift was observed. A first experimental application of separate WLG for OPA seeding was demonstrated by Baum *et al.* [182]. Two separate NOPAs in the VIS and the IR spectral range where interfered by frequency doubling the IR output. A coupling between the relative phase and the pump energy of one WLG was observed with a slope of around 0.5 rad/%. To estimate a relative phase noise introduced by using separate WLs to seed the spectral channels of the synthesizer, we performed a phase stability measurement by driving two separate WLG in each arm of a Mach-Zehnder interferometer (see Fig. 4.12a). A fraction of the available pulse energy of the cryogenically-cooled Ti:Sa laser system with 150 fs pulse duration is used to drive the experiment. A beam splitter splits the beam into two equal fractions with a pulse energy of each 1-10 µJ. The

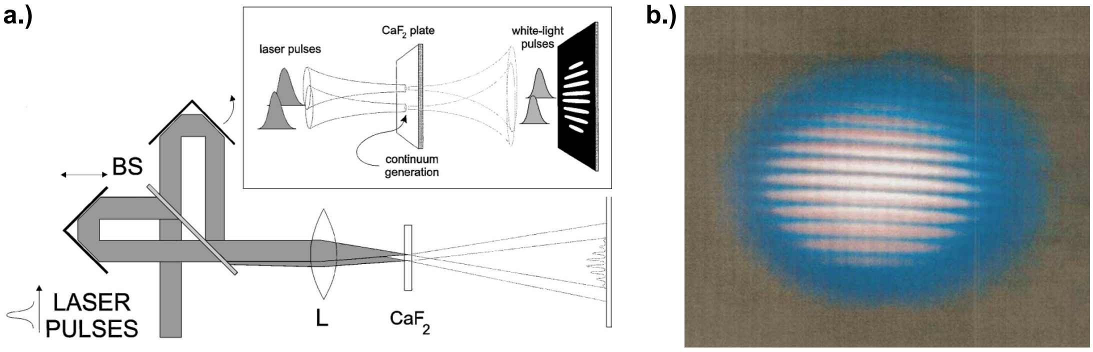

Figure 4.11: a.) Experimental setup with the generation of two identical pulse replicas spatially offset to focus at two displaced locations into CaF_2 to drive two separate WLGs. The slight spatial offset of the two sources create stable interference fringes in the far-field when the two WL-stages are coherent to each other. **b.)** Picture of the observed Young's fringes. Figures adapted from [181].

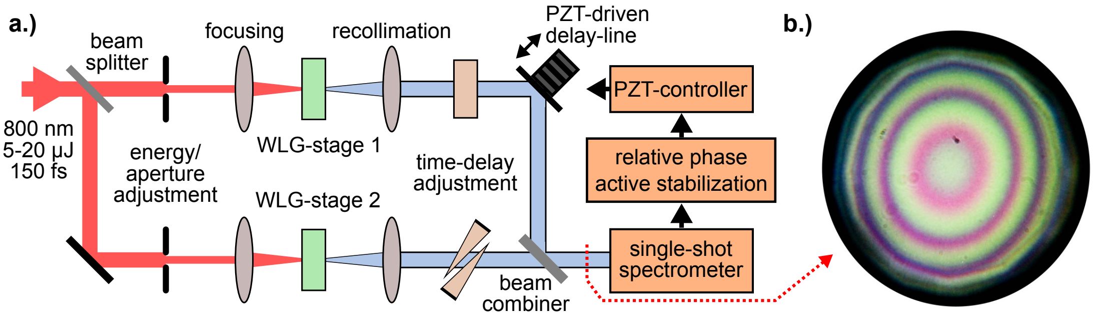

Figure 4.12: **a.)** Experimental setup for the non-common mode relative phase stability measurement from two WLG driven at 800 nm. The driving-pulse energy and aperture was adjusted for optimum WL generation. A spectrometer measures the observed spectral fringes and can actively lock the relative phase via a PZT-driven actuator manipulating the relative phase. **b.)** Observed spatial fringes from the beating of two WLG with almost no time-delay and good divergence matched beams.

numerical aperture of the beam is adjusted with an iris together with the focus position to generate a stable single-filament WLG in different materials and with different thicknesses. Most commonly YAG or sapphire with a thickness between 2-4 mm are used as WLG source with a driving beam focused with an f=100 mm lens. The WLG modes are carefully recollimated as well as temporally and spatially overlapped with a metallic beam splitter with a flat-spectral characteristic (LaserZentrum Hannover, Inconel-coating, NiCr alloy). If both WLG outputs are almost perfectly synchronized, spatial interference rings (Newton Rings) can be observed (see Fig. 4.12b). These spatial fringes were used to align the beam modes to achieve an almost perfect single-fringe across the whole spatial mode. Such a precise alignment is strictly required, because the energy of the WL is very low and in order to detect enough fringed signal as much of the mode as possible should be fed to the spectrometer. A mismatch in divergence will significantly decrease the spectral fringe contrast. Then a certain time offset between the WLGs is introduced by inserting and tilting a glass plate in one of the interferometer arms to adjust the frequency of the spectral fringes to be between DC and the maximum spectral resolution of the spectrometer (see Fig. 4.13a).

The spectrometer used to observe the spectral fringes is a home-made single-shot spectrometer optimized for narrowband operation with a high spectral resolution. The spectrometer is described in detail in Chapter 5.2.1. An FFT-based retrieval of the fringe phase within the spectrometer allows to control a piezo-driven delay line (Physik-Instrumente, P-753.1CD, see Chapter 3.6) via a PI-loop controller in order to actively lock the relative-phase between the two WLG.

The spectral contrast of the fringe beating observed around 550 nm is roughly 95 % of the theoretical maximum, proving the high degree of spatial coherence and a good match of the two WL divergences. The temporal evolution of the red highlighted section in Fig. 4.13a is shown for 10k consecutive laser shots in Fig. 4.13b. After activation of the relative phase lock, the remaining relative phase noise is characterized to be 32 mrad rms at 550 nm, corresponding to 9.4 as of temporal jitter. This result was achieved with both WLG driven in 2 mm of YAG. Further material and thickness combinations were evaluated and the corresponding residual relative phase noise is concluded in Tab. 4.1.

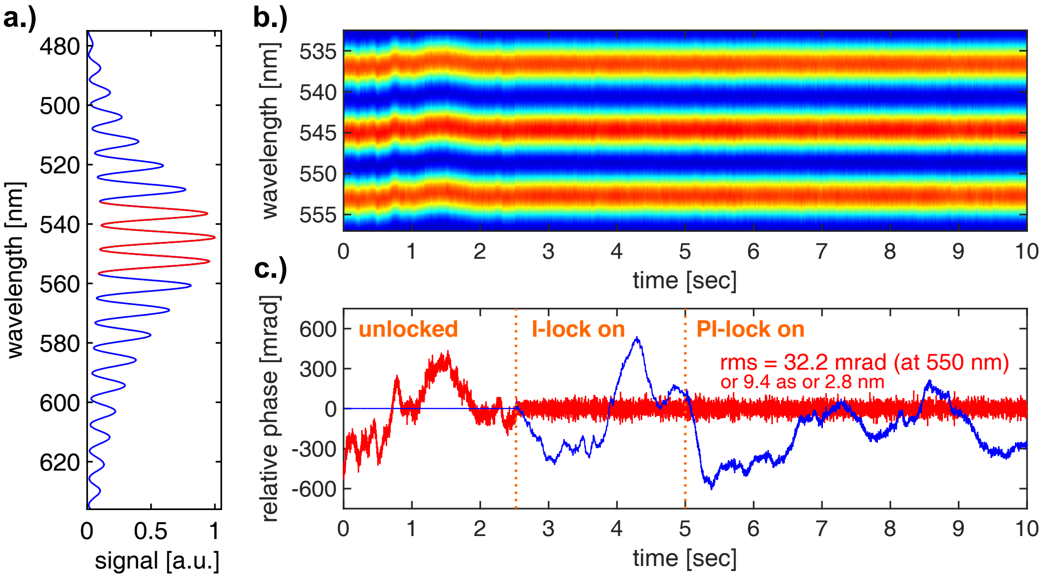

Figure 4.13: a.) Measured spectral fringes between two separate WLG with a high fringe contrast which proves a high degree of coherence. **b.)** Single-shot spectra (zoomed-in red section from a.)) evolving over 10 s. The relative phase is freely drifting until 2.5 s where a relative phase-lock is activated. **c.)** Retrieved relative phase (red) and the driving signal for the relative phase actuator (blue) upon feedback activation. When locked, the relative phase noise can be as low as 32 mrad rms.

Material 1	Material 2	Phase jitter (mrad rms (at 550nm))	Timing jitter as rms
2-mm YAG	2-mm YAG	32.2	9.4
3-mm sapphire	3-mm sapphire	41.6	12.2
3-mm sapphire	2-mm YAG	51.2	15.0
1-mm sapphire	3-mm sapphire	64.4	18.8

Table 4.1: Overview on relative phase noise (and the corresponding timing jitter) between two separate WLG if driven in different materials and thickness. Lowest phase noise is achieved if both WL materials are identical in material and thickness.

Comparing the material/thickness combinations and the corresponding achieved relative phase-noise level indicates that same materials with same thicknesses give the lowest relative phase noise performance. But even different materials with unequal thicknesses yield only slightly elevated noise level, well below the maximum phase noise acceptable to seed a parallel waveform synthesizer.
It is important to understand the main noise contributions in this experimental configuration. Due to the same driving wavelength only non-common sources of noise arising from within the WL generation process will be observed. A dependence of the absolute phase with respect to the driving pulse or the spectral phase characteristic of the broadened spectrum upon changes in the intensity of the driving pulse will not be measured, because they will affect both WLG in a similar way. Different configurations of material/thicknesses will result in an unequal expression of this coupling and a fraction of phase noise arising from e.g. intensity fluctuation will be apparent, leading to slightly elevated noise levels.

4.4.2 WLG Phase Stability with different Driving Wavelengths

To fully exploit the potential of a seeding scheme using separate WL but also utilizing different harmonics from a CEP-stable pulse to drive the WLG requires to evaluate the relative phase noise level in this configuration as well. Furthermore this experimental configuration allows to fully estimate the phase noise performance between the different seeds including the CEP noise as well as noise within the spectral phase. The relative phase noise-level is expected to be elevated in this configuration, while the different harmonics driving the WL allow to extend the seeding bandwidth for the synthesizer experiment further. To measure the relative phase for such a configuration, CEP-stable pulses are required. The generation of harmonics from CEP-stable pulses also include a multiplication of the CEP ($2\cdot\phi$ for SHG). If spectral broadening is performed afterwards until spectral overlapp occurs, the configuration is then a variation of an f-2f-setup (see Chapter 2.7). The CEP-stable pulses for this experiment are derived from our seeding front-end (see Fig. 4.14). A 2 µm CEP-stable beam is generated, frequency doubled in a BBO (type-I BBO, 0.5 mm) and the generated harmonic is separated from the fundamental with a dichroic beam splitter (HR2080, AR1040). The two separated beams at 2 µm and 1 µm with a pulse energy of a few µJ

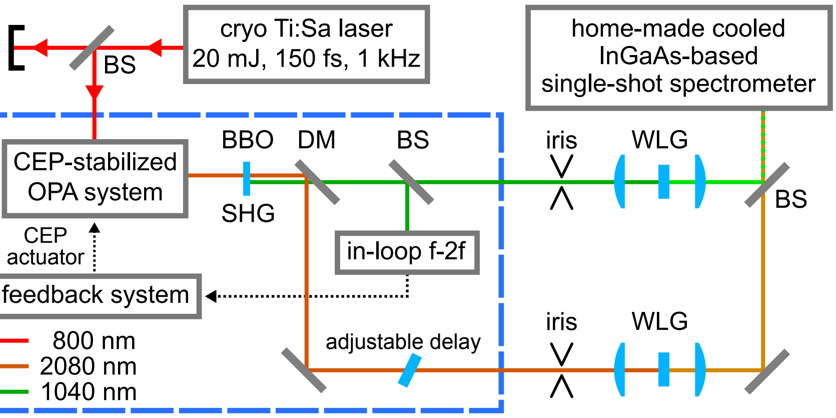

Figure 4.14: Setup of experiment where the CEP-stable seeding front-end generates CEP-stable pulses at 2080 nm. A SHG generates 1040 nm and is separated via a beam splitter. The two outputs each individually drive a WLG in bulk (2080 nm: 3 mm YAG and 1040 nm: 4 mm sapphire). The spectral interference is observed with a home-made InGaAs-based spectrometer. A feedback loop can be used to lock the relative phase between the two WL.

were used to drive WLG in 3 mm YAG and 4 mm in sapphire correspondingly. The two outgoing WL-modes have a quite different divergence, which made it difficult to match them and achieve a high spectral fringe contrast. A metallic beam splitter (LaserZentrum Hannover, Inconel-coating, NiCr alloy) is used to combine the recollimated WL modes. A measurement of the individually generated WL (see Fig. 4.15) proves that fundamental and SHG beams are separated from each other by at least two orders of magnitude. The spectra generated by the two WLG overlap in the IR spectral range. To observe spectral fringes in the IR-region a special InGaAs-based detector needs to be used instead of more common Si-based detectors. The home-made single-shot spectrometer system developed by the author is equipped with a TEC-cooled InGaAs-based line-array sensor (Hamamatsu, G9208-256W, see Chapter 5.2.2). The optical part of the spectrometer is configured to image a spectral range around 1.3 µm onto the detector. Upon careful alignment, spectral fringes can be observed when both WL are present and properly synchronized (see Fig. 4.16a). The achievable fringe contrast is significantly lower compared to the separate WLG driven both with 800 nm as in the previous experiment. The two WL divergences are quite different and it is experimentally difficult to achieve a mode match across the whole WL modes. Furthermore the spectrometer is significantly less sensitive and with

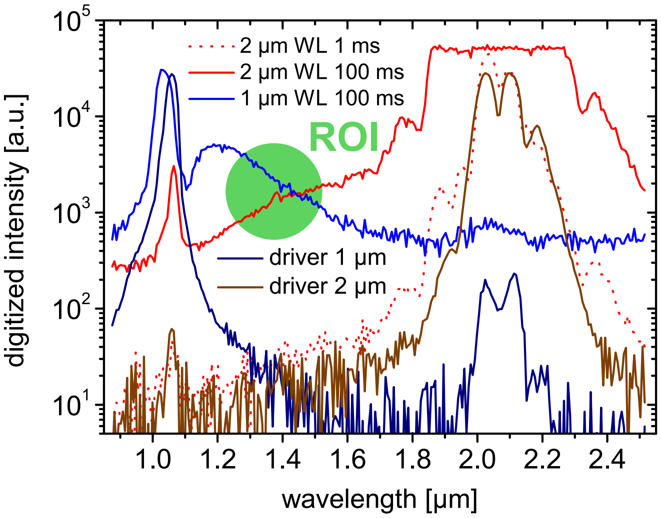

Figure 4.15: Spectra of the 2 µm driver and its SHG at 1 µm for driving the WLG (brown, dark blue) showing a good separation of fundamental and SH. The separate WL (red, blue) overlap spectrally and the spectral overlap around 1.3 µm is used to observe the spectral interference.

higher detection noise compared to a Si-based one. The spectral profiles and the fringe contrast stay constant once the setup is aligned and boxed. A single-shot time-trace over 1000 consecutive shots (1 s) shows a stable relative phase upon activation of the relative phase lock (see Fig. 4.16b). The relative phase noise is measured to be 172 mrad rms at 1250nm. This noise includes non-common noise as well as common mode noise contributions from the WLG itself. But also other sources of noise are measured, like the CEP noise of our CEP-stable front-end, noise in the SHG and the interferometric setup. The passive CEP noise of our front-end was characterized to be on the order of 150-200 mrad at 650 nm already. This would mean that the main noise in this experimental configuration already comes from CEP variations in the initial driving pulse. Furthermore also noise is introduced by our feedback loops to lock the relative phase of the two WLG. The intrinsic relative phase noise of the separate WLG seems to play a negligible role.

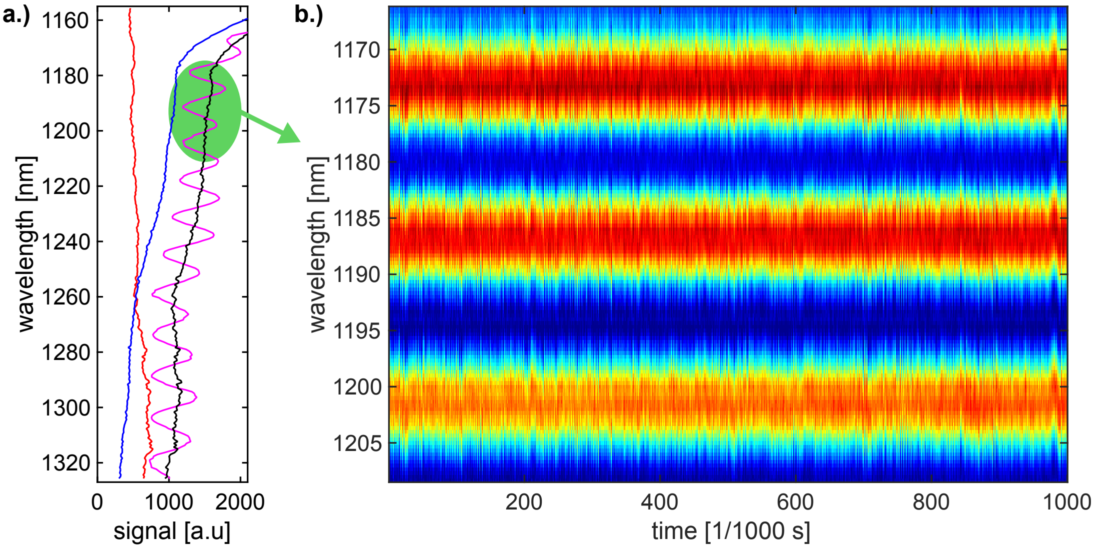

Figure 4.16: a.) Spectrum of WLG: driven with 2 µm (red), driven with 1 µm (blue), incoherent sum (black) and the coherent WL-WL interference fringes (violet) **b.)** Zoomed-in fringe trace (region indicated by green circle in a.)). Temporal evolution of the spectral fringes for 1000 laser shots (1 s) exhibiting a relative phase noise of 172 mrad rms with active stabilization.

4.5 Conclusions

Both experimentally observed phase noises among the two separate WL prove that indeed separate WLG, even driven at different driving wavelengths can be used to seed a parallel parametric waveform synthesizer with sufficiently low relative phase noise level for stable and reproducible waveform synthesis. This opens up important prospects for the simplification of experimental implementations of parallel synthesizers. Previously one single WLG should seed the whole system, but it was experimentally hard to drive the WLG in a regime where a broad bandwidth of two octaves is created while maintaining a stable spectral intensity and spectral phase. Now, after these findings, each channel can be equipped with its own WL stage, which can be tuned precisely to fit its seeding requirements without compromises on the phase-noise performance. The requirements on the dispersion management scheme are relaxed, because no special ultra-broadband beam splitters need to be used to split a single WLG into spectral sections to seed the corresponding synthesizer channels. A seed can be locally prepared and is not required to be transported over extended lengths before first amplification in an OPA takes place, which means the WL-mode degeneration is reduced to a minimum.

Chapter 5

Timing Stabilization and Control

The parallel approach to parametric waveform synthesis offers a good scalability with respect to output energy and bandwidth (see Chapter 3.1.5). Such a source holds unique potential for driving HHG with custom-sculptured waveforms to generate bright isolated attosecond pulses for exploration of new prospects in attosecond science (see Chapter 2.9). But the parallel approach also imposes strict requirements on the active timing synchronization system. Several (nonlinear) interferometers are formed as a result of this scheme. Timing instabilities arising from meters to tens of meter of separate beam propagation and tens to hundreds of optics the beams needs to pass. Furthermore, each individual OPA-stage forms another (nonlinear) interferometer between the pump and the (chirped) seed pulses. It was initially planned that a passive CEP-stable seed driver and balanced optical cross-correlators between the spectral channels feeding to delay lines at the spectral channel outputs are enough to achieve stable operation (see Fig. 3.8 on page 40). This approach was found to be dysfunctional in early synchronization experiments due to couplings and lack of relative phase active stabilization and control.

In this chapter, novel ultrafast timing tools based on the balanced optical cross-correlator for relative envelope timing were invented jointly by G. M. Rossi and the author to exploit the broadband nature of the output pulses emitted from the synthesizer channels. The author developed a special triggered photo-detector with internal integration and digitization with high-resolution for precise optical synchronization. Furthermore the method of spectral interference is introduced to the experiment to measure and gain control of relative-phases and CEP(s) of the involved pulses. The author developed a single-shot spectrometer with phase-retrieval based on fast Fourier transformation (FFT, [108]) calculated within an FPGA to allow for a reliable phase tracking and lowest possible feedback latency. Based on the insights of the timing dynamics in the synthesizer experiment a novel active timing synchronization scheme was invented by the author jointly with G. M. Rossi with contributions from Dr. G. Cirmi and other colleagues. The novel active synchronization scheme takes the unique timing behavior in such a complex optical system into account. When individual active synchronization loops would be used to stabilize all degrees of freedom, they would start to oscillate with each other due to complex couplings of the observables and actuators within the system. To decouple this synchronization loops a centralistic control system performing orthogonalization is required. The author developed an FPGA-based feedback infrastructure to implement this orthogonalization to decouple the individual timing parameters from each other while delivering high bandwidth active stabilization.

5.1 Relative Envelope Timing

The balanced-optical cross-correlator invented by Schibli *et al.* had the aim to lock the pulses emerging from two laser oscillators of different center wavelength to achieve a waveform synthesis. This timing method later achieved further significant results in other mainly oscillator based applications, like timing-distribution networks for large-scale electron accelerator facilities such as FELs [183, 184]. The BOC technique is suitable for locking the relative envelope timing of high-quality and low-noise laser sources like mode-locked oscillators. The BOC signal is acquired at the repetition-rate of the laser, which is in the MHz region. While the lock only needs to compensate noise components up to the acoustic range (tens of kHz). Any noise at higher frequencies than that is usually not originating from the laser sources but the detection itself. This difference between high measurement bandwidth and low required feedback bandwidth creates a very high margin for the active stabilization and can deliver significant attenuation of drifts and acoustic noise.

5.1.1 Limitations of the Two-Arm BOC

Different to locking laser oscillators via a BOC, in applications of a high-energy OPA-based synthesizer, no margin between detection bandwidth and required feedback bandwidth is present. The repetition rate in the kHz regime and the correspondingly low measurement-bandwidth limits the performance of the feedback system. Accordingly the overall noise-level of the BOC measurement itself should be as low as possible.

Another major difference between oscillators and OPA-based synthesizers is the energy stability of the laser pulses. The BOC in principle should cancel out every cross-sensitivity towards fluctuations of the pulse intensities. This is only true if both photo-detectors measure the same signal amplitude. Within the S-curve there is only one operation point which fulfills this condition, directly at the zero-crossing. Contrary to that, for a synthesizer it is important to set the envelope delay to any set point within the operation range to achieve custom-sculptured

waveforms.
The first implementation of the BOC, which was used to lock the relative envelope delay between two channels of the synthesizer setup, was a classic two-arm BOC. It was observed, that not only intensity fluctuations but also beam pointing and imperfections in the involved beam modes influence the measured timing jitter due to parasitic cross-sensitivities. The two-arm geometry is prone to furthermore create pointing side-sensitivities if the two BOC arms are not perfectly matched. Experimentally the two-arm BOC requires a huge footprint at the combining section of the synthesizer setup. Because of these challenges for our particular application scenario, G. M. Rossi and the author jointly invented a much simpler and more robust envelope timing method described in detail in the next sections. An emphasis was put to adapt the scheme to our application with the following goals in mind:

- reduce footprint and complexity of the optical setup to minimum possible
- reliable performance with increased pulse energy fluctuations
- less sensitive to beam pointing and imperfect spatial-modes
- locking to any set point on the BOC curve for pulse-shaping and control
- single-shot and every-shot detection capability with low latency for efficient feedback at kHz-range repetition rates

5.1.2 Relative Arrival Time Measurement (RAM)

This section presents content from the manuscript of the publication by R. E. Mainz *et al.* in Optics Express [185], which is reproduced with the consent of the authors and the publishing journal. The study was performed with equal contributions from R. E. Mainz and G. M. Rossi. For the invented timing method also a European Patent Application [186] was filed to protect a intellectual property associated with the parallel synthesizer and similar applications requiring timing synchronization. The paper is cited in the following until page 98.

» Begin of citation from R. E. Mainz *et al.* in Optics Express [185] «

On the extremely short time scale, mode-locked femtosecond lasers and high-harmonic generation in gases keep pushing the limit of the shortest man-made events, light pulses with duration down to a few tens of attoseconds [97]. Ultrashort pulses have also pushed the requirements on synchronization systems down to a time scale that cannot be fulfilled by conventional electronics.

5.1.3 RAM Method

The basic idea of the RAM method is sketched in Fig. 5.1. The red and yellow pulses 1 and 2 have to be synchronized in order to achieve a shot-to-shot stable synthesis (or a stable pump-seed temporal overlap in an OP(CP)A)). The small portions of the two pulses derived from a leakage of the beam combiner (BC) is stretched by a first dispersive element D_{RAM1}. In particular, we choose D_{RAM1} to stretch the yellow pulse significantly more than the red one. The nonlinear crystal NLC1, tuned to phase-match the sum frequency between the red pulse and the short-wavelength part of the yellow pulse, generates the first RAM signal S1. Afterwards, a second dispersive element D_{RAM2} (less dispersive than D_{RAM1}) changes the relative delay between the two pulses, and a second nonlinear crystal (NLC2) generates the second RAM signal S2 via sum frequency generation (SFG) of the red pulse with the long-wavelength part of the yellow pulse. Alternatively, instead of SFG also difference-frequency generation (DFG) can be used to obtain the RAM signals. When the ATD between the two pulses changes, either the long-wavelength or the short-wavelength components of the stretched yellow pulse have a larger overlap in time with the red pulse, leading to an increase of the corresponding SFG signal, and a decrease of the other competing SFG signal. When the ATD is scanned linearly, both S1 and S2 signals exhibit a bell-shape behavior, with the two bells being peaked at different ATD values. The difference between the two signals is then an S-shaped curve, or S-curve, that defines the measurement range. By employing a calibrated delay line to scan the ATD, it is possible to assign every point of the S-curve to a univocal ATD value. Similar results can be obtained by means of a single broadband nonlinear crystal, as we will discuss in details in a short while, placed after D_{RAM1}; in this case the two signals are derived from the broadband (and chirped) SFG via spectral filtering. The two signals S1 and S2 are then directed to a home-made detector that digitizes them. Such a digital signal is then fed to a home-made signal processing unit (SPU), based on a field-programmable gate array (FPGA), that calculates the ATD and uses it to generate the feedback values to be applied to a piezo-actuated delay line in order to stabilize the ATD. Compared to the conventional two-arm BOC, the new RAM scheme features three major advantages: first of all it is a compact all-inline scheme, that makes it intrinsically more robust towards beam pointing/intensity fluctuations of the laser beam and misalignment of the optical system due to thermal drifts. Second, the simplicity and compactness of the setup makes it suitable for applications that demand multiple ATD measurements. This is the case, for instance, in multi-stage multi-channel parametric waveform synthesizers [114, 115], where both pump-seed synchronization in the parametric amplifiers, and synchronization of the different channel outputs require ATD measurements and stabilization. Last but not least, the FPGA-based SPU allows for real-time calculation of the normalized difference (see Eq. (5.9)), allowing to lock to *any* point of an extended range (>3 times the range without normalization) with constantly high accuracy. This feature enables the possibility of controlling the delay of the different OP(CP)A channel outputs over a broad range of values, thus enabling a more flexible sculpting of the synthesized waveform $E(t)$. Furthermore, when it comes to ultra-broadband pulses, the dispersion, that is required in one of the two arms of the conventional BOC in order

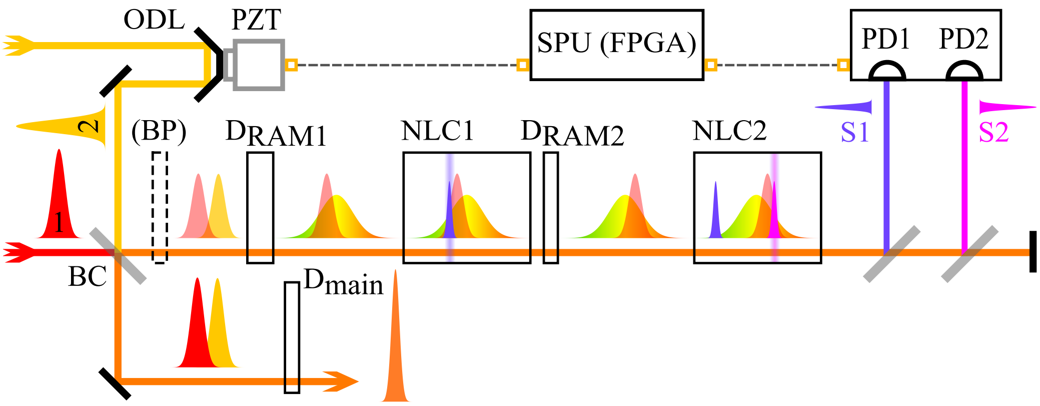

Figure 5.1: Scheme of the RAM setup: two laser pulses (1 and 2), whose spectra are centered at different wavelengths, are overlapped with the beam combiner BC. A leakage from the BC is directed to the RAM setup. The dispersive element D_{RAM1} is used to apply a significantly larger chirp on pulse 2 with respect to pulse 1. Signal S1 is generated in the nonlinear crystal NLC1 by SFG or DFG. A second dispersive element D_{RAM2} is used to adjust the time relation between the two pulses. A second signal S2 is generated in NLC2 at a wavelength different from S1. The two signals are separated spectrally and directed to two photodetectors (PD1 & PD2). An FPGA-based signal processing unit (SPU) performs the normalized difference between PD1 and PD2 (see Eq. (5.9)) to extract the arrival-time difference (ATD), that can then be used to actively stabilize the ATD by moving a piezoelectric actuator (PZT). The main output of the BC will experience the dispersion D_{main}, after which the two pulses can be temporally overlapped and compressed. In order to match the group-delay (GD) difference between the main output and the leakage, a birefringent plate (BP) can be used before D_{RAM1}.

to flip the ATD between the two pulses, can produce strong changes in the temporal profile of the pulses, with subsequent changes in the SFG response, with respect to ATD variations, from one arm to the other. This leads to a limited common-mode rejection ratio (CMRR) beyond the balanced point, located at the zero crossing. In the RAM setup, on the contrary, the possibility of independently tuning the two SFG signals to different spectral regions of the stretched pulse allows to generate two signals with almost identical responses with respect to ATD, permitting one to achieve a high CMRR all over the range. Furthermore, by tuning the SFG signals to different spectral regions also allows one to optimize the crossing point of the two cross-correlations in order to achieve a steep slope near the zero crossing while simultaneously ensuring a large range of the S-curve. Moreover, in RAM the second SFG signal does not suffer from the energy depletion of the two laser pulses caused by the first SFG signal generation, since the stretched pulse is being used in two separate spectral regions, and the depletion of the short laser pulse is limited by the small amount of energy in the phase-matching bandwidth of the stretched pulse that overlaps in time with it. Let us consider the synthesis of two broadband femtosecond pulses having carrier frequencies ω_1 and ω_2, with $\omega_1 \neq \omega_2$. In the context of a parametric waveform synthesizer, the two pulses in general will not overlap in time and will not be compressed at the beam combiner (BC), since those conditions must be achieved at the experimental point [115, 146], after propagating through a number of additional dispersive elements, such as a vacuum chamber window and chirped mirrors for final compression, here represented by D_{main}. If we assume the requirement of perfectly overlapped and compressed pulses (ATD = 0 s) at the experimental point, i.e., after D_{main}, then the group-delay (GD) difference between ω_1 and ω_2 introduced by D_{RAM1} must be close to the one introduced by D_{main}, i.e.,

$$\mathrm{GD}_{\mathrm{D_{RAM1}}}(\omega_1) - \mathrm{GD}_{\mathrm{D_{RAM1}}}(\omega_2) \approx \mathrm{GD}_{\mathrm{D_{main}}}(\omega_1) - \mathrm{GD}_{\mathrm{D_{main}}}(\omega_2). \tag{5.1}$$

At the same time, if we assume the two pulses to be fully recompressed after $\mathrm{D_{main}}$, while one of the two being chirped in the RAM setup, we require

$$\mathrm{GDD}_{\mathrm{D_{RAM1}}}(\omega_1) \neq \mathrm{GDD}_{\mathrm{D_{main}}}(\omega_1) \quad \text{and} \quad \mathrm{GDD}_{\mathrm{D_{RAM1}}}(\omega_2) \approx \mathrm{GDD}_{\mathrm{D_{main}}}(\omega_2). \tag{5.2}$$

Conditions (5.1) and (5.2) can be fulfilled in general by simply employing different materials for D_{RAM} and D_{main} with different thicknesses. If no convenient dispersion arrangement can be found, it is possible to decouple conditions (5.1) and (5.2) by means of a birefringent crystal (or wedge pair as in [187]), that can introduce a significant GD between the pulses with small intra-pulse dispersion. Once D_{RAM1} is chosen, in the RAM setup there will be two stretched replicas of the two pulses having similar ATD with respect to the main output. Let us next consider two different possible implementations of the RAM setup, named *I-crystal RAM* and *II-crystal RAM*. The benefits of implementing one or the other will also be discussed.

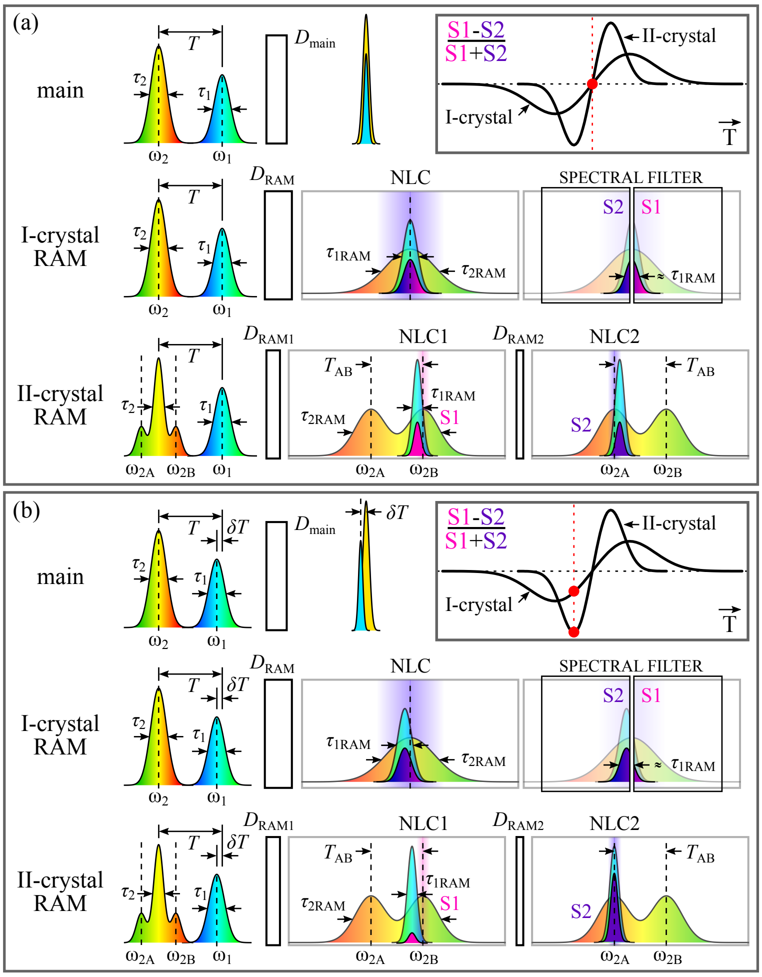

Figure 5.2: Optical scheme of RAM: (a) The left-hand side of each rows shows the two pulses after being combined with an ATD $= T$. In the *main* arm the pulses are compressed and overlapped in time (ATD $= 0$) after D$_{\text{main}}$. In the *I-crystal* RAM setup, D$_{\text{RAM}}$ stretches the ω_2 pulse such that $\tau_{2\text{RAM}} \gg \tau_{1\text{RAM}}$. The two signals S1 and S2 can be obtained by spectral filtering the broad (and chirped) sum frequency generated by NLC. In the *II-crystal* RAM setup, D$_{\text{RAM1}}$ modifies the durations of the two pulses such that $\tau_{2\text{RAM}} \gg \tau_{1\text{RAM}}$, then NLC1, phase-matched for $\omega_{2\text{B}} + \omega_1$, generates the first sum frequency S1. D$_{\text{RAM2}}$ delays slightly one pulse with respect to the other, without affecting significantly the durations. NLC2 generates the second sum frequency S2 of $\omega_{2\text{A}} + \omega_1$. In the top-right corner, the corresponding position on the S-curve is marked in red. (b) Same scheme as in panel (a), when the ATD is reduced by δT: the signal S1 decreases, while signal S2 increases.

RAM Method: I-Crystal

The *I-crystal* RAM makes use of a single dispersive element, D_{RAM}, and a single broadband nonlinear crystal (NLC) in order to perform SFG between the ω_1

and ω_2 pulses (see Fig. 5.2). The two signals S1 and S2 required to determine the ATD are generated by spectral filtering the broadband SFG, as we will see later in detail. We now present a simple model that describes the experiment, in order to derive some guidelines to set up a proper ATD measurement. For this task, we need to make the following assumptions: (i) the phase-matching condition of the nonlinear crystal is not significantly limiting the interacting bandwidths of the two pulses in the SFG process; (ii) the nonlinear crystal is not introducing significant dispersion and there is no group-velocity mismatch between the three pulses (the ω_1 pulse, the ω_2 pulse and the SFG pulse). As a rule of thumb, both (i) and (ii) are fulfilled for optical pulses in thin BBO crystals: for pulses in the 100-fs range one needs to use BBO crystals with $\approx$100 µm thickness, while for pulses in the 10-fs range a thickness of $\approx$10 µm is appropriate. To this end, both type-I and type-II phase-matching crystals were successfully tested and can be used, depending on the specific details of the pulses involved. Adopting the standard notation for linearly chirped pulses, the electric field of the ω_α pulse ($\alpha = 1, 2$) is given by $E_\alpha(t) = A_\alpha(t)e^{i(\omega_\alpha t+\dot{\omega}_\alpha t^2/2)}$, where $A_\alpha(t)$ is the temporal field envelope, ω_α is the carrier frequency of the spectrum, and $\dot{\omega}_\alpha$ is the (linear) chirping parameter. We now consider that the pulse at ω_2 has a broader bandwidth ($\Omega_2 > \Omega_1$) and, due to the chirp, a significantly longer pulse duration ($\tau_{2\mathrm{RAM}} \gg \tau_{1\mathrm{RAM}}$) with respect to the pulse at ω_1, implying that $\dot{\omega}_1 > \dot{\omega}_2$. This is the typical case for a parametric waveform synthesizer, since the outputs of the different OP(CP)As channels usually have different bandwidths. Moreover, this is also the case for a pump-seed pair of pulses in a broadband OP(CP)A. Under these assumptions the temporal envelope of the SFG cross-correlation has a duration comparable to $\tau_{2\mathrm{RAM}}$. It is now possible to express the electric field of the SFG signal as function of the ATD T between the two pulses as

$$\begin{aligned} E_{\mathrm{SFG}}(t,T) \propto E_1(t)E_2(t+T) &= A_1(t)A_2(t+T)e^{i(\omega_1 t+\omega_2(t+T)+\dot{\omega}_1 t^2/2+\dot{\omega}_2(t+T)^2/2)} \\ &\approx A_1(t)A_2(T)e^{i((\omega_1+\omega_2)t+\omega_2 T+\dot{\omega}_1 t^2/2+\dot{\omega}_2(t+T)^2/2)}, \end{aligned} \tag{5.3}$$

where, in the last step, we have considered the envelope of the shorter ω_1 pulse as $A_1(t) = A_1\delta(t)$, with $\delta(t)$ being the Dirac delta function, . This expression of the SFG electric field allows us to conclude that the instantaneous angular frequency of the SFG pulse is

$$\omega_{\mathrm{iSFG}}(t,T) = \omega_1 + \omega_2 + \dot{\omega}_1 t + \dot{\omega}_2(t+T). \tag{5.4}$$

Since in this derivation the SFG pulse is comoving with the reference frame of the ω_1 pulse, we can obtain its central angular frequency as

$$\omega_{\mathrm{SFG}}(T) = \omega_{\mathrm{iSFG}}(0,T) = \omega_1 + \omega_2 + \dot{\omega}_2 T, \tag{5.5}$$

that explicitly shows how the central frequency of the SFG signal is shifted by the ATD T between the two pulses. We can now generate the two signals S1 and S2 required to determine the ATD between the two pulses via spectral filtering of the broadband and chirped SFG. We can imagine to cut the SFG signal spectrum in halves with respect to its central frequency at $T = 0$ (i.e., $\omega_1 + \omega_2$): the low-frequency side, named S1, will be directed to photodetector PD1, while the high-frequency side, named S2, to PD2. The two photodetectors convert the electric field of the SFG into electric charge, and integrate it over the whole SFG pulse duration. This means that for $T = 0$ we can assume the two signals to be balanced (S1 = S2) and approximately at half of their dynamic range. We now want to derive a simple model that allows us to predict the ATD measurement range of the RAM with respect to the spectral bandwidth of the two pulses, $\Omega_1 = \dot{\omega}_1\tau_{1\text{RAM}}$ and $\Omega_2 = \dot{\omega}_2\tau_{2\text{RAM}}$, and their pulse durations in the RAM setup, $\tau_{1\text{RAM}}$ and $\tau_{2\text{RAM}}$. The RAM range is defined as the ATD ΔT that brings the signal S1 (or S2) from its maximum value to zero. Consequently, by assuming a symmetric behavior, $\Delta T/2$ will bring the signal from half of its dynamic range to zero (or to its maximum, depending on the sign). The condition S1 = 0 will be reached, when the lowest spectral component of the SFG signal is equal to $\omega_1 + \omega_2$, meaning that all the generated components are now in the S2 signal. Assuming $\dot{\omega}_2 > 0$, this can be written as

$$\begin{aligned} &\omega_{\text{iSFG}}^{\text{lowest}}(\Delta T/2) = \omega_{\text{iSFG}}(-\tau_{1\text{RAM}}/2, \Delta T/2) = \omega_1 + \omega_2 \\ &\Rightarrow \dot{\omega}_1(-\tau_{1\text{RAM}}/2) + \dot{\omega}_2((-\tau_{1\text{RAM}}/2) + (\Delta T/2)) = 0 \end{aligned} \tag{5.6}$$

that brings us to the equation

$$\Delta T = \tau_{1\text{RAM}} + \frac{\Omega_1}{\Omega_2}\tau_{2\text{RAM}}. \tag{5.7}$$

This equation is useful to determine how much chirp is required to achieve a desired measurement range. Nevertheless one needs to keep in mind the limits of its validity, that is $\Omega_2 > \Omega_1$ and $\tau_{2\text{RAM}} \gg \tau_{1\text{RAM}}$. Formula (5.7) also applies only to the case of splitting the SFG bandwidth in halves. In reality it is possible to obtain S1 and S2 from different kinds of spectral filtering. For instance, by blocking the central part of the SFG spectrum and using the right and the left wings as S1 and S2, it is possible to achieve faster signal variations with respect to the ATD, meaning shorter measurement range but higher time resolution, as will be shown in the next section. In general, the *I-crystal* RAM better suits pulses with bell-shaped spectral intensity profiles, since the phase-matching condition is optimum for the center $\vec{k}$ vectors of the pulses, i.e., $\Delta\vec{k} = \vec{k}_1 + \vec{k}_2 - \vec{k}_{\text{SFG}} = \vec{0}$. On the other hand, the spectra generated by ultra-broadband OP(CP)As (such as degenerate or noncollinear OP(CP)As) typically yield M-shaped amplified spectra, when trying to push the spectral bandwidth to the extreme; in this case, the *II-crystal* RAM can come in handy.

RAM Method: II-Crystal

This variation of the RAM setup is almost identical to the *I-crystal* one, but after D_{RAM} (here renamed D_{RAM1}) and NLC (here NLC1), a second dispersive element D_{RAM2} can be used to adjust the ATD between the two pulses, and a second nonlinear crystal (NLC2) generates a second, differently tuned SFG. As mentioned before, this scheme is particularly suitable for ultra-broadband pulses generated by OP(CP)As exhibiting an M-shaped spectrum. Moreover this configuration opens up the unprecedented opportunity of measuring relative *arrival time differences* between more than two pulses, with different spectral contents, at once. In this case, the longer, stretched pulse in the RAM setup could be overlapped with two (or more) shorter pulses. The phase-matching conditions of the two crystals would have to permit the SFG (or DFG) between the long and each of the two short pulses, producing two signal pairs in two different spectral regions, easily separable via spectral filters. To this end our detector already features four independent PDs. This application is of particular interest in parametric waveform synthesizers since it would allow one to access all the relative timing information between all the different spectral channels in a single RAM device, therefore avoiding any systematic errors and drifts that may arise by measuring the different ATDs in different positions of the optical setup with different BOC or RAM devices. In the *II-crystal* RAM, the two phase-matching conditions of NLC1 and NLC2 can be tuned to be fulfilled for the strongest spectral components of the ω_2 pulse, denoted as $\omega_{2\mathrm{A}}$ and $\omega_{2\mathrm{B}}$, i.e., $\Delta\vec{k}_{\mathrm{NLC1}} = \vec{k}_1 + \vec{k}_{2\mathrm{A}} - \vec{k}_{\mathrm{SFG1}} = \vec{0}$ and $\Delta\vec{k}_{\mathrm{NLC2}} = \vec{k}_1 + \vec{k}_{2\mathrm{B}} - \vec{k}_{\mathrm{SFG2}} = \vec{0}$. This way it is possible to avoid the problems that would arise from a limited phase-matching bandwidth and optimize the conversion efficiencies in the two SFG processes. The two signals S1 and S2 can now be obtained by bandpass filtering, with bandwidth Ω_3, around $\omega_1 + \omega_{2\mathrm{A}}$ and $\omega_1 + \omega_{2\mathrm{B}}$, respectively. In order to avoid cross-talk between the two signals, it is necessary that $(\omega_1 + \omega_{2\mathrm{B}}) - (\omega_1 + \omega_{2\mathrm{A}}) > \Omega_3$, that leads to $T_{\mathrm{AB}} > (\Omega_3 \tau_{2\mathrm{RAM}})/\Omega_2$, where T_{AB} is the ATD between the $\omega_{2\mathrm{B}}$ and $\omega_{2\mathrm{A}}$ components, which is easily fulfilled by choosing $\Omega_3 \ll \Omega_2$. In order to set up the correct working point for the RAM (at the zero crossing of the S-curve), we need to shift the relative ATD between the ω_1 and the ω_2 pulses such that the lowest frequency component of the spectrum of the higher-frequency SFG (the one generated by NLC1, for instance) is coincident with $\omega_1 + \omega_{2\mathrm{B}}$, meanwhile the highest frequency component of the spectrum of the lower-frequency SFG (the one generated by NLC2, for instance) is coincident with $\omega_1 + \omega_{2\mathrm{A}}$. Such an ATD shift, T_{shift}, can be achieved by the dispersive element $D_{2\mathrm{RAM}}$. The overall ATD shift can be estimated by observing that, according to Eq. (5.4), the lowest frequency component of the spectrum of the higher-frequency SFG at a time $\tilde{T}$ is $\omega_{\mathrm{iSFG}}^{\mathrm{lowest}}(\tilde{T}) = \omega_{\mathrm{iSFG}}(-\tau_{1\mathrm{RAM}}/2, \tilde{T}) = \omega_1 + \omega_{2\mathrm{B}} - \Omega_1/2 - (\Omega_2/2)(\tau_{1\mathrm{RAM}}/\tau_{2\mathrm{RAM}}) - (\Omega_2/\tau_{2\mathrm{RAM}})\tilde{T}$, that, when set equal to the central frequency of the filter $\omega_1 + \omega_{2\mathrm{B}}$, leads to $\tilde{T} = 1/2(\tau_{1\mathrm{RAM}} + \tau_{2\mathrm{RAM}}(\Omega_1/\Omega_2))$. The same considerations can be made for the highest frequency component of the spectrum of the lower-frequency SFG, that leads us to conclude that $T_{\text{shift}} = 2\tilde{T} + T_{\text{AB}} = \tau_{1\text{RAM}} + \tau_{2\text{RAM}}(\Omega_1/\Omega_2) + T_{\text{AB}}$. We can now estimate the required thickness of the two dispersive elements D_{RAM1} and D_{RAM2} to be

$$L_{D_{\text{RAM1}}} = \frac{cT_{\text{AB}}}{|n_g(\omega_{2\text{B}}) - n_g(\omega_{2\text{A}})|} \quad \text{and} \quad L_{D_{\text{RAM2}}} = \frac{cT_{\text{shift}}}{|n_g(\omega_{2\text{B}}) - n_g(\omega_1)|}\,, \tag{5.8}$$

where c is the speed of light in vacuum, $n_g(\omega_1)$, $n_g(\omega_{2\text{A}})$ and $n_g(\omega_{2\text{B}})$ are the group refractive indices of the ω_1 pulse and of the $\omega_{2\text{A}}$ and $\omega_{2\text{B}}$ components in the D_{RAM1} or D_{RAM2} dispersive media. Since it is typically true that $|n_g(\omega_{2\text{B}}) - n_g(\omega_1)| \gg |n_g(\omega_{2\text{B}}) - n_g(\omega_{2\text{A}})|$, we can expect $L_{D_{\text{RAM2}}}$ to be much smaller than $L_{D_{\text{RAM1}}}$, such that the temporal broadening (or compression) of the pulses due to the propagation in $L_{D_{\text{RAM2}}}$ can be neglected. Finally, we observe that the measurement range for the II-crystal RAM case is $\Delta T = \Omega_3/\dot{\omega}_2$, which shows that a higher time resolution can be achieved by narrow filtering.

RAM Method: Detection and Processing

The optical signals S1 and S2 are converted into the electrical signals A and B by two large-area photodetectors ($10 \times 10\,mm^2$), to accommodate the whole optical mode in order to prevent errors in the pulse-energy determination due to beam-pointing instabilities. In order to obtain the value of the ATD between the two pulses, we have to perform the difference between the two electrical signals. In the RAM, differently from other previous BOC implementations, the outputs of the photodetectors are not subtracted analogically via an operational amplifier. Instead, the amount of charge in each PD is determined, on a single-shot and every-shot basis, by means of a home-made detector, that comprises a gated integrator (triggered by the laser) and a high-resolution analog-to-digital converter ADC (effective number of bits, ENOB $\approx$ 17bits). The digital signals are available for processing within less than 100 µs after the laser pulse signals S1 and S2 arrive at the PDs. An FPGA-based signal processing unit (SPU) allows to perform operations in real time on the two PDs outputs, such as the generation of a proportional-integral (PI) control signal with custom finite-impulse-response filter (FIR), and to achieve low-latency and high-bandwidth active stabilization with customized frequency response. More importantly, the SPU can calculate the *normalized difference* (ND) between the two electric signals, defined as

$$\text{ND}(T) = \frac{\text{A}(T) - \text{B}(T)}{\text{A}(T) + \text{B}(T)}, \tag{5.9}$$

which allows to improve the CMRR over the whole measurement range, whereas the *unnormalized difference* $[A(T) - B(T)]$, which has commonly been used in BOCs, is exhibiting a good CMRR only at the zero crossing of the S-curve. This feature brings several distinct advantages as discussed in the measurement section. Additionally, this detector has proven to be very useful, especially while optimizing the ATD signals, because each cross-correlation can be individually plotted in real time, allowing to easily optimize its intensity and shape by tuning the optical components of the RAM setup.

5.1.4 ATD Measurement using the RAM Scheme

We used an exemplary benchmark system (see Fig. 5.3) to measure the ATD between the pulses from a Ti:sapphire chirped-pulse amplifier (800 nm, 150 fs, 20 mJ, 1 kHz) and pulses from a white-light-seeded visible noncollinear OPA (VIS-NOPA) [48]. The NOPA output and a portion of the laser fundamental are overlapped with a dichroic mirror, and split into two beams via a neutral density metallic beam splitter, afterwards each beam is directed to an independent RAM setup. The two RAM setups are virtually identical; the second one serves for out-of-loop validation of the achieved locking performance. Each of the two beams in the RAM consists of ≈ 300 µW of NOPA power and ≈3 mW of laser fundamental. The two different pulses of each beam travel through a 20-mm-thick SF10 glass plate, which stretches the VIS-NOPA pulse duration to ≈ 800 fs, while the 800-nm pulses are stretched only from 150 to 160 fs. These

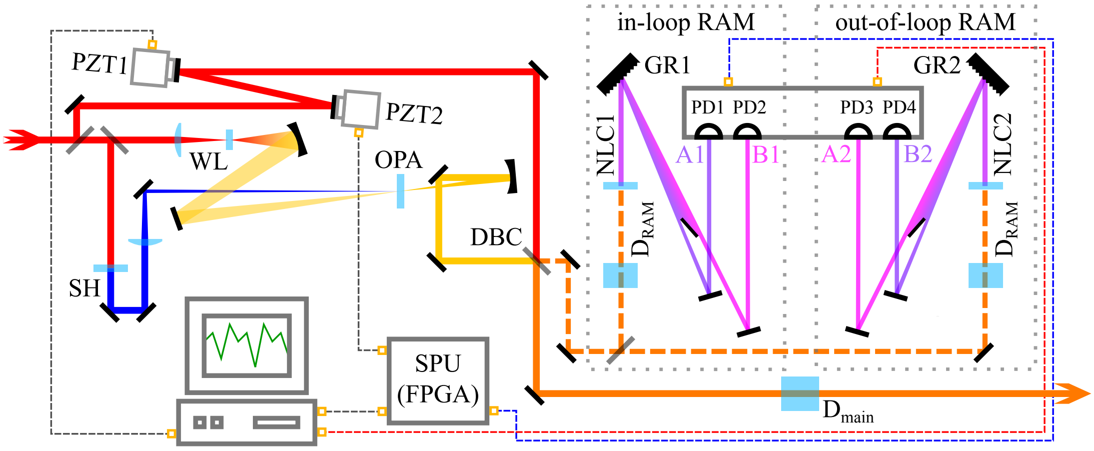

Figure 5.3: Stabilization of the ATD using the *I-crystal* RAM scheme: a portion of the pulses generated by a Ti:sapphire laser (150 fs, 800 nm, 20 mJ, 1 kHz) is split and sent to drive a white-light-seeded visible NOPA. The other part is sent to two piezo-actuated mirrors (PZT1 & PZT2), and recombined with the VIS-NOPA output with a dichroic beam combiner (DBC). A leakage from the DBC is sent to the two RAM setups. The first RAM setup is used inside the feedback loop acting back on PZT2 in order to stabilize the ATD. The out-of-loop RAM is used to verify the achieved accuracy of the measurement. All experimental data are acquired by a computer. In order to characterize the transfer function of the active stabilization, PZT1 can be driven by an arbitrary waveform.

pulse parameters fulfill the assumptions underlying Eq. (5.7) on page 87, so we can calculate an expected measurement range of ≈ 400 fs. The pulses are then loosely focused ($f = 300$ mm by a lens, beam waist ≈100 µm FWHM) and overlapped in a 100-µm-thick type-I beta-barium-borate (BBO) crystal. The *I-crystal* implementation of the RAM was chosen for its simplicity in this proof-of-principle experiment. The sum frequency (centered at 345 nm) emerging from the BBO is spectrally dispersed with a grating (600 grooves/mm, blaze wavelength 407 nm, blaze angle 7°, aluminum coated) and the two RAM signals (S1 and S2) are obtained by spatial filtering with razor blades. S1 and S2 are directed towards the two photodetectors A1 and B1 with UV-enhanced aluminum pick-up mirrors. In order to check the SFG dynamics with respect to the ATD, we measured the spectrum of the SFG signal and of the VIS-NOPA, after the RAM, during a triangular scan of one PZT, as shown in Fig. 5.4. As one would expect from Eq. (5.5) on page 86, the central frequency of the SFG signal is shifted with respect to the ATD between the two pulses. The spectrum of the VIS-NOPA shows a corresponding behavior, where a narrow depleted line moves with the ATD due to the contribution to the generation of the SFG-signal. The *II-crystal* configuration was tested as well and delivered almost identical results (green curve, plotted for comparison in Fig. 5.5), with the only difference that a lower amount of dispersive glass was required (5 mm of SF10 for D_{RAM1}, 1 mm of SF10 for D_{RAM2}), and two narrowband interference filters (340 nm and 350 nm, both 10 nm FWHM) were used to separate the two signals instead of a grating

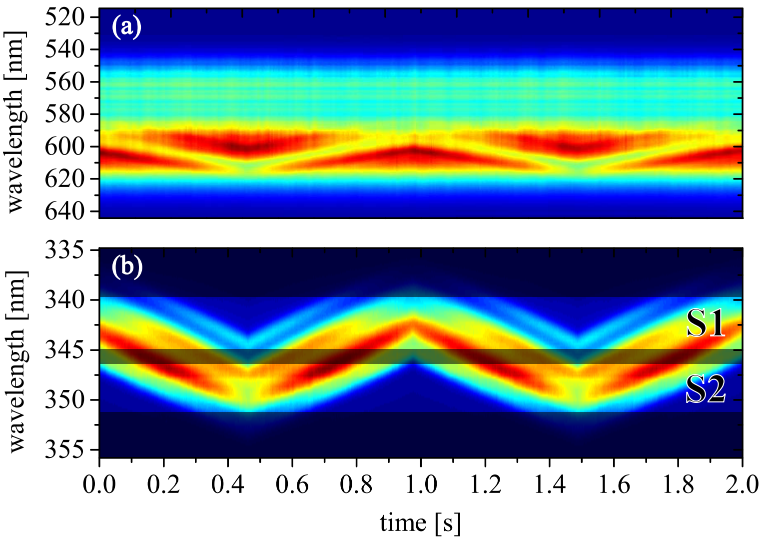

Figure 5.4: (a) Spectral evolution of the VIS-NOPA due to depletion from the SFG, during a triangular ATD scan. (b) Corresponding spectral evolution of the SFG. The shaded areas indicate the spectral regions that were blocked by the filter, while the integral over frequency of each of the bright areas corresponds to the S1 and S2 signals.

and a spatial filter. By applying different spectral filters to the different RAM schemes it is possible to modify the shape of the S-curve quite significantly and optimize the setup for measurement range or temporal resolution, as shown in the comparison of the S-curves in Fig. 5.5. In general, splitting the SFG spectrum in halves and directing the two halves to the two PDs leads to a longer measurement range, while stopping a wide band in the center of the SFG spectrum and directing the two opposite wings to the two PDs leads to a shorter range, but higher resolution (provided that the energy available is sufficient to fill the dynamic range of the PDs). Once the two signals have been digitized by the ADC, the FPGA-based SPU can be used to perform complex mathematical operations within few tens of µs (for example an FFT with 1024 points can be performed in less than 100 µs). With the commonly used plain subtraction of the two PD signals ($A_1(T) - B_1(T)$), a high CMRR can only be achieved if both signals are of similar intensities, which limits the operating range of the BOC close to the zero crossing of the S-curve. However, our SPU performs a real-time calculation of the *normalized difference* (see Eq. (5.9)). From one dataset obtained during linear ATD scans ($n = 326$ scans, 1000 data points per scan), the unnormalized S-curve and the normalized S-curve are calculated, and the rms noise of each ATD value from all S-curves is plotted in Fig. 5.6 for comparison. This yields the residual jitter function for each ATD position in the RAM range.

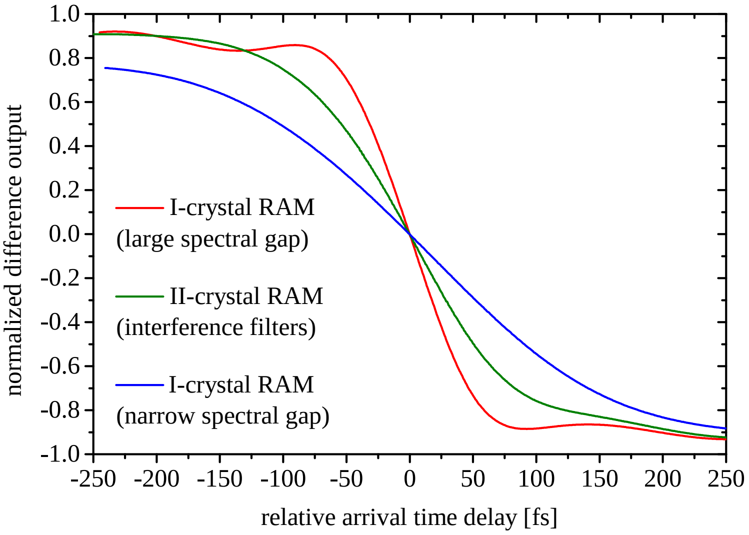

Figure 5.5: Influence of spectral filtering on S-curve. Blue curve: S-curve from *I-crystal* RAM obtained by splitting the SFG spectrum in two with a narrow spectral gap in between. Red curve: same as blue curve, but for a larger spectral gap. Green curve: S-curve from *II-crystal* RAM setup with narrowband interference filters. The measurement range and thus the temporal resolution can be tuned simply by applying different spectral filters. All S-curves here were obtained by measuring and averaging over few tens of curves.

The benefits of the normalized difference according to Eq. (5.9) are remarkable.

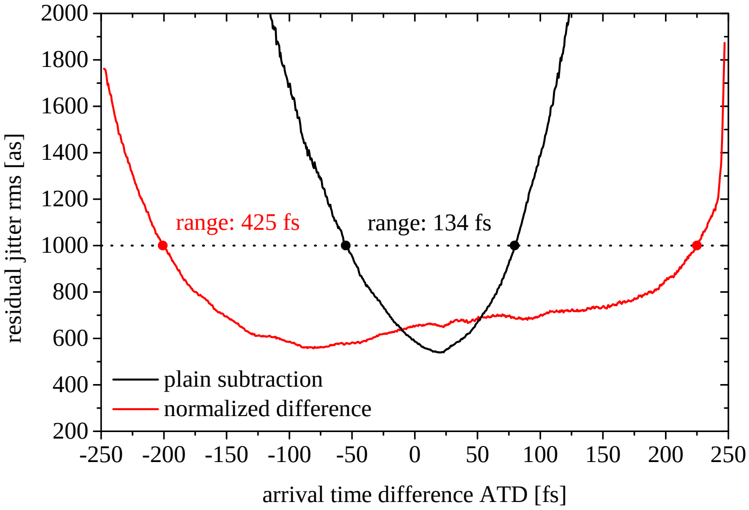

Figure 5.6: ATD rms for the cases of plain subtraction (black) and normalized difference (red) according to Eq. (5.9). Data extracted from $n = 326$ S-curve scans (hence a higher residual noise than for an active lock). The normalized difference allows for low detection noise over a much wider measurement range.

The range of the RAM is increased by a factor of > 3 while the noise level is kept constantly low over the measuring range. With RAM and the applied normalization it is possible to determine the ATD and to lock to *any* desired ATD value within the measurement range with an accuracy as low as 400 as rms at any point of the curve, spanning a range of 425 fs, in agreement with our estimate from Eq. (5.7). This results in a $1:1000$ ratio between residual noise and locking range, that is the best ratio, for a synchronization method based on balanced detection, ever demonstrated to our knowledge. By tuning the RAM to a higher sensitivity (see red curve in Fig. 5.5) it is possible to obtain a residual jitter as low as 287 as rms, integrated over the full Nyquist bandwidth (see Fig. 5.7). To compare those numbers to previously published results [138], which covered only a limited bandwidth, we integrated the noise spectrum from DC (1 Hz) to 30 Hz, resulting in 19 as of residual rms jitter, and from DC to 100 Hz, resulting in 56 as. These values compare favorably to the previous art, proving the enhanced accuracy of the RAM scheme. In the context of a parametric waveform synthesizer [114, 115], the RAM setup can be employed for the stabilization of the pump-seed overlap in the different OP(CP)A stages as well as for the actual synthesis from the different channel outputs. The benefits from the normalization are of particular interest, since in order to custom-tailor the synthesized electric field $E(t)$, it is desirable to control the ATD with high and constant accuracy over a wider range [114]. Once dealing with shorter pulses [115], we also expect to achieve higher accuracy (and even lower residual jitter) of the ATD measure-

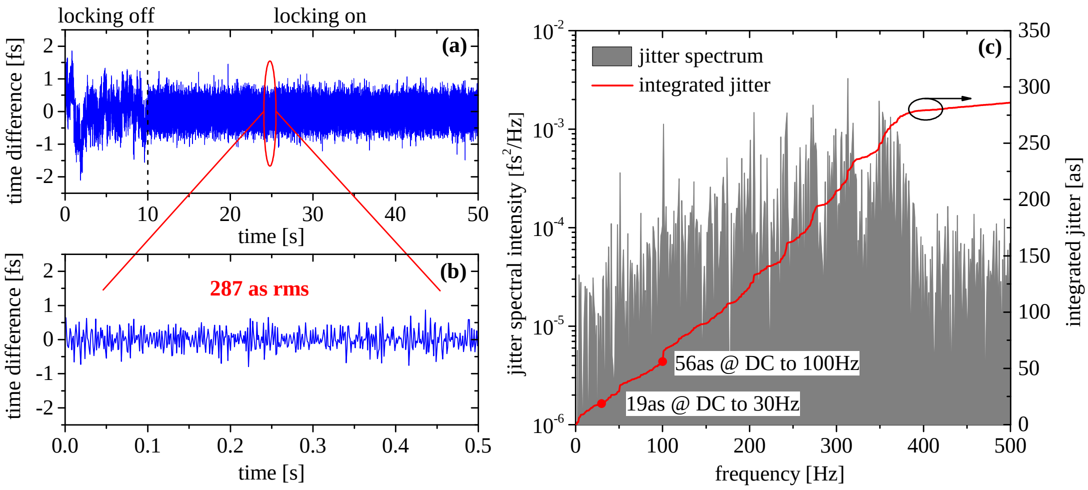

Figure 5.7: (a) Single-shot ATD measurement of an open/closed active stabilization loop over 50 seconds. (b) Zoomed-in portion of the ATD trace with 287 as residual jitter rms. (c) Jitter spectral density and integrated jitter with activated stabilization loop.

ment, at the expense of the range. Moreover, the simplicity and compactness of the RAM setup makes it particularly suitable for implementation in a complex system, which requires multiple ATD measurement and control devices. Last not least, as mentioned in the method section, the RAM technique could also be used to synchronize three (or more) synthesizer channels using a *single* RAM device.

5.1.5 ATD Stabilization and Out-of-loop Validation of Locking Performance

To evaluate the absolute accuracy of the RAM, two identical *I-crystal* RAM setups are simultaneously operated, one in an in-loop configuration (IL, signals A1/B1), the other in an out-of-loop configuration (OOL, signals A2/B2), and the corresponding single-shot and every-shot ATD measurements are recorded. Fig. 5.8 shows the individual signals of the two PDs and the corresponding normalized S-curves during a linear ATD scan, both for the IL and for the OOL RAM setups. Both RAM setups exhibit a similar behavior, as apparent from the virtually identical S-curves in Fig. 5.8. The *normalized difference* strongly suppresses the shot-to-shot amplitude noise, still clearly present in the individual PD traces. The ATD measurement and locking results from the IL RAM have been validated by comparison with the OOL measurement. The timing jitter spectral density and the integrated timing jitter, from a 100-s long measurement (10^5 laser shots), are shown in Fig. 5.9. The IL RAM yields an integrated residual jitter of 387 as rms, while the OOL residual jitter is 429 as rms. The

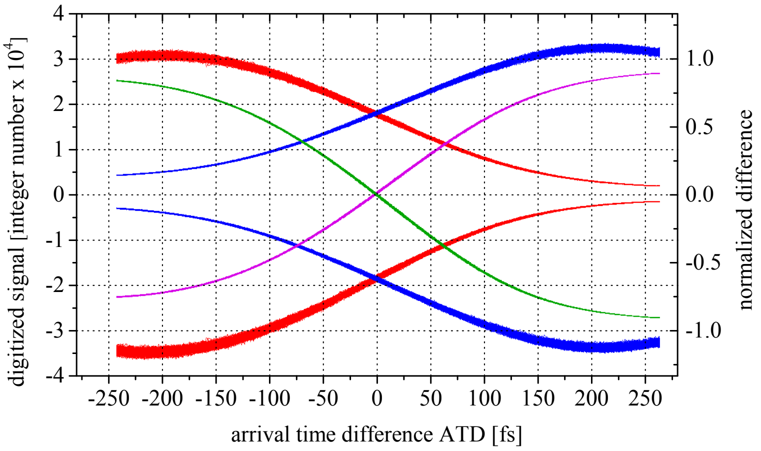

Figure 5.8: The outputs of the individual detectors of the IL and OOL RAM setups (IL: PD1/PD2 (A1/B1) on top red/blue, OOL: PD3/PD4 (A2/B2) on bottom red/blue with inverted sign) are plotted versus ATD (left vertical scale, $n = 326$ scans superimposed). The two corresponding normalized S-curves are plotted in green and violet (right vertical scale, the sign of the violet S-curve has been inverted for sake of clarity).

subtraction of the IL (A1) and OOL ATD results in a residual noise < 80 as rms noise, when integrated from 0.3 Hz to the Nyquist frequency. This clearly shows the high level of correlation between the two independent IL and OOL RAM measurements, resulting in an unprecedented precision for ATD determination, that is a residual rms(jitter)/range lower than 1 : 5000. Any noise component at a frequency below 0.3 Hz can be attributed to thermal drifts of the optical table and optomechanic components, that can be compensated with proper environmental isolation [188]. We are convinced that the simplicity of the RAM setup allows for such a high degree of reproducibility. Furthermore, the RAM setup has been operated for more than 2 weeks without requiring any realignment. Differently from ATD measurements of laser oscillators operating at repetition rates of tens to hundreds of MHz, few-kHz repetition rate laser amplifiers impose severe demands on the realization of a stabilization system designed to reduce the ATD jitter. In fact, any noise component whose natural frequency is above the Nyquist frequency is down-sampled producing aliasing [174]. Moreover, the higher energy of amplified pulses compared to oscillator ones, forces one to use large-aperture (thus heavy) mirrors in order to transport and delay the beams, a circumstance that severely limits the delay-actuator bandwidth. On the other hand, the low-kHz repetition rate opens the feasibility of performing analysis and feedback calculation with single-shot capability via an FPGA. Our FPGA-based signal processing unit SPU (see Fig. 5.10), for instance, allows to generate a custom FIR-filtered PI feedback signal $\approx 200\,\mu\mathrm{s}$ after the RAM signal pulses impinge on the photodetectors. Real-time operation with low latency is crucially

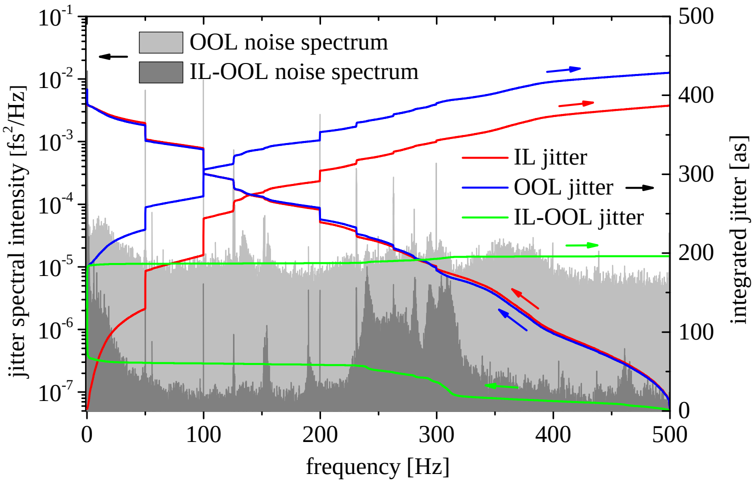

Figure 5.9: ATD spectral density of the IL RAM (grey) and of the difference between the IL RAM and OOL RAM (dark grey). Integrated ATD rms jitter of the IL and OOL RAM (red, blue) and of the difference between IL and OOL (green). Each jitter spectrum is integrated both starting from DC and starting from Nyquist frequency (integration direction is indicated by colored arrows).

important in order to achieve the highest possible bandwidth for the active stabilization. The sum of the latencies of the measurement, feedback computation and piezo actuator settling time defines the highest possible feedback bandwidth. Due to causality, a measured error from a random noise source can only be fed back to the next pulse, thus limiting the maximum feedback bandwidth to half the Nyquist frequency, i.e., 250 Hz, given the repetition rate of 1 kHz. This can be explained by considering that a certain frequency of the noise can only be damped by the proportional component (P) of a feedback loop, if its effect has a phase shift of less than 90° with respect to that frequency. For a P feedback, the Nyquist frequency corresponds to a 180° phase shift, thus in our system the 90° phase shift occurs at 250 Hz, meaning that, with minimum latency, only frequencies below this value could be damped. The currently used piezo actuator (Physik Instrumente, 753.1CD) allows to move to a desired position in the range of 20 µm within 1.25 ms, with a standard 1-inch mirror attached to it. This results in an effective action of the feedback delayed by one additional pulse, meaning that the theoretical cut-off frequency in our experiment is 125 Hz. To verify the performance of the active stabilization, we introduced a sweeping sinusoidal ATD spanning from 0.01 to 200 Hz with PZT1, with a corresponding ATD amplitude of 4.7 fs rms (13.3 $\mathrm{fs_{pp}}$), meanwhile the feedback performed a lock by acting back on PZT2. Figure 5.11 shows a comparison between the theoretical damping limit of a PI feedback versus our experimental results. The theoretical damping limit was calculated based on a feedback system with a proportional

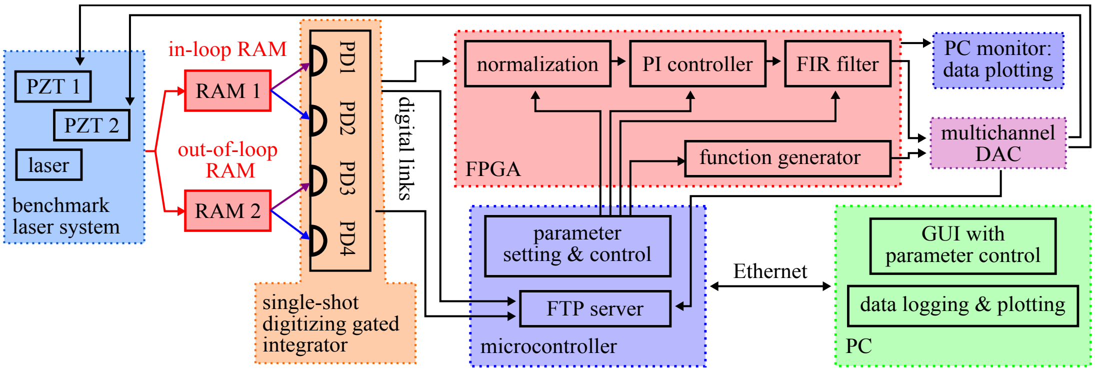

Figure 5.10: An in-loop and an out-of-loop RAM setup measure the ATD between two pulses from our benchmark laser system. A gated integrator determines the energy of the RAM signals separately, an ADC with 24-bit resolution (ENOB ≈ 17bits) digitizes the signals. The normalized difference as well as a PI controller and a custom finite-impulse-response (FIR) filter are implemented inside an FPGA, which generates a feedback signal to actively stabilize the ATD with piezo actuator PZT2. A monitor attached to the FPGA produces real-time data plots allowing for an intuitive system optimization. A microcontroller provides an interface between the FPGA and a computer via Ethernet for streaming data and controlling all the system parameters. Furthermore, a function generator is implemented to introduce artificial noise on the second piezo actuator PZT1.

feedback gain of 0 dB ($P_{gain} = 1$) and a latency of two pulses. The feedback reduces noise components in the range from 10 mHz (DC) to 80 Hz (−3 dB corner frequency). The excellent theoretical agreement suggests that with a piezo actuator capable of a 30 % shorter settling time, it would be possible to lock up to a −3 dB frequency close to 167 Hz. This would be possible to realize, for instance, by means of two different actuators, one with few µm travel range but faster settling time (<800 µs), that would take care of the P-component of the feedback, and a second actuator with wider travel range (e.g., a long-range motorized delay stage), that would take care of the slow I-component of the feedback. If the noise sources of a system, which needs to be locked, are known and are at least partly coherent, an active stabilization system with feedforward or predictive algorithms can be implemented, which can achieve a much higher damping ratio/bandwidth.

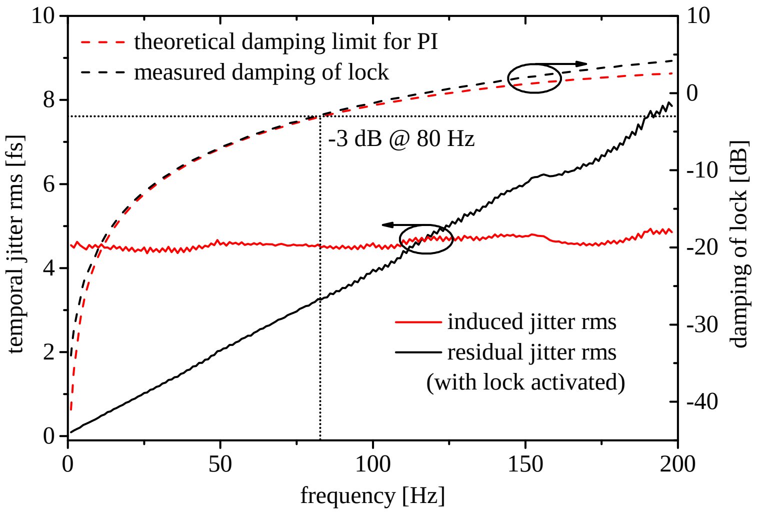

Figure 5.11: Characterization of the frequency response of the RAM setup with and without an active PI lock: a sinusoidal 13.3 fs (4.7 $\mathrm{fs_{rms}}$) peak-to-peak ATD is introduced with PZT1, while PZT2 is used in the feedback loop to lock the ATD. The frequency-dependent damping of such active locking exhibits a corner frequency of 80 Hz (−3 dB point), when optimized for high feedback bandwidth. The performance of the PI lock is compared with the theoretically achievable performance calculated considering a 0 dB proportional component and a latency of two laser pulses (2 ms).

5.1.6 Conclusions on RAM

In conclusion, we have proposed and experimentally demonstrated an ATD measurement and control method that exhibits a reproducibility of $<$ 80 as (integrated from 0.3 Hz to Nyquist) and allows to lock 150-fs long pulses with a residual integrated jitter of $<$ 400 as rms over a $>$ 400-fs range. The residual jitter is expected to scale to even lower values by employing shorter pulses [114, 115]. The simplicity, compactness and the high CMRR of the RAM scheme makes it especially suitable for implementation in parametric waveform synthesizers, where several ATD measurement devices are needed. The FPGA-based signal processing and active stabilization unit is a powerful tool that allows to perform all the signal processing required for sophisticated active stabilization in real-time and at the full repetition rate of kHz laser systems. Moreover, the possibility of synchronizing more than two pulses via a single RAM setup has been envisaged, a characteristic that could allow the final timing control of three (or more) channels of a parametric waveform synthesizer with a *single* and intrinsically drift-free device.

» End of citation from R. E. Mainz *et al.* in Optics Express [185] «

5.1.7 Triggered Gated Integrator with High Resolution

For the application in a BOC or RAM optical setup, balanced photo detectors need to be used. The balancing of the photo signals can be achieved by direct subtraction of the photo currents by connecting two photodiodes antiparallel or by balancing via an analog circuit based on operational amplifiers (see Fig. 5.12a). The direct balancing approach has the major disadvantage that the individual signals from the photodiodes are no longer accessible. Those signals are required to be read separately, to align the optical setup correctly and to ensure that the photodetectors are not driven in saturation. The analog subtraction via operational amplifiers (see Fig. 5.12b) is difficult to calibrate, because a mismatch in the temporal response of the analog circuits or parasitics within the operational amplifiers can cause additional distortions and nonlinear transfer functions.

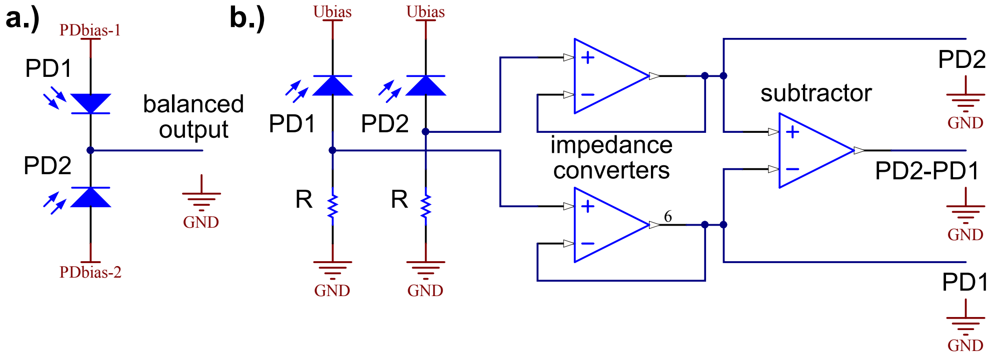

Figure 5.12: Commonly implemented schemes for balanced detection. **a.)** Direct balancing subtracts the charge Q by connecting two photo-diodes antiparallel. This leaves only the difference in charge at the output. **b.)** Operational amplifier based circuit with the option to measure also the individual signals via current-to-voltage converters and separate subtraction.

In general, a suitable readout scheme needs to be implemented to detect the optical intensities with low latency and high resolution. The commonly used technique for the measurement of low repetition-rate (Hz to kHz) ultrafast laser pulses is a sample-and-hold (SH) technique. This SH technique does not make use of the full signal and the hold signal is heavily influenced by timing jitter of the trigger signal with respect to the optical system. Another common technique for such pulsed photodetector signals are lock-in amplifiers. They also require a laser trigger signal but do not suffer from timing jitter. But in order to attenuate frequency components of the repetition rate and their higher harmonics, a low-pass filter needs to be used, which is usually set below $\sim$1/10th of the Nyquist frequency leading to significant loss of feedback bandwidth and introducing a high latency to the retrieved timing signal. The ideal way for kHz repetition-rate ultrafast pulses is to integrate the charge deposited on photodetector(s) in a time window around the arrival of the pulse. Due to the short nature of the laser pulses which translates to µs pulses in the electrical circuit, a majority of the detector noise, detector dark current and ambient light can be excluded if a rather narrow time-gate around the arrival of the laser pulse is used. For the repetitive measurement of pulses, the integrating circuit needs to be reset after each finished readout to prevent overflow/saturation of the electrical integrator (see Fig. 5.13a).

From previous experience it was already clear that a remote photo-detector inside an optical setup, whose signals are conventionally transmitted analogically via coaxial cables, will suffer significant distortions. Electro-magnetic interference (EMI), like coupled line-noise at 50 Hz, ground loops, etc. have a major impact on the signal integrity and signal-to-noise ratio (SNR). To overcome this common issue, one solution is to integrate a high resolution analog-to-digital converter (ADC) alongside the photo detectors and the integrating circuitry. A closed metal housing shields the system from any external interference and the digital data output allow to transport the signal without any degradation (see Fig. 5.14b). Furthermore following the good practice in data acquisition to always record the most raw and unprocessed signals with a measurement, the analog balancing (subtraction) was discarded in favor of recording the intensities of each photo diode separately, and leave any data processing to the noise free digital domain. With this demands in mind, a digitizing triggered gated integrator was designed and setup by the author (see Fig. 5.14a). The device is synchronized to the laser via a trigger input and features four independent photodetector channels. To accommodate large beam modes on the photo diodes and to avoid any focusing or pointing dependencies, large-area silicon PN-photo diodes are

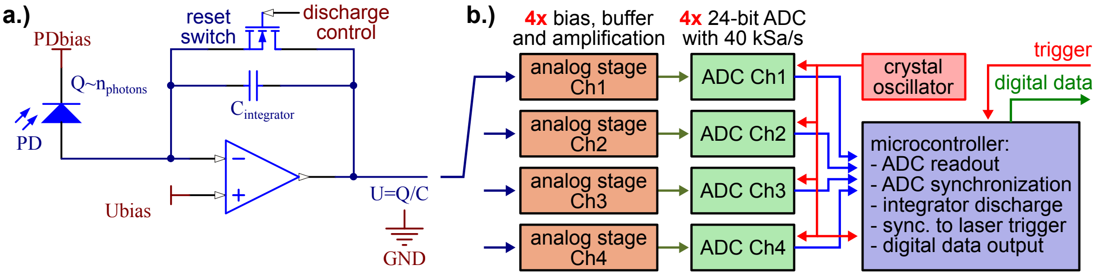

Figure 5.13: Signal-flow of the home-made integrating photodetector. **a.)** The charge Q deposited on the photo-diode is proportional to the number of photons n_{phot}. A high-impedance operational amplifier mirrors this charge into the integrating capacitor C. The low-impedance amplifier-output settles upon full integration of the charge into a voltage $U = Q_{PD}/C_{\text{int}}$. **b.)** An additional amplifier adjusts amplitude and offset to condition the signal further to feed to an analog-to-digital converter (ADC). The charge on the integrating capacitor is reset before every new measurement cycle. A microcontroller operates and synchronizes the system and send off the digitized data.

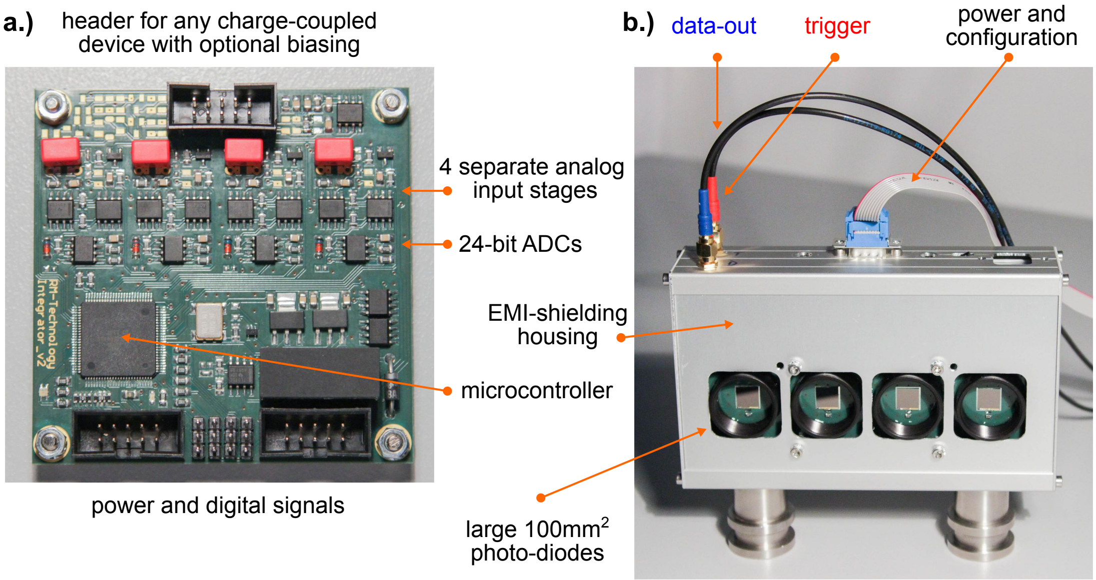

Figure 5.14: a.) PCB of the home-made gated integrators for pulsed photo-diode readout with 4 individual channels. **b.)** Full detector assembly in shielded enhousing for EMI suppression, four large-area photo diodes and digital-only input/output.

used (Silonex, SLCD-61N5, $A = 1\,cm^2$). The four integrated and digitized photo detector intensities are output as a fast serial data burst (UART, 4 Mbit/s) into a coax-cable. The core of the digitizing triggered gated-integration circuit is a microprocessor (Atmel, ATXMEGA128A1) which generates and synchronizes all required timing signals to the laser trigger. Four individual photo-detector channels feature each an operational amplifier with high-impedance JFET input (TL071, $R_i = 10^{12}\Omega$) which is used as integrator for the photo-diode signal with a feedback capacity of $C_{int} = 330\,pF$. The discharge switch in each channel is a small-signal MOSFET with a very low gate-to-source and gate-to-drain charge (BSS131, Q =2.1 nC). A second operational amplifier stage (TL071) in each channel acts as impedance transducer and adjusts the voltage offset and dynamic range to feed the signal to a 40 kSa/s analog-to-digital converter (ADC) with a resolution of 24 bits (TI, ADS1252). A reference voltage is supplied by a drift-compensated voltage reference (AD680) and a precise clock is provided by a crystal oscillator (16 MHz). A typical measurement cycle is shown in Fig. 5.15 with all relevant signals.

The center of the oscilloscope trace is $t = 0$ with respect to the laser trigger. The reset switch of the integrator is closed around +150 µs (green line) and released at −200 µs after all the charge on the integrating capacitor is eliminated. Upon release of the MOSFET-switch the gate-to-source charge deposits a small parasitic charge themselves on the integrator. Around −40 µs before the laser shot is impinging on the photo detector, the ADC records a 'dark'-sample (grey

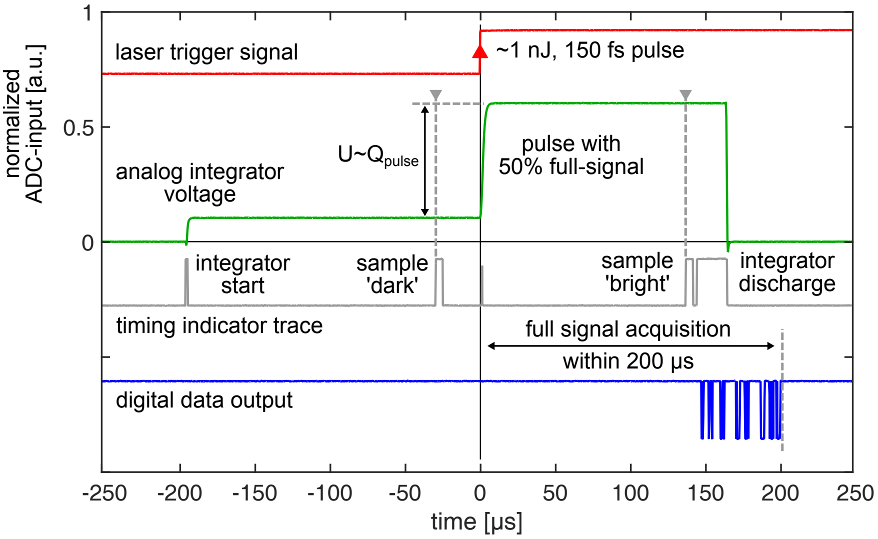

Figure 5.15: Full measurement cycle of the home-made photo-detector system. The plot shows the analog integrator-voltage (green), sampling-indicators of the ADC-acquisition (grey), and the digital output of the result (blue) with respect to the laser trigger (red).

marker). The integrating value (green line) is slowly increasing due to the dark-current of the photo diode and ambient light influences. At $t = 0$ the integrating signal exhibits a step which corresponds to the desired intensity of the laser pulse. Around +150 µs, after all the charge is integrated, another sample is taken with the ADC which is considered the 'bright'-sample. After digital subtraction of the two ADC-samples, an dark-current and ambient-light reduced measurement is achieved. The complete control of the system via a microprocessor allows to change the above mentioned timing parameters (e.g. reset and integration intervals) and to adapt the detector to various applications by loading new parameters/software into the device. Any photo diode can be used with this circuit and can also be biased with ±10 V or operated without bias potential.
In the current configuration with large area Si-photodetectors (sensitivity of 0.55 A/W at 940 nm) the detectors achieve a signal-to-noise ratio of 46000:1 (15.5 ENOB, full-scale) per detector. This corresponds to a resolution in absolute energy of 43 fJ with a dynamic range of 2 nJ. Such a performance allows to use the detector even with very weak BOC signals while not limiting the temporal resolution by detection noise. Any further data processing, such normalization or PI-feedback generation is then performed by the feedback unit (see Chapter 5.3.2).

5.2 Relative Phase/CEP Measurement and Stabilization

The relative phase between two pulses or the CEP of one pulse can be measured by (spectral) interference methods (see Chapter 2.7). A direct spectral beating can be observed if the involved laser pulses are coherent to each other and have overlapping spectral components. If this is not the case, a coherent spectral extension can be achieved by spectral broadening techniques, e.g. WLG in bulk or PCF generated white-light. The main difficulty of these phase measurements is the detection and processing of the optical signal. Especially OPAs, as secondary laser sources have elevated output beam parameter instabilities such as changes in the spectral intensity profile $I(\omega)$. Furthermore the spectral fringe frequency can vary due to intended changes in the synthesis parameters such as the relative envelope delay. An appropriate method for phase-retrieval in such an environment is the use of a photo-detector line-array to observe multiple fringes over some spectral bandwidth. A windowed Fourier-transform of the fringe pattern allows to retrieve the fringe phase and also track it over extended ranges (see Fig. 5.16). Unwrapping the phase $\phi \in [-\pi; \pi]$ of the frequency bin corresponding to the spectral fringe frequency yields a continuous phase. This unwrapped phase can be used as an error signal in an active stabilization scheme (e.g. PI-feedback) in order to drive an actuator within the optical system to affect the relative phase or the CEP correspondingly. The first implementation of this technique was realized for a relative phase lock between two channels of the synthesizer experiment and based on a commercial spectrometer and a PC running a MATLAB instance (see Chapter 3.4.2). This implementation rans with a high latency of 7 ms which drastically limited the feedback bandwidth. The latency is mainly accumulated by transferring data to the PC and the result back to an actuator. Furthermore,

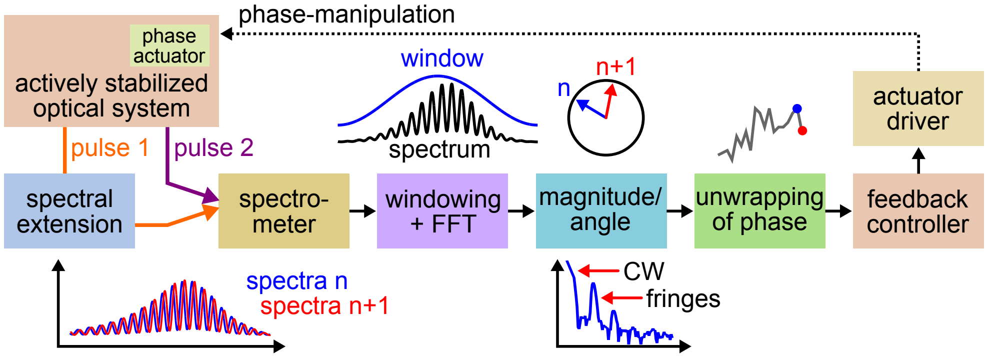

Figure 5.16: Signal path to process spectral fringes of two interfereing pulses to measure a phase parameter such as RP or CEP (via f-2f). Via a FFT and phase unwrapping an error signal can be fed to a feedback controller in order to actively stabilize a phase parameter.

commercial spectrometers are designed to measure the broadest possible spectral range (e.g. USB2000: 200-850 nm), which limits the data points per fringe period in typical measurements to just a few pixels of the photo-detector array and thus increases the phase noise of the retrieved phase. Also the commercial spectrometer could not be locked to the 1 kHz repetition rate of the laser and due to the data transfer to the PC, the fringe spectra of every second laser shot were missed. This circumstance raises a very crucial point in phase-retrieval methods; if the relative phase drifts more than π from one measurement to the next one, the unwrapping function will lose track of the actual phase (phase jumps). The chance of phase jumps increases drastically if laser shots are missed. When the control system loses track of the actual phase(s) within the synthesizer experiment, the feedback will lock to another synthesis point and hence the synthesized waveform will be completely different. For efficient and reliable active phase measurement and active stabilization, the following parameters require improvements on the spectral fringe detection and processing (see Tab. 5.1).

property	**commercial spectrometer**	**ideal spectrometer**
triggered by laser	no → loss of shots	yes, every-shot acquisition
integration time	$> 1\,\mathrm{ms} \rightarrow$ multiple shots	$< 10\,\mu\mathrm{s}$, single-shot
resolution	broadband operation	narrowband (50 to 200 nm)
spectral range	fixed	adjustable
entrance slit	optimized for resolution	optimized for sensitivity
phase retrieval	external calculation (PC)	real-time system
latency	7 ms round-trip time	$< 1\,\mathrm{ms}$, ideally $< 300\,\mu\mathrm{s}$

Table 5.1: Comparison of the used commercial spectrometer and an ideal spectrometer for fringe detection and phase-retrieval. As commercial spectrometer, the specifications of the Ocean Optics USB2000 are listed.

5.2.1 Single-shot FPGA-based Spectrometer for low-latency Phase Retrieval

There is no commercial spectrometer available to realize the experimental demands states in Tab. 5.1 for phase-retrieval in the synthesizer experiment. As the retrieved phase should be an error signal within a complex active stabilization system, a low-latency processing is strictly required, alongside an every-shot operation which needs to be triggered by the laser system. This task includes readout of a photo-detector line-array at the repetition rate of the laser (1 kHz) and high-speed computation of an FFT which can only be realized by dedicated electronics.

There are also special demands on the optical part of the spectrometer, which requires a custom-made system (see Fig. 5.17). The implemented spectrometer is a straight forward Czerny-Turner configuration with an entrance-slit in the focal plane of a concave mirror (1 inch, f=5 cm) to let parallel beams diffract on a blazed grating (e.g. Thorlabs, GR25-1205, 1200 lines/mm). A second concave mirror (2 inch, f=100 mm) images the Fourier domain to a plane on the photo-detector array. The components and geometry of the optical spectrometer can be altered to deliver an adjustable spectral bandwidth with tunable center wavelength. This allows to match the rather narrow-band nature of spectral fringe beatings, which are usually at 50-200 nm of bandwidth to be imaged at the center of a photo detector line-array.

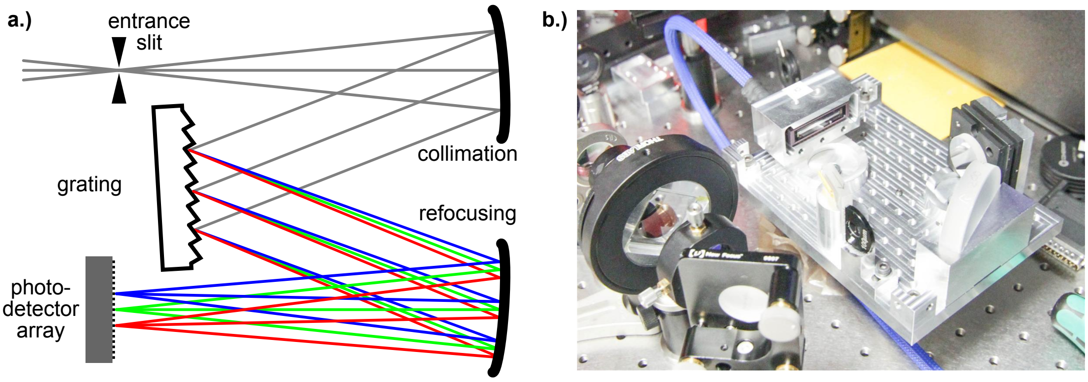

Figure 5.17: a.) Scheme of a Czerny-Turner-type spectrometer. **b.)** Picture of the home-made implementation optimized with wide entrance-slit and low, adjustable spectral range (∼100 nm) for spectral fringe measurements.

As line-array detector a common purpose silicon-based detector with 1024 pixels was selected (Hamamatsu, S10453, see Fig. 5.18b). The detector provides a simple interface for data readout. The integration time is controlled via the ST-pin and can be as low as 10 µs [189]. After integration the sensor readout takes about 103 µs with a pixel clock (CLK) of 10 MHz (see Fig. 5.18a). The sensor outputs the data of the photo-detector array in a serial fashion in form of an analog voltage at the VIDEO-pin. A printed circuit board (PCB) was designed and built by the author to digitize this frame-data with high resolution (see Fig. 5.19). The analog output range is matched by a operational amplifier with differential output (Analog Devices, AD8139) to be fed into a 80 MS/s, 16-bit analog-to-digital converter (TI, ADS5562). Due to the strict timing requirements and the high frequencies involved in the readout procedure, a field-programmable-gate-array (FPGA) need to be used (see Fig. 5.19). The FPGA is an Altera EP4CE10E22C8 common purpose FPGA which is configured using an onboard flash memory (Altera, EPCS4SI8N) after power-up. The FPGA configuration is synthesized using Very High Speed Hardware Description Language (VHDL) after all sub-systems were verified for correct logical operation and timing performance via Tool-command language (Tcl). The FPGA derives all required control signals synchronized to the laser trigger and buffers the digitized CCD-

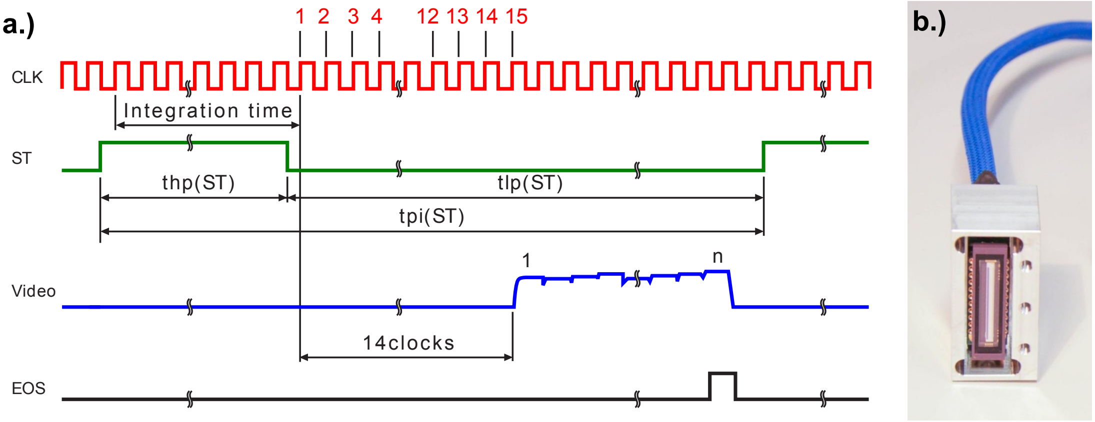

Figure 5.18: a.) Timing diagram of the Hamamatsu S10453 photo-detector array with clock (CLK), integration/readout control (ST) and the analog video output. Adapted from [189]. **b.)** Front-view of the photo-sensor in an aluminum housing and attached video cable to the processing unit. (blue).

frame into internal M9K Block-RAM. The sensor is set to only integrate a narrow time-window around the arrival of the laser pulse. Around 110 µs after the laser pulse impinged on the sensor, the readout is finished and the data is available for processing within the FPGA. From here the acquired sensor data takes two separate paths of processing.

The first data path multiplies a window function (e.g. Hanning) onto the detector frame and feed it into a 1024-point FFT-implementation in the FPGA (see Fig. 5.20). The computation of a N-point FFT takes $N \cdot log_2(N) = 10240$ computations for the 1024 pixel spectra and is finished 300 µs after the pulse hit the detector. The FFT-computation involves a bit-reversal and so-called butterfly calculations which includes complex multiplications and sine/cosine lookup tables. The internal computation is implemented using 48-bit broad signed integers to prevent overflow during the multistage multiply-accumulate of 16-bit broad input-variables in the FFT-algorithm. An efficient arctan and logarithmic function (log_2) is implemented to calculate the phases and logarithmic magnitudes from the complex result of the FFT. Two phase values from the result can be selected and are send digitally to the active stabilization unit via a coax-cable for feedback signal generation (see Chapter 5.3). The retrieved phase noise for signals which fills around one tenth of the dynamic range of the sensor was characterized to be on the order of 300 µrad which includes noise from the photodetector, the digitization noise from the ADC, quantization noise of the used integer numbers and noise introduced due to the use of many approximations along the computation.

The first data path, as described above allows for low-latency phase retrieval to perform active stabilization of the fringe phase. Another path of data is required to log the raw data and allow to perform enhanced analysis in post-processing

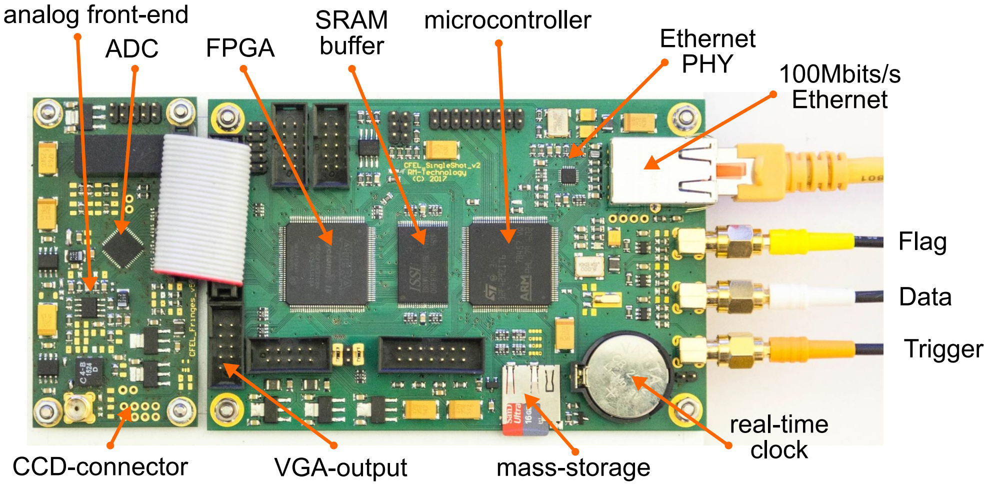

Figure 5.19: Main PCB for the developed spectral fringe spectrometer featuring the analog front-end, the FPGA for FFT-calculation, an SRAM data buffer and a microcontroller. An Ethernet interface together with an embedded FTP-server allows for single-shot and every-shot data streaming to a computer. Furthermore the selected fringe phase (data) is send via a coax-cable to the feedback unit.

to understand the behavior of the optical system under test. A data rate of 16 Mbit/s (1 kHz · 1024 pixel · 16 bit/pixel) is necessary to transfer the raw-data to a computer, this requires a high-bandwidth interface. There are two common options, a USB-link and an Ethernet-link. Both links are very difficult to implement in an FPGA due to their complex protocol structure. Usually a programmable system like a microprocessor is used to implement such complex communication protocols. Ethernet was favored over USB because Ethernet does not require dedicated drivers on the PC, it has been an open standard for decades, it is easily scalable (e.g. the Internet) and well documented (IETF RTCs). A high-performance microcontroller (ST Electronics, STM32F429ZIT) was selected to provide a data bridge between the FPGA and the PC via Ethernet (see Fig. 5.19). The microcontroller is programmed using C, compiled with GNU-gcc and the resulting hex-file is uploaded to the internal FLASH memory and executed after reset or power-up. The microcontroller already contains an Ethernet media-access controller (ETH-MAC) to interface to a physical layer interface chip (ETH-PHY, Microchip, LAN8720A) via the reduced-media-interface (RMII) providing a 100 Mbit/s Ethernet port. Within the microcontroller a TCP/IP-stack is implemented to perform standard connectivity to any computer. The spectrometer device is configured automatically by a control computer after connection via an implemented DHCP-client and an NTP-based time-synchronization protocol. It pulls automatically an IP-address from the network and associates a domain name (e.g. 'ss0.syn'). The internal clock is synchronized via the NT-protocol to tag the data with a correct timestamp. A TELNET-server in the microcontroller

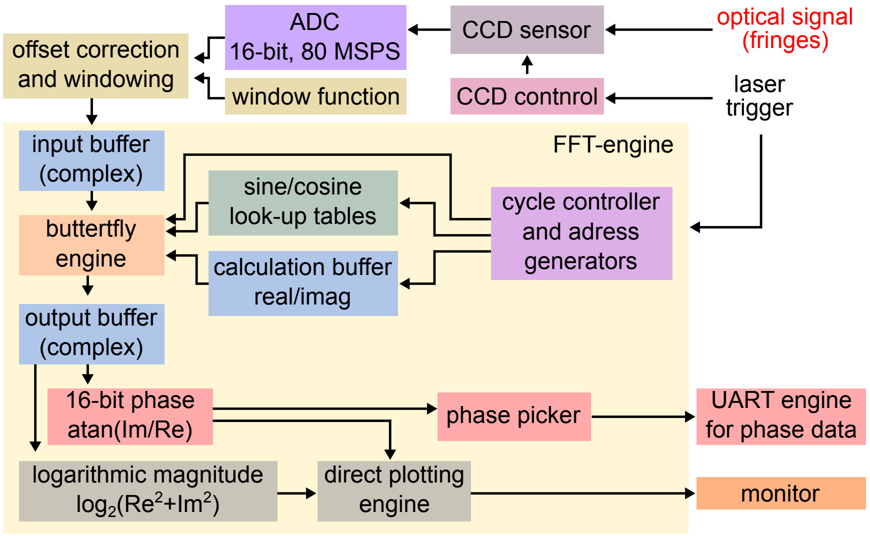

Figure 5.20: Scheme of the dataflow within the FPGA-based single-shot spectrometer. The digitized sensor signal is windowed and offset corrected before it enters the FFT-engine. The complex output of the FFT is transformed into polar coordinates and logarithmic magnitude. The selected fringe phase is send off digitally 300 µs after the pulse illuminated the detector.

allows to set and review basic parameters through console commands via a standard TELNET-port and synchronizes the parameters with the FPGA. For more automated and more complex configurations of the device, a raw TCP interface was implemented, which allows to read/write every parameter from within any programming environment (e.g. MATLAB, Python, C, etc.). For the data transfer of the raw spectra a File-Transfer-Protocol-based server (FTP-server) was implemented in the microcontroller as well. This allows to reliably stream data to the PC with a standalone program (e.g. FileZilla FTP-client) or any FTP-implementation in any programming environment.
Ethernet is per definition a not reliable and a time-asynchronous link, this includes drop of data packets, arrival of the packets in out-of-order and other distortions during transmission. To overcome this possible distortions, the TCP-protocol was already defined in the early days of the Internet. Dropped or corrupted data packets are detected by the protocol and are retransmitted by the sender until they are properly acknowledged by the receiver. This drops or short interruptions of the data transmission requires to buffer a certain amount of data within the sender until they are properly transmitted. A 32 Mbit static-RAM (ISSI, IS61WV102416ALL) is used to keep the raw data of the last 1000 acquired spectra ($\sim$ 1 s buffer at 1 kHz) within the device for possible retransmission (see Fig. 5.19). Drops in data transmission are very unlikely to be more than a fraction of this.
To provide a responsive and intuitive user interface, a graphic output is also gen-

erated within the FPGA to drive a regular PC-screen via a VGA-interface (see Fig. 5.21). This built-in feature of the spectrometer plots the raw spectrogram, the logarithmic magnitudes and phases of the FFT-computation in real time. The temporal evolutions of the two selected fringe phases, which are send off digitally to the feedback unit, are shown alongside all internal parameters. This custom-made spectrometer-system proves a crucial tool to intuitively understand the optical system under test and to perform advanced measurements and active stabilization. The electronic platform developed by the author is an integral part of the timing infrastructure of the synthesizer experiment due to its unique capabilities and its high customizability. An emphasis was put to only transmit data digitally from one device to another to avoid signal degradation and ground loops. Because the devices are integrated into an Ethernet network, they can be controlled from every computer at the experiment but the integrated plotting also allows complete standalone operation. The data acquisition has proven very reliable and was used in almost all performed measurements with the synthesizer.

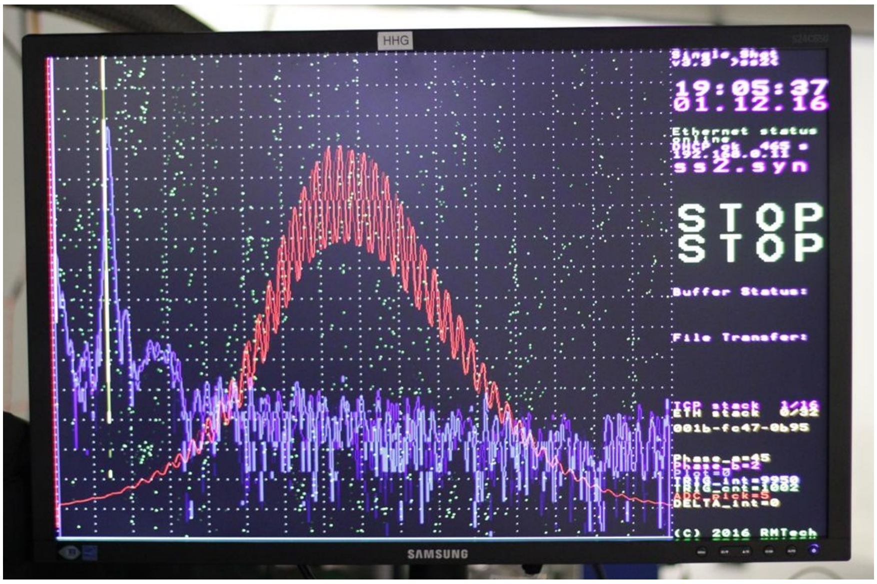

Figure 5.21: Picture of a PC screen showing the FPGA generated real-time plotting of the spectrum (red), the magnitude of its Fourier transformation (blue) and the corresponding spectral phases (green dots). Furthermore the current status of acquisition and internal parameters are displayed (right side).

5.2.2 Extension to an InGaAs-detector for NIR/IR-sensitivity

The implemented sensor for the single-shot spectrometer is an easy-to-use silicon based detector. Due to the silicon bandgap, only photons below 1.1 µm can be detected. To extend the range for experiments and locking applications to the NIR and IR, an InGaAs-based detector needs to be used. The InGaAs-based detector allows to detect photons up to a wavelength of 2.55 µm. A line array sensor based on this semiconductor material is the Hamamatsu G9208-256W with 256 pixels [190]. Those sensors are more expensive and more complicated to operate compared to silicon-based ones. The low bandgap requires cooling of the sensor to at least to $-10°C$ to prevent thermal photons from increasing the noise floor of the sensor significantly. The chosen InGaAs-sensor already includes a two-stage thermo-electric cooler (TEC) and a temperature sensor. To operate this sensor, a separate temperature control circuit is implemented directly at the back of the sensor (see Fig. 5.22a). The sensor-controller is controlled by the main spectrometer system to set the cooling temperature as well as modifying advanced detector settings, which e.g. increases the sensitivity 20-fold [190]. The heat generated from the TEC at the back of the detector is passively removed by use of heat-pipes and cooling ribs.

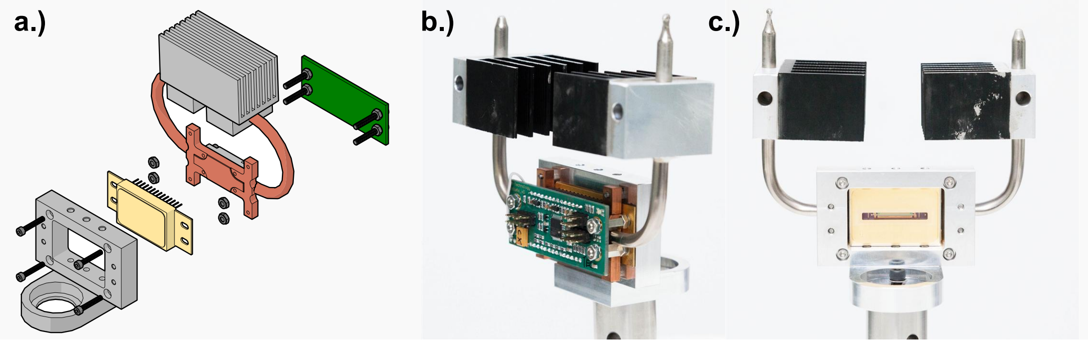

Figure 5.22: **a.)** CAD-explosion of the InGaAs-sensor assembly. The copper back-plate and the heat-pipe transport the heat generated between the backside of the sensor (yellow) and the sensor control-circuit (green). **b.)** Picture of the back-side of the sensor showing the sensor control-ciruit and the video-output pins. **c.)** Front-view with its 256-pixels 1-inch by 250 µm wide photo-detector array.

Another peculiarity is the sensors unevenness of the sensitivity and dark current for each pixel. The absence of techniques like pixel-shifting in InGaAs requires that every pixel has his own charge integrating circuit. Manufacturing imperfections lead to varying offset-currents and sensitivities for each photodiode/integrator (see Fig. 5.23). This poses a special problem to the FPGA-based phase retrieval, because the random inhomogeneity pattern on the sensor increases the noise floor of the phase measurement. To compensate, the offset needs to be subtracted and then the sensitivity needs to be uniformized. For that a calibration measurement at a given sensor temperature is required within the FPGA signal processing. With this sensor, a complementary sensor in the NIR/IR is implemented and was e.g. used in the NIR white-light phase noise measurement (see Chapter 4.4.2).

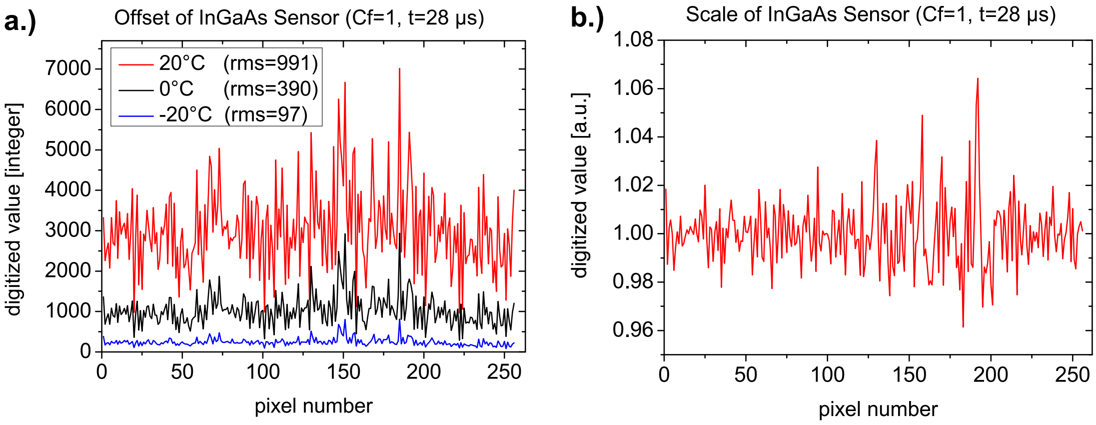

Figure 5.23: Characterization of the InGaAs-detector: **a.)** Measured dark current and offset signal of the InGaAs-sensor array for different sensor temperatures. The -40 K TEC-based cooling achieves a significant reduction of the dark-current offset. **b.)** Measurement of the inhomogeniety of the sensor sensitivity. Deviations from up to 6% occur and require to normalize each measured frame with this sensitivity function.

5.2.3 Multi-Spectrometer Synchronization

The modular design of the spectrometer as well as the decision to use Ethernet as transport medium for streaming the data to a computer turns out to have another advantage, which is its scalability. Commonly in an experiment involving the waveform synthesizer, several phase-observables need to be measured using multiple spectrometers. To compare measurements of different observables to each other, two requirements need to be fulfilled: One is the single- and every-shot capability and the other is synchronization of the involved spectrometer data. The trigger-signal is used to synchronize an internal unique identifier (ID) in the spectrometer network. This ID is added to every data frame alongside the spectra, in the following the data traces can be synchronized in data post-processing and analysis. This allows to perform shot-to-shot coherent analysis of the relation between the different measured spectra of the optical system under test.

5.2.4 Online Data Analysis and User Interface

The spectra at each spectrometer can be directly observed in real time at the graphics output of the FPGA, or with a latency of around 50-200 ms also at the screen of a recording computer (see Fig. 5.24). A stand-alone executable file (.exe) is compiled from a MATLAB-based graphical user interface (GUI, MATLAB GUIDE) based on a MATLAB script using the MATLAB Application Compiler. This standalone GUI-program can be executed multiple times, each occupying one CPU core (→ multi-core scaling). Each GUI can be used to observe any spectrometer data currently recording and can perform complex and custom online data-analysis. This includes e.g. information on the evolution of the rms phase noise over time or the spectral-fringe contrast. Such secondary observables are helpful to align the optical system under test also with respect to achieve a low phase-noise performance.

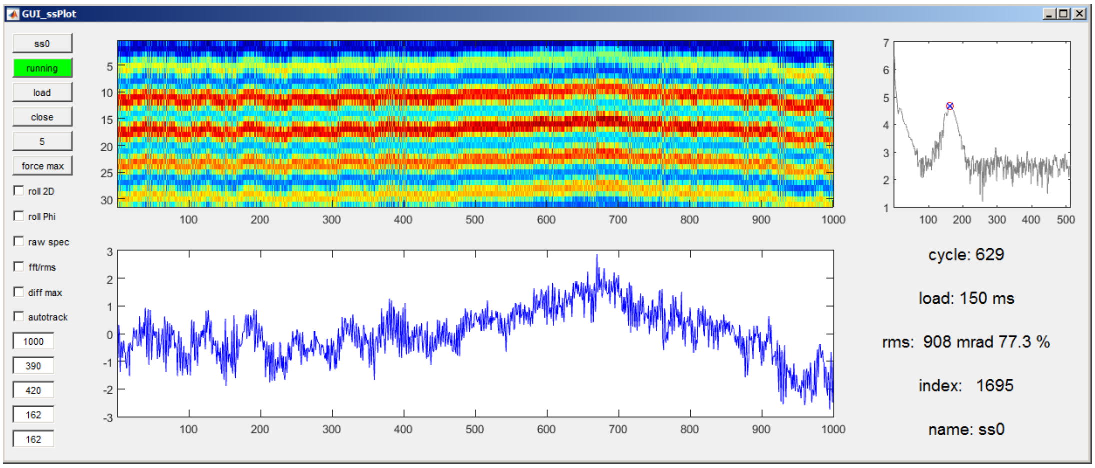

cycle: 629

load: 150 ms

rms: 908 mrad 77.3 %

index: 1695

name: ss0

Figure 5.24: Screenshot of the standalone-GUI for the single-shot spectrometer streaming data of spectral fringes from the CEP measurement within the CEP-stable seeding front-end. The GUI also offers secondary data analysis such as the rms of the phase-noise, its long-term temporal evolution and can track the current fringe frequency autonomously.

5.3 Timing Infrastructure for a Parallel Synthesizer

The parallel implementation of the optical parametric waveform synthesizer is a complex and nonlinear multi-path interferometer. Every OPA stage within the system needs to have a temporal overlap between the pump and seed pulses. Even more challenging is the synchronization between the outputs of the individual amplifying channels with respect to relative envelope timing and relative phase. Beam paths over several meters need to be stabilized to a fraction of their output wavelengths which should be synthesized. In this case a few tens of nanometer are the maximum allowed fluctuation in beam path length. A high level of passive stability is strictly required, but not sufficient. A complex system of sensors and actuators need to be implemented to allow for active stabilization techniques as well as control on the synthesized waveform.

In previous works, it was expected to obtain a stable waveform output by locking the relative arrival time between two OPA channel outputs using a timing tool, such as a BOC. In these schemes it was assumed that the passive CEP stability of the seeding front-end is sufficient for a relative and CE-phase stability at the synthesis point. Neither the actual synthesized waveform nor its CEP or the relative phases/relative envelope timing between the channels were characterized by earlier studies at the same time [114, 115, 134, 136, 137]. Initial experiments on our synthesizer (see Chapter 3.4.3) indicated that besides the relative envelope timing between the spectral channels outputs, also the relative phase and CEP(s) need to be observed and actively controlled. The shape of the synthesized pulse depends heavily upon its relative timing characteristics between the amplified pulses as well as the pump and seed envelopes during the successive amplification in multiple OPA-stages.

One of the core challenges of the synthesizer experiment resides in an active stabilization system, which features a network of sensors and actuators to measure and control several timing parameters without uprising of a chaotic oscillation between the different control loops. This network of sensors and actuators should measure and manipulate a full set of parameters to fully stabilize and control the waveform. For a proper decoupling of a full set of observables an orthogonalization needs to be performed to actively stabilize and control the individual observables. Similarly the locations for measuring and actuation should be chosen in order to fully exploit the intrinsic dynamics of the optical setup while keeping the number of sensors and actuators to the bare minimum.

5.3.1 Optimized Feedback Scheme for Parallel Synthesis

The synthesizer experiment is a complex interferometer affected by thermal drifts, technical noise and nonlinear couplings. A CEP-stable and CEP-controlled seed is required for seeding of the amplifying modules. Furthermore in principle every OPA stage within the amplifier modules would require a pump-seed delay measurement and active stabilization thereof. This would mean already 9 BOC devices and 9 driven delay lines within the amplifier modules of the three spectral channels. Further loops would be required to correct for relative-phase drifts between the output of the different spectral channels. Such a system would be too complex to implement and therefore cannot reach a stable point of operation. Any active control introduces noise into the optical system due to the measurement noise of the observable as well as imperfections within the corresponding actuator (e.g. nonlinear response, pointing). Based on the initial experiments (see Chapter 3.4) and a careful reconsideration of the overall required timing control, a new feedback system needs to be developed with the following constraints:

- control of a full set of parameters to fully determine the synthesized waveform
- lowest possible number of measurement devices and actuators
- observables need to be sampled at a representative point and measured with a low-noise technique
- fast actuators placed in locations where mainly one observable is modulated
- centralized control system to allow for feedback decoupling (orthogonalization)

The central idea when designing the new timing infrastructure of the synthesizer was to keep the complexity as low as possible without sacrificing the degree of control required to create and maintain a stable waveform. A good starting point for a stable synthesis is to increase the passive stability of the optical setup to the highest level possible (see Chapter 6.1). Especially because feedbacks have only limited noise canceling efficiency at medium repetition-rate driven optical systems. A system sampled at 1 kHz can only be actively controlled with significant noise attenuation up to 100-200 Hz.

Another very crucial point is raised by the initial experiments (see Chapter 3.4) and the study of CEP dependence upon pump-seed synchronization (see Chapter 4.2). An actuation, e.g. with a piezo-driven delay line within the optical system is likely to not only modulate one observable but also others. A group of independent feedback loops would inevitably start to oscillate with each other due to couplings between them. A method to avoid such a behavior is well known in linear algebra as orthogonalization, where a new set of orthogonal vectors are determined such that they span a particular subspace. Starting from a linearly independent set of vectors $\vec{v}_1 \ldots \vec{v}_k$ in an inner product space, orthogonalization results in a set of orthogonal vectors $\vec{u}_1 \ldots \vec{u}_k$ that generate the same subspace as the vectors $\vec{v}_n$. The new set of vectors $\vec{u}_n$ are orthogonal to each other and have the same linear span as the initial vectors. Such techniques require a centralistic control unit which collects all the measured observables within the optical system, compares them with the corresponding set-points and distributes orthogonalized feedback to the actuators in the optical system.

Initially Dr. G. Cirmi proposed to actuate the pump-seed delay as feedback for the BOC measurement to leave the relative phase mainly unaffected. In the following, the new timing scheme was decisively invented by the author and G. M. Rossi with contributions from Dr. G. Cirmi and other colleagues. It was realized that this novel timing infrastructure was the first full scheme to allow stable waveforms from parallel parametric waveform synthesizers. The scheme was generalized and applied for patents in the EU and the USA [191, 192] and can be seen in Fig. 5.25. The Ti:Sa pump laser system delivers two outputs, one of which is compressed and carries 5 mJ of energy, the other carries 15 mJ and can be propagated till the point of use, where an external compressor (Coherent) compresses these pulses. From the compressed beam of the laser the CEP-stable

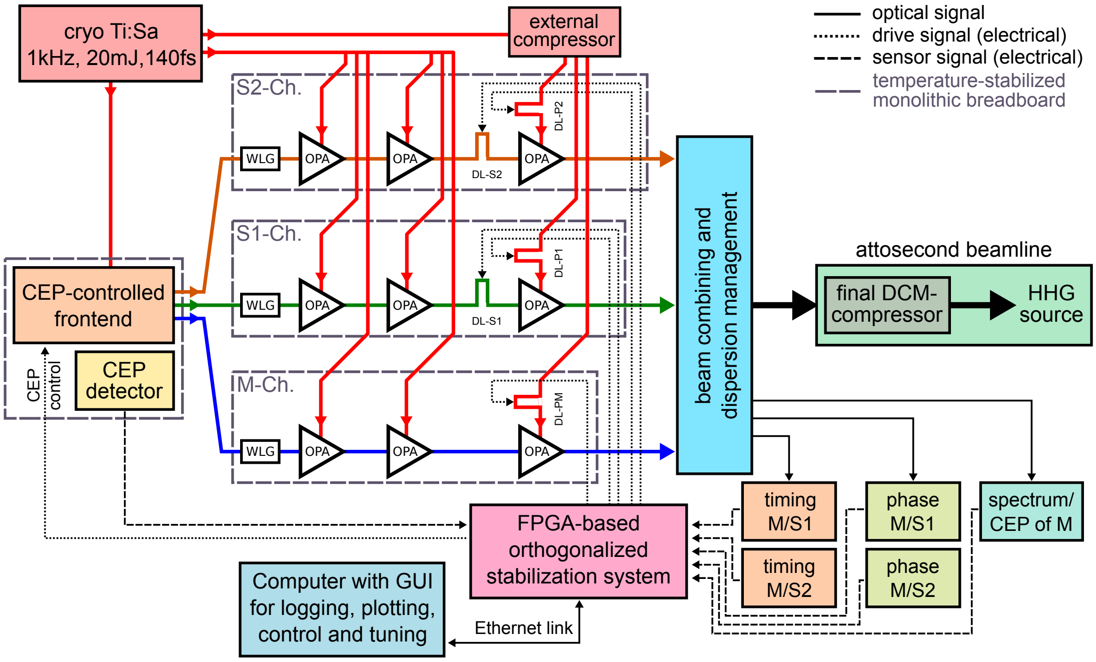

Figure 5.25: Scheme of the Synthesizer with an emphasis on the network of sensors and actuators for active stabilization and control of the synthesized waveform. The passively CEP-stable seeding front-end contains an active CEP control (CEP detector and actuator). One amplifying channel is defined as master channel (M-Ch.) and the relative phase and relative envelope is measured relative to the slave channel (S1/S2). The timing sensors are fed with a few % leakage of the beam combination optics. The relative envelope timing is actuated by a piezo-driven delay line (DL-Px) on the last-stage pump. The relative phase is manipulated by a delay line on the signal-beam path before the last amplification stage (DL-Sx). A centralistic control system performs orthogonalization in order to decouple the individual stabilization loops.

seeding front-end pump is derived as well as the pump for the first two amplification stages in all spectral channels. Because a chirped pulse amplification with 150 fs long pulses (corresponds to $50\,\mu$m in space) is performed within the OPAs the pump-seed overlap in this stages relies on passive stability only and is sufficiently stable. The other laser output is compressed close to the 3rd amplification stages to avoid nonlinearities during the long beam transport. The external compressor will transfer pointing instabilities partly into arrival-timing fluctuations, which need to be compensated for.

Beside the active CEP-stabilization in the seeding front-end (see Chapter 4.1), all other timing parameters are measured at the point of beam combination by using an intentionally designed leakage in the custom designed dichroic combining mirrors. At this point the individual outputs are collinearly combined and therefore can no longer experience any interferometric instabilities. The measured timing parameters are therefore a most representative copy of the parameters at the synthesis point. One spectral channel should be defined as *master channel* and the relative phase and envelope timing of each *slave channel* is referenced to that master. The CEP of the master-channel itself needs to be fixed absolutely by means of a CEP measurement or by other spectral characteristics.

The actuation scheme is changed significantly compared to the original proposed timing scheme (see Chapter 3.1.5). The relative envelope delay of the slave-channel(s) output is adjusted by moving the pump-arrival time at the last OPA-stage in each spectral channel. The high gain of an OPA results in the fact that a majority of the output pulse energy of the signal is supplied in the last amplification stage (*booster stage*). The output envelope is therefore predominantly defined by the arrival-time of the last-stage pump pulse. This type of actuation affects predominantly the relative envelope arrival time but also affects the CEP and relative phase slightly (see Chapter 6.4.2). A 20 µm-range piezo-driven actuator is used (Physik Instrumente, 753.1CD), because the externally compressed pump can drift some ten femtoseconds in time with respect to the signal pulses.

A manipulation of the relative phase is achieved by introducing a 3 µm-range delay line in the signal path (Noliac, NAC2125-A01, see Fig. 3.21 on page 54). Such a delay line is positioned before the booster-stage in the slave channels. In that position, the signal is already at medium pulse energies and is not focused hard into the next OPA stage, otherwise possible pointing introduced by the actuator might affect the spatial pump-seed overlap significantly. The beam is also not at too high energies, such that a large-diameter mirror would be required and might slow down the actuation due to its higher mass. This actuator allows to manipulate predominantly the relative phase but also affects the relative envelope timing and CEP slightly.

All measured timing parameters are fed to a centralistic control unit. This unit is required to generate a complex set of correction signals based on multiple input timing parameters. Furthermore an easy control of the state of the active stabilization system is required to perform secondary functionality such as system tuning procedures or the final waveform control of the synthesized output.

5.3.2 FPGA-based Feedback System

The requirement to generate orthogonalized feedback upon multiple inputs of the various timing measurements with the lowest possible latency demands a dedicated computation unit. An FPGA is well suited for this task and allows for low-latency feedback generation. The ultimate goal is to correct and control the path lengths within the setup based on the measurement of one pulse before the next pulse propagates through the system.

Another important aspect of such a control unit is that all the inputs and outputs need to be recorded on a single-shot and every-shot basis to understand the system-behavior, to judge the performance of the active stabilization and to synchronize or tag the data recorded in an experiment using the synthesized pulses.

Hardware

The field-proven hardware and associated software-tools developed by the author for the single-shot spectrometer already set a good basis for an orthogonalized feedback unit (see Chapter 5.2.1). The computation of the feedback will be performed within the FPGA, but it is crucial to have a well-established channel for transferring data from the FPGA to the computer for tuning, logging and system analysis. Also the other data-flow direction from a User-Interface on the computer to the FPGA states a difficult technical challenge. Such a bidirectional interface is needed to control the synthesizer manually or by a routine. Furthermore a standalone and homogeneous set of devices for the timing system is desirable to allow for fast customizations and uninterrupted operation. The developed control unit for the feedback fits seamless into the existing infrastructure and allows to get triggered by the laser system and to be synchronized to all other home-made measuring devices.

Aside from the completely different configuration in the FPGA, the main hardware modification was the addition of an 8-channel digital-to-analog converter (DAC) to output the corrections signals from the FPGA as analogue voltages to drive the different piezo-actuator systems. This DAC-unit is based on a DAC with 16-bit resolution (TI, DAC8568) and less than 10 µs setting time. A precise voltage reference (AD680) and a low linearity error of <4 LSB (least-significant-bits) allows for linear digital-to-analog conversion. The 8 DAC-outputs are buffered by operational amplifiers, scaled to a range from -10 V to +10 V and output via SMA-terminals (see Fig. 5.26). An increment of the 16-bit wide DAC-value results in a voltage step of 300 µV with an output noise of 1 mV_{rms} at the terminals. This FPGA system also features real-time plotting in standalone operation as the single-shot spectrometers have (see Fig. 5.21 on page 109).

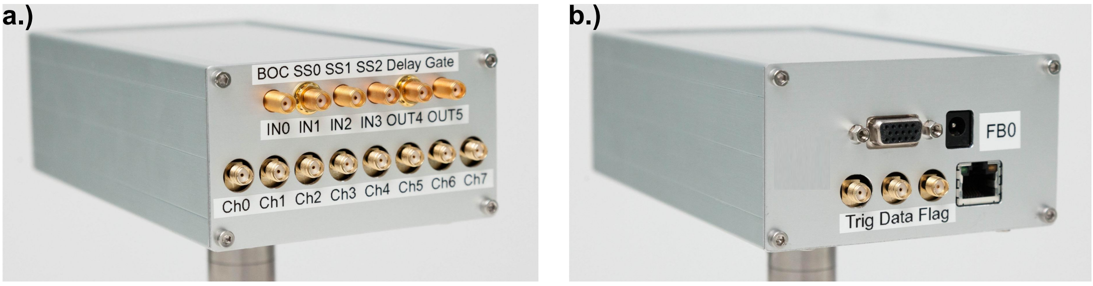

Figure 5.26: Picture of the active feedback unit: **a.)** with digital inputs/output for the digitized measurement data and trigger signals (top). And analog outputs to drive the different PZT-driven actuators within the optical system (bottom). **b.)** Power-inlet, Ethernet network interface and real-time plotting VGA-output of the feedback system

Feedback Generation

The demands on a feedback unit is to accept several input signals and perform a feedback generation with orthogonalization to generate multiple output signals to drive the system actuators. All computations in this feedback unit should be performed directly after all input signals are present and within the shortest time possible. This can be realized in an FPGA to generate low latency correction signals, which in the best case already moved all actuators to a new position before the next laser pulse passes the optical system.

The input signals either come from individual photodetectors, e.g. in an optical BOC configuration (see Chapter 5.1), from the FPGA-based spectral fringe spectrometer (see Chapter 5.2.1). In both cases the input signals arrive already digitized to prevent any distortion during transmission, but they need to undergo further preprocessing. The fringe spectrometer delivers a 16-bit-wide value representing a phase-value within $-\pi$ to π. This phase needs to be unwrapped first to a continuous value. The digitizing photodetector delivers up to 24-bit of intensity information from each of the four photo-detectors. In a BOC configuration subtraction or favorably normalized subtraction need to be performed (see Eq. 5.9 on page 89).

These processed input signals $y(t)$ need to be compared to the set points $r(t)$ and the resulting regulation deviation (error) $e(t)$ need to be converted into a correction signal $u(t)$ applied to the actuators (see Fig. 5.27). Aside from the transfer function of the loop-controller $K(s)$ also the actuator transfer function $G_{\text{act}}(s)$ and the plant transfer function $G_{\text{plant}}(s)$ (optical system) need to be considered. Most of the loop components can be assumed to have a flat transfer-function $G = 1/s$, additional latency is added by the measurements, the feedback calculation and the PZT displacement, upon that, the loop controller needs to be optimized. Those transfer functions K and G can easily be multiplied in the Laplace transformation s and modeled in MATLAB. There are many ways to

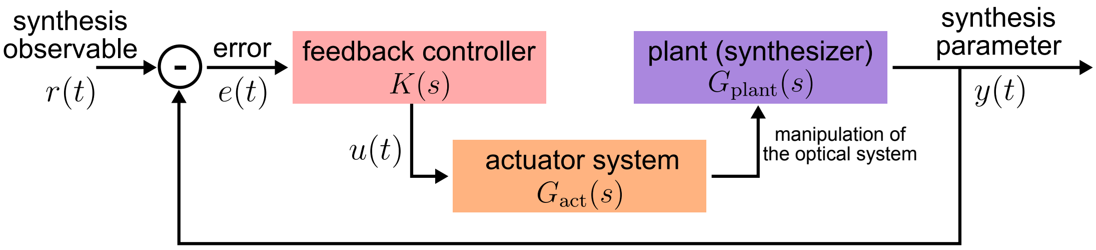

Figure 5.27: Scheme of the feedback loop with transfer functions for the feedback controller, the actuator and the optical system.

implement a loop controller. The easiest to compute and most common one is the proportional-integral-differential (PID) controller with:

$$\begin{aligned} e(t) &= r(t) - y(t) \\ u(t) &= \underbrace{K_P \cdot e(t)}_{\text{P}} + \underbrace{K_I \int e(\tau) \cdot d\tau}_{\text{I}} + \underbrace{K_D \cdot \frac{de(t)}{dt}}_{\text{D}} \end{aligned}$$

This feedback controller requires only basic computations and no direct knowledge about the transfer characteristic of the system/the actuators and its distortions. The PID method is chosen due to its stability and low latency while still offering some flexibility to shape the spectral response. The furthermore required orthogonalization can be performed by multiplying the feedback signal vector $u(\vec{t}, n)$ with the transfer matrix to yield an orthogonalized output vector. The transfer-matrix can be retrieved by a principle axis transformation to find an orthogonal eigenbasis. In practice, the matrix can be found by a tuning procedure where an introduced sinusoid is attenuated in secondary observables by coupling different actuators with variable strength to that modulation of the primary observable under test. These coupling values then give one row/column of the orthogonalized matrix.

Filters in the feedback loop were also tested to optimize the quality of the feedback. Unfortunately the fundamentally low phase margin between detection bandwidth (500 Hz) due to the medium repetition rate of the laser (1 kHz) and the latency of at least one laser shot makes any filter within the feedback loop very ineffective at the laser repetition rate (see Fig. 5.28b). But finite-impulse response filters (FIR-filter, [193]) can be implemented to shape the spectrum of the step response of the PZT-actuators from quantized 1 kHz feedback calculation updates. These FIR-filer can be modified by the *cepstrum*-method [194] to decompose the filter into low latency causal and anti-causal halves [195, 196]. Drifts and slow vibrations can easily be actively stabilized (see Fig. 5.28a) but already technical noise like the natural vibration modes of standard optics mounts around 200-300 Hz can hardly be attenuated or might even be amplified. An FIR-filter for shaping the DAC-output of the feedback system on the contrary allows to prevent exciting resonances of the piezo-actuator beyond 1 kHz.

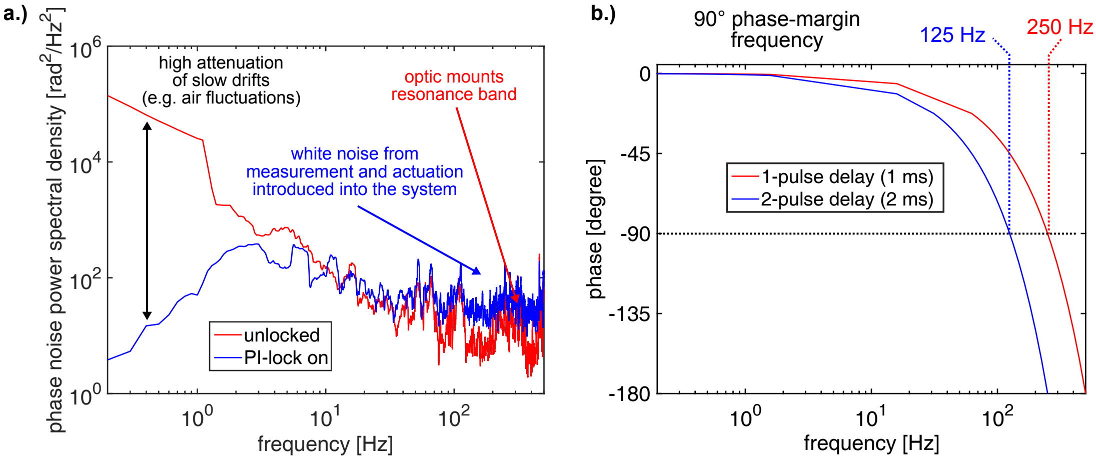

Figure 5.28: a.) Exemplary noise power spectral density of the phase noise between the NIR and IR-channel open-loop (red) and active PI-loop optimized for lowest overall noise (blue). Mainly slow drifts are attenuated but already at medium frequency the measurement introduces additional noise into the optical setup via the feedback sytem. **b.)** Bode plot for the 90° phase margin within a simple time-discreet delay element with one laser shot (red) and two laser shots latency (blue).

Additional technical considerations need to be made and correspondingly implemented into the feedback unit. All signal processing is performed digitally which allows for noise-free computation, but digital variables can overflow which destabilize the whole system due to sudden steps. At critical points within the data flow, the result of the computations needs to be checked for overflowing variables. Depending on the sub-signal a reset or a clamping of the variable can be desirable. If e.g. a CEP/RP should be stabilized and the actuator is running close to one end of its dynamic range, a defined reset by $n \cdot 2\pi$ yields the same CEP and recovers the dynamic range of the actuator without distorting the system.

A feedback unit furthermore should be able to allow an arbitrary signal (e.g. sine, step, etc.) to be injected into different parts of the feedback system, e.g. as separate input signal, as set point of a feedback loop or as distortion signal. Signals are required to be scalable, deactivatable or need to be ramped to avoid system instabilities at start-up. The feedback system is constantly adapted to the specific experimental needs, a generalized block diagram can be found in Fig. 5.29.

As with the fringe spectrometer (see Chapter 5.2.1) the feedback system features a microcontroller as a gateway between the FPGA and the control computer(s). An FTP-server in the feedback unit allows to stream all input and output data alongside selected internal signals from the FPGA. A TCP-port allows to set and modify any factor or data array in the FPGA from the Computer (e.g. by a GUI or script). All units within the active stabilization system are triggered by the laser system and tag every laser shot with an ID. This ID can be used to trigger or induce timing marks in other data acquisition systems (e.g. HHG-spectrometer). The time synchronization between the various separate measurements during data analysis can then be automated easily, e.g. via a MATLAB script. This synchronization allows to correlate a set of *synthesis parameters* (set of timing parameters) to the characteristics of experimental data (e.g. HHG-spectra).

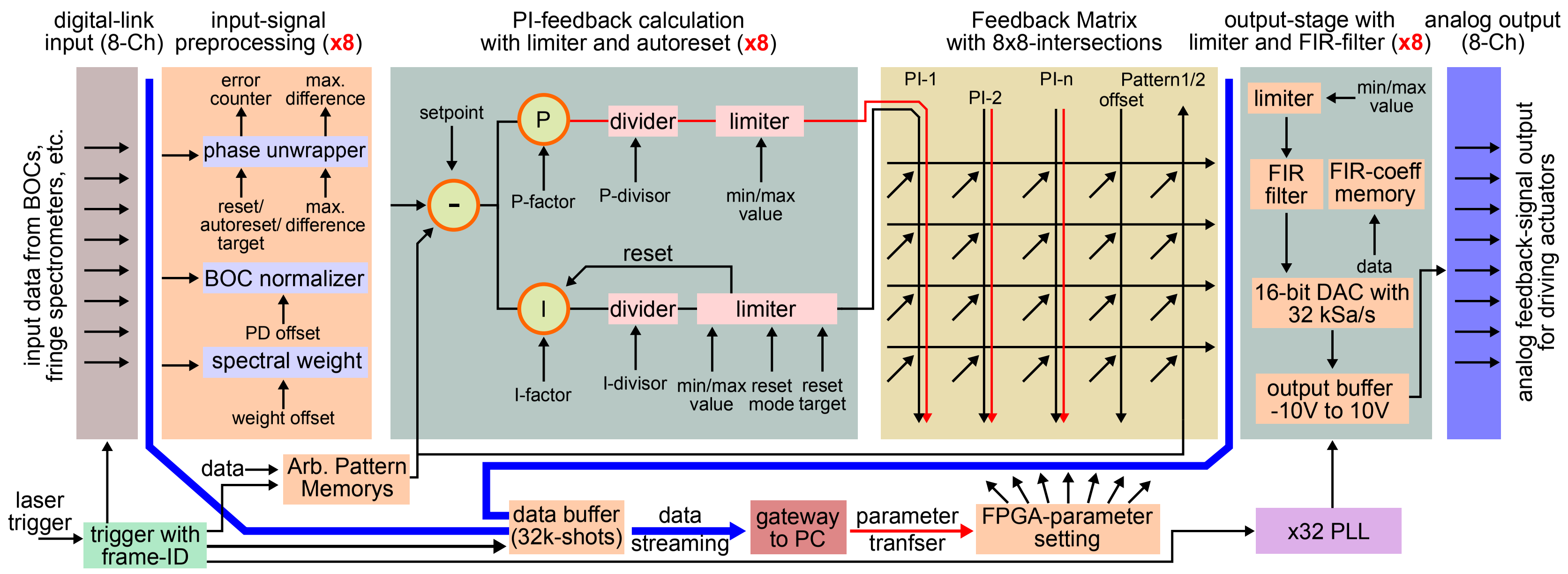

Figure 5.29: Scheme of the FPGA-based feedback system: Observables enter the system as digital signals which are retrieved by separate measurement devices. Normalization (BOC) or phase-unwrapping (e.g. for CEP, RP) can be performed. An enhanced PI-controller avoids overflow or clamping of signals. The feedback signals enter a matrix system so what every signal can be coupled with a variable strength and polarity to any actuator. Additionally arbitrary signals can be injected for scanning and tuning. An FIR-filter allows to shape the PZT-driving spectrum and a DAC prepares 8 analog voltages to drive the PZT-amplifiers. All system parameters are also exchanged with a PC for logging and control. The system only adds a 50 µs of latency to the signal chain.

User Interface

The control PC with the GUI plays an important role in the active stabilization system. The FPGA allows for fast but also rather simple algorithms to be executed with a very high reliability. A PC on the other end can cover the demand for very complex computations but is also prone to system crashes. An example for a complex process is e.g. an automated tuning procedure, where the PC sends arbitrary signals into the FPGA driving the actuators to induce distortions in the optical system while analyzing the system response. The modularity of the active stabilization system and its network interface enables the user to connect to any device from multiple PCs and control the synthesizer experiment. Dedicated standalone GUIs were programmed by the author to display and analyze measurements while other GUIs were used to control e.g. the parameters for the active stabilization (see Fig. 5.30). With this approach measurement routines can be automated and third-party devices can be easily included in these routines. A GUI programmed in MATLAB offers the great flexibility, that the executed program code can be changed and adapted while the GUI and the back-end is continuously running and communicating with the feedback unit.

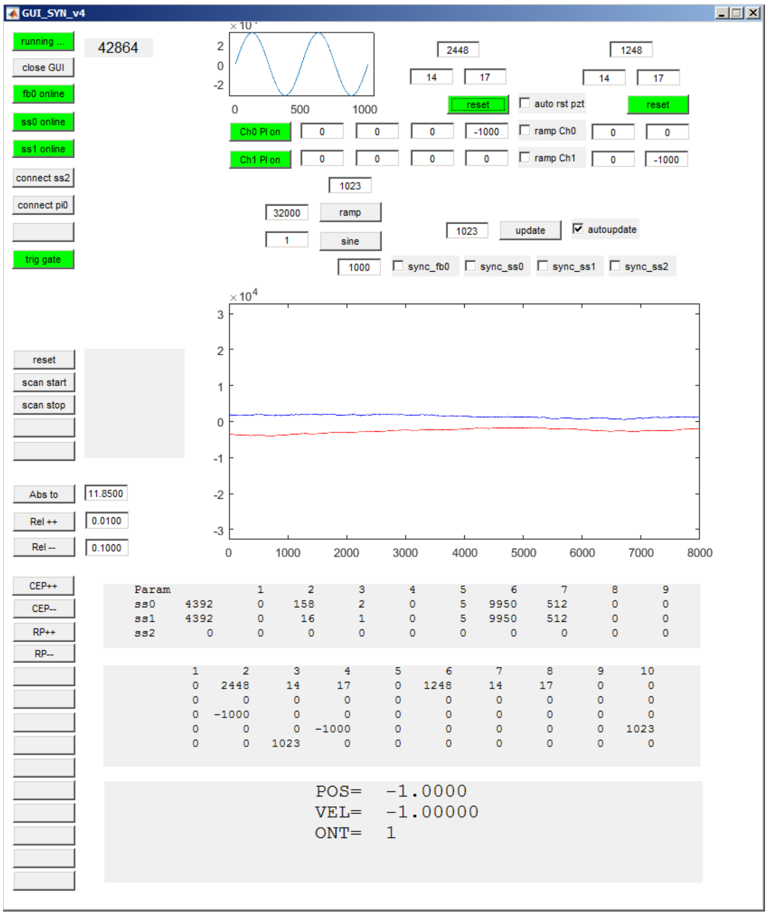

```
Param              1       2       3       4       5       6       7       8       9
ss0     4392       0     158       2       0       5    9950     512       0       0
ss1     4392       0      16       1       0       5    9950     512       0       0
ss2        0       0       0       0       0       0       0       0       0       0
```

```
      1       2       3       4       5       6       7       8       9      10
      0    2448      14      17       0    1248      14      17       0       0
      0       0       0       0       0       0       0       0       0       0
      0   -1000       0       0       0       0       0       0       0       0
      0       0       0   -1000       0       0       0       0       0    1023
      0       0    1023       0       0       0       0       0       0       0
```

```
POS=  -1.0000
VEL=  -1.00000
ONT=  1
```

Figure 5.30: Screenshot from the MATLAB GUI used to control the feedback system of the synthesizer and third-party actuators. All important system parameters of the feedback system can be reviewed, manually modified or controlled via a sequence-script. The graph in the middle currently shows the feedback signal of the two active feedbacks driving two PZT-actuators, one for active stabilization of the CEP in the seeding front-end and one actuator to stabilize the relative phase between two synthesizer outputs.

Chapter 6

Upgraded Synthesizer and HHG from Synthesized Pulses

This chapter will report on the current state of the upgraded synthesizer experiment and the first HHG driven with synthesized waveforms from that system. Working towards this first demonstration of the advances parallel parametric waveform synthesis as well as the creation of intense sub-cycle pulses, we encountered manifold challenges. Several new methods, schemes and technical implementations were introduced to the setup by the author and G. M. Rossi, and have been partly described in the previous chapters. Solving those challenges was essential to allow for extended stable synthesis, as required by advanced attosecond experiments like attosecond streaking and attosecond-pump-probe experiments. The following list summarizes the upgrades implemented over the first synthesizer prototype at CFEL:

- Modular sub-systems with custom breadboards and low-drift optic mounts
- Each module is boxed and equipped with precise temperature stabilization
- Home-made CEP-stable frontend with passive and active CEP stabilization
- Separate and optimized seed generation for each spectral channel
- Transport of the high-energy pump beam for the 3rd-stage OPAs via relay-imaging in vacuum
- Beam-pointing stabilizers implemented at crucial locations and referenced to the corresponding breadboard modules
- First full timing infrastructure for a parallel parametric synthesizer envisioned
- New *RAM* timing tool based on a novel balanced optical cross-correlator
- Development of an FPGA-based single-shot spectrometer performing as low-latency CEP sensor and relative-phase meter
- Network of sensors, actuators and an orthogonalization control for performing active stabilization with highest bandwidth
- Actuator placement for synthesis control exploits peculiarities of the setup
- Simplified dispersion management scheme with higher throughput
- Ultra-broadband and fast-acquiring pulse characterization technique (2DSI)

All these modifications were introduced to reduce the complexity and increase the stability of operation. In the following, the most recent status of the experimental setup is described and the first HHG driven with synthesized pulses will be presented.

6.1 Reengineered Synthesizer Implementation

The high degree of complexity of the optical synthesizer setup, the demands for long-term stability and the requirements to individually setup, (pre)align and maintain one functional system separately requires modularization. The mechanical reengineering of the first synthesizer prototype was decisively led by G. M. Rossi with contributions from the author. The design requirements were set by the experience from experiments that were performed at the first synthesizer prototype. The setup was split in functional modules, where each module is separately housed and temperature controlled. Therefore, the synthesizer experiment is split in four module groups: CEP-stable seeding front-end, external high-power grating compressor, amplification channel(s) with 3 OPA-stages (incl. WLG-based seed generation, partial dispersion management and timing actuators) and adjustable long-range delay lines (see Fig. 6.1). All those modules are customized individual breadboards with active temperature stabilization. Only few components are left outside of these housed modules, mainly for beam splitting, beam routing and pointing stabilization (TEM, Aligna 4D BeamLock). The beam routing is designed to propagate timing critical beams in close proximity to reduce temporal jitter and drifts (e.g. 1st/2nd-stage OPA-pump and CEP-stable seed pulses). The detectors of the pointing stabilizer systems are referenced to the breadboard of the seeding front-end. Two more pointing stabilizers are being installed in order to perfectly overlap the outputs of each spectral channel (see Chapter 5.3.1). The high-energy pump beam (15 mJ in total) for the third stages are relay-imaged in vacuum for lower beam pointing at the external compressor and at the 3rd stages themselves. The relative envelope and phase timing tools are implemented close to the beam-combination section. Furthermore a 2DSI-setup is in place to routinely characterize the output pulse(s) while the main energy of the synthesized pulses is directed towards the attosecond beamline.

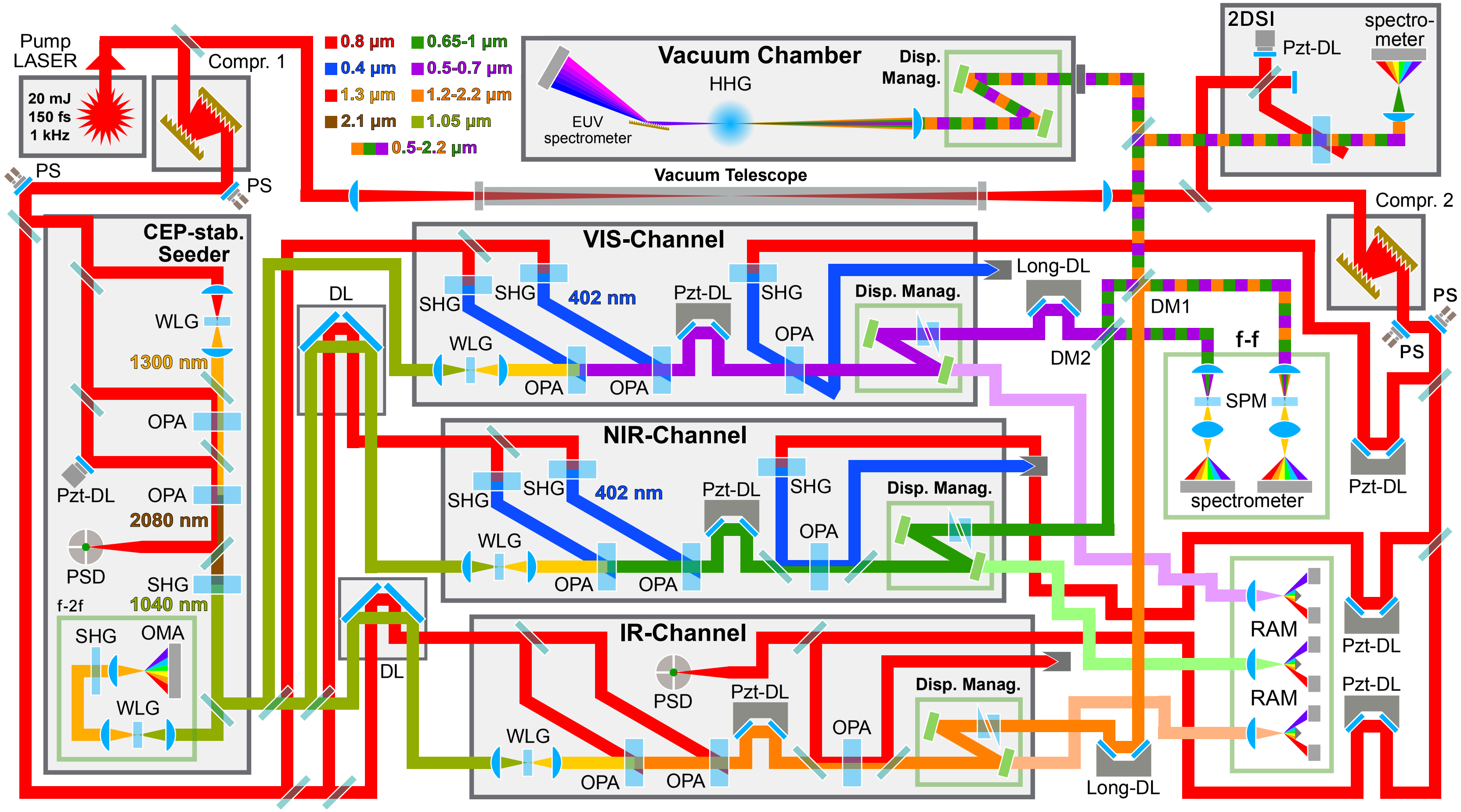

Figure 6.1: Scheme of the current state-of-the-art experimental implementation. The setup shows components of the pump-laser system, the seeding front-end, the amplifying channels (VIS-channel not implemented yet), the delay lines (DL, PZT-DL), the pointing stabilizer system (PS, PSD) and the timing tools (f-f, RAM) at the beam-combination section. Furthermore the HHG beamline and the pulse characterization setup (2DSI) are illustrated. Figure adapted from [171].

6.1.1 Customized Breadboards with Active Temperature Stabilization

Especially the temperature stability is a basic and crucial requirement to achieve alignment free operation for prolonged periods of time (weeks to months). During experiments on the synthesizer, it was noticed that fluctuations/failures of the air conditioning in the lab lead to irreversible drifts of commercial optics mounts even with just small changes in temperature ($\sim 0.5\,\mathrm{K}$), which requires time-consuming realignment of the setup. To prevent these air-conditioning failures from having an immediate impact, a box around the optical setup helps as a thermal low-pass filter. A complex temperature stabilization system needs to be implemented on the individual breadboard modules to fully prevent drifts in general, as it ensures a stable temperature at any point in the setup.

A common method for temperature stabilization is to use a water-cooled breadboard together with a temperature-controlled chiller. This technique is necessary if heat-load is dissipated on the breadboard, but due to the passive nature of the OPA-based synthesizer, no significant heat load is present. Furthermore, the water pump and the water flux itself can induce vibrations, and water-cooled breadboards are significantly more expensive as well as hard to build with custom configurations. On the contrary, a different and easy to implement method is the active heat-up of the breadboards by electric heaters. With this approach, a cheap, compact, and almost failure-free method was implemented by the author. The customized breadboards have a cut-out structure at the bottom, where the heaters are thermally coupled to the breadboard by thermally-conducting adhesive (see Fig. 6.2b). High-power resistors are used as heaters (16x $39\,\Omega$, $17\,\mathrm{W}$). Each modular breadboard is equipped with 16 resistors grouped in 8 temperature zones, which allow to control each section of the breadboard separately. To prevent an excessive conduction of heat into the main optical table, the breadboards are thermally isolated by a 4-mm-thick silicon mat placed between the breadboard and the optical table (see Fig. 6.2a). This mat furthermore helps to level the force along the whole surface, effectively preventing tipping point behavior or mechanical motion. The silicon mat has a low thermal conductivity of $0.14\,\mathrm{W/mK}$, which translates to $8\,\mathrm{W}$ per K for a $\sim 0.45\,\mathrm{m}^2$ module. Additionally, high frequency vibrations from the main optical table are attenuated.

To achieve active stabilization, the temperature of the different zones must be measured and a corresponding feedback signal needs to be generated. For this purpose, the author developed a home-made temperature measurement and control system. This system is based on surface mount platinum temperature sensors (Pt-1000) which are thermally coupled to the breadboard surface in the center of each corresponding temperature zone (see Fig. 6.3a). The sensor readout is performed by a high-resolution ADC with 24-bits resolution (Linear Technology, LTC2440). The ADC measures the temperature of the sensor via a 4-wire circuit. The probe current is switched off while no measurement is performed to prevent

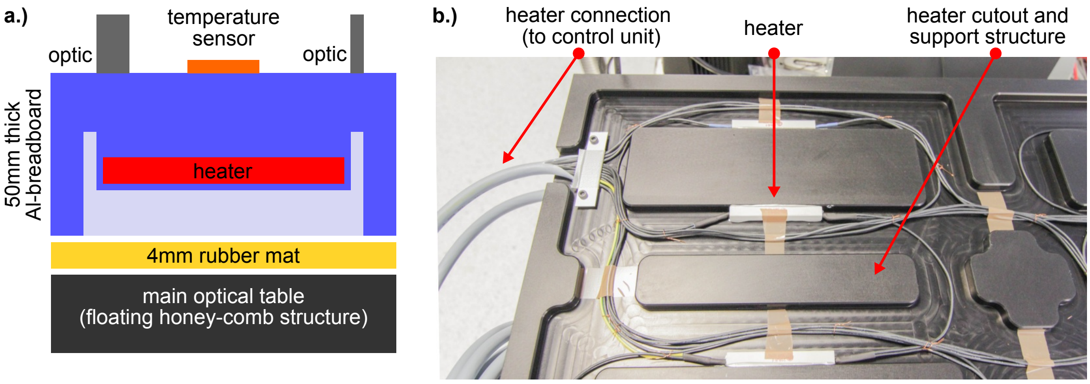

Figure 6.2: Temperature stabilization of the custom breadboard modules. **a.)** Schematic of the composition: the 50-mm-thick aluminum breadboard rest on a 4-mm-rubber mat. Cut-outs on the bottom of the breadboard allow to mount heaters for active temperature stabilization. A precise temperature sensor is attached on the top-side close to the optics mounts. **b.)** Picture of the bottom of the breadboard with resistors thermally glued onto the cut-out regions. A total of 16 resistors per breadboard are grouped in 8 temperature zones.

self-heat-up of the sensor. A readout noise of 300 µK and a precision of 2 mK is achieved with this circuit. To serve more sensors, a multiplexer is implemented allowing the serial readout of 8 sensors. The data processing is performed by a microcontroller (Atmel, XMEGA32A4), including an 8-channel PI-control system (see Fig. 6.3b). On each breadboard one readout circuit is placed close to the sensors. A ribbon cable delivers the circuit with power, allows for bidirectional communication and sends the control signals to an external power unit for driving the heaters. Two independent layers of security are implemented to prevent malfunctions, which could damage the optical system. All parameters are send to a PC and are logged. The active stabilization parameters can be set by a console on the PC to adjust the feedback parameters. The system is scalable and currently implemented in all synthesizer breadboards. This results in 30 independently controlled temperature zones across the setup (area $\sim 3\,\mathrm{m}^2$). The temperature set-points need to be a balanced choice between heat-migration into the main optical table and the range where a failure of the air-conditioning can be compensated for (dynamic range). A typical set-point temperature of 3 K above room temperature covers most AC failures. If the breadboard is boxed, a temperature stability of <2.2 mK rms can be achieved (see Fig. 6.4). The temperature control systems have proven to run and stabilize the temperature without any interruption for a year enabling almost drift-free and alignment-free synthesizer modules.

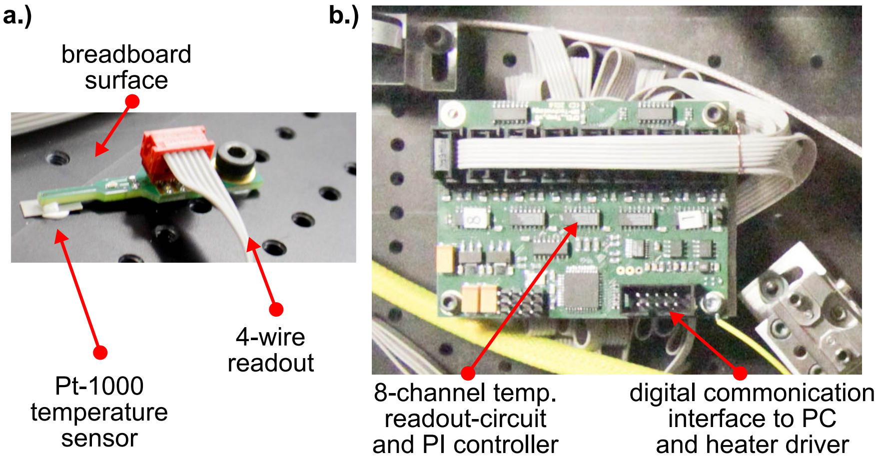

Figure 6.3: a.) Picture of one Pt-1000 temperature sensor which is thermally coupled to the breadboard surface. **b.)** System for reading the sensors of the 8 temperature zones with mK resolution and to generate appropriate feedback signals to the 8 breadboard heater-zones. A digital communication interface allows for reliable communication to the heater-driver and to the PC for logging and control.

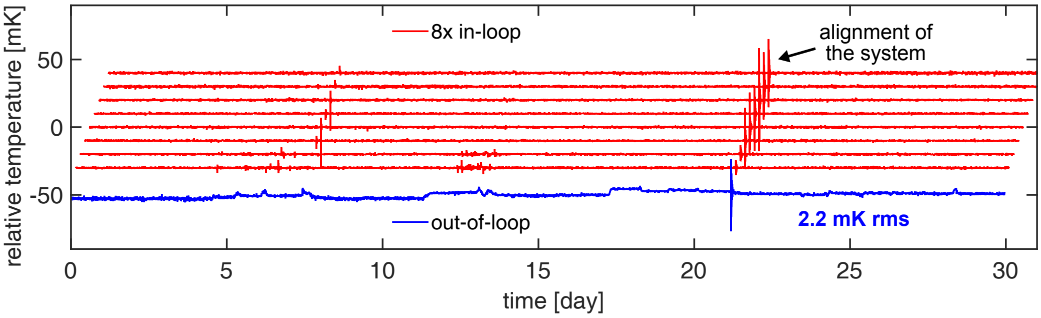

Figure 6.4: Long-term temperature stability of the 8 zones for the CEP-stable seeding front-end when fully boxed (red). Additionally an out-of-loop relative temperature measurement (blue) shows 2.2 mK rms over the course of a month. The traces were given an offset for better visibility.

6.1.2 Low-drift Optics Mounts

Usually optical setups employ commercial optic mounts which allow to align every optic in various ways to achieve an overall good alignment of the optical system. If the optical setup and its required degrees of freedom are already known alongside its performance, a second implementation of the setup can reduce the optical path length and reduce the unnecessary degrees of freedom of the optics mounts. Every degree of freedom potentially introduces drifts to the optics position. A good example is e.g. beam pointing introduced from linear stages used as retro-reflector delay lines. Each optic mount in the system was considered and if possible replaced with a low-degree of freedom custom-made aluminum part (see Fig. 6.5). Also techniques of mounting optics are usually introducing stress and drifts. In the reengineered setup, most of the optics were glued by UV-cured glue (Nolan, Type 65) which achieves a completely stress- and drift-free method of attachment.

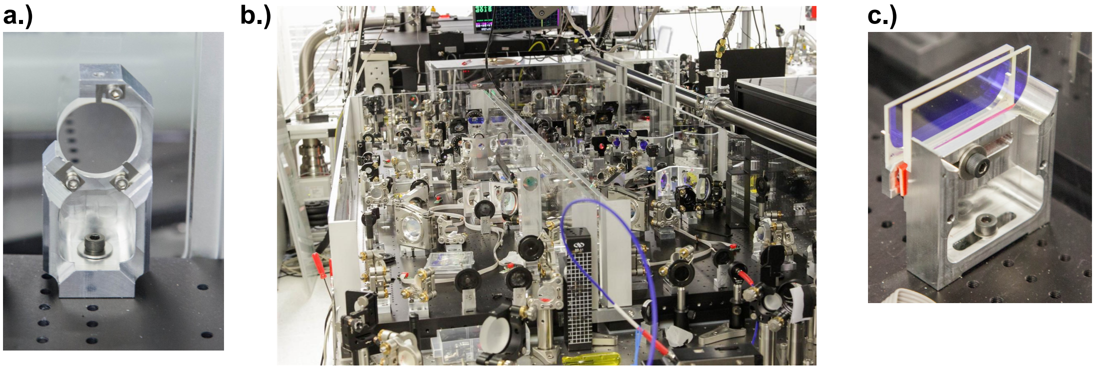

Figure 6.5: Pictures of the reengineered components and the optical setup. **a.)** Home-made completely passive and compact 1-inch mirror mount with spring-loaded holding mechanism. **b.)** Picture of the reengineered optical setup showing the two separate spectral channels (NIR/IR-channel) **c.)** Precision delay lines (for narrowband pulses) and dispersion compensation (for broadband pulses) is implemented by glass wedges and its insertion/extraction from the corresponding beam. The optics are attached via UV-cured glue.

6.2 Design and Output of the NIR/IR-Channel

Compared to the first prototype of the synthesizer experiment also a significant beam-path reduction from 30 m to 10 m is achieved with the reengineering efforts. The details on the setup and performance of the CEP-stable seeding front-end were already covered in Chapter 4.1. In the following a brief overview is given over the optical setup of the amplifier modules of the synthesizer experiment. Three identical modules were CAD-designed by G. M. Rossi and accept the temporally synchronized pump beam for the first two OPA-stages together with the CEP-stable pump beam for the seed generation via WLG (see Fig. 6.6). For the NIR- and VIS-channel, separate SHG are performed to prepare the 400-nm-pump beams. After each OPA-stage, partial recompression is achieved with DCMs and glass wedges. The booster-stage pump (last OPA stage) enters the module on the opposite site coming from the external compressor. The output pulse is finally compressed via several bounces on DCMs. Currently the NIR-channel produces >100 µJ of pulse energy after the dispersion management. The IR-channel instead produces >500µJ after compression. The implementation of the VIS-channel is ongoing. The spectra cover roughly a bandwidth (foot-to-foot) of 680-1000 nm for the NIR and 1300-2200 nm for the IR-channel (see Fig. 6.7). A single-shot energy-meter (Coherent LabMax Top, J-25MT-10KHZ) allowed to characterize the energy stability of the output of the amplifier modules and yields 1.22 % rms (NIR-channel) and 1.15 % rms (IR-channel). Due to the operation in depletion of the 3rd-stage OPAs the output energy fluctuations are mainly imprinted by the pump beam energy fluctuation. Via this method the energy fluctuation can be very low, although the 3rd-stage seed is derived by a WLG and then amplified by several orders of magnitude from the first two OPA-stages.

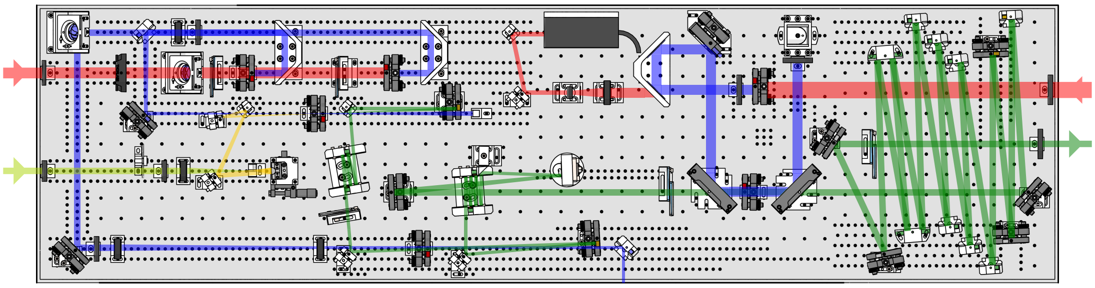

Figure 6.6: CAD drawing of one amplification module featuring the implemented 3-stage OPA chain. Left: the CEP-stable seed driver (green) and the pump beam for the first two stages (red) enter the module. After the seed generation via WLG, a 3-stage amplification is performed with intermediate dispersion management via DCMs and glass wedges. Right: The booster-stage pump beam (thick, red) enters the module coming from the external compressor. The final signal beam is compressed and leaves the module for synthesis. A PZT-driven delay line on the 3rd-stage seed allows to modulate the relative phase with respect to the master channel. Figure adapted from [171].

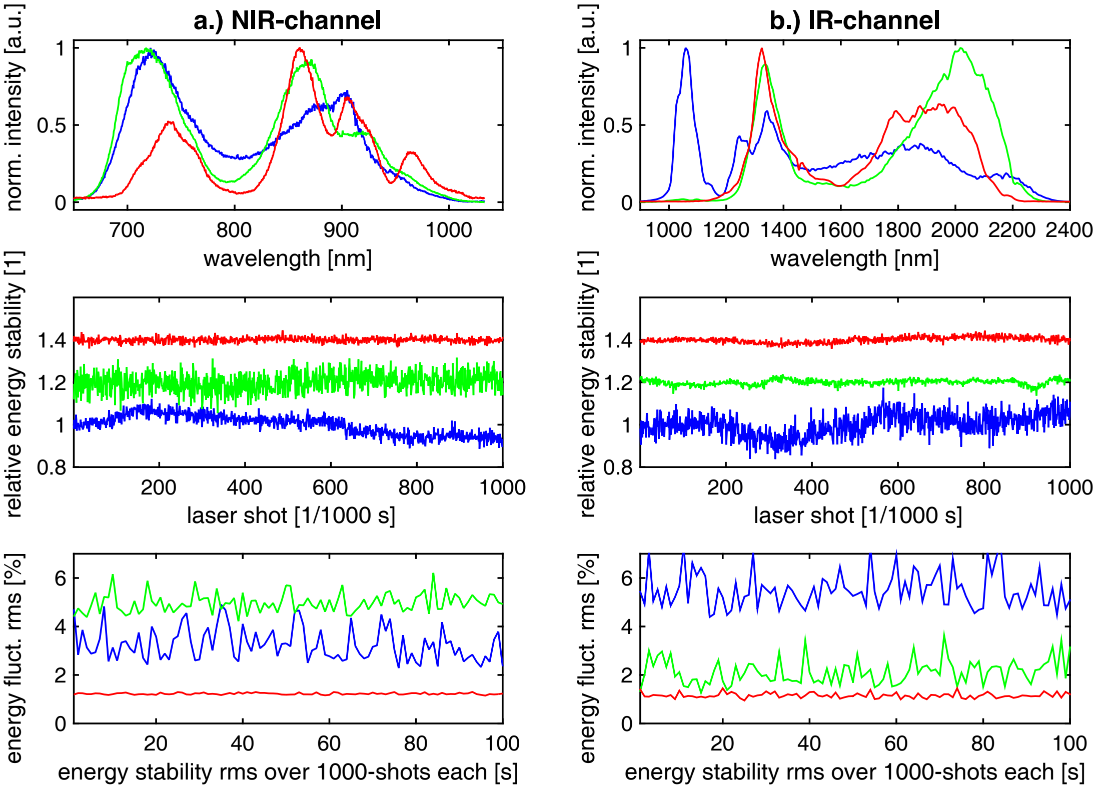

Figure 6.7: Spectra (top) and relative energy stability (middle) characterization for the NIR (**a.)**) and IR (**b.)**) spectral channel after each OPA-stage (**1st-stage**, **2nd-stage**, **3rd-stage**). Rolling evolution of the relative intensity noise rms over 100 s and 1000 shots each (bottom).

6.3 Pulse Compression and Dispersion Management

The main modifications to the dispersion management scheme arise from the different seeding scheme (see Chapter 4.3). Before, a common WLG was spectrally split to seed each channel, now every channel has his own (optimized) WL seed and no spectral splitting is required. The two-color output of the seeding front-end furthermore offers a choice on which output to use for seed-derivation. Especially the VIS-part of the seed suffers from long WLG materials, which are in return required for wide IR spectral coverage. The amplification occurs in few mm-long BBOs for all spectral channels. In-house designed chirped mirrors from S.-H. Chia are used for partial recompression ((DCM1 (IR), DCM2 (NIR), DCM3 (VIS)), see Fig. 6.8). Another technical challenge is the bulk material used for fine tuning the compression. While for the NIR- and VIS-channel fused-silica wedges (FS) can be used, the zinc-selenide-based wedges (ZnSe) in the IR-channel suffer a high nonlinearity and it is difficult to achieve a perfect surface quality with this material. The outputs of the synthesizer channels are combined via dichroic mirrors (DM1, DM2), before being transported to the HHG-source chamber of the attosecond beamline. A 6-mm-thick CaF_2 is used as entrance window and the final compression is performed with ultra-broadband DCMs (DCM0). The pulse characterization is performed by the 2DSI-technique

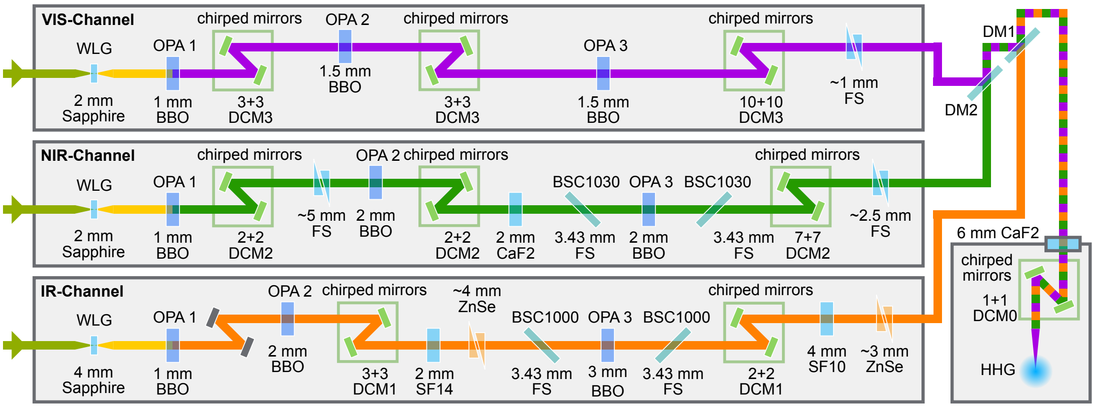

Figure 6.8: Dispersion management scheme of the current synthesizer experiment. The main difference over the previous prototype is the separate WLG seeding. The OPAs are all BBO-based and the dispersion management employs wedges and custom designed DCMs. Figure adapted from [171].

(see Chapter 2.10). A compact 2DSI was designed and setup by G. M. Rossi and further developed and applied to different sources by F. Scheiba [197]. The required ancillary pulses are derived by narrow-line interference filters (Semrock MaxLine, 3.5 nm bandwidth) from a replica of the 800-nm-pump beam and usually have a spectral shear of 3.5 to 5 nm. The up conversion is performed in a 10 to 20 µm-thick type-II BBO to avoid bandwidth-limitations due to phase matching. The 2DSI-traces are recorded with an HR4000 spectrometer (Ocean Optics) and the spectral phase retrieval is based on FFT (see Fig. 6.9). The individually characterized 2DSI-traces show a well-behaved and compressed spectral phase in both synthesizer channels. In the time domain these few-cycle pulses are compressed close to their corresponding Fourier-transform-limited pulse duration (see Fig. 6.10a/b). The CEP cannot be measured with the 2DSI so that the pulses are characterized with one degree-of-freedom left. For the NIR and IR-pulses a common CEP can be assumed and the two fields can be theoretically combined with an arbitrary temporal offset to yield a synthesized sub-cycle pulse with a pulse-duration below 4 fs (see Fig. 6.10c). Synthesized pulse durations down to 3.2 fs were achieved with the 2DSI-measurement as well. With the timing synchronization system, these synthesis parameters can be set and controlled to actually synthesize such a waveform and use it to drive HHG. The retrieved pulses can also be superimposed with a variable time-delay to demonstrate the significant shortening of the pulse duration via synthesis (see Fig. 6.11). Even

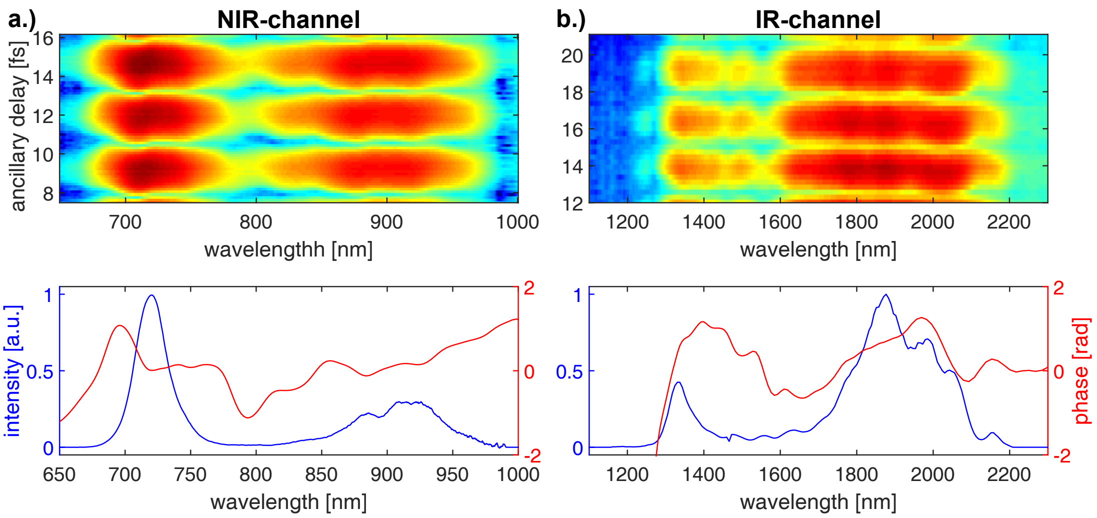

Figure 6.9: Pulse characterization of the compressed NIR (**a.)**) and IR-channel output (**b.)**) via 2DSI. Raw 2DSI-fringes (top) and extracted fundamental spectra (blue, bottom) and spectral phase (red, bottom). Data taken by F. Scheiba.

with a pulse-separation multiple times greater than the pulse durations of the involved pulses, each pulse modulates the peak intensity of the other at changing delays. Such an intensity modulation should be clearly observable as a change in the characteristics of the HHG spectral shape, if applied to such a highly nonlinear process.

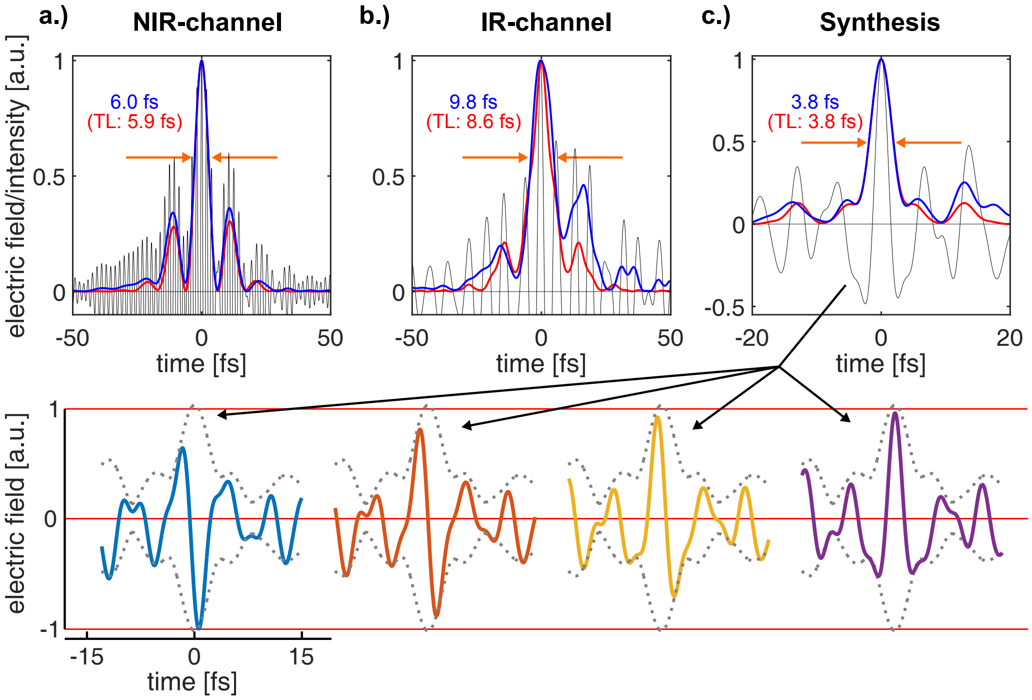

Figure 6.10: Top: The two outputs of the synthesizer channels exhibit a pulse duration of (**a.)**) 6.0 fs (TL: 5.9 fs) for the NIR-channel and (**b.)**) 9.8 fs (TL: 8.6 fs) for the IR-channel. (**c.)**) When the two few-cycle pulses are combined with the present energy ratio of 1:5 (NIR-to-IR), a sub-cycle pulse with a pulse duration of 3.8 fs (TL: 3.8 fs) is synthesized. Bottom: The synthesized pulse is varied with respect to its CEP in $\pi/2$-steps showing different resulting non-sinusoidal sub-cycle transients.

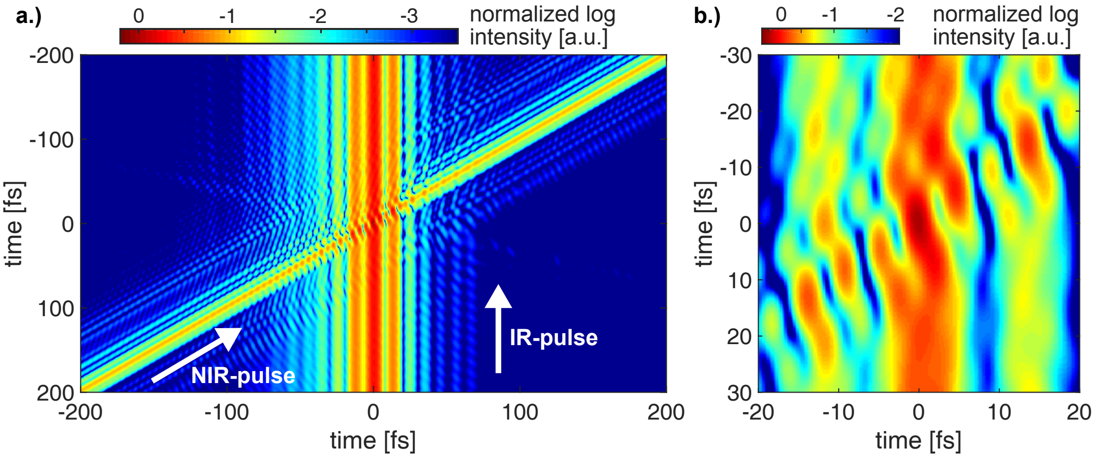

Figure 6.11: a.) Theoretical temporal superposition of the two (via 2DSI) retrieved pulses from the two spectral channels and the resulting electric field intensity trace. The pulses already start to modulate each other with a significant temporal separation. **b.)** Zoomed-in view of the direct temporal overlap region, where an intense sub-cycle electric field transient is synthesized.

6.4 Timing Synchronization and Synthesis

The implementation of the full timing-synchronization system as envisioned (see Chapter 5.3.1) is ongoing as the whole setup of the experiment. Currently the relative arrival time of the third-stage pumps can be delayed by two 20 μm PZT-driven mirror mounts (Physik-Instrumente, P-753.1CD). Those are currently manually adjusted by optimizing the output spectrum of the corresponding spectral channel. The two output pulses from the two spectral channels can be translated with respect to each other by a motorized delay stage (Physik-Instrumente, M112.1DG, 25 mm range), rigidly moving the pulses both in relative envelope timing and relative phase with respect to each other. An implementation of a BOC/RAM to measure the relative arrival time and feedback to the pump delay lines is still to come.
The feedback system is currently able to control the CEP of the seeding front-end and the relative phase between the output of the NIR and IR spectral channel. The relative phase can be shifted by 6π via a PZT in the IR-channel. The relative phase and relative envelope timing can be rigidly actuated by the motorized delay line. With these control knobs a broad range of phase relations/CEPs between the two output pulses can be synthesized already.

6.4.1 Relative/CE-phase Stabilization

The CEP of the seeding front-end routinely achieves around 160 to 210 mrad rms of single-shot phase noise (see Chapter 4.1). For the relative phase measurement between the NIR and IR spectral channel two different techniques were experimentally investigated and are discussed in the following. In the first technique the IR output can be frequency doubled to spectrally beat with the NIR output. Such a setup then resembles a classic f-2f interferometer (see Fig. 6.12a), with its separate (but similar) spectral broadening via a WLG stage (see Fig. 6.12b). This classic technique observes a sum of the CEP and relative phase among the two synthesizer outputs (NIR+IR) due to the involved frequency doubling (SHG). Differently, if the recombined beams where set such that the IR-part contains significantly more energy than the NIR, a spectral broadening stage after the recombination would predominantly broaden those IR pulses sufficiently to spectrally beat with the NIR output (see Fig. 6.12c). This technique in theory should see exclusively the influence of the relative phase and not the CEP additionally. Both techniques were experimentally investigated and compared (see Fig. 6.13). It is noticeable that the commonly implemented SHG method is afflicted of significant measurement noise in this experiment. A relative phase lock achieved hardly less than 600 mrad rms and was very unstable (e.g. occurring phase jumps). In contrast to that observation, the WLG method achieved relative phase locks with a remaining in-loop noise of less than 80 mrad rms. Such achieved residual relative phase noise proves the excellent passive stability of

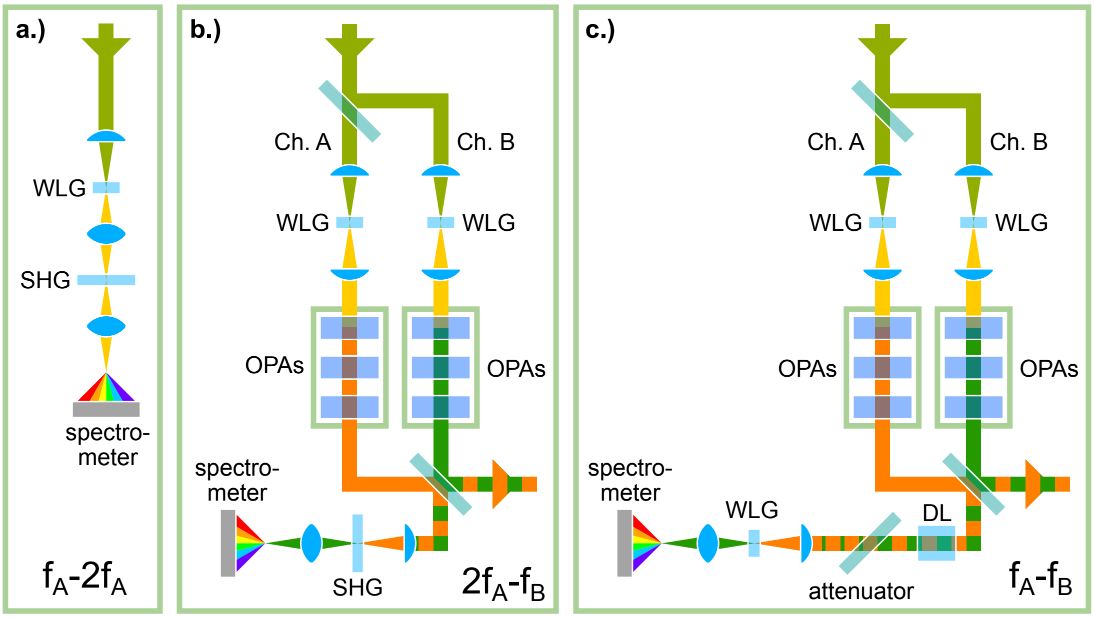

Figure 6.12: Comparison of a common f-2f interferometer for CEP measurement and two tested methods for the measurement of the relative phase between the NIR and IR channel. **a.)** In a regular f-2f interferometer the PUT is broadened via WLG and the red leg is frequency doubled to beat with the blue leg. **b.)** A similar setup is formed between the NIR and IR channel if the IR-channel is frequency doubled (SHG) to beat with the NIR output. **c.)** Here the IR channel is spectrally broadened to create a broadband beat with the NIR channel. Figure adapted from [171].

the reengineered synthesizer setup and delivers a solid basis for stable waveform synthesis. A weak observed modulation of the measured relative phase by the CEP (coupling 3 %) is attributed to a drift of the temporal envelope and can be fully suppressed by the orthogonalized feedback system.

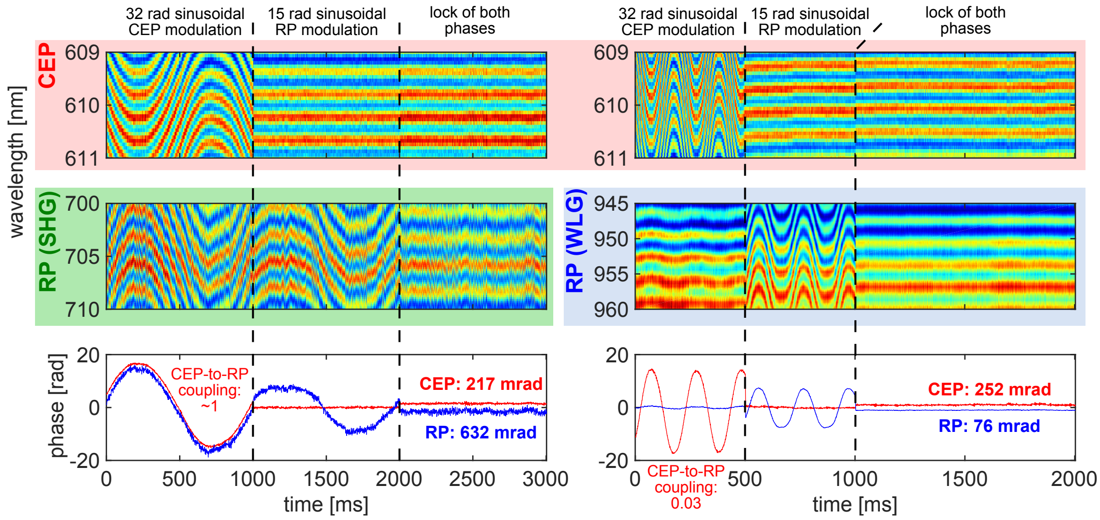

Figure 6.13: a.) Test of a RP measurement between the NIR/IR-channel via SHG **b.)** RP-measurement performed via the WLG method. (see Fig. 6.12b/c). The top row shows the CEP measurement in the seeding front-end (red), the middle row shows the two different RP measurement methods and the bottom row plots the two extracted fringe phases. For each method in the first temporal section a CEP modulation in the seeding front-end is introduced, in the second section a RP modulation is conducted and finally a lock of both phases. The WLG method does not have a co-sensitivity to the CEP of the pulses (coupling $< 3\%$) and reaches a significantly lower measurement noise with less than 76 mrad rms.

6.4.2 Relative Envelope-Timing Manipulation

One central idea of the new timing infrastructure for the synthesizer experiment is the actuation of the pump arrival time in the last OPA amplification stage (booster-stage, see Chapter 5.3.1) to correct for relative envelope drifts in the chirped domain. Currently no BOC/RAM is implemented yet to measure and control the relative envelope delay between the output pulses of the synthesizer. But the pump arrival time can be modulated up to 120 $\mathrm{fs_{pp}}$ by two already installed PZT-actuators. According to our study on the CEP dependence in OPAs upon pump-seed modulation (see Chapter 4.2) we expect a low CEP and relative phase coupling by a pump arrival time modulation due to the amplification of chirped pulses which are recompressed afterwards. A corresponding measurement was performed at the synthesizer experiment while a SHG-based relative phase measurement was performed (see Fig. 6.14). Even massive modulations of up to 120 $\mathrm{fs_{pp}}$ of the 3rd-stage pump-arrival time in each of the NIR/IR-channels yields only a very weak coupling to the measured relative phase. Despite that there is a clear intensity modulation observable in the fringe trace. This intensity modulations are indicating significant spectral intensity shifts in the individual

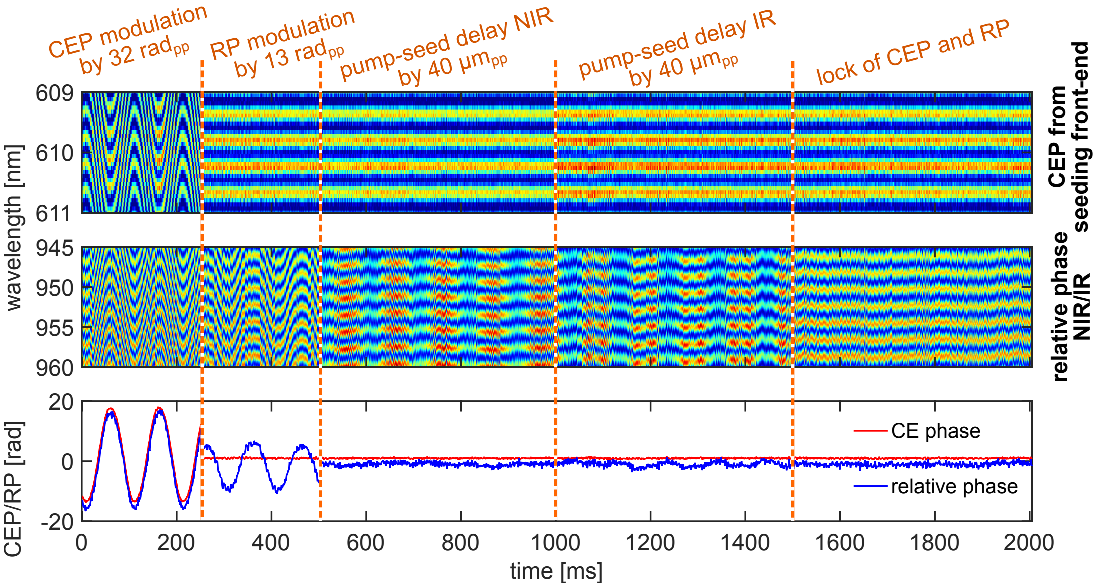

Figure 6.14: Influence on the relative phase between the NIR and IR channel output of the synthesizer setup during modulations of the pump arrival time. In the third/fourth temporal section of the CEP and RP tracks the pump-beam arrival time for the 3rd-stage pumps were modulated sinusoidally by 120 fs_{pp}. While a strong intensity modulation in that section is visible, a coupling to the RP is only very weak.

NIR/IR-pulses. This measurements prove that an actuation of the booster-stage pump is an appropriate tool for relative envelope actuation in the chirped domain due to the low influence on phase-properties (CEP/RP) in parallel parametric waveform synthesizers. However it is worth noticing that the arrival time of the amplified pulses at the experimental point is only marginally affected by the pump-seed timing due to the compression close to the Fourier-transform limit that greatly reduces the envelope shift.

6.5 Attosecond Beamline

To apply the synthesized pulses to strong-field experiments but also to exploit the full potential of the pulse characterization via attosecond streaking an attosecond-beamline was built alongside the synthesizer experiment (see Fig. 6.15). This attosecond beamline is decisively built and operated by Dr. Y. Yang with minor contributions from the author and is extensively explained in [198]. After the synthesis, the pulses need to pass a vacuum window to enter the first vacuum chamber. To avoid excessive nonlinear distortions during transmission (B-integral) the pulses remain not fully compressed. The final compression is achieved with ultra-broadband DCMs, and the fully compressed pulses can be split and can be focused into an HHG-source. In a second differentially pumped vacuum chamber a gold-coated toroidal mirror allows under grazing incidence to refocus the generated XUV radiation. A thin metal membrane can be used to filter out the HHG-driving radiation. The generated XUV beam can be recombined interferometrically with the optical pulse via a holey mirror and the optical-to-XUV delay can be controlled via a PZT-driven delay line. A third chamber contains a time-of-flight (TOF) electron spectrometer (Kaesdorff, ETF11) alongside a low density gas source ($p \sim 10^{-6}$ mbar). Both, the XUV and the optical pulse can be overlapped and focused to the entrance nozzle of the TOF. This experimental configuration, depending on the input pulse parameters can operate as HHG spectrometer, or e.g. perform RABBIT or attosecond streaking. Finally a XUV spectrometer (McPherson, 251MX) allows to observe the spectrum of the HHG via a cooled XUV-CCD (Andor, Newton). Exchangeable gratings allow to cover an energy range of 15.5 to 62 eV and 62 to 248 eV (300 and 1200 grooves/mm correspondingly). An important aspect of this beamline is its full vibration isolation by resting all vacuum chambers on separate frames. This decoupling prevents mechanical vibrations from the huge turbomolecular pumps (e.g. Pfeiffer HiPace 1500) to propagate to and distort the sensitive synthesizer setup.

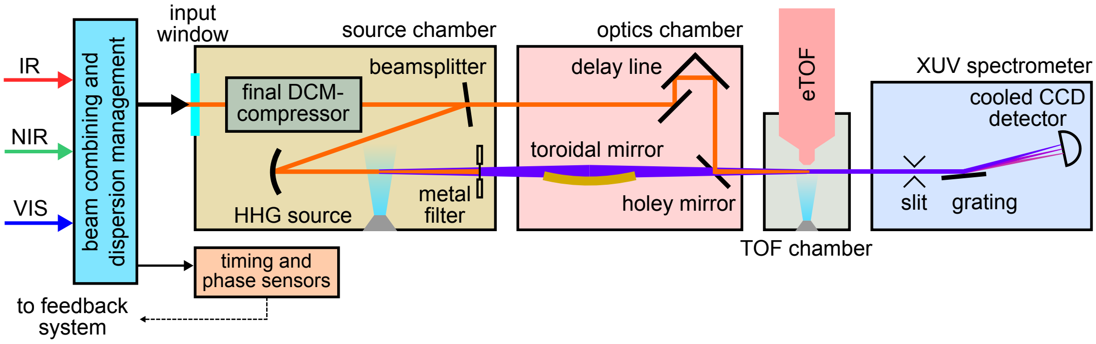

Figure 6.15: Schematic of the attosecond beamline as implemented in the CFEL labs. The synthesized pulse is entering a source chamber where the final compression is performed. A beam splitter can be used to derive a replica of the optical pulse, but the main energy is directed to drive HHG in gas. The generated HHG can be stripped off the driving field by means of a few hundred-nm-thick metal foil. A recollimation of the HH-emission can be achieved by a gold-coated toroidal mirror. The generated HH can be observed via a XUV spectrometer and by means of an electron spectrum during direct ionization of a secondary gas source in the time-of-flight (TOF) chamber. This setup is, depending on the laser source, able to perform RABBIT measurements as well as attosecond streaking.

6.6 HHG from Synthesized Pulses

As a first experiment to showcase the advances of the parametric waveform synthesis, we generated high harmonics from pulses synthesized by combining the NIR and IR spectral channel and varying the CEP and RP. In this experiment, the HHG exhibit a fringes spectrum, if only the NIR pulse is present. As this pulse is few cycles long, discrete HH orders are present indicating an APT (see Fig. 6.16a). The IR channel alone also creates HH, but the XUV detector is required to integrate significantly longer. The low HH flux is mainly due to the fact that this source is currently neither optimized nor phase-matched for IR-driven HHG (see Fig. 6.16b). At the moment the CE-phase of the seeding front-end is actively controlled (<250 mrad rms) and the RP between the channels can be locked (<100 mrad rms) as well as manipulated. The RP can be modulated within a 15 rad range by a PZT actuator between the 2nd- and 3rd-stage OPAs in the IR-channel (see Fig. 6.1 on page 127). To extend this range, a motorized delay line (Physik Instrumente, M112.1DG) is implemented between the output of the IR channel and the beam combination. This stage can move down to 500 nm steps but does not have a precise position feedback and some backlash dynamics. The stage is controlled by the synthesizer control GUI via a COM-port. Contrary to that, the current PZT-actuator has a low travel-range and a RP lock can be unstable if the PZT actuator comes close to the edges of its dynamic range. To perform an extended synthesis scan between the IR and NIR outputs while observing the spectrum of the generated HH, a coordinated movement of

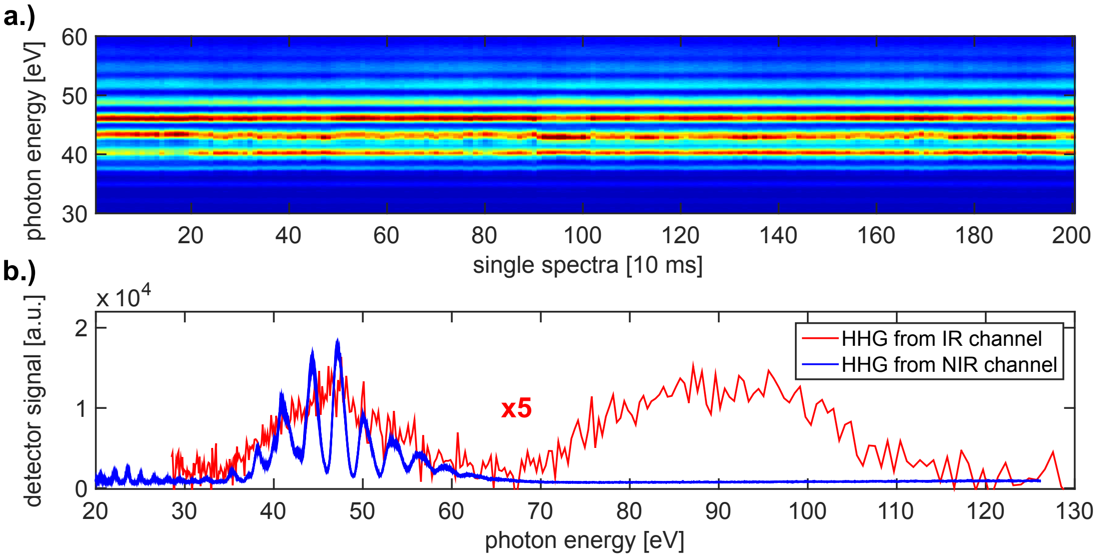

Figure 6.16: a.) Stability of the HHG emission emerging from argon when driven with the NIR channel alone (240 mbar, 40 µJ, f=375 mm, t_{int}=10 ms). **b.)** Individual HHG spectra in argon with NIR (blue, 20 samples from a.) superimposed) and HHG from IR (red, 300 mbar, 300 µJ, f=500 mm t_{int}=30 s).

the stage and the PZT actuator is required. Most profoundly, the RP must be measured continuously without any occurring phase-jump to relate the generated HH spectral shape to the synthesis parameter. In such scanning synthesis mode, the lock needs to be switched off when the motorized stage moves and constant activation and deactivation introduces possible phase jumps. Luckily the HHG is so intense, that an acquisition time of the spectrometer of 25 ms is sufficient to gather plenty of signal (HHG in Ar, 280 mbar, f=500 mm, 50 µJ from NIR-ch. and 400 µJ from IR-ch.). In order to synchronize the HHG-spectrogram stream to the measured set of synthesis parameters (CEP, RP), an LED flashes light into the XUV spectrometer which fully exposes the spectrogram. This LED is flashed with a characteristic pattern by the feedback unit of the synthesizer control. To acquire most efficient HHG-data from such a RP scan, the following experimental configuration is used:

- RP is not actively synchronized but constantly tracked
- PZT-actuator affecting the RP is driven with an asymmetric triangular function over a range of 15 rad with a frequency of 1 Hz
  (containing a 900 ms linear ramp)
- A motorized stage is moved in 0.5 µm steps every 4 s by the GUI
  (equals 1 µm in double pass)
- The recorded HHG spectra can be synchronized to the feedback data in post-processing due to the LED flash pattern

The raw HHG-spectra are analyzed by a script to find the time-markers based on the overexposed frames induced by the LED (see Fig. 6.17a). This extracted timing pattern is synchronized to the feedback system containing the information on the CEP and RP (see Fig. 6.17b). During a RP-scan over 1000 rad ($\sim$ 500 fs), the RP-measurement was keeping track without any occurring phase jump, despite the constantly scanning PZT-actuator and the sudden steps of the motorized stage. In this mode of measurement the HHG-spectra now contain several distorted spectra, e.g. when the ramp of the PZT returns, when the motorized stages moves or when the HHG spectrum is (over-)exposed by the LED-flashes. All those spectra ($\sim$ 10 %) are blanked out by the post-processing script and the remaining spectra contain undistorted HHG-spectra with the associated RP information. Those spectra are sorted according to the RP and binned within $\pi/10$-wide phase bins. The bin spacing is chosen to not wash out RP-dependent dynamics of the HHG but to also collect enough spectra in each bin. Each bin contains on average 7 spectra which are averaged and can be plotted over the RP (see Fig. 6.18b-e). In this experiment, the observed HHG is predominantly driven by the NIR channel and the IR component acts as a modulation to it, although it carries more energy. To compare the observed HH spectral shape with the theoretical peak intensity of the synthesized field, the two separate 2DSI measurements on the two spectral channels were scanned

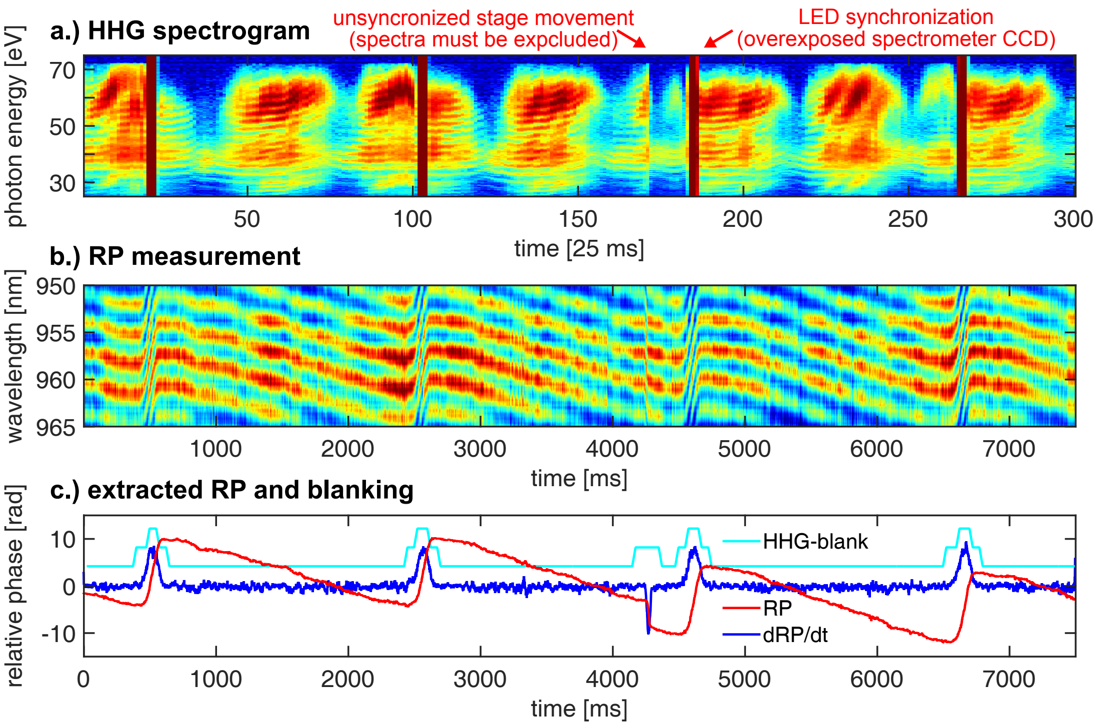

Figure 6.17: Data acquisition of HHG from synthesized pulses (NIR+IR) in argon during a long range RP scan. **a.)** HHG spectrograms recorded with $\tau_{\text{int}} = 25\,\text{ms}$ integration time, where a LED exposes the CCD in a characteristic pattern to synchronize it to the RP measurement. **b.)** Raw spectral fringes of the WLG-based RP meter between the NIR/IR channel. **c.)** Extracted RP (red) where steep slopes (dRP/dt, blue) are due to the PZT-actuator ramp-return or the unsynchronized motor-stage movement. Those HHG spectra as well as overexposed spectra (LED sync) yield a blank marker (cyan). Those spectra (and adjacent) will be discarded in further data analysis.

through each other similarly as in the experiment. As the HHG is driven predominantly by the NIR channel in the experiment, the peak intensity of the NIR pulse modulated by the IR pulse is extracted from this simulation and plotted along the measured HH spectra (see Fig. 6.18a).
Overall three characteristic sections can be observed in the scan (see Fig. 6.18c-e): For temporally displaced NIR/IR pulses, narrow HHG orders are observed, which are modulated slightly in photon energy by changes of the RP. Temporal wings of the IR pulse will slightly modulate the central wavelength of the NIR pulse thus slightly shifting the HH lines (see Fig. 6.19c). Within a region of direct temporal overlap, periodic changes including transitions to HH continua are observed. The two main interaction sections (see Fig. 6.19d/e) exhibit an area with an intensity suppression and with an intensity enhancement. In both cases broadband HHG emission can be observed but potential pre-ionization dynamics from the IR pulse arriving before the NIR pulses might lead to this section

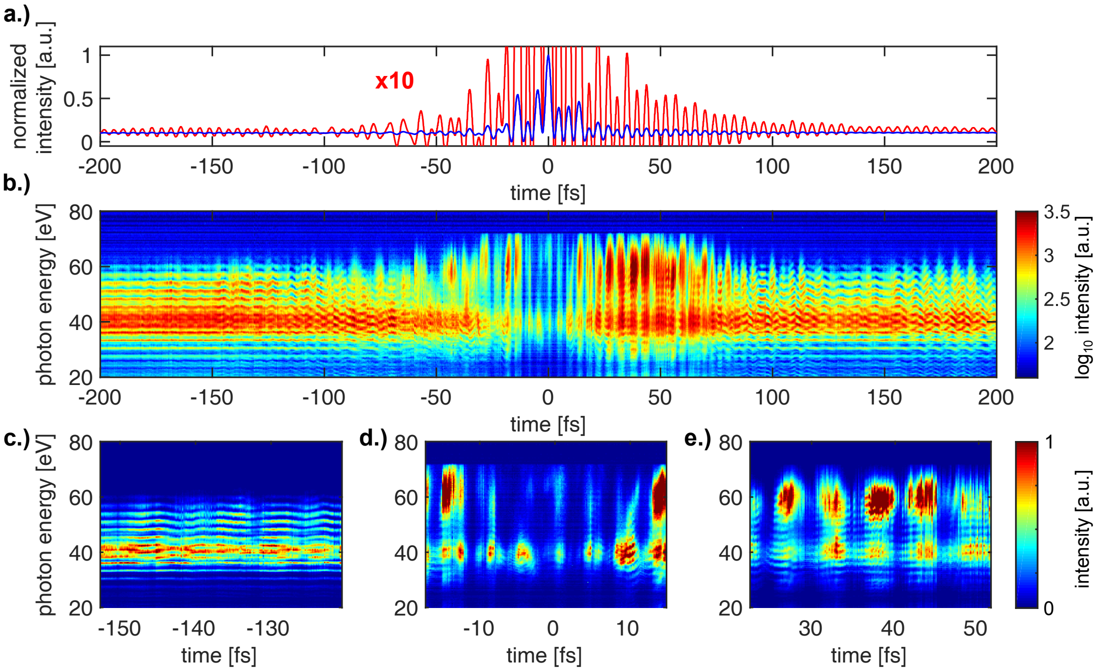

Figure 6.18: a.) Theoretical peak-intensity of the NIR pulse if modulated by the IR pulse at various delays, retrieved from the 2DSI-measurements with fixed CEPs and varying time delay (see Fig. 6.11 on page 136). An energy ratio of 1:9 (NIR/IR) was used and the peak intensity of the NIR is modulated around 0.11. **b.)** Experiment: RP-resorted HHG-spectra from 6.17 with logarithmic color scale to illustrate the dynamics of the spectral modulation with different RPs. Three zoom-in regions: **c.)** NIR and IR-pulses temporally separated **d-e.)** NIR/IR temporal pulse overlap: HHG suppression regime (d) and HHG enhancement regime (e).

with an overall HHG-signal reduction. From the raw dataset the most narrow, respective most broadband spectra, each containing 25 laser shots ($t_{\mathrm{intr}} = 25\,\mathrm{ms}$) are shown in Fig. 6.19. The HHG spectra from synthesized pulses can exhibit broadband emission and an increment in the overall flux (compared to HHG from the NIR channel alone). The precise emission characteristics exhibit a rich dependence upon changes in the RP and the CEP. Such HH emission is at or close to a regime for isolated attosecond pulse production without any gating technique being applied. Up to 0.6 mJ of pulse energy concentrated in a synthesized (sub-cycle) pulse are currently available to drive HHG. While HH emission from the individual channels is stable, the spectral shape for synthesized pulses experiences elevated fluctuations. Still the level of stability is sufficient to reveal complex dynamics with respect to changes of the RP. Increased stability will be achieved once the planned 3rd-stage-pump beam pointing stabilizers are in place. Furthermore the current mode matching of the two beams need to be characterized and optimized as well. This is an initial result and it needs to be

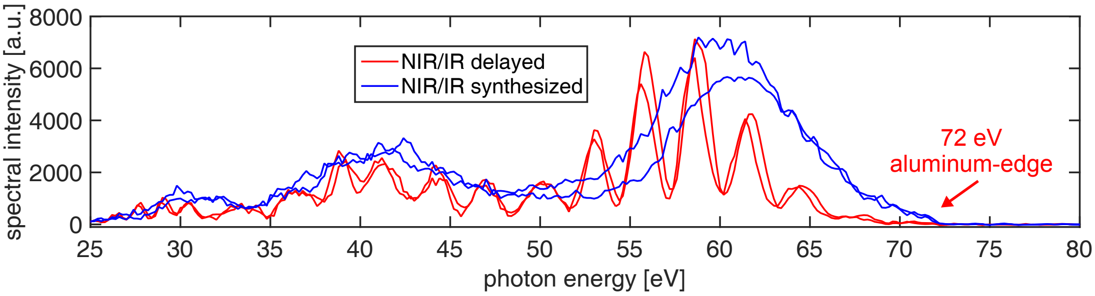

Figure 6.19: HHG emission from synthesized pulses (NIR/IR channel) in argon, where a fringed HHG spectra (red) is observed if both pulses are temporally displaced and strongly RP and CEP-dependent emission characteristics are observed when both pulses overlap temporally. This includes very broadband pulses (blue) potentially indicating IAPs.

carefully evaluated in which regime the HHG should be driven for optimal results with respect to energy ratios, beam modes of the NIR/IR, focusing and phase matching in the HHG source.

Chapter 7

Conclusions and Outlook

During this work our team reached the first stable operation of the parametric waveform synthesizer. We also demonstrated first and initial HHG emerging from such an advanced laser source. A repeatable spectral response and rich dynamics from the HHG in argon were observed when changing the synthesis parameters, including a shift of the cut-off photon energy. Active timing stabilization experiments on the first synthesizer prototype proved that such an interferometric setup could at least be stabilized well enough to allow for stable and repeatable waveform synthesis. The developed active timing synchronization infrastructure and instrumentation altogether with a reengineering of the whole setup achieved the overall required performance. The residual CEP and RP noise performance can even outperform commercial Ti:Sa amplifier systems and demonstrates that OPA based laser systems can have comparable or even better phase-noise performance. Via 2DSI measurements it was proven that the output of each spectral channel can be compressed close to its Fourier-transform limit and the synthesized pulses were characterized to be below one optical cycle ($\sim$0.6 cycles at 1.8μm). With these initial results an important milestone in next-generation laser sources is achieved.

Currently we are improving on remaining instabilities of the beam pointing and prepare the experiment for attosecond streaking. A full retrieval of the synthesized light-field transient via streaking will fully characterize this source and demonstrate the available range of synthesized waveforms. Furthermore an in-depth study on the HHG driven with sub-cycle pulses with non-sinusoidal transients could reveal new levels of control on the IAP production. Beside the extraordinary capability to generate IAPs without additional gating methods, this can also include enhanced control on the spectral shape of the IAP and potentially even its attochirp [89]. While attosecond science cooled down a bit to look for new laser sources for IAP generation, we now reached a point with our experiment to look for novel and suitable attosecond-science experiments.

Currently the HHG is driven in argon and emits mainly around 50-80 eV, although the synthesizer with its center-wavelength in the IR is optimized for higher photon cutoff energies in the water-window (284 eV to 543 eV). To drive this regime, neon or helium as source gas and a high-pressure gas cell is required and currently under development to properly phase-match the HHG in this region. With our synthesizer and the developed attosecond beamline we will be able to perform pump-probe experiments, where a sub-cycle optical pump and an IAP probe pulse is used. Such time-resolved experiments will be conducted with IAPs which have an advanced spectral shape and bandwidth due to custom-sculptured waveforms. Also the optical sub-cycle transient could give impulses to femto chemistry [199]. Great potential is also hold in achieving attosecond-pump attosecond-probe experiments and directly observe electron-dynamics in matter on their natural time scale. A sophisticated experimental design and tight focusing is required to achieve sufficient signal levels from IAP-IAP pump-probe experiments due to their low pulse energy in the nJ-range. Nevertheless solids can be studied and also molecules absorbed on surfaces offer a meaningful path to study photo chemistry and catalysis. One particular experiment would be observing the charge transfer time of sulphur atoms adsorbed to a ruthenium surface (c(4x2)S/Ru(0001)) which was studied by Föhlisch *et al.* with core-hole clock spectroscopy at a synchrotron facility [200]. In collaboration with the group of Prof. Wurth we plan to apply our synthesized IAPs centered at 160 eV (pump) and 40 eV (probe) to this system to study the earlier indirectly inferred charge-transfer time of 320 as directly in the time domain.

The fully passive nature of OP(CP)As offers a unique scaling potential if combined with the parallel synthesis approach to create mJ-level sub-cycle pulses. The OP(CP)As themselves or techniques like intra-pulse DFG allow to generate a spectral range from the UV [45] into the THz regime [158, 201]. Coherent combination can then synthesize sub-cycle pulses with multi-octaves of spectral bandwidth. OPA based amplifiers furthermore allow to implement chirped pulse amplification and with this ability a clear route to generate below few-cycle pulses from picosecond high-energy pump laser systems is given. Such high-power pump laser sources are Yb-doped thin-disk lasers or fiber-lasers and are slowly maturing for the demanding requirements of a parametric synthesizer. The demonstrated synthesizer can be implemented with Yb-based pump lasers, provided that a sufficient stability of the pump is reached and that the pulse duration allows for WL generation. In the parallel synthesizer scheme the beam emerging from the pump laser system are split off into multiple OP(CP)A pump beams. This circumstance could also be exploited by further extending the parallel approach further upstream intro the pump-laser system and use several laser amplifiers in parallel as proposed by G. M. Rossi [171]. This way the well-developed Ti:Sa laser technology could be scaled in repetition rate or total output a factor of 2, 4 or even 8 (depending on the number of output beams) over a single laser amplifier as currently used. This approach does not require any particular change to the current synthesizer scheme.

Bibliography

[1] Albert Einstein. Zur Quantentheorie der Strahlung. *Physikalische Zeitschrift*, 18:121–128, 1917.

[2] Theodore H Maiman. Stimulated optical radiation in ruby. *Nature*, 187(4736):493–494, 1960.

[3] B. P. Abbott etal. GW170817: Observation of Gravitational Waves from a Binary Neutron Star Inspiral. *Physical Review Letters*, 119(16):30–33, 2017.

[4] Thomas Gaumnitz, Arohi Jain, Yoann Pertot, Martin Huppert, Inga Jordan, Fernando Ardana-Lamas, and Hans Jakob Wörner. Streaking of 43-attosecond soft-X-ray pulses generated by a passively CEP-stable mid-infrared driver. *Optics Express*, 25(22):27506, 2017.

[5] E Goulielmakis, M Schultze, M Hofstetter, V S Yakovlev, J Gagnon, M Uiberacker, A L Aquila, E M Gullikson, D T Attwood, and R Kienberger. Single-Cycle Nonlinear Optics. *Science*, 320:1614–1618, 2008.

[6] Franck Lépine, Misha Y Ivanov, and Marc JJ Vrakking. Attosecond molecular dynamics: fact or fiction? *Nature Photonics*, 8(3):195, 2014.

[7] Mauro Nisoli, Piero Decleva, Francesca Calegari, Alicia Palacios, and Fernando Martín. Attosecond electron dynamics in molecules. *Chemical Reviews*, 117(16):10760–10825, 2017.

[8] Christopher Kupitz, Shibom Basu, Ingo Grotjohann, Raimund Fromme, Nadia A Zatsepin, Kimberly N Rendek, Mark S Hunter, Robert L Shoeman, Thomas A White, Dingjie Wang, et al. Serial time-resolved crystallography of photosystem II using a femtosecond x-ray laser. *Nature*, 513(7517):261, 2014.

[9] Henry N Chapman, Petra Fromme, Anton Barty, Thomas A White, Richard A Kirian, Andrew Aquila, Mark S Hunter, Joachim Schulz, Daniel P DePonte, Uwe Weierstall, et al. Femtosecond x-ray protein nanocrystallography. *Nature*, 470(7332):73, 2011.

[10] Zenghu Chang. Controlling attosecond pulse generation with a double optical gating. *Physical Review A*, 76(5):051403, 2007.

[11] Giuseppe Sansone, Luca Poletto, and Mauro Nisoli. High-energy attosecond light sources. *Nature Photonics*, 5(11):655, 2011.

[12] F. J. McClung and R. W. Hellwarth. Giant optical pulsations from ruby. *Journal of Applied Physics*, 33(3):828–829, 1962.

[13] Hans W. Mocker and R. J. Collins. Mode competition and self-locking effects in a Q-switched ruby laser. *Applied Physics Letters*, 7(10):270–273, 1965.

[14] D. E. Spence, P. N. Kean, and W. Sibbett. 60-fsec pulse generation from a self-mode-locked Ti:sapphire laser. *Optics Letters*, 16(1):42, 1991.

[15] D. H. Sutter, G. Steinmeyer, L. Gallmann, N. Matuschek, F. Morier-Genoud, U. Keller, V. Scheuer, G. Angelow, and T. Tschudi. Semiconductor saturable-absorber mirror-assisted Kerr-lens mode-locked Ti:sapphire laser producing pulses in the two-cycle regime. *Optics Letters*, 24(9):631, 1999.

[16] P. F. Moulton. Spectroscopic and laser characteristics of Ti:Al2O3. *Journal of the Optical Society of America B*, 3(1):125, 1986.

[17] Edmond B. Treacy. Optical Pulse Compression With Diffraction Gratings. *IEEE Journal of Quantum Electronics*, 5(9):454–458, 1969.

[18] R. L. Fork, O. E. Martinez, and J. P. Gordon. Negative dispersion using pairs of prisms. *Optics Letters*, 9(5):150, 1984.

[19] F. X. Kärtner, N. Matuschek, T. Schibli, U. Keller, H. A. Haus, C. Heine, R. Morf, V. Scheuer, M. Tilsch, and T. Tschudi. Design and fabrication of double-chirped mirrors. *Optics Letters*, 22(11):831, 1997.

[20] Nicolai Matuschek, X K Franz, and Ursula Keller. Theory of Double-Chirped Mirrors. *IEEE Journal on Selected Topics in Quantum Electronics*, 4(2):197–208, 1998.

[21] Li-Jin Chen, Michelle Y. Sander, and Franz X. Kärtner. Kerr-lens mode locking with minimum nonlinearity using gain-matched output couplers. *Optics Letters*, 35(17):2916–2918, 2010.

[22] E. P. Ippen. Principles of passive mode locking. *Applied Physics B Laser and Optics*, 58(3):159–170, 1994.

[23] G. Herink, B. Jalali, C. Ropers, and D. R. Solli. Resolving the build-up of femtosecond mode-locking with single-shot spectroscopy at 90 MHz frame rate. *Nature Photonics*, 10(5):321–326, 2016.

[24] R Ell, U Morgner, F. X. Kärtner, J G Fujimoto, E P Ippen, V Scheuer, G Angelow, T Tschudi, M J Lederer, A Boiko, and B Luther-Davies. Generation of 5-fs pulses and octave-spanning spectra directly from a Ti:sapphire laser. *Optics Letters*, 26(6):373, 2001.

[25] L Matos, D Kleppner, O Kuzucu, T R Schibli, J Kim, E P Ippen, and Franz X. Kärtner. Direct frequency comb generation from an octave-spanning, prismless Ti:sapphire laser. *Optics Letters*, 29(14):1683–1685, 2004.

[26] Shih-Hsuan Chia, Li-Jin Chen, Qing Zhang, Oliver D. Mücke, Guoqing Chang, and Franz X. Kärtner. Broadband continuum generation in mode-locked lasers with phase-matched output couplers. *Optics Letters*, 39(6):1445, 2014.

[27] M. Nisoli, G. Sansone, S. Stagira, S. De Silvestri, C. Vozzi, M. Pascolini, L. Poletto, P. Villoresi, and G. Tondello. Effects of carrier-envelope phase differences of few-optical-cycle light pulses in single-shot high-order-harmonic spectra. *Physical Review Letters*, 91(21):1–4, 2003.

[28] A. Apolonski, P. Dombi, G. G. Paulus, M. Kakehata, R. Holzwarth, Th Udem, Ch Lemell, K. Torizuka, J. Burgdörfer, T. W. Hänsch, and F. Krausz. Observation of Light-Phase-Sensitive Photoemission from a Metal. *Physical Review Letters*, 92(7):1–4, 2004.

[29] Michael Krüger, Markus Schenk, and Peter Hommelhoff. Attosecond control of electrons emitted from a nanoscale metal tip. *Nature*, 475(7354):78–81, 2011.

[30] Long-sheng Ma, Zhiyi Bi, Albrecht Bartels, Lennart Robertsson, Massimo Zucco, Robert S Windeler, Guido Wilpers, Chris Oates, Leo Hollberg, and Scott A Diddams. Optical Frequency Synthesis and Comparison with Uncertainty at the 10-19 Level. *Science*, 303(5665):1843–1845, mar 2004.

[31] S. Naumov, A. Fernandez, R. Graf, P. Dombi, F. Krausz, and A. Apolonski. Approaching the microjoule frontier with femtosecond laser oscillators. *New Journal of Physics*, 7, 2005.

[32] D. Strickland and G. Mourou. Compression of amplified chirped optical pulses. *Optics Communications*, 55(6):447–449, 1985.

[33] Isao Matsushima, Hidehiko Yashiro, and Toshihisa Tomie. 10 kHz 40 W Ti:sapphire regenerative ring amplifier. *Optics Letters*, 31(13):148–149, 2005.

[34] J. Seres, E. Seres, A. J. Verhoef, G. Tempea, C. Streli, P. Wobrauschek, V. Yakovlev, A. Scrinzi, C. Spielmann, and F. Krausz. Analysis and suppression of parasitic processes in noncollinear optical parametric amplifiers. *Nature*, 433(1):596, 2005.

[35] Tenio Popmintchev, Ming Chang Chen, Dimitar Popmintchev, Paul Arpin, Susannah Brown, Skirmantas127Ališauskas, Giedrius Andriukaitis, Tadas Balčiunas, Oliver D. Mücke, Audrius Pugzlys, Andrius Baltuška, Bonggu Shim, Samuel E. Schrauth, Alexander Gaeta, Carlos Hernández-García, Luis Plaja, Andreas Becker, Agnieszka Jaron-Becker, Margaret M. Murnane, and Henry C. Kapteyn. Bright coherent ultrahigh harmonics in the kev x-ray regime from mid-infrared femtosecond lasers. *Science*, 336(6086):1287–1291, 2012.

[36] A. Couairon and A. Mysyrowicz. Femtosecond filamentation in transparent media. *Physics Reports*, 441:47–189, 2007.

[37] L. Bergé, S. Skupin, R. Nuter, J. Kasparian, and J. P. Wolf. Ultrashort filaments of light in weakly ionized, optically transparent media. *Reports on Progress in Physics*, 70(10):1633–1713, 2007.

[38] M. Nisoli, S. De Silvestri, and O. Svelto. Generation of high energy 10 fs pulses by a new pulse compression technique. *Applied Physics Letters*, 68(20):2793–2795, 1996.

[39] M. Nisoli, S. De Silvestri, O. Svelto, R. Szipöcs, K. Ferencz, Ch. Spielmann, S. Sartania, and F. Krausz. Compression of high-energy laser pulses below 5 fs. *Optics Letters*, 22(8):522, 1997.

[40] Samuel Bohman, Akira Suda, Tsuneto Kanai, Shigeru Yamaguchi, and Katsumi Midorikawa. Generation of 50 fs, 50 mJ pulses at 1 kHz using hollow-fiber pulse compression. *Optics Letters*, 35(11):1887, 2010.

[41] A. L. Cavalieri, E. Goulielmakis, B. Horvath, W. Helml, M. Schultze, M. Fiess, V. Pervak, L. Veisz, V. S. Yakovlev, M. Uiberacker, A. Apolonski, F. Krausz, and R. Kienberger. Intense 1.5-cycle near infrared laser waveforms and their use for the generation of ultra-broadband soft-x-ray harmonic continua. *New Journal of Physics*, 9(07):1–12, 2007.

[42] R. R. Alfano and S. L. Shapiro. Observation of self-phase modulation and small-scale filaments in crystals and glasses. *Physical Review Letters*, 24(11):592–594, 1970.

[43] Andrius Baltuška, Zhiyi Wei, Maxim S. Pshenichnikov, and Douwe A. Wiersma. Optical pulse compression to 5 fs at a 1-MHz repetition rate. *Optics Letters*, 22(2):102, 1997.

[44] F. Silva, D. R. Austin, A. Thai, M. Baudisch, M. Hemmer, D. Faccio, A. Couairon, and J. Biegert. Multi-octave supercontinuum generation from mid-infrared filamentation in a bulk crystal. *Nature Communications*, 3(807):1–5, 2012.

[45] Giulio Cerullo and Sandro De Silvestri. Ultrafast optical parametric amplifiers. *Review of Scientific Instruments*, 74(1 I):1–18, 2003.

[46] J. A. Armstrong, N. Bloembergen, J. Ducuing, and P. S. Pershan. Interactions between Light Waves in a Nonlinear Dielectric. *Physical Review*, 127(6):1918–1939, 1962.

[47] David S Hum and Martin M Fejer. Quasi-phasematching. *Comptes Rendus Physique*, 8(2):180–198, 2007.

[48] Giulio Cerullo, M Nisoli, S Stagira, and Sandro De Silvestri. Sub-8-fs pulses from an ultrabroadband optical parametric amplifier in the visible. *Optics letters*, 23(16):1283–1285, 1998.

[49] Akira Shirakawa, Isao Sakane, and Takayoshi Kobayashi. Pulse-front-matched optical parametric amplification for sub-10-fs pulse generation tunable in the visible and near infrared. *Optics Letters*, 23(16):1292–1294, 1998.

[50] D. Brida, C. Manzoni, G. Cirmi, M. Marangoni, S. Bonora, P. Villoresi, S. De Silvestri, and G. Cerullo. Few-optical-cycle pulses tunable from the visible to the mid-infrared by optical parametric amplifiers. *Journal of Optics A: Pure and Applied Optics*, 12(1), 2010.

[51] D Brida, G Cirmi, C Manzoni, S Bonora, P. Villoresi, S. De Silvestri, and G Cerullo. Sub-two-cycle light pulses at 1.6 μm from an optical parametric amplifier. *Optics Letters*, 33(7):741, 2008.

[52] A. Dubietis, G. Jonušauskas, and A. Piskarskas. Powerful femtosecond pulse generation by chirped and stretched pulse parametric amplification in BBO crystal. *Optics Communications*, 88(4-6):437–440, 1992.

[53] Audrius Dubietis, Rytis Butkus, and Algis Petras Piskarskas. Trends in chirped pulse optical parametric amplification. *IEEE Journal on Selected Topics in Quantum Electronics*, 12(2):163–172, 2006.

[54] Alexander Gaydardzhiev, Ivailo Nikolov, Ivan Buchvarov, Valentin Petrov, and Frank Noack. Femtosecond optical parametric generators and amplifiers for the near infrared based on BiB 3 O 6. *Optics Express*, 16(4):750102, 2009.

[55] G. Arisholm, R. Paschotta, and T. Sudmeyer. Limits to the power scalability of high-gain optical parametric oscillators and amplifiers. *Journal of Optical Society of America B.*, 21(3):262, 2003.

[56] J. Bromage, J. Rothhardt, S. Hädrich, C. Dorrer, C. Jocher, S. Demmler, J. Limpert, A. Tünnermann, and J. D. Zuegel. Analysis and suppression of parasitic processes in noncollinear optical parametric amplifiers. *Optics Express*, 19(18):16797, 2011.

[57] Jan Rothhardt, Stefan Demmler, Steffen Hädrich, Jens Limpert, and Andreas Tünnermann. Octave-spanning OPCPA system delivering CEP-stable few-cycle pulses and 22 W of average power at 1 MHz repetition rate. *Optics Express*, 20(10):10870, 2012.

[58] Stephan Prinz, Matthias Haefner, Catherine Yuriko Teisset, Robert Bessing, Knut Michel, Yeon Lee, Xiao Tao Geng, Seungchul Kim, Dong Eon Kim, Thomas Metzger, and Marcel Schultze. CEP-stable, sub-6 fs, 300-kHz OPCPA system with more than 15 W of average power. *Optics Express*, 23(2):1388, 2015.

[59] Jochen Doerring, Alexander Killi, Uwe Morgner, Alexander Lang, Max Lederer, and Daniel Kopf. Period doubling and deterministic chaos in continuously pumped regenerative amplifiers. *Optics Express*, 12(8):1759, 2004.

[60] L. Xu, T. W. Hänsch, Ch. Spielmann, A. Poppe, T. Brabec, and F. Krausz. Route to phase control of ultrashort light pulses. *Optics Letters*, 21(24):2008, 1996.

[61] David J. Jones, Scott A. Diddams, Jinendra K. Ranka, Andrew Stentz, Robert S. Windeler, John L. Hall, and Steven T. Cundiff. Carrier-envelope phase control of femtosecond mode-locked lasers and direct optical frequency synthesis. *Science*, 288(5466):635–639, 2000.

[62] R Holzwarth, Th Udem, and T W Hänsch. Optical Frequency Synthesizer for Precision Spectroscopy. *Physical Review Letters*, 85(11):2264–2267, 2000.

[63] G. G. Paulus, F. Lindner, H. Walther, A. Baltuška, E. Goulielmakis, M. Lezius, and F. Krausz. Measurement of the phase of few-cycle laser pulses. *Physical Review Letters*, 91(25):1–4, 2003.

[64] A. M. Sayler, Tim Rathje, Walter Müller, Klaus Rühle, R. Kienberger, and G. G. Paulus. Precise, real-time, every-single-shot, carrier-envelope phase measurement of ultrashort laser pulses. *Optics Letters*, 36(1):1, 2011.

[65] William P. Putnam, Richard G. Hobbs, Phillip D. Keathley, Karl K. Berggren, and Franz X. Kärtner. Optical-field-controlled photoemission from plasmonic nanoparticles. *Nature Physics*, 13(4):335–339, 2017.

[66] A McPherson, G Gibson, H Jara, U Johann, T S Luk, I A Mcintyre, K Boyer, and C K Rhodes. Studies of multiphoton production of vacuum-ultraviolet. *Journal of the Optical Society of America B*, 4(4):595–601, 1987.

[67] M Ferray, A L'Huillier, X F Li, L A Lompre, G Mainfray, and C Manus. Multiple-harmonic conversion of 1064 nm radiation in rare gases. *Journal of Physics B: Atomic, Molecular and Optical Physics*, 21(3):31–35, 1988.

[68] Michael Yu Kuchiev. Atomic antenna. *JETP Letters*, 45(7):404–406, 1987.

[69] P. B. Corkum. Plasma perspective on strong field multiphoton ionization. *Physical Review Letters*, 71(13):1994–1997, 1993.

[70] D. von der Linde, T. Engers, G. Jenke, P. Agostini, G. Grillon, E. Nibbering, J.-P. Chambaret, P. F. Curley, A. Mysyrowicz, and A. Antonetti. Generation of High Order Harmonics from Solid Surfaces by Intense Femtosecond Laser Pulses. *Physical Review A*, 52(1):319–323, 1996.

[71] P. M. Kraus, A. Rupenyan, and H. J. Wörner. High-harmonic spectroscopy of Oriented OCS molecules: Emission of even and odd harmonics. *Physical Review Letters*, 109(23):1–6, 2012.

[72] N. Dudovich, O. Smirnova, J. Levesque, Y. Mairesse, M. Yu Ivanov, D. M. Villeneuve, and P. B. Corkum. Measuring and controlling the birth of attosecond XUV pulses. *Nature Physics*, 2(11):781–786, 2006.

[73] D. Schulze, M. Dörr, G. Sommerer, J. Ludwig, P. V. Nickles, T. Schlegel, W. Sandner, M. Drescher, U. Kleineberg, and U. Heinzmann. Polarization of the 61st harmonic from 1053-nm laser radiation in neon. *Physical Review A - Atomic, Molecular, and Optical Physics*, 57(4):3003–3007, 1998.

[74] Randy A. Bartels, Ariel Paul, Hans Green, Henry C. Kapteyn, Margaret M. Murnane, Sterling Backus, Ivan P. Christov, Yanwei Liu, David Attwood, and Chris Jacobsen. Generation of spatially coherent light at extreme ultraviolet wavelengths. *Science*, 297(5580):376–378, 2002.

[75] Richard L. Sandberg, Ariel Paul, Daisy A. Raymondson, Steffen Hädrich, David M. Gaudiosi, Jim Holtsnider, Ra'anan I. Tobey, Oren Cohen, Margaret M. Murnane, Henry C. Kapteyn, Changyong Song, Jianwei Miao, Yanwei Liu, and Farhad Salmassi. Lensless diffractive imaging using tabletop coherent high-harmonic soft-x-ray beams. *Physical Review Letters*, 99:098103, 2007.

[76] Tenio Popmintchev, Ming-chang Chen, Alon Bahabad, Michael Gerrity, Pavel Sidorenko, Oren Cohen, Ivan P Christov, Margaret M Murnane, and Henry C Kapteyn. Phase matching of high harmonic generation in the soft and hard X-ray regions of the spectrum. *PNAS*, 106(26):10516–10521, 2009.

[77] Andy Rundquist, Charles G. Durfee, Zenghu Chang, Catherine Herne, Sterling Backus, Margaret M. Murnane, and Henry C. Kapteyn. Phase-matched generation of coherent soft x-rays. *Science*, 280(5368):1412–1415, 1998.

[78] Angela Pirri, Chiara Corsi, and Marco Bellini. Enhancing the yield of high-order harmonics with an array of gas jets. *Physical Review A - Atomic, Molecular, and Optical Physics*, 78(1):1–4, 2008.

[79] Henry Kapteyn, Oren Cohen, Ivan Christov, and Margaret Murnane. Harnessing attosecond science in the quest for coherent X-rays. *Science*, 317(5839):775–778, 2007.

[80] Mette B. Gaarde, Jennifer L. Tate, and Kenneth J. Schafer. Macroscopic aspects of attosecond pulse generation. *Journal of Physics B: Atomic, Molecular and Optical Physics*, 41(13), 2008.

[81] M. Lewenstein, Ph Balcou, M. Yu Ivanov, Anne L'Huillier, and P. B. Corkum. Theory of high-harmonic generation by low-frequency laser fields. *Physical Review A*, 49(3):2117–2132, 1994.

[82] Jeffrey L. Krause, Kenneth J. Schafer, and Kenneth C. Kulander. High-order harmonic generation from atoms and ions in the high intensity regime. *Physical Review Letters*, 68(24):3535–3538, 1992.

[83] J. Tate, T. Auguste, H. G. Muller, P. Salières, P. Agostini, and L. F. Dimauro. Scaling of wave-packet dynamics in an intense midinfrared Field. *Physical Review Letters*, 98(1):1–4, 2007.

[84] P. Colosimo, G. Doumy, C. I. Blaga, J. Wheeler, C. Hauri, F. Catoire, J. Tate, R. Chirla, A. M. March, G. G. Paulus, H. G. Muller, P. Agostini, and L. F. Dimauro. Scaling strong-field interactions towards the classical limit. *Nature Physics*, 4(5):386–389, 2008.

[85] EL Falcão-Filho, VM Gkortsas, Ariel Gordon, and Franz X Kärtner. Analytic scaling analysis of high harmonic generation conversion efficiency. *Optics express*, 17(13):11217–11229, 2009.

[86] Giovanni Cirmi, Chien-Jen Lai, Eduardo Granados, Shu-Wei Huang, Alexander Sell, Kyung-Han Hong, Jeffrey Moses, Phillip Keathley, and Franz X. Kärtner. Cut-off scaling of high-harmonic generation driven by a femtosecond visible optical parametric amplifier. *Journal of Physics B: Atomic, Molecular and Optical Physics*, 45(20):205601, oct 2012.

[87] Chien-jen Lai, Giovanni Cirmi, Kyung-Han Hong, Jeffrey Moses, Shu-wei Huang, Eduardo Granados, Phillip Keathley, Siddharth Bhardwaj, and Franz X. Kärtner. Wavelength Scaling of High Harmonic Generation Close to the Multiphoton Ionization Regime. *Physical Review Letters*, 111(073901):1–5, 2013.

[88] A Gordon and F X Kärtner. Scaling of keV photon yield with drive wavelength. *Optics Express*, 13(8):2941, 2005.

[89] Dong Hyuk Ko, Kyung Taec Kim, Juyun Park, Jae Hwan Lee, and Chang Hee Nam. Attosecond chirp compensation over broadband high-order harmonics to generate near transform-limited 63 as pulses. *New Journal of Physics*, 12, 2010.

[90] Ferenc Krausz and Misha Ivanov. Attosecond physics. *Reviews of Modern Physics*, 81(1):163–234, 2009.

[91] Philippe Antoine, Anne L'huillier, and Maciej Lewenstein. Attosecond pulse trains using highâĂŞorder harmonics. *Physical Review Letters*, 77(7):1234–1237, 1996.

[92] P. M. Paul, E. S. Toma, P. Breger, G. Mullot, F. Augé, Ph Balcou, H. G. Muller, and P. Agostini. Observation of a train of attosecond pulses from high harmonic generation. *Science*, 292(5522):1689–1692, 2001.

[93] Frederik Böhle, Martin Kretschmar, Aurélie Jullien, Mate Kovacs, Miguel Miranda, Rosa Romero, Helder Crespo, Uwe Morgner, Peter Simon, Rodrigo Lopez-Martens, and Tamas Nagy. Compression of CEP-stable multi-mJ laser pulses down to 4 fs in long hollow fibers. *Laser Physics Letters*, 11(9), 2014.

[94] Reinhard Kienberger, Eleftherios Goulielmakis, Matthias Uiberacker, Andrius Baltuska, Vladislav Yakovlev, Ferdinand Bammer, Armin Scrinzi, Th Westerwalbesloh, Ulf Kleineberg, Ulrich Heinzmann, et al. Atomic transient recorder. *Nature*, 427(6977):817, 2004.

[95] N. H. Burnett, C. Kan, and P. B. Corkum. Ellipticity and polarization effects in harmonic generation in ionizing neon. *Physical Review A*, 51(5):3418–3421, 1995.

[96] Jie Li, Xiaoming Ren, Yanchun Yin, Kun Zhao, Andrew Chew, Yan Cheng, Eric Cunningham, Yang Wang, Shuyuan Hu, Yi Wu, Michael Chini, and Zenghu Chang. 53-attosecond X-ray pulses reach the carbon K-edge. *Nature Communications*, 8(1):1–5, 2017.

[97] Kun Zhao, Qi Zhang, Michael Chini, Yi Wu, Xiaowei Wang, and Zenghu Chang. Tailoring a 67 attosecond pulse through advantageous phase-mismatch. *Optics Letters*, 37(18):3891, 2012.

[98] E Goulielmakis. Direct Measurement of Light Waves. *Science*, 305(5688):1267–1269, 2004.

[99] M Hentschel, R Kienberger, Ch Spielmann, G A Reider, N Milosevic, T Brabec, P Corkum, U Heinzmann, M Drescher, and F Krausz. Attosecond metrology. *Nature*, 414, 2001.

[100] Eiji J. Takahashi, Pengfei Lan, Oliver D. Mücke, Yasuo Nabekawa, and Katsumi Midorikawa. Attosecond nonlinear optics using gigawatt-scale isolated attosecond pulses. *Nature Communications*, 4:1–9, 2013.

[101] Cheng Jin, Guoli Wang, Hui Wei, Anh Thu Le, and C. D. Lin. Waveforms for optimal sub-keV high-order harmonics with synthesized two- or three-colour laser fields. *Nature Communications*, 5:1–6, 2014.

[102] Cheng Jin, Guoli Wang, Anh Thu Le, and C. D. Lin. Route to optimal generation of soft X-ray high harmonics with synthesized two-color laser pulses. *Scientific Reports*, 4, 2014.

[103] L. E. Chipperfield, J. S. Robinson, J. W G Tisch, and J. P. Marangos. Ideal waveform to generate the maximum possible electron recollision energy for any given oscillation period. *Physical Review Letters*, 102(6):2–5, 2009.

[104] D J Kane and R Trebino. Characterization of Arbitrary Femtosecond Pulses Using Frequency-Resolved Optical Gating. *IEEE Journal of Quantum Electronics*, 29(2):571–579, 1993.

[105] Rick Trebino and Daniel J. Kane. Using phase retrieval to measure the intensity and phase of ultrashort pulses: frequency-resolved optical gating. *Journal of the Optical Society of America A*, 10(5):1101, 1993.

[106] Jonathan R. Birge, Helder M. Crespo, and Franz X. Kärtner. Theory and design of two-dimensional spectral shearing interferometry for few-cycle pulse measurement. *Journal of the Optical Society of America B*, 27(6):1165, 2010.

[107] Rocio Borrego-Varillas, Aurelio Oriana, Federico Branchi, Sandro De Silvestri, Giulio Cerullo, and Cristian Manzoni. Optimized ancillae generation for ultra-broadband two-dimensional spectral-shearing interferometry. *Journal of the Optical Society of America B*, 32(9):1851–1855, 2015.

[108] James W Cooley and John W Turkey. An Algorithm for the Machine Calculation of Complex Fourier Series. *Mathematics of Computation*, 19(90):297–301, 1965.

[109] Y Mairesse and P. Salieres. Attosecond Synchronization of High-Harmonic Soft X-rays. *Science*, 320(1843):1540–1543, 2003.

[110] Eleftherios Goulielmakis, Vladislav S Yakovlev, Adrian L Cavalieri, Matthias Uiberacker, Volodymyr Pervak, A Apolonski, Reinhard Kienberger, Ulf Kleineberg, and Ferenc Krausz. Attosecond control and measurement: lightwave electronics. *Science*, 317(5839):769–775, 2007.

[111] Y. Mairesse and F. Quéré. Frequency-resolved optical gating for complete reconstruction of attosecond bursts. *Physical Review A - Atomic, Molecular, and Optical Physics*, 71(1):1–4, 2005.

[112] O. V. Chekhlov, J. L. Collier, I. N. Ross, P. K. Bates, M. Notley, C. Hernandez-Gomez, W. Shaikh, C. N. Danson, D. Neely, P. Matousek, S. Hancock, and L. Cardoso. 35 J broadband femtosecond optical parametric chirped pulse amplification system. *Optics Letters*, 31(24):3665, 2006.

[113] T. W. Hänsch. A proposed sub-femtosecond pulse synthesizer using separate phase-locked laser oscillators. *Optics Communications*, 80(1):71–75, 1990.

[114] Cristian Manzoni, Oliver D. Mücke, Giovanni Cirmi, Shaobo Fang, Jeffrey Moses, Shu Wei Huang, Kyung Han Hong, Giulio Cerullo, and Franz X. Kärtner. Coherent pulse synthesis: Towards sub-cycle optical waveforms. *Laser and Photonics Reviews*, 9(2):129–171, 2015.

[115] Oliver D. Mücke, Shaobo Fang, Giovanni Cirmi, Giulio Maria Rossi, Shih Hsuan Chia, Hong Ye, Yudong Yang, Roland Mainz, Cristian Manzoni, Paolo Farinello, Giulio Cerullo, and Franz X. Kärtner. Toward Waveform Nonlinear Optics Using Multimillijoule Sub-Cycle Waveform Synthesizers. *IEEE Journal on Selected Topics in Quantum Electronics*, 21(5), 2015.

[116] A Bartels, S A Diddams, T M Ramond, and L Hollberg. Mode-locked laser pulse trains with subfemtosecond timing jitter synchronized to an optical reference oscillator. *Optics Letters*, 28(8):663–665, 2003.

[117] Han-Sung Chan, Zhi-Ming Hsieh, Wei-Hong Liang, A. H. Kung, Chao-Kuei Lee, Chien-Jen Lai, Ru-Pin Pan, and Lung-Han Peng. Synthesis and Measurement of UltrafastWaveforms from Five Discrete Optical Harmonics. *Science*, 331(March):1165–1168, 2011.

[118] A V Sokolov, D R Walker, D D Yavuz, G Y Yin, and S E Harris. Raman Generation by Phased and Antiphased Molecular States. *Physical Review Letters*, 85(3):562–565, 2000.

[119] Nicolas K Fontaine, Ryan P Scott, Linjie Zhou, Francisco M Soares, J P Heritage, and S J B Yoo. Real-time full-field arbitrary optical waveform measurement. *Nature Photonics*, 4:248–254, 2010.

[120] S E Harris and A V Sokolov. Subfemtosecond Pulse Generation by Molecular Modulation. *Physical Review Letters*, 81(14):1–4, 1998.

[121] Robert K Shelton. Phase-Coherent Optical Pulse Synthesis from Separate Femtosecond Lasers. *Science*, 293(5533):1286–1289, aug 2001.

[122] Lia Matos, Oliver D. Mücke, Jian Chen, and Franz X. Kärtner. Carrier-envelope phase dynamics and noise analysis in octave-spanning Ti:sapphire lasers. *Optics Express*, 14(6):2497–2511, 2006.

[123] Andrew J. Benedick, James G. Fujimoto, and Franz X. Kärtner. Optical flywheels with attosecond jitter. *Nature Photonics*, 6(2):97–100, 2012.

[124] T. R. Schibli, J. Kim, O. Kuzucu, J. T. Gopinath, S. N. Tandon, G. S. Petrich, L. A. Kolodziejski, J. G. Fujimoto, E. P. Ippen, and Franz X. Kärtner. Attosecond active synchronization of passively mode-locked lasers by balanced cross correlation. *Optics Letters*, 28(11):947, jun 2003.

[125] J. A. Cox, W. P. Putnam, A. Sell, A. Leitenstorfer, and F. X. Kärtner. Pulse synthesis in the single-cycle regime from independent mode-locked lasers using attosecond-precision feedback. *Optics Letters*, 37(17):3579, 2012.

[126] Zhiyi Wei. Generation of two-color femtosecond pulses by self-synchronizing Ti:sapphire and Cr:forsterite lasers. *Optics Letters*, 26(22):1806–1808, 2001.

[127] A. Wirth, M. Th Hassan, I. Grguraš, J. Gagnon, A. Moulet, T. T. Luu, S. Pabst, R. Santra, Z. A. Alahmed, A. M. Azzeer, V. S. Yakovlev, V. Pervak, F. Krausz, and E. Goulielmakis. Synthesized light transients. *Science*, 334(6053):195–200, 2011.

[128] M. Th Hassan, A. Wirth, I. Grguraš, A. Moulet, T. T. Luu, J. Gagnon, V. Pervak, and E. Goulielmakis. Attosecond photonics: Synthesis and control of light transients. *Review of Scientific Instruments*, 83(11), 2012.

[129] E. Goulielmakis, A. Wirth, I. Grguras, M. Hassan, J. Gagnon, A. Moulet, T. T. Luu, V. Pervak, and F. Krausz. Sub-Optical-Cycle Waveform Synthesis of Light. In *CLEO/Europe and EQEC 2011 Conference*. (Optical Society of America, 2013), talk: 5943029, 2011.

[130] T T Luu, M Garg, S. Yu. Kruchinin, A Moulet, M. Th. Hassan, and E Goulielmakis. Extreme ultraviolet high-harmonic spectroscopy of solids. *Nature*, 521:498–502, 2015.

[131] Yu-Chen Cheng, Chih-Hsuan Lu, and Yuan-Yao Lin. Supercontinuum generation in a multi-plate medium. *Optics Express*, 24(7):462–465, 2016.

[132] Peng He, Yangyang Liu, Kun Zhao, Hao Teng, Xinkui He, Pei Huang, Hangdong Huang, Shiyang Zhong, Yujiao Jiang, Shaobo Fang, Xun Hou, and Zhiyi Wei. High-efficiency supercontinuum generation in solid thin plates at 0.1 TW level. *Optics Letters*, 42(3):474, 2017.

[133] Yunpei Deng, Alexander Schwarz, Hanieh Fattahi, Moritz Ueffing, Xun Gu, Marcus Ossiander, Thomas Metzger, Volodymyr Pervak, Hideki Ishizuki, Takunori Taira, Takayoshi Kobayashi, Gilad Marcus, Ferenc Krausz, Reinhard Kienberger, and Nicholas Karpowicz. Carrier-envelope-phase-stable, 12 mJ, 1.5 cycle laser pulses at 2.1 μm. *Optics Letters*, 37(23):4973, 2012.

[134] Hanieh Fattahi, Helena G. Barros, Martin Gorjan, Thomas Nubbemeyer, Bidoor Alsaif, Catherine Y. Teisset, Marcel Schultze, Stephan Prinz, Matthias Haefner, Moritz Ueffing, Ayman Alismail, Lénárd Vámos, Alexander Schwarz, Oleg Pronin, Jonathan Brons, Xiao Tao Geng, Gunnar Arisholm, Marcelo Ciappina, Vladislav S. Yakovlev, Dong-Eon Kim, Abdallah M. Azzeer, Nicholas Karpowicz, Dirk Sutter, Zsuzsanna Major, Thomas Metzger, and Ferenc Krausz. Third-generation femtosecond technology. *Optica*, 1(1):45, 2014.

[135] C Manzoni and G Cerullo. Design criteria for ultrafast optical parametric amplifiers. *Journal of Optics*, 18(10):103501, 2016.

[136] Shu-Wei Huang, Giovanni Cirmi, Jeffrey Moses, Kyung-Han Hong, Siddharth Bhardwaj, Jonathan R. Birge, Li-Jin Chen, Enbang Li, Benjamin J.

Eggleton, Giulio Cerullo, and Franz X. Kärtner. High-energy pulse synthesis with sub-cycle waveform control for strong-field physics. *Nature Photonics*, 5(8):475–479, aug 2011.

[137] Shu-Wei Huang, Giovanni Cirmi, Jeffrey Moses, Kyung-Han Hong, Siddharth Bhardwaj, Jonathan R. Birge, Li-Jin Chen, Irina V. Kabakova, Enbang Li, Benjamin J. Eggleton, Giulio Cerullo, and Franz X. Kärtner. Optical waveform synthesizer and its application to high-harmonic generation. *Journal of Physics B: Atomic, Molecular and Optical Physics*, 45(7):074009, apr 2012.

[138] C. Manzoni, S.-W. Huang, G. Cirmi, P. Farinello, J. Moses, F. X. Kärtner, and G. Cerullo. Coherent synthesis of ultra-broadband optical parametric amplifiers. *Optics Letters*, 37(11):1880, 2012.

[139] Thomas Nubbemeyer, Martin Kaumanns, Moritz Ueffing, Martin Gorjan, Ayman Alismail, Hanieh Fattahi, Jonathan Brons, Oleg Pronin, Helena G. Barros, Zsuzsanna Major, Thomas Metzger, Dirk Sutter, and Ferenc Krausz. 1 kW, 200 mJ picosecond thin-disk laser system. *Optics Letters*, 42(7):1381, 2017.

[140] Adolf Giesen and Jochen Speiser. Fifteen years of work on thin-disk lasers: Results and scaling laws. *IEEE Journal on Selected Topics in Quantum Electronics*, 13(3):598–609, 2007.

[141] Marco Kienel, Michael Müller, Arno Klenke, Jens Limpert, and Andreas Tünnermann. 12 mJ kW-class ultrafast fiber laser system using multidimensional coherent pulse addition. *Optics Letters*, 41(14):3343, 2016.

[142] T. Y. Fan. Laser beam combining for high-power, high-radiance sources. *IEEE Journal on Selected Topics in Quantum Electronics*, 11(3):567–577, 2005.

[143] Tino Eidam, Stefan Hanf, Enrico Seise, Thomas V. Andersen, Thomas Gabler, Christian Wirth, Thomas Schreiber, Jens Limpert, and Andreas Tünnermann. Femtosecond fiber CPA system emitting 830 W average output power. *Optics Letters*, 35(2):94, 2010.

[144] Hüseyin Çankaya, Anne-Laure Calendron, Chun Zhou, Shih-Hsuan Chia, Oliver D. Mücke, Giovanni Cirmi, and Franz X. Kärtner. 40-uJ passively CEP-stable seed source for ytterbium-based high-energy optical waveform synthesizers. *Optics Express*, 24(22):25169, 2016.

[145] Hanieh Fattahi, Catherine Yuriko Teisset, Oleg Pronin, Atsushi Sugita, Roswitha Graf, Vladimir Pervak, Xun Gu, Thomas Metzger, Zsuzsanna

Major, Ferenc Krausz, and Alexander Apolonski. Pump-seed synchronization for MHz repetition rate, high-power optical parametric chirped pulse amplification. *Optics Express*, 20(9):9833, 2012.

[146] Shih-Hsuan Chia, Giovanni Cirmi, Shaobo Fang, Giulio M. Rossi, Oliver D. Mücke, and Franz X. Kärtner. Two-octave-spanning dispersion-controlled precision optics for sub-optical-cycle waveform synthesizers. *Optica*, 1(5):315–322, 2014.

[147] D Herrmann, C Homann, R Tautz, M Scharrer, P St J Russell, F Krausz, L Veisz, and E Riedle. Approaching the full octave: Noncollinear optical parametric chirped pulse amplification with two-color pumping. *Optics Express*, 18(18):2459–2461, 2010.

[148] L Veisz, D Rivas, G Marcus, X Gu, D Cardenas, J Mikhailova, A Buck, T Wittmann, C M S Sears, S Chou, J Xu, and G Ma. Generation and applications of sub-5-fs multi- 10-TW light pulses. In *In CLEO: 2013.* (Optical Society of America, 2013), talk: CG-4-3, 2013.

[149] L Veisz, D Rivas, G Marcus, X Gu, D Cardenas, J Mikhailova, A Buck, and T Wittmann. Sub-5-fs Multi-TW Optical Parametric Synthesizer. In *CLEO Pacific Rim Conference 2013.* (Optical Society of America, 2013), talk: CG-4-3, 2013.

[150] Anne Harth, Marcel Schultze, Tino Lang, Thomas Binhammer, Stefan Rausch, and Uwe Morgner. Two-color pumped OPCPA system emitting spectra spanning 1.5 octaves from VIS to NIR. *Optics Express*, 20(3):3076, 2012.

[151] Bruno E. Schmidt, Nicolas Thiré, Maxime Boivin, Antoine Laramée, François Poitras, Guy Lebrun, Tsuneyuki Ozaki, Heide Ibrahim, and François Légaré. Frequency domain optical parametric amplification. *Nature Communications*, 5(May):1–8, 2014.

[152] A M Weiner. Femtosecond Optical Pulse Shaping and Processing. *Progress in Quantum Electronics*, 19(94):161–237, 1995.

[153] Jerome Faure, Jiro Itatani, Subrat Biswal, Gilles Cheriaux, Leah R Bruner, Glen C Templeton, and Gerard Mourou. A spatially dispersive regenerative amplifier for ultrabroadband pulses. *Optics Communications*, 159:68–73, 1999.

[154] Nikolai B. Chichkov, Udo Bünting, Dieter Wandt, Uwe Morgner, Jörg Neumann, and Dietmar Kracht. Spatially dispersive regenerative amplification of ultrashort laser pulses. *Optics Express*, 17(26):24075, 2009.

[155] C P Hauri, M Bruck, W Kornelis, J Biegert, and U Keller. Generation of 14.8-fs pulses in a spatially dispersed amplifier. *Optics Letters*, 29(2):201–203, 2004.

[156] V Gruson, G Ernotte, P Lassonde, A Laramée, R Bionta, M Chaker, L Mauro, P B Corkum, H Ibrahim, B E Schmidt, and F Legaré. 2.5 TW two-cycle IR laser pulses via frequency domain optical parametric amplification. *Optics Express*, 25(22):2459–2461, 2017.

[157] Steven T. Cundiff and Andrew M. Weiner. Optical arbitrary waveform generation. *Nature Photonics*, 4(11):760–766, 2010.

[158] J. Ahn, A. Efimov, R. Averitt, and A. Taylor. Terahertz waveform synthesis via optical rectification of shaped ultrafast laser pulses. *Optics Express*, 11(20):2486, 2003.

[159] Stefan Rausch, Thomas Binhammer, Anne Harth, Franz X. Kärtner, and Uwe Morgner. Few-cycle femtosecond field synthesizer. *Optics Express*, 16(22):17410, 2008.

[160] Erik Zeek, Kira Maginnis, Sterling Backus, Ulrich Russek, Margaret Murnane, Gérard Mourou, Henry Kapteyn, and Gleb Vdovin. Pulse compression by use of deformable mirrors. *Optics Letters*, 24(7):493, 1999.

[161] Philippe Lassonde, Nicolas Thir, Tsuneyuki Ozaki, Antoine Larame, Maxime Boivin, and Heide Ibrahim. High Gain Frequency Domain Optical Parametric Amplification. *IEEE Journal on Selected Topics in Quantum Electronics*, 21(5), 2015.

[162] N Minkovski, G I Petrov, S M Saltiel, O Albert, and J Etchepare. Nonlinear polarization rotation and orthogonal polarization generation experienced in a single-beam configuration. *Journal of the Optical Society of America A*, 21(9):1659–1664, 2004.

[163] Theresa Buberl, Ayman Alismail, and Haochuan Wang. Self-compressed, spectral broadening of a Yb:YAG thin-disk amplifier. *Optics Express*, 24(10):4746–4748, 2016.

[164] Hanieh Fattahi, Haochuan Wang, Ayman Alismail, Gunnar Arisholm, Vladimir Pervak, Abdallah M. Azzeer, and Ferenc Krausz. Near-PHz-bandwidth, phase-stable continua generated from a Yb:YAG thin-disk amplifier. *Optics Express*, 24(21):24337, 2016.

[165] Hanieh Fattahi. Sub-cycle light transients for attosecond, X-ray, four-dimensional imaging. *Contemporary Physics*, 57(4):580–595, 2016.

[166] J. Moses, S.-W. Huang, K.-H. Hong, Oliver D. Mücke, E. L. Falcão-Filho, A. Benedick, F. Ö. Ilday, A. Dergachev, J. A. Bolger, B. J. Eggleton, and F. X. Kärtner. Highly stable ultrabroadband mid-IR optical parametric chirped-pulse amplifier optimized for superfluorescence suppression. *Optics Letters*, 34(11):1639, 2009.

[167] F. Tavella, A. Marcinkevičius, and F. Krausz. Investigation of the superfluorescence and signal amplification in an ultrabroadband multiterawatt optical parametric chirped pulse amplifier system. *New Journal of Physics*, 8, 2006.

[168] Thomas R Schibli, Onur Kuzucu, Jung-Won Kim, Erich P Ippen, James G Fujimoto, Franz X. Kärtner, Volker Scheuer, and Gregor Angelow. Toward Single-Cycle Laser Systems. *IEEE Journal on Selected Topics in Quantum Electronics*, 9(4):990–1001, 2003.

[169] L Veisz, D Rivas, G Marcus, X Gu, D Cardenas, J Mikhailova, A Buck, T Wittmann, C M S Sears, S Chou, J Xu, and G Ma. Timing jitter characterization of a high-energy sub-cycle optical waveform synthesizer. In *Advanced Solid State Lasers 2014 (ASSL)*. (Optical Society of America, 2013), talk: ATu5A-3, 2013.

[170] Physik Instrumente. *Datasheet - Piezo Actuator P-753.1CD.*

[171] Giulio Maria Rossi. *Parametric Waveform Synthesis.* PhD thesis, Universität Hamburg, 2018.

[172] Giulio Maria Rossi, Lu Wang, Roland E. Mainz, Hüseyin Çankaya, Franz X. Kärtner, and Giovanni Cirmi. CEP dependence of signal and idler upon pump-seed synchronization in optical parametric amplifiers. *Optics Letters*, 43(2):178, 2018.

[173] Andrius Baltuška, Matthias Uiberacker, Eleftherios Goulielmakis, Reinhard Kienberger, Vladislav S. Yakovlev, Thomas Udem, Theodor W. Hänsch, and Ferenc Krausz. Phase-Controlled Amplification of Few-Cycle Laser Pulses. *IEEE Journal on Selected Topics in Quantum Electronics*, 9(4):972–989, 2003.

[174] Christoph Gohle, Jens Rauschenberger, Takao Fuji, Thomas Udem, Alexander Apolonski, Ferenc Krausz, and Theodor W Hänsch. Carrier envelope phase noise in stabilized amplifier systems. *Optics Letters*, 30(18):2487, 2005.

[175] E Gagnon, I Thomann, A Paul, A L Lytle, S Backus, M M Murnane, H C Kapteyn, and A S Sandhu. Long-term carrier-envelope phase stability from

a grating-based, chirped pulse amplifier. *Optics Letters*, 31(12):1866–1868, 2006.

[176] Andrius Baltuška, Takao Fuji, and Takayoshi Kobayashi. Controlling the Carrier-Envelope Phase of Ultrashort Light Pulses with Optical Parametric Amplifiers. *Physical Review Letters*, 88(13):133901, 2002.

[177] C. Manzoni, G. Cirmi, D. Brida, S. De Silvestri, and G. Cerullo. Optical-parametric-generation process driven by femtosecond pulses: Timing and carrier-envelope phase properties. *Physical Review A - Atomic, Molecular, and Optical Physics*, 79(3):1–10, 2009.

[178] S. Hädrich, J. Rothhardt, M. Krebs, S. Demmler, J. Limpert, and A. Tünnermann. Improving carrier-envelope phase stability in optical parametric chirped-pulse amplifiers by control of timing jitter. *Optics Letters*, 37(23):4910, 2012.

[179] Kent R Wilson and Vladislav V Yakovlev. Ultrafast rainbow: tunable ultrashort pulses from a solid-state kilohertz system. *Journal of Optical Society of America B.*, 14(2):444–448, 1997.

[180] Anne-Laure Calendron, Hüseyin Çankaya, Giovanni Cirmi, and Franz X. Kärtner. White-light generation with sub-ps pulses. *Optics Express*, 23(11):13866, 2015.

[181] Marco Bellini and Theodor W. Hänsch. Phase-locked white-light continuum pulses: toward a universal optical frequency-comb synthesizer. *Optics Letters*, 25(14):1049, 2000.

[182] P Baum, S Lochbrunner, J Piel, and E Riedle. Phase-coherent generation of tunable visible femtosecond pulses. *Optics letters*, 28(3):185–187, 2003.

[183] Kemal Safak, Ming Xin, Qing Zhang, Shih-Hsuan Chia, Oliver D. Mücke, and Franz X. Kärtner. Jitter analysis of timing-distribution and remote-laser synchronization systems. *Optics Express*, 24(19):21752, 2016.

[184] Ming Xin, Kemal Safak, Michael Y. Peng, Aram Kalaydzhyan, Patrick T. Callahan, Wenting Wang, Oliver D. Mücke, and Franz X. Kärtner. Breaking the Femtosecond Barrier in Multi-Kilometer Timing Synchronization Systems. *IEEE Journal on Selected Topics in Quantum Electronics*, 23(3), 2017.

[185] Roland E. Mainz, Giulio Maria Rossi, Giovanni Cirmi, Yudong Yang, Oliver D. Mücke, and Franz X. Kärtner. High-dynamic-range arrival time control for flexible, accurate and precise parametric sub-cycle waveform synthesis. *Optics Express*, 25(4):3052, 2017.

[186] Giulio Maria Rossi, Roland E. Mainz, Franz X. Kärtner, Oliver D. Mücke, and Giovanni Cirmi. Device and method for determining a temporal relationship of laser pulses, and applications thereof, *Published European Patent Application* EP3264540A1, 2018.

[187] Daniele Brida, Cristian Manzoni, and Giulio Cerullo. Phase-locked pulses for two-dimensional spectroscopy by a birefringent delay line. *Optics Letters*, 37(15):3027, 2012.

[188] Ming Xin, Kemal Safak, Michael Y. Peng, Aram Kalaydzhyan, Wen Ting Wang, Oliver D. Mücke, and Franz X. Kärtner. Attosecond precision multi-kilometer laser-microwave network. *Light: Science and Applications*, 6(1):1–7, 2017.

[189] Hamamatsu. *Datasheet - CMOS Linear Image Sensor S10453*.

[190] Hamamatsu. *Datasheet - Near Infrared Image Sensor G9208-256W*.

[191] Roland E. Mainz, Giulio Maria Rossi, Franz X. Kärtner, Oliver D. Mücke, and Giovanni Cirmi. Optical parametric waveform synthesizer and method for synthesizing optical waveforms, *Published European Patent Application* EP3273550, 2018.

[192] Roland E. Mainz, Giulio Maria Rossi, Franz X. Kärtner, Oliver D. Mücke, and Giovanni Cirmi. Optical parametric waveform synthesizer and method for synthesizing optical waveforms, *Issued United States Patent* US2018024415, 2018.

[193] B. A. Shenoi. *Introduction to Digital Signal Processing and Filter Design*. Wiley, 2006.

[194] B P Bogert, M J R Healy, and J W Tukey. The quefrency alanysis of time series for echoes: Cepstrum, pseudo-autocovariance, cross-cepstrum, and saphe cracking. *Time Series Analysis*, 15:209–243, 1963.

[195] Thomas Drugman, Baris Buzkurt, and Thierry Dutoit. Causal-anticausal decomposition of speech using complex cepstrum for glottal source estimation. *Speech Communication*, 53(2011):855–866, 2005.

[196] Soo-chang Pei and Huei-shan Lin. Minimum-Phase FIR Filter Design Using Real Cepstrum. *IEEE Transactions on Circuits and Systems*, 53(10):1113–1117, 2006.

[197] Shih-Hsuan Chia, Fabian Scheiba, Giulio M. Rossi, Oliver D ücke, and Franz X Kärtner. Optimized octave-spanning ti:sapphire laser oscillator characterized by novel two-dimensional shearing interferometry. In

XXIth Conference on Ultrafast Phenomena 2018. (European Physical Society 2018), paper: CF-13-3, 2017.

[198] Yudong Yang. *A Novel Optical Tool for Controlling and Probing Ultrafast Surface Dynamics*. PhD thesis, Universität Hamburg, 2017.

[199] Ahmed H Zewail. Femtochemistry: Atomic-scale dynamics of the chemical bond. *The Journal of Physical Chemistry A*, 104(24):5660–5694, 2000.

[200] A. Föhlisch, P. Feulner, F. Hennies, A. Fink, D. Menzel, D. Sanchez-Portal, P. M. Echenique, and W. Wurth. Direct observation of electron dynamics in the attosecond domain. *Nature*, 436(7049):373–376, 2005.

[201] Haim Suchowski, Peter R. Krogen, Shu-Wei Huang, Franz X. Kärtner, and Jeffrey Moses. Octave-spanning coherent mid-IR generation via adiabatic difference frequency conversion. *Optics Express*, 21(23):28892, 2013.

Eidesstattliche Erklärung/Declaration on oath

Hiermit versichere ich an Eides statt, die vorliegende Dissertationsschrift selbst verfasst und keine anderen als die angegebenen Hilfsmittel und Quellen benutzt zu haben. Die eingereichte schriftliche Fassung entspricht der auf dem elektronischen Speichermedium. Die Dissertation wurde in der vorgelegten oder einer ähnlichen Form nicht schon einmal in einem früheren Promotionsverfahren angenommen oder als ungenügend beurteilt.

Ort Datum Unterschrift